Inverse modeling of carbonyl sulfide to constrain photosynthesis across scales

Ara Cho





Propositions

1. Uncertainties in the carbonyl sulfide budget limit the use of carbonyl sulfide for global gross primary productivity estimation. (this thesis)
2. Inverse modeling outcomes depend as strongly on methodological settings as on observational constraints. (this thesis)
3. Climate change limits the applicability of fixed leaf relative uptake ratios for gross primary productivity estimation. (this thesis)
4. Ineffective communication reduces society's ability to take meaningful action against climate change.
5. Interdisciplinary research operates on the limits of individual expertise.
6. Implementing complex coupling processes in models does not guarantee process understanding.
7. Artificial intelligence lowers barriers to research participation for structurally disadvantaged groups.

Propositions belonging to the thesis, entitled

Inverse modeling of carbonyl sulfide to constrain photosynthesis across scales

Ara Cho
Wageningen, 10 June 2026

Inverse modeling of carbonyl sulfide to constrain photosynthesis across scales

Ara Cho

Thesis committee

Promotor

Prof. Dr M.C. Krol
Professor Air Quality and Atmospheric Chemistry
Wageningen University & Research

Co-promotor

Dr L.M.J. Kooijmans-de Vries
Energy Data Expert, System Operations
Alliander N.V., Arnhem

Other members

Prof. Dr R.D. Sheil, Wageningen University & Research
Dr L. Wingate, French National Institute for Agriculture, Food and Environment, Villenave d'Ornon, France
Prof. Dr S.C. Dekker, Netherlands Institute of Ecology (NIOO-KNAW), Utrecht University
Prof. Dr S. Houweling, Vrije Universiteit Amsterdam

This research was conducted under the auspices of the Graduate School for Socio-Economic and Natural Sciences of the Environment (SENSE)

Inverse modeling of carbonyl sulfide to constrain photosynthesis across scales

Ara Cho

Thesis

submitted in fulfilment of the requirements for the degree of doctor
at Wageningen University
by the authority of the Rector Magnificus,
Prof. Dr C. Kroeze,
in the presence of the
Thesis Committee appointed by the Academic Board
to be defended in public
on Wednesday 10 June 2026
at 3:30 p.m. in the Omnia Auditorium.

Ara Cho
Inverse modeling of carbonyl sulfide to constrain photosynthesis across scales
162 pages.

PhD thesis, Wageningen University, Wageningen, the Netherlands (2026)
With references, with summary in English

https://doi.org/10.18174/681148

Contents

Contents i

1 Introduction 1
- 1.1 Climate Change . . . 1
- 1.2 Global carbon cycle . . . 2
- 1.3 GPP estimation . . . 3
  - 1.3.1 Limitations of previous methods . . . 3
  - 1.3.2 New approach with carbonyl sulfide . . . 5
  - 1.3.3 Leaf Relative Uptake . . . 6
  - 1.3.4 Diurnal variation of CO_2 and COS . . . 7
- 1.4 COS global cycle . . . 9
  - 1.4.1 Global atmosphere mole fractions . . . 9
  - 1.4.2 COS sources and sinks . . . 10
  - 1.4.3 Unknown sources and sinks for COS . . . 13
- 1.5 COS observations . . . 15
  - 1.5.1 Plant chamber experiments . . . 15
  - 1.5.2 Canopy observation . . . 16
  - 1.5.3 Global observations . . . 16
- 1.6 Simulating COS at different scales . . . 17
  - 1.6.1 Leaf conductance model . . . 18
  - 1.6.2 Land surface model . . . 18
  - 1.6.3 Global chemical transport model . . . 19
- 1.7 Inverse modeling . . . 19
  - 1.7.1 Cost function . . . 20
  - 1.7.2 Optimizers and 4D-Var . . . 20
  - 1.7.3 Evaluation . . . 21
- 1.8 Objective and thesis outline . . . 22

2 Leaf chamber experiments on the COS compensation point 25
- 2.1 Introduction . . . 26
- 2.2 Materials and Methods . . . 27
  - 2.2.1 Leaf gas-exchange measurements . . . 27
  - 2.2.2 Conductance model . . . 31
  - 2.2.3 Indirectly derived COS compensation point . . . 37
  - 2.2.4 Parameter optimization . . . 38
  - 2.2.5 Error statistics . . . 42
- 2.3 Results . . . 43
  - 2.3.1 Experiments . . . 43

2.3.2 Model-assisted analysis . . . 45
2.4 Discussion . . . 50
2.4.1 Uncertainties in measurements and models . . . 52
2.4.2 Possible causes of a COS compensation point . . . 53
2.4.3 Impact of COS compensation point on $V_{\mathrm{max,CA}}$ . . . 55
2.4.4 Consequences for the COS global budget . . . 55

3 Optimizing parameters in the simple biosphere model 56
3.1 Introduction . . . 58
3.2 Methodology . . . 60
3.2.1 Modelling COS leaf uptake . . . 60
3.2.2 Observations . . . 62
3.2.3 Optimization . . . 65
3.2.4 SiB4 simulations . . . 68
3.2.5 Error reduction and statistics . . . 68
3.3 Results and discussion . . . 69
3.3.1 Impact of each conductance . . . 69
3.3.2 Optimization performance . . . 69
3.3.3 Optimized parameters . . . 70
3.3.4 Optimized temperature response . . . 72
3.3.5 Application in SiB4 . . . 73
3.4 Conclusion . . . 77
A3. Appendices . . . 79
A3.1 State variable error settings . . . 79
A3.2 Posterior uncertainties . . . 79

4 Simultaneous optimization of global COS and CO_2 83
4.1 Introduction . . . 85
4.2 Data and methods . . . 87
4.2.1 In-situ observations . . . 88
4.2.2 Aircraft observations . . . 88
4.2.3 Forward simulation of CO_2 and COS atmospheric mole fraction . . . 88
4.2.4 Land surface model . . . 92
4.2.5 Coupling of CO_2 and COS . . . 93
4.2.6 Inverse model . . . 93
4.2.7 Optimization scenarios . . . 95
4.2.8 Statistical indices . . . 95
4.3 Results . . . 96
4.3.1 Convergence results . . . 96
4.3.2 Evaluation with surface-based observations . . . 97
4.3.3 Evaluation of the simulated vertical profiles . . . 100
4.3.4 Optimized COS surface fluxes . . . 102
4.3.5 Optimized CO_2 surface fluxes . . . 108
4.4 Discussion . . . 114
4.4.1 Direction to improve the coupling system . . . 114
4.4.2 Evaluation of COS vegetation flux scenarios . . . 116
4.4.3 Implications for the global budgets of CO_2 and COS . . . 117
4.5 Conclusion . . . 118
A4. Appendices . . . 120

5 General discussion & Synthesis **124**
5.1 Integrated summary across scales . . . 124
5.2 Methodological limitations and uncertainties . . . 125
5.2.1 Limitations in COS observations . . . 126
5.2.2 Limits to identify parameters . . . 127
5.2.3 Structural simplification in land surface model . . . 128
5.3 Cross-scale linkages and interpretation . . . 128
5.3.1 Mesophyll conductance and COS compensation point . . . 128
5.3.2 Stomatal conductance and diurnal dynamics . . . 129
5.3.3 Remaining gaps in the global COS budget . . . 131
5.4 Future research directions . . . 131
5.4.1 Refining the physiological basis of COS leaf uptake . . . 131
5.4.2 Improving land surface models . . . 132
5.4.3 Enhancing the global CO_2–COS coupled 4D-Var system . . . 132
5.5 Outlook for estimating GPP from COS vegetation flux . . . 133

References **135**

Summary **154**

Acknowledgements **155**

Authorship statement **157**

List of Publications **159**

Education certificate **160**

Chapter 1

Introduction

1.1 Climate Change

The 2011–2020 global surface temperatures increased with 1.1 °C compared to the period 1850–1900, mainly due to increasing greenhouse gas (GHG) emissions (Intergovernmental Panel on Climate Change, 2023). According to the IPCC 2023 report, the largest share and growth in gross GHG emissions occurred in carbon dioxide (CO_2) from fossil fuel combustion and industrial processes, followed by methane (CH_4). The atmospheric mole fractions (hereafter referred to as "concentrations" in IPCC terminology) of these gases are primarily driven by human activities and significantly contribute to the greenhouse effect and global warming.

While increases in the mole fractions of the CO_2 and CH_4 are primarily driven by human activities, the dynamics of water vapor (H_2O)—the most abundant GHG in the atmosphere—are primarily governed by natural processes. Water vapor levels are influenced by temperature through processes such as evaporation and condensation. Unlike CO_2 and CH_4, variations in H_2O primarily act as a feedback mechanism that amplifies warming (Manabe et al., 1967). As atmospheric temperatures increase due to the enhanced greenhouse effect from CO_2 and CH_4, this warmer air can hold more water vapor, leading to higher H_2O levels through enhanced evaporation. Thus, while water vapor itself does not initiate warming, it significantly strengthens the warming effect initiated by other GHGs through a positive feedback loop. This feedback process highlights the critical role of CO_2 and CH_4 in climate change.

The atmospheric mole fractions of CO_2 have increased markedly above preindustrial levels since the onset of the industrial era. CO_2 mole fractions rose from about 278 $\mu\mathrm{mol\,mol}^{-1}$ in 1750, a commonly used reference for preindustrial conditions, to 419.3 $\pm$ 0.1 $\mu\mathrm{mol\,mol}^{-1}$ by 2022 (Friedlingstein et al., 2025). During the early industrial era, this increase was primarily driven by deforestation and land-use changes (Canadell et al., 2023). Since the 1950s, however, fossil fuel combustion has become the dominant source of emissions, and its contribution has continued to rise (Friedlingstein et al., 2023). These trends are clearly illustrated in Fig. 1.1, where lower panel shows the sharp increase in greenhouse gas emissions, particularly CO_2 from fossil fuels and industry, and upper panel depicts the corresponding rise in atmospheric mole fractions of CO_2, CH_4, and N_2O, as assessed in IPCC AR6 (Intergovernmental Panel on Climate Change, 2023). Together, these panels illustrate the close correspondence between human-driven emissions and atmospheric mole fractions of the GHGs, emphasizing the importance of quantifying surface fluxes for better prediction of future GHG mole fractions. Particularly, CO_2 surface fluxes collectively constitute the global carbon cycle, which integrates sources, sinks, and exchanges of carbon between the atmosphere, land, and oceans. The following section describes the global carbon cycle in more detail.

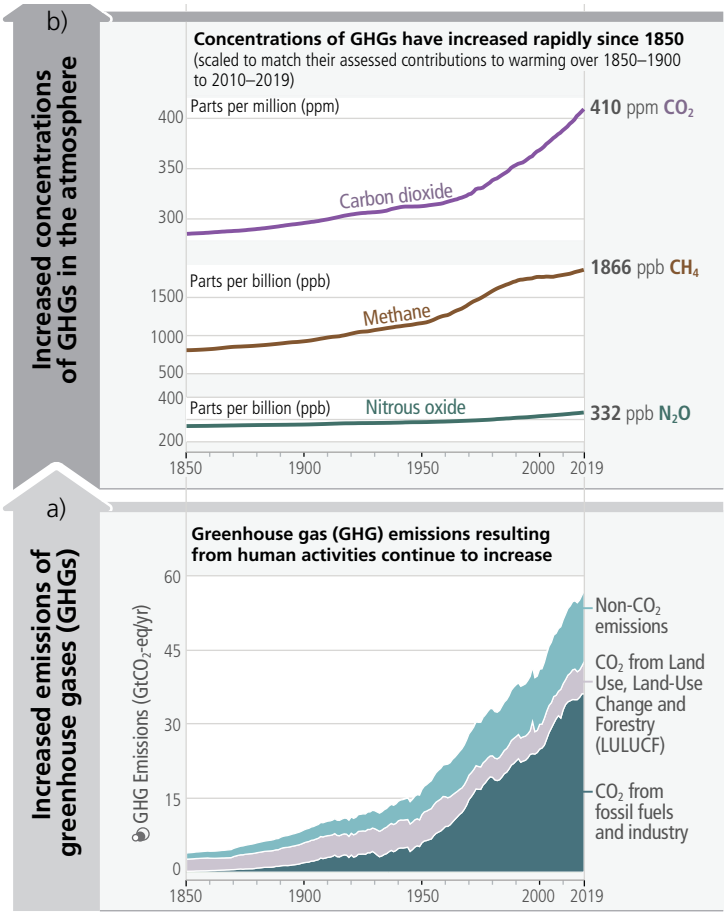


Figure 1.1: Increase in greenhouse gases (GHGs) emissions (a, lower) and corresponding rise in atmospheric mole fractions of GHGs (b, upper) from 1850 to 2019. Adapted from (Intergovernmental Panel on Climate Change, 2023). Texts in the original figure use the term "concentration", while we use the more correct term mole fraction.

1.2 Global carbon cycle

The atmospheric mole fractions of CO_2 are regulated by the balance between global sources and sinks. These include (1) fossil fuel combustion and industrial processes (F_{ff}), (2) land-use changes caused by human activity (F_{luc}), (3) ocean uptake (F_{oc}), and (4) terrestrial biosphere uptake (F_{bio}).

Figure 1.2 illustrates the global CO_2 budget between 2014 and 2023 based on bottom-up calculations (Friedlingstein et al., 2025). During this period, F_{ff} and F_{luc} dominate the sources, while F_{oc} and F_{bio} act as major sinks, with the residual stored in the atmosphere. The thin arrows indicate the large gross natural carbon exchanges that underlie the net fluxes. On land, gross primary production (GPP) and total ecosystem respiration (TER) each amount

to roughly $\pm$ 130 Pg C yr^{-1}, nearly balancing each other and yielding only a small net land-atmosphere flux (sink, $\approx$ 3.2 Pg C yr^{-1}). Similarly, the ocean exhibits large gross uptake and outgassing fluxes that largely cancel, resulting in a comparatively small net oceanic sink ($\approx$ 2.9 Pg C yr^{-1}). Together, these gross fluxes highlight the dynamic character of the natural carbon cycle, in contrast to the predominantly unidirectional anthropogenic emissions. Building on this context, the source–sink framework is further employed in Chapter 4, where CO_2 and COS are coupled within an atmospheric chemical transport model.

In the Global Carbon Budget framework based on bottom-up estimates, F_{luc} represents a broad category of processes, including deforestation, afforestation, forest degradation, regrowth, peat burning, and peat drainage (Friedlingstein et al., 2025). In contrast, in the inverse modeling framework applied in Chapter 4 of this thesis, anthropogenic fire emissions are represented explicitly as F_{fr}, whereas natural wildfires are included within the net biosphere flux, F_{bio}. This distinction underscores a fundamental difference between bottom-up and top-down approaches in the treatment of land-use change and fire emissions.

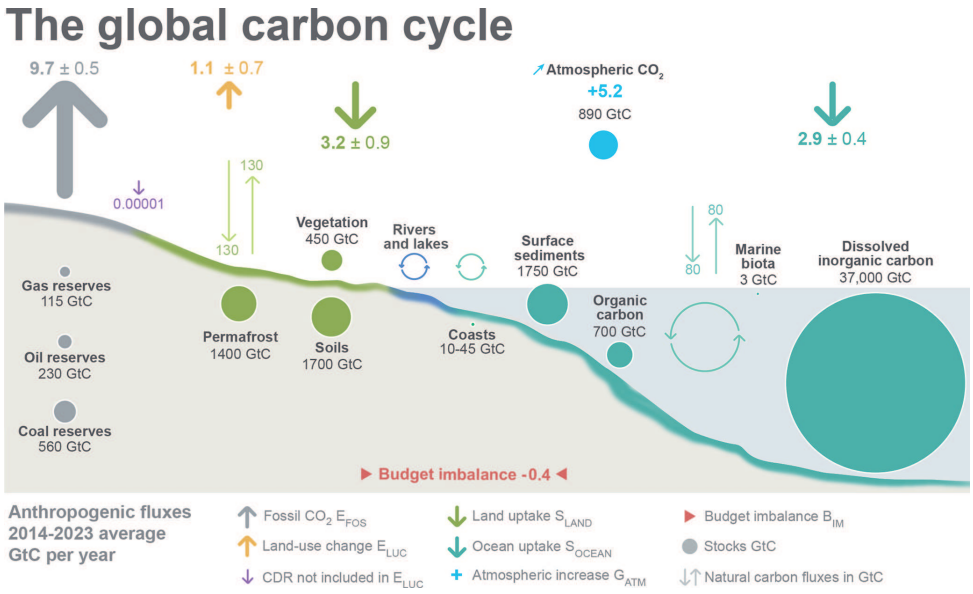


Figure 1.2: Global carbon cycle from 2014 to 2023. The values are the fluxes with their uncertainty given in units Gt C yr^{-1} (1 Gt C yr^{-1} = 1 Pg C yr^{-1}). The figure is adopted from Friedlingstein et al. (2025). Notation in parentheses (e.g., F_{ff}, F_{luc}, F_{bio}, and F_{oc}) corresponds to that used consistently throughout this dissertation. Upward direction indicates sources, and downward direction indicates sinks.

1.3 GPP estimation

1.3.1 Limitations of previous methods

F_{bio}, also known as net ecosystem exchange (NEE), represents the net balance of CO_2 absorbed by ecosystems (GPP) and released through respiration (TER). As illustrated by the thin arrows in Fig. 1.2, NEE corresponds to the small imbalance of these two large opposing fluxes, which makes it highly sensitive to uncertainties in either GPP or TER.

Figure 1.3 shows GPP estimates from multiple processes based terrestrial ecosystem models (Sitch et al., 2015), as plotted by Stinecipher et al. (2022). Although the models were driven by the same climate forcings, differences in ecosystem process parameterizations led to large variations in simulated GPP, particularly in low-latitude regions. Inter-model variability directly propagates into NEE estimates, resulting in divergent representations of the global carbon budget.

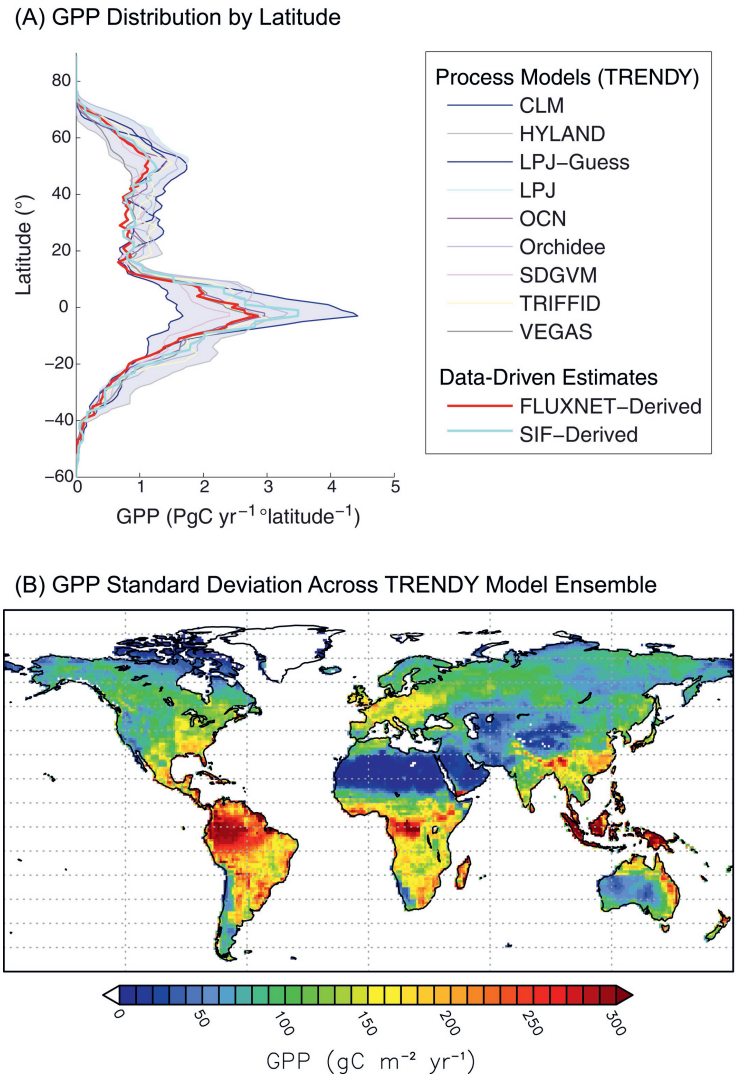


Figure 1.3: Latitudinal distribution of estimated GPP (A) from multiple process-based terrestrial ecosystem models and from observation-based estimates, and the standard deviation of GPP across the model ensemble (B). Adapted from Stinecipher et al. (2022).

While NEE can be directly measured using the eddy covariance (EC) method, estimat-

ing GPP is more challenging due to the simultaneous occurrence of TER. Several indirect approaches have been developed to partition NEE into GPP and TER, but uncertainties remain. The traditional method relies on nighttime NEE, assumed to represent respiration, in combination with temperature response curves (Reichstein et al., 2005). However, this approach is limited by the difficulty of measurements in the stable nocturnal boundary layer (Aubinet, 2008) and by the fact that temperature-based assumptions, largely derived from temperate ecosystems, are less applicable in tropical regions where other environmental drivers dominate respiration (Restrepo-Coupe et al., 2013).

Machine learning techniques have also been applied to improve flux partitioning. More recently, deep learning–based hybrid approaches, such as multi-layer neural networks, have shown potential to better capture nonlinear responses and site-specific variability in flux partitioning. However, despite these advances, their sensitivity to input dataset quality, limitations in training sample representativeness, and reduced performance in out-of-sample or disparate climate/biome regimes indicate that improvements over traditional methods are not uniformly large. (Desai et al., 2008; Tramontana et al., 2020; Chen et al., 2024).

The regression method using satellite-derived solar-induced fluorescence (SIF) has also been widely investigated (Van Der Tol et al., 2014; Frankenberg et al., 2011; Frankenberg et al., 2012; Parazoo et al., 2014; Bowman et al., 2017), yet its application remains limited by the incomplete characterization of how SIF–GPP relationships vary across environmental and phenological contexts (Chen et al., 2021; Paul-Limoges et al., 2018; Norton et al., 2019). Wang et al. (2021) emphasized that the GPP–SIF relationship is jointly regulated by multiple climate variables, and its sensitivity to environmental conditions across regions highlights the need to account for climate differences when modeling GPP using satellite-based SIF.

Isotopic flux partitioning, which uses stable isotopic signatures in photosynthesis and respiration, presents another alternative, but is restricted by insufficient knowledge of isotopic behavior and precision of measurement (Wehr et al., 2015).

1.3.2 New approach with carbonyl sulfide

Alternative tracers for GPP estimation, such as carbonyl sulfide (COS), have been proposed to improve constraints on global GPP estimates (Campbell et al., 2008; Montzka et al., 2007; Berry et al., 2013). COS is a trace gas in the atmosphere with a relatively stable mole fraction of approximately 500 parts per trillion ($\mathrm{pmol\,mol^{-1}}$) and a long atmospheric life time (2–3 years), which allows it to be well mixed globally (Montzka et al., 2007). This gas is taken up by plants in a manner similar to CO_2 during photosynthesis, but unlike CO_2, it is assumed not to be released during respiration. This unique property makes COS an effective proxy for isolating GPP from NEE.

Berry et al. (2013) introduced a modeling framework for COS leaf uptake, assuming that COS exchange can be linearly expressed based on CO_2 assimilation pathways. Building on this foundation, Lai et al. (2024) provided global GPP estimates from COS uptake that are more consistent with isotope- and respiration-based constraints, particularly strengthening tropical GPP estimates where satellite-based approaches face observational limitations.

To understand how COS functions as a tracer at the leaf level, Figure 1.4 illustrates the conceptual cross-section of leaf exchange for COS and CO_2 (Berry et al., 2013). The figure highlights four sequential processes: (1) boundary layer diffusion, (2) stomatal conductance, (3) mesophyll diffusion, and (4) biochemical activity. In this dissertation, however, processes (3) and (4) are collectively referred to as mesophyll conductance, consistent with the terminology adopted in the following chapters. Both gases enter the leaf through the same physical pathway, consisting of the leaf boundary layer and the stomatal pores. The conductance along

this pathway is commonly inferred from H_2O diffusion and further modulated by the specific molecular properties of each gas.

Once inside the mesophyll cells, COS undergoes rapid and effectively irreversible hydrolysis, primarily catalyzed by the enzyme carbonic anhydrase (CA) (Protoschill-Krebs et al., 1996). Due to the short residence time of COS in leaves, this reaction proceeds efficiently before COS can diffuse back out (Gillon et al., 2001). In contrast, CO_2 is fixed more slowly through carboxylation by RuBisCO, whose catalytic rate is orders of magnitude lower than that of CA. This enzymatic contrast is reflected in the biochemical activity conductance values: 0.233 $\mathrm{mol\,m^{-2}\,s^{-1}}$ for COS versus only 0.023 $\mathrm{mol\,m^{-2}\,s^{-1}}$ for CO_2 in Fig. 1.4. Consequently, the mole fractions of COS decline much more steeply from ambient air to the mesophyll cells compared to CO_2.

Hydrolysis of COS by CA produces CO_2 and H_2S through the following reaction (Schenk et al., 2004):

$$COS + H_2O \leftrightarrow HCOOS^- + H^+ \leftrightarrow H_2S + CO_2. \tag{1.1}$$

COS reacts with water in the mesophyll cells to form $HCOOS^{-1}$ and H^+, which further decompose into H_2S and CO_2. The high solubility of $HCOOS^-$ and H_2S in plant and soil water makes the reverse reaction highly unfavorable (Schenk et al., 2004). This property establishes COS as a reliable tracer for GPP estimation, offering a unique advantage over traditional methods.

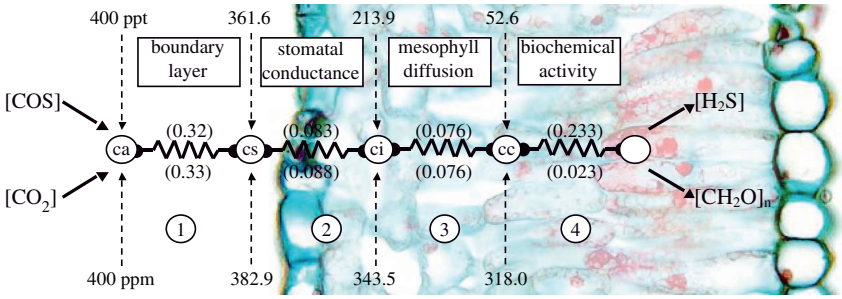


Figure 1.4: Schematic leaf uptake pathways of COS and CO_2 in C_3 plants (adopted from Berry et al. (2013)). Four conductances ($\mathrm{mol\,m^{-2}\,s^{-1}}$), indicated by numbers in parentheses in the figure, are known to play a role in the exchange process: (1) Boundary layer conductance, (2) stomatal conductance, (3) mesophyll conductance, (4) biochemical conductance. c_a, c_s, c_i, and c_c indicate the mole fractions at the interface of each two layers. In this dissertation, conductances (3) and (4) are collectively referred to as mesophyll conductance.

1.3.3 Leaf Relative Uptake

Assuming a highly unfavorable reverse reaction of COS leaf uptake, the COS leaf uptake has a linear relationship with CO_2 photosynthesis rate (Sandoval-Soto et al., 2005; Campbell et al., 2008). Consequently, GPP can be estimated if we know the leaf relative uptake (LRU, -) of COS and CO_2 (Asaf et al., 2013; Commane et al., 2015; Kooijmans et al., 2019; Spielmann et al., 2023). LRU is defined as the ratio of the deposition velocity of COS (V_{COS}, $\mathrm{mol\,m^{-2}\,s^{-1}}$) to that of CO_2 (V_{CO2}, $\mathrm{mol\,m^{-2}\,s^{-1}}$), normalized by ambient mole fractions:

$$LRU = \frac{V_{COS}}{V_{CO2}} = \frac{A_{COS}}{[COS]_a}(\frac{A_{CO2}}{[CO_2]_a})^{-1}. \quad (1.2)$$

Here, A_{COS} ($\mathrm{pmol\,m^{-2}\,s^{-1}}$) and A_{CO2} ($\mu\mathrm{mol\,m^{-2}\,s^{-1}}$) represent the leaf uptake rates of COS and CO_2, respectively, while $[COS]_a$ ($\mathrm{pmol\,mol^{-1}}$) and $[CO_2]_a$ ($\mu\mathrm{mol\,mol^{-1}}$) denote their ambient mole fractions. Campbell et al. (2008) reported an LRU value of approximately 2.2 on the leaf scale and 5.7 on the ecosystem scale, where the latter represents total net CO_2 flux consisting of A_{CO2} and respiration instead of considering only A_{CO2}.

If the LRU would remain constant across all environments, GPP could be readily estimated when global COS uptake by the biosphere would be known. However, recent studies show that LRU varies with environmental conditions and plant physiological traits, including species-specific differences (e.g., Stimler et al., 2010). Studies in various regions have explored how LRU is influenced by changes in environmental factors. For instance, data from Hyytiälä, Finland (see Figure 1.5) demonstrate how LRU varies with photosynthetically active radiation (PAR) (Stimler et al., 2010; Stimler et al., 2011; Sun et al., 2018b; Maseyk et al., 2014; Kooijmans et al., 2019), vapor pressure deficit (VPD)(Protoschill-Krebs et al., 1996; Kooijmans et al., 2019; Stimler et al., 2010; Sun et al., 2018b), and temperature (Kooijmans et al., 2019; Commane et al., 2015; Stimler et al., 2010). These results highlight the distinct responses of COS and CO_2 uptake to environmental variations.

First, LRU increases exponentially under low PAR conditions, as A_{COS} proceeds even when A_{CO2} is nearly zero. This is because CO_2 leaf uptake via the RuBisCO pathway depends on light, whereas COS uptake by CA is light-independent. Consequently, under low PAR, A_{CO2} approaches zero when stomata remain open, allowing A_{COS} to persist, resulting in very high LRU value (Wehr et al., 2017; Kooijmans et al., 2019). Taking advantage of this light-independence, COS absorption has been employed as a proxy for stomatal conductance to water vapor. Recent studies have employed ecosystem-level measurements of COS fluxes to estimate this conductance, highlighting the distinct contributions of stomatal adjustments and biochemical processes to CO_2 uptake (Wohlfahrt et al., 2018; Cochavi et al., 2021).

Second, LRU decreases with increasing temperatures and VPD measured in pine trees with branch chambers (Kooijmans et al., 2019). In Figure 1.5b and c, COS leaf uptake was found to decrease when VPD increases from 0.5 to 2.5 kPa or when temperatures increase from 13 to 23 °C. In contrast, CO_2 uptake remained relatively stable under these conditions (Kooijmans et al., 2019). This VPD-driven reduction in LRU occurs possibly because COS uptake is generally diffusion-limited rather than enzyme-limited, making it highly sensitive to stomatal closure under high VPD, whereas CO_2 uptake is primarily enzyme-limited and thus less affected by changes in stomatal conductance (Protoschill-Krebs et al., 1996; Stimler et al., 2010; Sun et al., 2018b). Although COS uptake is also substantially influenced by enzyme activity, CA and RuBisCO have different optimal operating temperatures for catalyzing uptake of COS and CO_2, respectively, which may contribute to temperature-induced variations in LRU. Together, these mechanisms could explain why LRU responds differently to VPD and temperature changes.

Overall, these findings underline that the relationship between COS and CO_2 uptake is not fixed but varies with environmental and physiological conditions.

1.3.4 Diurnal variation of CO_2 and COS

Diurnal cycles of COS and CO_2 fluxes have been observed in chamber measurements. Figure 1.6 shows the averaged diurnal variations of COS and CO_2 fluxes (F_{COS} and F_{CO2}), and LRU from two chamber measurements at Hyytiälä, Finland (evergreen needleleaf forest), conducted between May and July by Kooijmans et al. (2019). F_{COS} exhibit continuous uptake

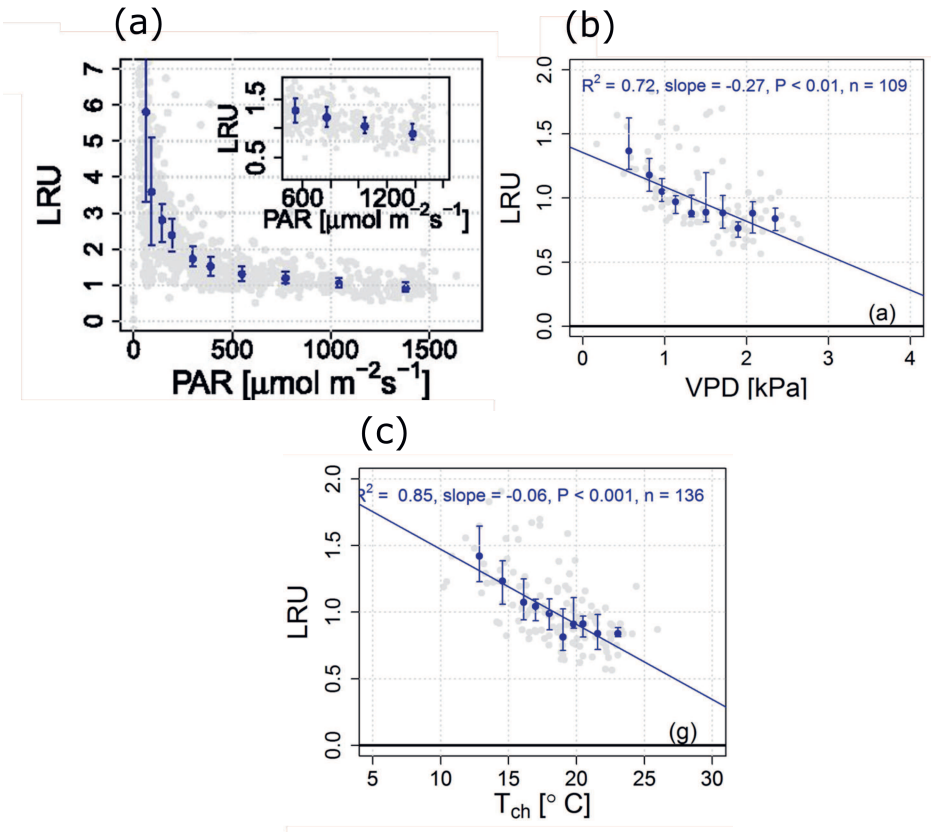


Figure 1.5: Leaf relative uptake of COS and CO_2 in response to light intensity (PAR) (a), vapor pressure deficit (VPD) (b), and a chamber temperature (c) from Hyytiälä, Finland. The data correspond to Chamber 1, and the panels were combined from figures originally reported in the main text (a) and Supplementary Information (b and c) of Kooijmans et al. (2019).

throughout the day, whereas F_{CO2} show a clear day–night contrast, with positive (respiratory) values at night and strong sink values during daytime. The uptake peak of F_{COS} occurs approximately one hour earlier than that of F_{CO2}, a feature also observed in a deciduous forest in China (Geng et al., 2006).

Figure 1.6b shows the corresponding diurnal pattern of LRU. The LRU exhibits a pronounced diurnal variation, largely driven by the diurnal cycle of PAR. This reflects the contrasting light dependence of COS and CO_2 uptake described previously in Sect.1.3.3: COS uptake is light-independent, whereas CO_2 uptake is strongly suppressed under low-light conditions around sunrise and sunset. Together, these observations demonstrate that the physiological mechanisms controlling COS and CO_2 uptake lead to distinct temporal patterns of LRU.

These different diurnal fluxes also influence the diurnal pattern of atmospheric mole fractions. Figure 1.7 illustrates the diurnal variations of COS and CO_2 mole fractions at low and above canopy in southwest Washington State, USA, observed by Rastogi et al. (2018). While ecosystem respiration causes nighttime accumulation of CO_2, COS continues to be taken up,

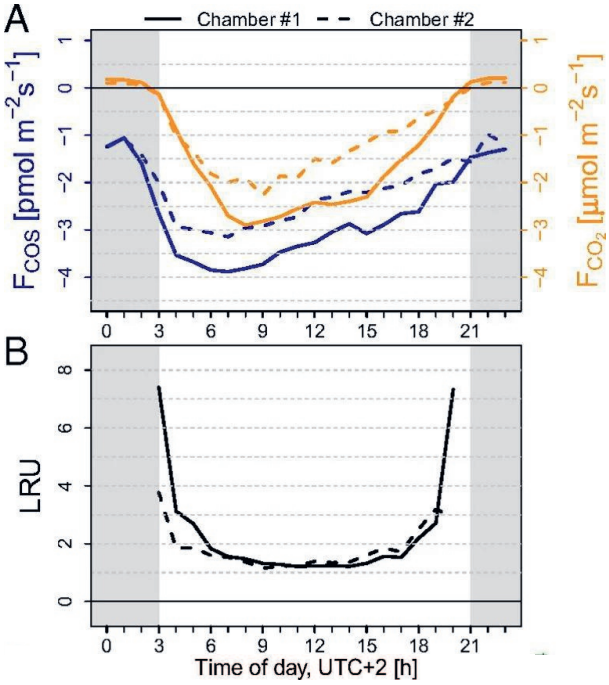


Figure 1.6: Diurnal variation of COS and CO_2 leaf flux (a) and LRU (b) in Hyytiälä, Finland (Kooijmans et al., 2019).

often reaching minimum values before sunrise. After sunrise, boundary layer mixing dilutes the nighttime COS-depleted air, leading to a daytime increase. Understanding these diurnal dynamics provides a crucial link between leaf-scale physiological processes and atmospheric observations, and is essential for interpreting surface fluxes in inverse modeling frameworks discussed in later chapters.

Accurate estimates of COS uptake by the global biosphere require a thorough understanding of the global COS budget. Therefore, the following section broadens the perspective from leaf- and canopy-scale processes to the global scale, examining how COS is distributed and cycled in the atmosphere.

1.4 COS global cycle

1.4.1 Global atmosphere mole fractions

The trace gas COS, the most abundant atmospheric sulfur compound, is essential in the global sulfur cycle. Its low solubility and long atmospheric lifetime enable significant amounts to reach the stratosphere. There, it undergoes photolysis under intense ultraviolet radiation, producing sulfur dioxide (SO_2), which leads to the formation of sulfate aerosol particles (Ravishankara, 1997; Mauldin et al., 2012). These particles contribute to the stratospheric sulfate aerosol (SSA) layer, a critical component in regulating Earth's climate through its cooling effect (Chin et al., 1995; Brühl et al., 2012).

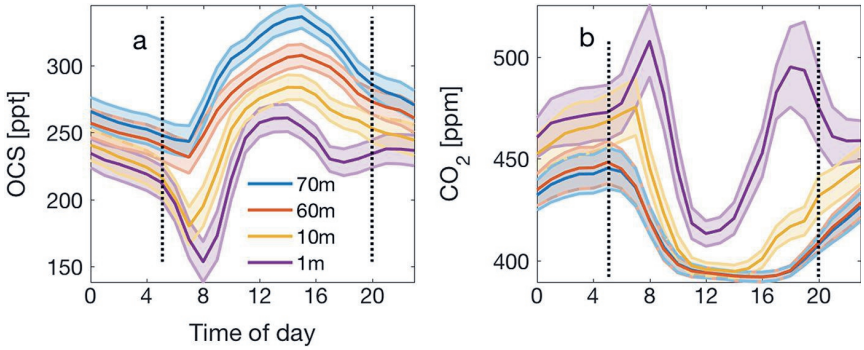


Figure 1.7: Averaged diurnal variation of atmospheric mole fractions of COS (a) and CO_2 (b) at low canopy (1 m and 10 m) and above canopy (60 m and 70 m) in southwest Washington State, USA (Rastogi et al., 2018). The shaded areas indicate standard errors, and the dashed vertical lines represent sunrise and sunset.

Historical records from ice cores reveal that global COS mole fractions have fluctuated over the past 54,000 years. During the Last Glacial Maximum, levels ranged between 250 and 300 $\mathrm{pmol\,mol^{-1}}$, but declined by 80–100 $\mathrm{pmol\,mol^{-1}}$ during the glacial-interglacial transition, reaching a minimum of 160–210 $\mathrm{pmol\,mol^{-1}}$ at the start of the Holocene (Aydin et al., 2016). Mole fractions increased again during the late Holocene, peaking during the industrial era in the 1980s (Campbell et al., 2017).

Since the early 2000s, flask samples of ambient air collected at sites in both hemispheres have provided systematic records of COS. Serio et al. (2023) applied the Empirical Mode Decomposition (EMD) method to analyze inter-annual trends in COS mole fractions over two decades, based on observations from the National Oceanic and Atmospheric Administration (NOAA) global flask network. Fig. 1.8 shows the global monthly mean time series together with smoothed trends estimated using different statistical methods. Their results show relatively stable COS mole fractions from 2000 to 2005, suggesting a balance between global sources and sinks, consistent with the findings of Montzka et al. (2007). Recently, the global average mole fraction exhibited a slight increase until 2015, followed by a decrease from 2015 to 2020. Periods of increasing atmospheric COS imply that global emissions exceed total removal, whereas declining mole fractions indicate that sinks dominate over sources on the global scale. Therefore, the decreasing trend indicates a recent imbalance between global COS sources and sinks (Serio et al., 2023).

Complementary satellite records from the Atmospheric Chemistry Experiment Fourier Transform Spectrometer (ACE-FTS) further support these trends. Schmidt et al. (2024) reported that COS mixing ratios increased from 2004 to 2017 and then shifted into a decline. Together with the NOAA flask records, these satellite observations provide independent evidence for a turning point in the global COS budget.

1.4.2 COS sources and sinks

Understanding sources and sinks is essential, not only for closing the global COS budget but also for applications such as using COS as a tracer of photosynthesis. The global and regional distribution of atmospheric COS is shaped not only by surface fluxes and atmospheric chemistry but also by atmospheric transport, which governs how local flux signals propagate

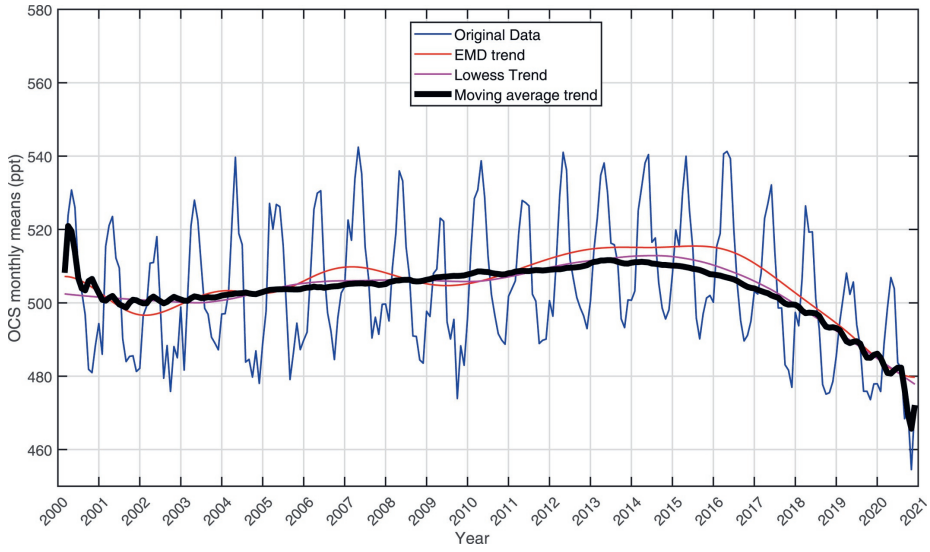


Figure 1.8: Global monthly mean COS mole fractions time series from NOAA flask measurements from 2000 to 2020 (blue) with smoothed trend lines estimated using EMD (red), Lowess (magenta), and moving average (black). Adopted from Serio et al. (2023).

through the atmosphere.

Figure 1.9 synthesizes the global COS budget compiled by Remaud et al. (2022), which includes estimates from Kettle et al. (2002), Montzka et al. (2007), Suntharalingam et al. (2008), Berry et al. (2013), Launois et al. (2015b), and Ma et al. (2021). The spread among these estimates reflects a combination of surface flux variability, methodological differences, and uncertainties in flux estimations. As shown in Fig. 1.8, global COS mole fractions remained relatively stable before 2015. Most studies covered the period before 2015, except for Remaud et al. (2022), which estimated yearly fluxes from 2008 to 2019. Nevertheless, a substantial portion of the Remaud et al. (2022) analysis still falls within the pre-2015 stable period. Consequently, the spread in budget estimates is more plausibly attributed to uncertainties in surface flux estimates rather than interannual variability.

The dominant sinks for COS are plant and soil uptake, with plant uptake accounting for the major global sink. By contrast, soil uptake mediated by microbial CA is generally much smaller, and soils can also act as a source under certain conditions. For instance, COS emissions have been reported from anoxic wetlands and agricultural soils (De Mello et al., 1994; Whelan et al., 2013; Maseyk et al., 2014). Recent studies have also suggested potential emissions from both vascular and non-vascular plants (Goldan et al., 1988; Kesselmeier et al., 1993; Kuhn et al., 2000; Geng et al., 2004; Maseyk et al., 2014; Belviso et al., 2022). More recently, (Spielmann et al., 2025) observed COS emissions from rapeseed and soybean under drought stress, further challenging the assumption of unidirectional uptake by leaves.

In addition to terrestrial removal, COS is destroyed in the atmosphere through photolysis in the stratosphere and reaction with hydroxyl radicals (OH) in the troposphere (Watts, 2000; Kettle et al., 2002). These processes follow first-order kinetics, meaning their removal rate scales directly with atmospheric COS mole fractions, and they are collectively represented as "atmospheric chemical loss" in Fig. 1.9.

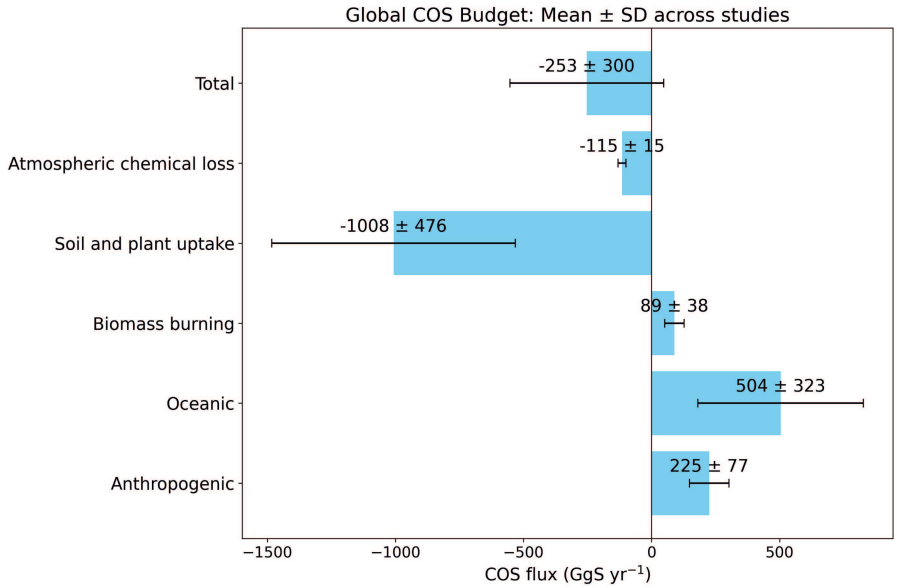


Figure 1.9: Global COS budget (mean ± standard deviation) synthesized from previous studies compiled in Remaud et al. (2022), including Kettle et al. (2002), Montzka et al. (2007), Suntharalingam et al. (2008), Berry et al. (2013), Launois et al. (2015b), and Ma et al. (2021). Notably, Berry et al. (2013) increased the oceanic emissions reported by Kettle et al. (2002) by 600 Gg S yr^{-1} to balance the global budget, whereas Ma et al. (2021) introduced a category of 'unknown source', which was subsequently optimized. In this figure, oceanic and anthropogenic emissions include the indirect contributions from precursor gases (CS_2 and DMS). Anoxic soil emissions are not considered separately but are included in the total flux category.

Oceans act as both sinks and sources of COS. They remove COS through uncatalyzed hydrolysis (Flöck et al., 1996), but also produce it via photochemical and light-independent processes (Von Hobe et al., 2001; Uher et al., 1997), with potential additional contributions from biological activity (Flöck et al., 1996) and radical-driven reactions (Pos et al., 1998). The magnitudes of these processes remain poorly constrained, making current estimates of oceanic fluxes highly uncertain (Launois et al., 2015b; Lennartz et al., 2017; Whelan et al., 2018). As evident in Fig. 1.9, the error bars for soil/plant uptake and oceanic fluxes are particularly large, reflecting the difficulty in constraining these fluxes in the global COS budget.

Anthropogenic activities are another major source of COS, with rayon production as the primary contributor (Campbell et al., 2015). Other significant sources include coal combustion, aluminum smelting, pigment production, shipping, tire wear, vehicle emissions, and coke production (Blake et al., 2008; Chin et al., 1993; Du et al., 2016; Lee et al., 2016; Watts, 2000; Zumkehr et al., 2018). Zumkehr et al. (2018) reported larger anthropogenic COS emissions than earlier estimates by Kettle et al. (2002), with most emissions originating in Asia. Additional sources, such as biodigesters and organic waste processing facilities, have been identified in the Netherlands but are not yet included in emission inventories (Zanchetta et al., 2023). Regional studies indicate some inventories may substantially overestimate emissions, as shown for France (Belviso et al., 2023).

Biomass burning is an additional source of COS. Airborne campaigns detected elevated COS mole fractions in air masses affected by nearby fires (Blake et al., 2008). Biofuels, open combustion, and burning of agricultural residue are significant contributors to COS emissions from biomass burning (Campbell et al., 2015).

In addition to direct emissions, COS is produced indirectly through the oxidation of precursor gases (Kettle et al., 2002). Carbon disulfide (CS_2), from both oceanic and anthropogenic sources, has a high conversion yield to COS ($83 \pm 8\%$) (Stickel et al., 1993). Dimethyl sulfide (DMS), from oceanic and terrestrial sources, is another potential precursor, but with a much lower reported yield ($0.7 \pm 0.2\%$) (Barnes et al., 1996). Although this yield is low, DMS is the most abundant biogenic reduced sulfur compound emitted to the atmosphere, such that even a small conversion efficiency could result in a non-negligible contribution to the global COS budget. Despite this low yield, recent studies highlight the complexity of the DMS oxidation pathways, particularly via hydroperoxymethyl thioformate (HPMTF), and the large uncertainties associated with these processes (Veres et al., 2020; Jernigan et al., 2022; Von Hobe et al., 2023). Because the ocean is a major source of DMS and CS_2, estimates of oceanic indirect COS fluxes remain highly uncertain (Launois et al., 2015b; Lennartz et al., 2017; Whelan et al., 2018).

Minor COS sources include volcanic activity, which releases COS into the troposphere (Whelan et al., 2018), and wetlands, which can emit COS but may act as sinks in hot climates (Whelan et al., 2013).

1.4.3 Unknown sources and sinks for COS

Previous studies have used inverse modeling to estimate global COS sources and sinks by minimizing discrepancies between observed and modeled mole fractions, and they suggested the presence of unknown sources or smaller sinks in tropical regions, as well as unknown sinks or overestimated sources in high-latitude areas of the Northern Hemisphere (Berry et al., 2013; Kuai et al., 2014; Lennartz et al., 2017; Ma et al., 2021). For example, Ma et al. (2021) optimized residual COS surface fluxes within a global inversion framework to close the global COS budget. As illustrated in Figure 1.10, their posterior residual fluxes exhibit a spatial pattern characterized by positive values in tropical regions and negative values at high latitudes in the Northern Hemisphere, consistent with previous inverse modeling studies.

Much of this debate has centered on the tropics, where a persistent "missing source" has been suggested in multiple inversion studies. Berry et al. (2013) implemented a COS biosphere flux module within the SiB3 model and inferred that an additional source of about $600\,\mathrm{Gg\,S\,yr^{-1}}$ was required to balance updated biosphere and soil sinks, which they allocated to the ocean. Building on this, Kuai et al. (2015) used TES-Aura satellite data to optimize surface fluxes and suggested underestimated tropical ocean sources. However, direct oceanic measurements by Lennartz et al. (2017) contradicted these estimates, indicating much smaller direct oceanic emissions ($\approx 130\,\mathrm{Gg\,S\,yr^{-1}}$). More recently, the attribution of the tropical missing source to underestimated oceanic precursors has been supported by inverse studies (Remaud et al., 2022; Ma et al., 2024), although large uncertainties remain in the conversion pathways of oceanic DMS and CS_2 (Lennartz et al., 2017).

Beyond sources, the possibility of biosphere sink overestimation has been raised. Using MIPAS satellite data, Stinecipher et al. (2022) suggested that the tropical plant sink may be smaller than previously estimated, potentially explaining 25—67% of the missing source. Consistently, Ma et al. (2021) showed that accounting for spatial–temporal variations in background COS mole fractions reduces the inferred tropical biospheric sink while increasing the sink at higher latitudes.

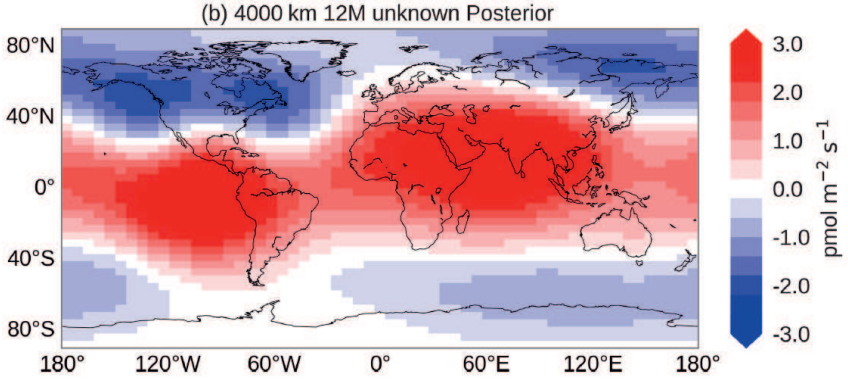


Figure 1.10: Spatial distribution of posterior residual COS surface fluxes ("unknown" emissions) inferred from a global inversion of Ma et al. (2021). The figure corresponds to the spatio-temporal correlation lengths (4000 km spatial and 12 months temporal) identified as the best-performing configuration in that study. Results are averaged over 2008–2011.

At high latitudes, underestimation of the COS biosphere sink has been repeatedly suggested. The COS biosphere flux is generally estimated assuming a linear relationship with GPP using land surface models. However, GPP at high latitudes is known to be highly uncertain, comparable to the uncertainties in tropical GPP (Norton et al., 2019). Moreover, seasonal changes in GPP driven by climate change are particularly difficult to constrain in these regions (Forkel et al., 2016). Kuai et al. (2022) applied atmospheric inversion of COS to northern high latitudes and found that GPP-based COS uptake was underestimated relatively to inversion results, suggesting that regional GPP may also be underestimated. Nonetheless, they cautioned that part of this discrepancy could arise from unresolved transport processes or nocturnal stomatal conductance. Consequently, the COS biosphere uptake at high latitudes also carries substantial uncertainty.

Recent ecosystem-scale flux measurements revealed that boreal wetlands act as substantial COS sinks, shifting their role from a small source in earlier inventories to a considerable sink ($\approx$ 13 Gg S yr^{-1}) when upscaled in land surface models (Vries et al., 2025). However, even with this additional contribution, a missing sink in the Northern Hemisphere persists, highlighting the need for more boreal flux measurements and refined wetland parameterizations in models.

In summary, a comprehensive evaluation of all sources and sinks is essential. However, the limited number of observational stations outside of North America challenges the application of inverse approaches on a global scale. Addressing these issues through expanded observational networks and improved modeling approaches is crucial not only for advancing our understanding of the global COS cycle but also to improve the accuracy of the GPP estimation by COS information.

Because plant uptake is the dominant biospheric sink of COS and tightly coupled to photosynthetic activity, improving its representation in models is critical for applying COS to GPP estimation. Observational constraints are essential in refining parameterizations of plant uptake processes and in reducing uncertainties in inverse modeling of the global COS budget. The next section, therefore, turns to the observational basis needed for these improvements.

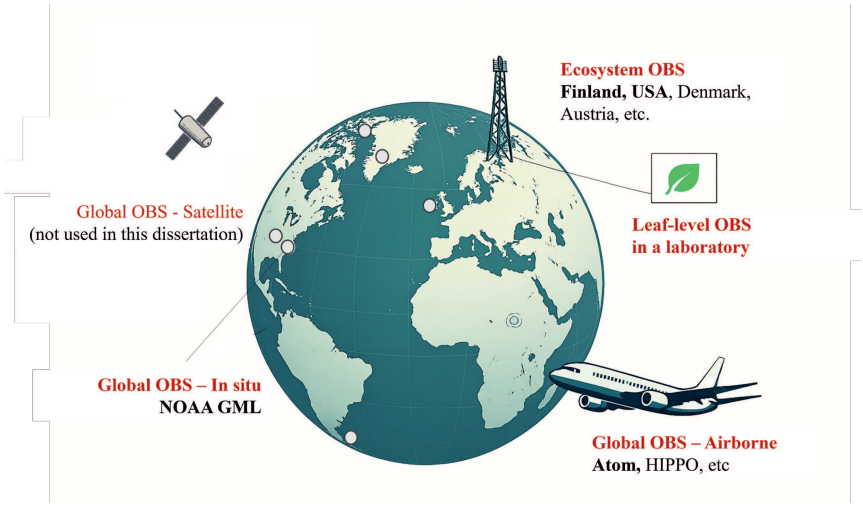


Figure 1.11: Schematic overview of COS observational approaches across spatial scales. Leaf-level chamber measurements, canopy-scale (ecosystem) eddy covariance fluxes, global in situ networks (NOAA GML), and airborne campaigns (ATom, HIPPO) are used in this dissertation. Satellite observations are shown to illustrate the broader observing system but are not used in this work. Together, these approaches enable multi-scale assessment of the global COS budget. Approaches in bold indicate datasets used in this dissertation.

1.5 COS observations

Understanding the exchange of COS between the vegetation and the atmosphere requires measurements across a wide range of spatial scales. Fig. 1.11 provides a schematic overview of the major observational approaches, spanning from leaf-level chamber measurements and canopy-scale fluxes to regional and global perspectives from tower networks, airborne campaigns, and satellite. In this dissertation, I make use of measurements from leaf chambers, ecosystem-scale eddy covariance fluxes, global in situ networks (NOAA GML), and airborne campaigns (e.g., ATom and HIPPO). Satellite observations (e.g., TES, ACE-FTS, MIPAS, and IASI) are shown to illustrate the broader observing system, but are not directly employed in the analyses in this thesis.

1.5.1 Plant chamber experiments

Laboratory experiments allow measurements of leaf-scale gas exchange of COS, CO_2, and H_2O under controlled conditions, with environmental factors varying independently. This independence is a major advantage compared to field observations, where environmental drivers change simultaneously and cannot be disentangled as easily. Open gas exchange systems, such as the commercial LI-6800 systems for H_2O and CO_2, combined with specialized laser spectrometers (e.g., quantum cascade laser spectrometers, QCLS) for COS (Stimler et al., 2010; Asaf et al., 2013; Kooijmans et al., 2016), can precisely quantify inflowing and outflowing mole fractions of these gases in a plant chamber. By observing changes in mole fractions in response to environmental variations, indicators such as LRU (Stimler et al., 2010) and the potential COS compensation point (Gimeno et al., 2017) can be obtained.

Careful consideration of potential errors in plant chamber experiments is essential. Long et al. (2003) highlighted several limitations of gas exchange systems. First, elevated CO_2 mole fractions can suppress leaf respiration (Amthor et al., 1992; Drake et al., 1997). Second, gas leakage may occur through the gasket, which requires blank-chamber measurements without leaves to correct for such artifacts (Long et al., 2003). Third, COS emission from chamber materials has been reported (Maseyk et al., 2014), necessitating similar correction procedures. These limitations underscore the need for rigorous methodology and proper error correction in plant chamber experiments. A detailed description of these experiments is provided in Chapter 2.

1.5.2 Canopy observation

Canopy-scale observations provide a critical link between leaf-level and ecosystem-scale carbon and water exchange. By integrating the combined effects of all leaves, stems, and understory vegetation within the measurement footprint, these observations capture the net COS and CO_2 fluxes under natural environmental variability. The footprint of a canopy flux measurement typically extends up to hundreds of meters from the tower, encompassing the local ecosystem structure and environmental conditions (Pastorello et al., 2020). This scale allows assessment of how canopy structure, species composition, and environmental drivers influence net ecosystem uptake, providing valuable constraints for biosphere models.

Most canopy-scale COS flux observations are conducted at long-term ecosystem sites within networks such as FLUXNET, ICOS, and AmeriFlux, which also provide standardized measurements of CO_2, H_2O, and meteorological variables (Pastorello et al., 2020; Herig Coimbra et al., 2024). At the local scale, the eddy covariance (EC) method is the reference technique for directly and continuously quantifying surface turbulent fluxes (Valentini et al., 1996; Moncrieff et al., 1997; Fowler, 1995). EC measurements are based on high-frequency sampling of vertical wind velocity and scalar mole fractions, requiring fast-response gas analyzers. While EC has been widely applied to CO_2, H_2O, CH_4, and N_2O, the application to COS requires specialized instrumentation such as QCLS (Bielecki et al., 2015).

EC fluxes can be biased by changes in scalar storage within the canopy airspace, particularly during periods of weak turbulence such as nighttime and early morning. At night, when turbulence is minimal, COS uptake by vegetation and soils is not effectively transported upward, leading the EC system to underestimate actual fluxes. In contrast, during early morning, the onset of turbulence mixes the canopy air, releasing COS-depleted air that accumulated overnight. This results in an apparent flux peak that does not reflect real-time ecosystem exchange. Consequently, correcting for the so-called storage term is essential for obtaining accurate COS fluxes (Kooijmans et al., 2017). Storage-corrected datasets (Kooijmans et al., 2021) were used in this dissertation for COS flux analysis at Hyytiälä, Finland, and Harvard Forest, USA (Chapter 3).

1.5.3 Global observations

While canopy-scale measurements provide net ecosystem exchange information within a local footprint, global-scale observations of atmospheric mole fractions extend the perspective to regional and continental fluxes. Such large-scale observations are essential for improving our understanding of the global COS cycle and for predicting its variability under changing environmental conditions. When combined with concurrent CO_2 observations, they further enable assessments of the coupled exchange of COS and CO_2, which is particularly valuable for constraining GPP at broad spatial scales.

The Global Monitoring Laboratory (GML) within NOAA's Earth System Research Laboratory-Global Monitoring Division operates a flask program that provides data on CO_2 and COS mole fractions. The CO_2 dataset used in this dissertation is based on the GLOBALVIEWplus v6.1 ObsPack product, which compiles measurements from 172 stations worldwide (Schuldt et al., 2021). In contrast, COS measurements, available from 14 stations, are mainly concentrated in North America (Montzka et al., 2007).

These ground-based measurements typically have footprints ranging from tens to several hundred square kilometers, integrating the influence of surface fluxes over large upwind regions (Herig Coimbra et al., 2024). Atmospheric towers provide continuous records of mole fractions, which are sensitive to variations in regional surface CO_2 and COS fluxes and can be assimilated into inverse modeling frameworks to infer surface fluxes (Ramonet et al., 2020; Ciais et al., 2010). In this dissertation, surface measurements of both gases are incorporated into global inversions, with CO_2 serving as a benchmark constraint and COS providing additional information for evaluating GPP (Chapter 4).

To complement surface networks, aircraft-based observations provide vertical profiles and horizontal gradients of atmospheric COS, which cannot be resolved by sparse ground networks or coarse-resolution global models (Wofsy, 2011). Large-scale programs such as the HIAPER Pole-to-Pole Observations (HIPPO, 2009–2011) (Wofsy, 2011) and Atmospheric Tomography (ATom, 2016–2018) (Wofsy et al., 2018) were designed to investigate atmospheric composition, chemical processes, and transport. Both campaigns included COS measurements across multiple altitudes, with extensive coverage over remote marine regions in the Pacific and Atlantic Oceans. In this dissertation, ATom data are used to evaluate COS and CO_2 mole fractions simulated by a chemical transport model, both before and after flux optimization (Chapter 4).

To achieve global coverage, satellite instruments retrieve COS information from measured radiation spectra. These include the Tropospheric Emission Spectrometer (TES) (Kuai et al., 2014), Atmospheric Chemistry Experiment–Fourier Transform Spectrometer (ACE-FTS) (Bernath et al., 2021), Michelson Interferometer for Passive Atmospheric Sounding (MIPAS) (Glatthor et al., 2017), and Infrared Atmospheric Sounding Interferometer (IASI) (Camy-Peyret et al., 2017; Anthony Vincent et al., 2017; Cartwright et al., 2025). While the MIPAS mission was terminated in April 2012 and TES in January 2018, IASI and ACE-FTS remain operational. ACE-FTS provides information of stratospheric COS and its isotopologues (Yousefi et al., 2019). However, current satellite instruments lack the sensitivity needed to resolve near-surface COS mole fractions, limiting their utility for accurately assessing surface fluxes (Whelan et al., 2018; Cartwright et al., 2025). For this reason, this dissertation does not employ satellite data and instead focuses on ground- and aircraft-based observations.

1.6 Simulating COS at different scales

While observations from the leaf to the global scale provide factual constraints on COS and CO_2 exchange, they are limited in capturing detailed physiological mechanisms for individual plant species and in providing continuous coverage across space and time. Moreover, estimating global-scale GPP from COS requires spatially and temporally resolved information on vegetation COS fluxes, which cannot be obtained from observations alone. To address these limitations, this dissertation employs model simulations of both COS and CO_2 at multiple scales: (1) a leaf conductance model to represent leaf-level uptake processes, (2) a land surface model to simulate canopy-scale dynamics, and (3) a chemical transport model for global-scale analysis. Importantly, the leaf conductance and land surface models also simulate H_2O exchange, thereby linking the three gases within a coupled framework of plant physiology and

surface–atmosphere interactions.

1.6.1 Leaf conductance model

The leaf conductance model (Adnew et al., 2020) used in this dissertation provides process-based estimates of gas transport and uptake within leaves, offering a quantitative framework for interpreting laboratory experiments. While earlier applications focused on GPP tracers such as the $\Delta^{17}O$ and Δ_{47} isotopic composition of CO_2 (Adnew et al., 2020; Adnew et al., 2021), its structure is well suited for COS and CO_2, as it resolves internal mole fraction gradients and separates the influence of boundary, stomata, and mesophyll conductances. The model was originally designed to optimize conditions for laboratory leaf experiments, including the ratio of internal and ambient mole fractions, as well as the isotopic composition of the gases.

The model calculates mole fractions within successive leaf layers and derives net gas exchange from the differences between inflowing and outflowing air in the leaf chamber, under the assumption that equilibrium is reached during the experiment. For this dissertation, new modules were implemented to explicitly represent COS uptake and its coupling to CO_2 and H_2O exchange. These extensions enable a mechanistic interpretation of chamber experiments (Chapter 2).

1.6.2 Land surface model

While the leaf conductance model is well suited for plant chamber experiments, providing detailed mechanistic insights under controlled conditions, it is inherently limited to equilibrium scenarios and to the leaf scale. This focus allows precise analysis of stomatal responses and gas exchange processes, but does not account for the interactions among leaves, canopy structure, soil, and atmosphere.

In contrast, land surface models (LSMs) simulate the coupled exchange of water, energy, and carbon at the ecosystem scale, integrating leaf conductance calculations across entire canopies. By representing processes over spatially explicit grid cells, LSMs can represent variability across landscapes and compute global fluxes. This makes them essential for estimating global-scale GPP, which requires information on COS vegetation fluxes at comparable scales.

Biosphere exchange of COS and CO_2 at the ecosystem level has been implemented in LSMs such as the Simple Biosphere Model, version 4 (SiB4) (Haynes et al., 2019) and the ORCHIDEE model (Launois et al., 2015b; Maignan et al., 2021). We employed SiB4 in Chapter 3 and Chapter 4. SiB4 is an advanced version of the original SiB model (Sellers et al., 1986), developed through multiple improvements over earlier generations. For example, unlike SiB3, which relies on satellite-based vegetation inputs, SiB4 uses a process-based approach to simulate phenology and carbon fluxes (Haynes et al., 2019). It simulates photosynthesis responses to temperature, humidity, radiation, and precipitation, while also accounting for stress factors such as water limitation and extreme temperatures. While simulating CO_2 dynamics, the model also resolves canopy-level H_2O exchange, providing a mechanistic link to stomatal conductance. The model represents multiple vegetation types and phenological stages, including leaf-out, growth, maturity, senescence, and dormancy.

A dedicated COS module was recently incorporated into SiB4 (Haynes et al., 2019). This module calculates vegetation COS fluxes using a combination of conductances and atmospheric COS mole fractions, with conductances scaled from CO_2 values (Berry et al., 2013). As part of my Ph.D. research, I extended this module by implementing spatially and temporally varying atmospheric COS mole fractions into the SiB4 framework. This enhancement, later adopted in Kooijmans et al. (2021) and Ma et al. (2021), substantially reduced simulated

COS biosphere uptake in tropical regions, highlighting the critical role of accounting for atmospheric variability. Nonetheless, the improved model still could not close the global COS budget, particularly in the tropics and high latitudes in the Northern Hemisphere, pointing to the need for further refinement.

In addition to vegetation exchange, SiB4 includes a soil COS flux module, with uptake regulated by diffusion processes influenced by soil porosity and water-filled pore space (Van Diest et al., 2008; Ogée et al., 2016; Sun et al., 2015; Whelan et al., 2016). In this dissertation, I adopt the Ogée et al. (2016) soil scheme, which uses a steady-state analytical solution under uniform soil conditions. This approach is computationally efficient and well-suited for integration into SiB4 for global soil COS flux estimation (Kooijmans et al., 2021).

1.6.3 Global chemical transport model

While LSMs provide estimates of global biosphere COS and CO_2 fluxes, global chemical transport models (CTMs) use these fluxes, together with other natural and anthropogenic sources and sinks, to simulate the three-dimensional distribution of atmospheric mole fractions over time. CTMs explicitly resolve atmospheric transport processes such as advection, convection, and turbulent mixing, and, where relevant, chemical reactions.

In this dissertation, I used the Tracer Model version 5 (TM5) (Krol et al., 2005). In Chapter 4, TM5 was configured at a horizontal resolution of $3^\circ \times 2^\circ$ with 34 vertical layers extending up to 0.1 kPa, driven by meteorological reanalysis data from the European Centre for Medium-Range Weather Forecasts (ECMWF). The framework has been widely applied in inversion studies of gases such as CO_2 (Pandey et al., 2016; Basu et al., 2018), CH_4 (Meirink et al., 2008; Houweling et al., 2014), CO (Krol et al., 2008; Hooghiemstra et al., 2011), OH (Naus et al., 2022), and COS (Ma et al., 2021; Ma et al., 2023; Ma et al., 2024).

In this dissertation, TM5 is applied to simulate atmospheric mole fractions of CO_2 and COS and to perform inversions that refine their source and sink estimates (Chapter 4). Biosphere fluxes from SiB4 are used as inputs, enabling us to evaluate how alternative SiB4 parameterizations influence simulated mole fractions and how these fluxes can be improved through the inversion framework. Details of the inversion methodology are provided in the following section.

1.7 Inverse modeling

While forward simulations provide continuous spatial and temporal coverage, they remain subject to uncertainties arising from incomplete process understanding, limitations in parameterizations, and inaccuracies in input data. These uncertainties can propagate through the modeling chain and introduce uncertainties and potential biases in simulated outcomes.

Inverse modeling mitigates these challenges by optimizing unknown fluxes or model parameters so that simulated outputs (e.g., mole fractions) are more consistent with observations (Enting, 2002). In this dissertation, inverse methods are applied in three contexts: (1) to optimize parameters in the leaf conductance model using plant chamber measurements, (2) to refine biosphere COS flux parameterizations in SiB4 with canopy-scale observations, and (3) to update surface fluxes in TM5 through atmospheric inversion using NOAA ground-based observations. The overall workflow of this inversion framework is summarized in Fig. 1.12, where fluxes or parameters are iteratively adjusted until a convergence criterion is satisfied, after which posterior simulations using the optimized fluxes are validated against independent observations.

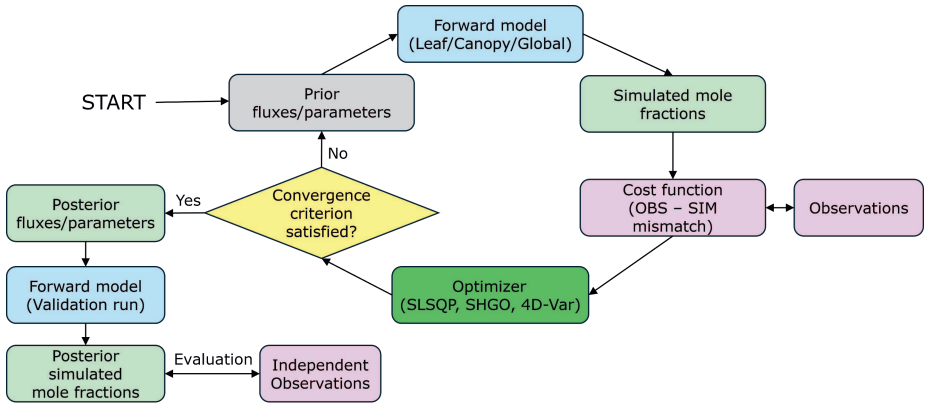


Figure 1.12: Flowchart of the inverse modeling framework applied in this dissertation. The framework iteratively optimizes fluxes or parameters until a convergence criterion is satisfied. Posterior fluxes and parameters are then used in the forward model to simulate mole fractions, which are validated against observations. The Optimizer module in the flowchart represents all optimization algorithms used in this dissertation: SLSQP in Chapter 2, SHGO in Chapter 3, and 4D-Var in Chapter 4

This section introduces the cost function underlying the inversion, the optimization algorithms, and the evaluation methods used to assess the inversion performance.

1.7.1 Cost function

The inverse modeling framework is based on Bayes' theorem, which combines prior knowledge with observational evidence to estimate the most probable state of a system (Tarantola et al., 1982; Brasseur et al., 2017). In practice, this is formulated as a cost function (J) that combines two components: the deviation of state variables from their prior estimates, and the mismatch between model predictions and observations. The optimal solution corresponds to the state $\mathbf{x}$ that minimizes J.

$$J(x) = J_{bg}(\mathbf{x}) + J_{obs}(\mathbf{x}) = (\mathbf{x} - (\mathbf{x_a}))^T \, \mathbf{B}^{-1} \, (\mathbf{x} - \mathbf{x_a}) + (\mathbf{H}(\mathbf{x}) - \mathbf{y})^T \, \mathbf{R}^{-1} \, (\mathbf{H}(\mathbf{x}) - \mathbf{y}). \quad (1.3)$$

In this formulation, the first term (J_{bg}) represents the deviation of state variables from their prior values ($\mathbf{x_a}$), weighted by the prior error covariance $\mathbf{B}$. The second term (J_{obs}) quantifies the mismatch between model predictions ($\mathbf{H}(\mathbf{x})$) and observations ($\mathbf{y}$), weighted by the observational error covariance $\mathbf{R}$. Typically, $\mathbf{B}$ includes off-diagonal elements, while $\mathbf{R}$ is often treated as diagonal under the assumption of independent observations.

When optimizing multiple gases simultaneously (e.g., CO_2 and COS), separate J_{obs} terms are included for each gas. Because the number of observations and their uncertainties may differ substantially between tracers, weights are often introduced to balance their contributions.

1.7.2 Optimizers and 4D-Var

Inverse modeling requires minimizing the cost function introduced in the previous section, which is achieved through numerical optimization algorithms (hereafter referred to as optimizers). Depending on the complexity and scale of the problem, different optimizers are appropriate.

In this dissertation, different inversion setups employed optimizers tailored to each problem's scale. For the inversion of the leaf conductance model and the land surface model, whose modules are relatively simple, I used the Sequential Least Squares Programming (SLSQP; a local optimization method) (Kraft, 1988) and the Simplicial Homology Global Optimization (SHGO; a global method) (Endres et al., 2018) algorithms from the Python SciPy library, respectively. SLSQP follows the local gradient from an initial guess, while SHGO systematically explores the broader parameter space to avoid being trapped in local minima.

By contrast, the TM5 cannot be efficiently optimized with such standard algorithms due to its high dimensionality and computational cost. Instead, I employed a four-dimensional variational (4D-Var) inversion framework. 4D-Var is a data assimilation technique originally developed in numerical weather prediction (Talagrand et al., 1987) and widely applied in atmospheric inverse modeling (Chevallier et al., 2005; Meirink et al., 2006). It exploits the adjoint of the forward model to efficiently compute gradients with respect to very large control vectors, enabling the optimization of surface fluxes against extensive observational datasets.

In this dissertation, I used the adjoint configuration of TM5-4DVar (Meirink et al., 2008) to optimize surface fluxes of COS and CO_2. The inversion begins with a forward simulation to calculate the cost function, followed by a backward integration of the adjoint model to obtain the gradient with respect to the control vector, which quantifies the sensitivity of the model–observation mismatch to each control parameter. These gradients are then used in an iterative minimization to adjust prior fluxes toward values more consistent with observations. Mathematically:

$$\nabla J(\mathbf{x}) = \mathbf{B}^{-1}(\mathbf{x} - \mathbf{x_a}) + \mathbf{H}^{\mathrm{T}}\mathbf{R}^{-1}(\mathbf{H}(\mathbf{x}) - \mathbf{y}), \tag{1.4}$$

where the first term reflects prior (background) information and the second term incorporates the mismatch between simulated and observed values via the observation operator $\mathbf{H}$ and its adjoint $\mathbf{H}^{\mathrm{T}}$.

Regarding the minimization method, the CONGRAD algorithm (Lanczos, 1950) offers computational efficiency for strictly linear problems, whereas for weakly nonlinear systems, quasi-Newton methods such as M1QN3 (Gilbert et al., 1989) are often preferred despite their higher computational cost due to slower convergence. In this dissertation, TM5-4DVar inversions were conducted using the M1QN3 optimizer, as described in Chapter 4.

1.7.3 Evaluation

To assess the robustness of the inversion framework and to quantify posterior uncertainties for the relatively simple inverse problems of the leaf conductance model and the land surface model, a Monte Carlo–based optimization approach is employed (Chapter 2 and Chapter 3). This method is particularly suited for evaluating the ability of the inversion system to constrain the target parameters beyond the linear error propagation assumptions (Tarantola, 2005). Monte Carlo approaches have been widely applied in atmospheric inversions and land surface modeling studies to characterize posterior uncertainties (Chevallier et al., 2007; Bosman et al., 2023). For the TM5-4DVar inversions, posterior error estimation was not performed due to computational constraints.

The Monte Carlo procedure consists of running an ensemble of independent optimizations in which random perturbations are applied both to the control vector ($\mathbf{x}$) and to the observations ($\mathbf{y}$). These perturbations, denoted $\epsilon_{\mathbf{a}}$ and $\epsilon_{\mathbf{y}}$, are sampled from zero-mean Gaussian distributions with prescribed standard deviations σ_a and σ_y, respectively. The modified cost function for a single ensemble member is then expressed as:

$$J(\mathbf{x}) = \frac{(\mathbf{x} - \mathbf{x_a} + \epsilon_\mathbf{a})^2}{2\ {\sigma_\mathbf{a}}^2} + \frac{(\mathbf{y} - \mathbf{H}(\mathbf{x}) + \epsilon_\mathbf{y})^2}{2{\sigma_\mathbf{y}}^2}. \tag{1.5}$$

The ensemble of perturbed optimizations yields a distribution of posterior solutions, from which parameter uncertainties are quantified as the standard deviation across the ensemble (Tarantola, 2005).

To evaluate the inversion performance, the chi-squared metric (χ^2) is employed throughout this work. This measure evaluates the agreement between model outputs and observations, accounting for the number of data points and their associated uncertainties (Tarantola, 2005). It provides a normalized measure that tests whether the inversion results are statistically consistent with the observational uncertainties and with the tolerance implied by the prior constraints:

$$\chi^2 = \frac{1}{n} \sum_{i=1}^{n} \frac{(k - k_{\text{true}})^2}{\sigma^2}. \tag{1.6}$$

In this formulation, k denotes the quantity being assessed, such as a model-derived estimate or a state variable, while k_{true} refers to the corresponding reference value, which could be taken from observations or prior estimates. The parameter n specifies the sample size, and σ characterizes the uncertainty associated with k_{true}. A posterior chi-squared value (χ^2_{post}) close to 1 indicates a statistically consistent fit, meaning that model predictions are compatible with observational uncertainties and prior constraints. Values of χ^2_{post} significantly larger than 1 suggest that the model–observation mismatch exceeds the assumed error bounds, whereas values substantially smaller than 1 may indicate either overfitting or an overestimation of the prescribed uncertainties (Tarantola, 2005).

1.8 Objective and thesis outline

Although COS provides valuable information on photosynthetic carbon uptake, significant knowledge gaps remain across multiple scales. At the leaf scale, our mechanistic understanding of how COS and CO_2 respond differently to environmental drivers is still incomplete. At the canopy scale, current land surface models typically infer COS fluxes from CO_2 photosynthesis rates, without adequately accounting for the unique physiological properties of COS. As a result, global vegetation flux estimates based on such simplified assumptions remain uncertain. Inversion-based studies have suggested potential biases in the COS global budget, such as overestimated sinks (or underestimated sources) in low latitudes and underestimated sinks (or overestimated sources) at higher latitudes (Berry et al., 2013; Kuai et al., 2014; Lennartz et al., 2017; Ma et al., 2021).

In many modeling and inversion frameworks, a simplified linear formulation is adopted, whereby the COS vegetation flux (F_{COS}) is assumed proportional to GPP, often expressed as:

$$F_{COS} \approx \alpha\ GPP. \tag{1.7}$$

In this formulation, α is typically linked to the LRU. While convenient, this approach collapses environmental dependencies into a single coefficient (Stimler et al., 2010; Kooijmans et al., 2019; Sun et al., 2018b; Spielmann et al., 2025). As subsequent chapters demonstrate, this proportionality holds only under certain conditions and breaks down when stomatal or mesophyll processes diverge between COS and CO_2.

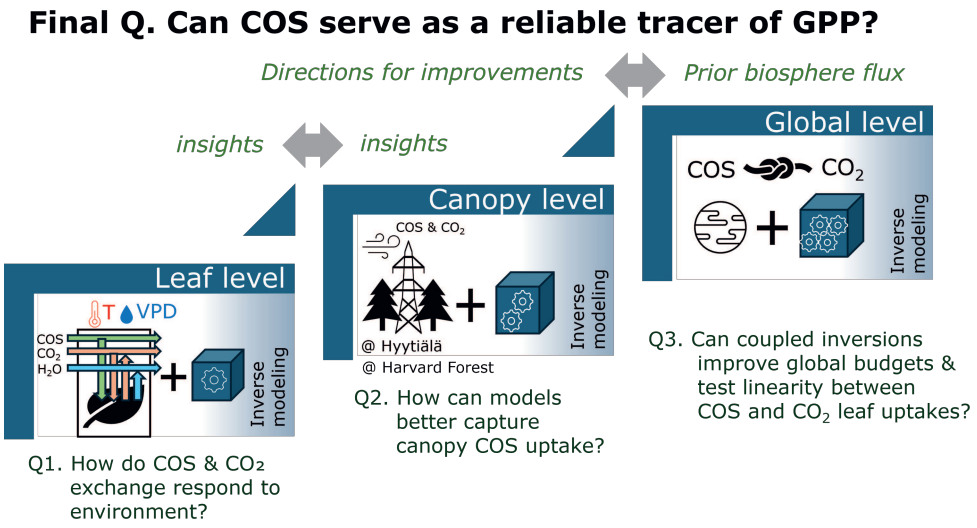


Figure 1.13: Conceptual overview of this dissertation framework linking analyses across leaf, canopy, and global scales. At each scale, inverse modeling is applied to address a key research question (Q1–Q3), ultimately converging on the central question: Can COS serve as a reliable tracer of GPP?

A central question motivating this dissertation is whether the apparent unknown sources and sinks of COS can be explained by revisiting and improving vegetation flux estimates. Equally important, another central question is to what extent vegetation uptake of COS can serve as an independent and reliable constraint on GPP. Addressing these questions requires a mechanistic understanding of COS uptake from the leaf to the canopy scale, along with the refinement of insufficiently constrained model parameters through inverse modeling. By obtaining improved vegetation flux estimates, this dissertation evaluates not only the closure of the COS budget but also the potential of COS as a tracer for global GPP.

To address these challenges, this dissertation analyzes the leaf- and canopy-scale exchange dynamics of COS and CO_2 under diverse environmental conditions, optimizes key parameters via inverse modeling, and applies a global flux inversion framework. Figure 1.13 summarizes this three-step workflow.

Chapter 2: Experimental study on leaf exchange of CO_2 and COS

This chapter investigates how leaf uptake of CO_2 and COS responds to environmental changes under controlled laboratory conditions. By independently manipulating temperature and vapor pressure deficit, the experiments disentangle the individual effects of environmental drivers that are often confounded in field observations.

To interpret the observed variations in CO_2 and COS mole fractions across leaf layers, an existing conductance model was extended by incorporating dedicated modules for both gases. The model inversion made use of CO_2, COS, and H_2O observations, allowing us to constrain gas-specific parameters with experimental data. This approach establishes the mechanistic

foundation needed to evaluate how environmental factors shape the COS–GPP relationship at the leaf scale.

Chapter 3: Optimization of the COS module in the land surface model

This chapter investigates canopy-scale COS exchange by optimizing key parameters of the SiB4 land surface model at two observational sites. A central question is whether the distinct temperature dependence of mesophyll conductance, identified at the leaf scale, also emerges at the ecosystem level. To test this, a new temperature response function for COS mesophyll conductance is introduced, and stomatal conductance parameters are optimized using canopy flux observations.

These refinements address the broader modeling challenge that vegetation COS flux is often simplified as proportional to GPP (Eq. 1.7). By incorporating mechanistic constraints into SiB4, the model provides more reliable prior estimates of COS vegetation fluxes, which in turn serve as the foundation for the global-scale inversions presented in Chapter 4.

Although Chapter 3 may appear to follow logically from the experimental insights of Chapter 2, the modeling work in Chapter 3 was conducted prior to the completion of the laboratory experiments. The ordering of Chapters 2 and 3 in this dissertation therefore reflects the progression from leaf to canopy scale, rather than the chronological order in which the studies were carried out.

Chapter 4: Coupling of the global budget for CO_2 and COS

This chapter scales up the analysis to the global level using a newly developed coupled inversion framework, in which surface fluxes of both CO_2 and COS are optimized simultaneously against atmospheric observations. The motivation is to evaluate the general assumption, widely adopted in land surface models, that COS vegetation flux can be approximated as proportional to GPP (Eq. 1.7). Building on the leaf- and canopy-scale findings that revealed departures from strict linearity, the global framework provides a way to test how such simplifications hold—or fail—when applied across diverse biomes and timescales.

Beyond methodological novelty, this coupled framework marks a step toward integrating COS into carbon cycle assessments. It shows that coupled inversions depend strongly on vegetation priors, which shape flux constraints and condition the reduction of model–observation mismatches. Yet, sparse COS observations and structural uncertainties remain major challenges. Linking insights across scales, this chapter examines how far COS can serve as an independent and robust tracer of GPP at the global scale.

By integrating analyses at the leaf, canopy, and global scales, this dissertation bridges key gaps in understanding the coupled COS and CO_2 cycles. It advances methods for estimating GPP with COS, offers insights into parameter optimization across scales, and demonstrates the potential of COS to provide unique constraints on photosynthesis. At the same time, it points to the need for improved observations and model development to fully realize this potential in global carbon cycle assessments.

Chapter 2

Leaf chamber experiments on sunflowers indicate a temperature-dependent compensation point of carbonyl sulfide

Carbonyl Sulfide (COS) is a potential tracer for estimating gross primary productivity (GPP), due to its co-uptake with CO_2 in leaves and the assumed absence of re-emission. However, the effectiveness of COS as a GPP tracer depends on understanding the differential responses of COS and CO_2 uptake to environmental factors such as temperature and humidity.

We conducted three sets of leaf gas exchange experiments on sunflower leaves. In each experiment, we varied only one environmental factor: COS mole fraction (at two temperatures), humidity, or temperature. During the experiments, COS and CO_2 fluxes were measured, and the data were used to optimize a leaf conductance model.

We identified the existence of a COS compensation point, which increases with higher temperatures, suggesting potential emissions at higher temperatures when atmospheric COS concentrations are low. Our gas exchange measurements detected a COS compensation point of $58.9 \pm 52.4\ \mathrm{pmol\,mol^{-1}}$ at 20 °C and $139.9 \pm 26.0\ \mathrm{pmol\,mol^{-1}}$ at 25 °C. As vapor pressure deficit increased and stomatal conductance decreased, we observed that COS leaf uptake decreased more rapidly than CO_2 assimilation. Consequently, the leaf relative uptake ratio (LRU) of COS to CO_2 also decreased when stomatal conductance decreased. The optimized conductance model indicated that the optimum temperature for COS and CO_2 enzymatic uptake was around 35 °C. However, the maximum net deposition velocity for COS lies between 20 and 25 °C, due to its temperature-dependent compensation point.

COS and CO_2 exchange with leaves are jointly regulated by stomatal conductance, internal biochemical activity, and the compensation point. The LRU increases when stomata open, but declines at higher temperatures due to the compensation point. Accurate GPP estimation using COS biosphere uptake requires accounting for different LRU responses to humidity and temperature, and the COS compensation point at higher temperatures.

Cho, A., Kooijmans, L. M. J., Driever, S. M., Wassenaar, M., Koren, G., Baartman, S. L., Mossink, L., and Krol, M. C. (2025). Leaf chamber experiments on sunflowers indicate a temperature-dependent compensation point of carbonyl sulfide. *Open Research Europe*, 5:223. https://doi.org/10.12688/openreseurope.20235.1

2.1 Introduction

Gross primary productivity (GPP) quantifies the largest terrestrial CO_2 uptake flux in the global carbon cycle. However, when measuring the net ecosystem exchange (NEE) of CO_2, separating the GPP signal from respiration is challenging (Reichstein et al., 2005; Wohlfahrt et al., 2015). To address this limitation, carbonyl sulfide (COS) is an atmospheric trace gas that has been identified as a promising tracer for GPP, and several studies have explored its utility extensively (Montzka et al., 2007; Campbell et al., 2008; Asaf et al., 2013; Kohonen et al., 2022). COS primarily originates from anthropogenic sources and oceans, while vegetation predominantly acts as its sink (Berry et al., 2013; Kettle et al., 2002).

The application of COS to estimate GPP has been suggested because COS uptake by leaves proceeds through a stomatal pathway similar to uptake of CO_2. Importantly, COS is assumed not to be released by plants due to its irreversible hydrolysis catalyzed by carbonic anhydrase (CA) (Protoschill-Krebs et al., 1996; Notni et al., 2007; Stimler et al., 2010). With this advantage of COS, the leaf relative uptake ratio (LRU) of deposition velocities of COS and CO_2 has been introduced to scale COS leaf uptake to photosynthesis (Sandoval-Soto et al., 2005; Campbell et al., 2008). However, previous studies have emphasized that LRU responds differently to environmental factors such as leaf temperature (T_{leaf}) and vapor pressure deficit (VPD), implying that it is not constant under varying conditions (Stimler et al., 2010; Sun et al., 2018b; Wohlfahrt et al., 2018; Kooijmans et al., 2019; Cochavi et al., 2021).

Unlike photosynthesis, COS uptake by CA remains unaffected by light, rendering it a robust proxy for stomatal conductance to water vapor (g_{sw}). Accordingly, recent studies have used ecosystem-level COS exchange as a proxy for g_{sw}, highlighting differences between stomatal and biochemical contributions to CO_2 uptake (Wohlfahrt et al., 2018; Cochavi et al., 2021).

Differences in COS and CO_2 responses to changes in T_{leaf} and VPD were observed under constant light conditions, but their causes remain unclear (Stimler et al., 2010; Sun et al., 2018b; Kooijmans et al., 2019). Kooijmans et al. (2019) measured that LRU decreases with increasing temperatures (from 13 to 23 °C) or increasing VPD (from 0.5 to 2.5 kPa) at the boreal forest site Hyytiälä in Finland, while CO_2 uptake remained relatively stable. Understanding these variations is imperative for utilizing COS measurements to infer information about GPP.

To address these open questions, we investigate three potential explanations for the different responses of COS and CO_2 uptake to increasing T_{leaf} and VPD under high-light conditions. First, the pronounced reduction in COS leaf uptake compared to CO_2 uptake at higher T_{leaf} might be due to a potential COS compensation point (Γ_{COS}) at higher T_{leaf} (Goldan et al., 1988; Kesselmeier et al., 1993; Kuhn et al., 2000; Geng et al., 2004; Maseyk et al., 2014; Belviso et al., 2022). These measured Γ_{COS} values are lower than typical atmospheric COS mole fractions ($\approx$ 500 $\mathrm{pmol\,mol^{-1}}$), which is why net COS uptake is observed. Stimler et al. (2010) also observed a Γ_{COS} of 60.7 $\mathrm{pmol\,mol^{-1}}$, though statistically indistinguishable from zero, and interpreted it as a possible diffusional feedback under high COS mole fractions. More recently, Gimeno et al. (2017) demonstrated temperature-dependent COS emissions in nonvascular bryophytes, suggesting that biochemical processes such as protein degradation could contribute to COS release at elevated T_{leaf}. However, Γ_{COS} of vascular plants and its temperature dependence remain poorly constrained.

Second, COS leaf uptake might respond more strongly to stomatal closure than CO_2 uptake (Farquhar et al., 1982). In contrast, the internal COS concentration is assumed to be much lower than ambient levels due to the higher catalytic efficiency of CA (Protoschill-Krebs et al., 1996; Tcherkez et al., 2006; Seibt et al., 2010). Thus, decreasing g_{sw} is expected to reduce COS uptake more than CO_2 uptake.

Third, the enzyme CA could behave optimally at a lower temperature than RuBisCO (Stim-

ler et al., 2010; Cho et al., 2023). Optimum temperatures for CA enzyme activity range from 15–40 °C (Sun et al., 2015; Ogée et al., 2016; Cho et al., 2023), significantly lower than the optimal temperature of RuBisCO (≈ 50 °C) (Salvucci et al., 2001).

To complement these experiments, we developed a coupled CO_2–COS–H_2O conductance model based on a previous model for isotopic CO_2 tracers (Adnew et al., 2020; Adnew et al., 2021; Adnew et al., 2023). This model jointly optimizes gas-exchange parameters through the shared stomatal pathway and allows inference of unmeasurable internal variables.

Finally, to validate the three hypotheses, we investigate COS compensation points and the responses of COS and CO_2 uptake to varying g_{sw} and T_{leaf}. We present leaf gas exchange measurements from sunflowers and interpret them using the coupled model optimized against the experimental dataset.

2.2 Materials and Methods

2.2.1 Leaf gas-exchange measurements

2.2.1.1 leaf cuvette system

We measured deposition velocities of COS and CO_2 (V_{COS} and V_{CO2}), i.e., fluxes normalized by mole fractions in air, using a leaf cuvette system. These experiments were conducted using sunflower plants (*Helianthus Annuus* L. cv. 'Sunsation'), which are C_3 photosynthesis type plants cultivated in a local plant nursery (Evanthia, Maasdijk, Netherlands). The species *Helianthus annuus* was originally described by Linnaeus (*Species Plantarum*, Vol.2, p.904, 1753). Each sunflower plant was used for a maximum of 5 daytime hours to minimize physiological stress caused by prolonged exposure to experimental conditions.

T_{leaf} was monitored within the leaf cuvette using a thermocouple touching the abaxial side of the leaf. A synthetic air mixture, composed of 79% nitrogen and 21% oxygen, was mixed and controlled using mass flow controllers (Bronkhorst, Veenendaal, the Netherlands) and humidified using a dew point generator (LI-610, Li-Cor). CO_2 and COS were supplied from controlled gas cylinders and then added to the air-stream entering the LI-6800 system. CO_2 mole fractions in the leaf cuvette were kept around 445.1 ± 3.5 $\mu\mathrm{mol\,mol^{-1}}$. COS was introduced from a gas mixture with synthetic air with a COS mole fraction of around 700 $\mathrm{nmol\,mol^{-1}}$, regulated by a mass flow controller (Analyt-MTC, Müllheim, Germany). Except for the first experiment to check Γ_{COS}, COS mole fraction levels were intentionally elevated (in the range of 900 to 1100 $\mathrm{pmol\,mol^{-1}}$), relative to typically atmospheric mole fractions (approximately 500 $\mathrm{pmol\,mol^{-1}}$) to improve the detectability of COS uptake. Air in the leaf cuvette was mixed by a fan, operated at approximately 10 000 rpm, and the boundary conductance near the leaf surface was maintained at about 2.44 $\mathrm{mol\,m^{-2}\,s^{-1}}$.

To control g_{sw}, adjustments were made to the VPD. Initial g_{sw} ($\mathrm{mol\,m^{-2}\,s^{-1}}$) values were estimated by measuring the total conductance of H_2O (g_{tw} ($\mathrm{mol\,m^{-2}\,s^{-1}}$)) and applying a corresponding boundary conductance of H_2O (g_{bw} ($\mathrm{mol\,m^{-2}\,s^{-1}}$)) according to the LI-6800 manual. We assumed equal distribution of stomata between the upper to lower side of the leaf and therefore applied a stomatal ratio of $K = 0.5$.

COS and CO_2 mole fractions of the inflowing and outflowing air were measured using a quantum cascade laser spectrometer (QCLS) (Aerodyne Research Inc., Billerica, MA, USA). The air subjected to QCLS analysis was initially passed through a magnesium perchlorate ($Mg(ClO_4)_2$) drying trap to eliminate water vapor. For this purpose, magnesium perchlorate hexahydrate (99% purity; Sigma-Aldrich, Product Code: 309303-100G, Linear Formula: $Mg(ClO_4)_2 \cdot 6H_2O$) was used. The water vapor scrubber tubes employed were 50 cc stainless

steel tubes with 0.25-inch tube fittings. Measurements of air from cylinders with known COS and CO_2 mole fractions were performed for hourly calibration.

Once a leaf reached steady-state under the given conditions, data were recorded. The LI-6800 measured every second and was set to log data automatically every 3 minutes. Each log consisted of an average taken over 15 measurements within the preceding 15 seconds. The QCLS was set to automatically record data every second, totaling 150 measurements over each 150-second period. Then, the median over this 150-second interval was taken as the "data point". Each QCLS interval had a corresponding LI-6800 log.

The air was passed through the analyzer at an approximate flow rate (AF ($\mathrm{mol\,s^{-1}}$) of 0.35 $\mathrm{mmol\,s^{-1}}$. Subsequently, leaf assimilation rates (F_{gas}) of COS (F_{COS} ($\mathrm{pmol\,m^{-2}\,s^{-1}}$)) and CO_2 (F_{CO2} ($\mu\mathrm{mol\,m^{-2}\,s^{-1}}$)) were calculated by:

$$F_{\mathrm{gas}} = \frac{AF}{S}\left([\mathrm{gas}]_{\mathrm{in}} - [\mathrm{gas}]_{\mathrm{out}}\right). \tag{2.1}$$

Here, the $[gas]_{\mathrm{in}}$ and $[gas]_{\mathrm{out}}$ represent the mole fractions of COS ($\mathrm{pmol\,mol^{-1}}$) and CO_2 ($\mu\mathrm{mol\,mol^{-1}}$) in the air entering and exiting the chamber, which are measured by the QCLS on a dry-air basis. The leaf area S ($\mathrm{m^2}$) was 9 $\mathrm{cm^2}$. Although transpiration slightly increases the outlet air flow due to the addition of water vapor (Caemmerer et al., 1981), the resulting increase in total molar flow (< 3% under $[H_2O]_{\mathrm{out}}$ = 15—30 $\mathrm{mmol\,mol^{-1}}$) was neglected in Equation 1 for simplicity. Since this was only a small effect, it was not considered in the flux calculations and was consistently omitted throughout the model analysis. The CO_2 leaf assimilation rates obtained from the QCLS measurements closely matched those from the LI-6800 ($R = 0.96$, mean difference = 0.18 $\mu\mathrm{mol\,m^{-2}\,s^{-1}}$), confirming the accuracy of the CO_2 flux measurements.

Hourly calibration corrected potential QCLS drift, and the data points were excluded when the dew point temperature approached or exceeded the air temperature in any experiment.

To account for COS emissions at higher temperatures from chamber material (Maseyk et al., 2014), we conducted empty chamber experiments using inflowing COS mole fractions of 750–900 $\mathrm{pmol\,mol^{-1}}$, which were adequate for evaluating chamber emissions, across a similar range of temperatures with experimental conditions. Additional experiments with low mole fraction (40–75 $\mathrm{pmol\,mol^{-1}}$) were conducted to evaluate potential emission increases originating from large concentration gradients between sampling air and chamber materials. Fig. 2.1 shows a slight increase in COS emissions with rising temperature, with no significant effect from inflowing COS mole fractions. Measurements were conducted under 40% relative humidity (RH), to avoid potential condensation or other artifacts during the empty chamber experiment. Leaf COS flux measurements were corrected using a linear fit of emissions against temperature in the empty chamber ($R^2 = 0.45$) with chamber emissions averaging 6.7% of observed leaf COS flux.

2.2.1.2 Experiments

Table 2.1 lists the environmental factors that were used in the three experiments. We manipulated inflowing COS mole fractions, humidity, and air temperatures while keeping other environmental conditions constant, as specified in each experimental design. All environmental changes were introduced gradually to allow the leaf sufficient time to adapt to chamber conditions. For instance, we applied humidity (to achieve a desired g_{sw}) and temperature changes of approximately 0.8 $\mathrm{mol\,m^{-2}\,s^{-1}}$ and 10 °C, respectively, over a period of two hours. This gradual adjustment ensured that measurements reflect steady-state conditions and minimize transient effects from rapid environmental changes. To exclude the effects of light on V_{COS} and

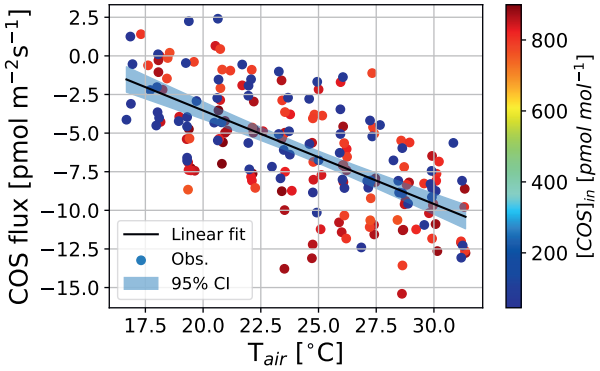


Figure 2.1: Measurements of COS flux at different air temperatures in the empty chamber. Dots represent measurement data points and their colors indicate injected COS mole fractions in a chamber, the black line represents the linear fit, and the shaded area indicates the 95% confidence interval.

V_{CO2}, high light intensity similar to growth conditions (600 $\mu mol\, m^{-2}\, s^{-1}$) was maintained throughout all experiments.

The first experiment (Experiment 1) aimed to detect COS compensation points and their temperature dependence. To determine the existence of Γ_{COS} and its temperature response, we measured F_{COS} at four distinct inflow COS mole fractions ranging from 94 to 589 $pmol\, mol^{-1}$ at two different leaf temperatures (19.8 °C and 25.0 °C). As in Gimeno et al. (2017), the values of the Γ_{COS} were subsequently calculated for each temperature by extrapolating the COS mole fraction at which F_{COS} reaches zero using a linear regression.

The second experiment (Experiment 2) aimed to compare responses of COS and CO_2 uptake to stomatal closure. We examined the responses of V_{COS} and V_{CO2} to g_{sw} while keeping other environmental factors constant, including air temperature (approximately 25 °C). Thus, changes in V_{COS} and V_{CO2} predominantly reflect responses to changes in g_{sw}. The modulation of g_{sw} was accomplished by adjusting humidity within the leaf cuvette—hence modifying VPD—using the humidifier.

The last experiment (Experiment 3) aimed to compare responses of COS and CO_2 uptake to changing temperatures. We observed V_{COS} and V_{CO2} while controlling the air temperature (T_{air}) within the leaf cuvette and maintaining other variables constant, including g_{sw}. The desired g_{sw} value was sustained by manipulating chamber humidity and thus VPD when necessary. The resulting leaf temperatures varied between 19.0 and 30.9 °C.

Regarding a repetition of experiments, Experiment 1 was executed once with a single sunflower plant (Sunflower 1), while Experiments 2 and 3 were replicated with three different sunflower plants over three days (Sunflower 2, 3, and 4). During the measurement of COS, CO_2, and H_2O mole fractions in Experiment 3, the complete temperature range could not be covered consistently across all three repetitions due to fluctuating g_{sw} conditions. Due to this limitation, data from Sunflower 3 were omitted from the analysis of Experiment 3. Overall, we collected 15 data points from Experiment 1 and 48 data points from Experiments 2 and 3.

Table 2.1: Environmental conditions during the three experiments. Controlled variables are shown as ranges (minimum–maximum), while constant variables are presented as mean ± standard deviation. Experiment 1 (Sunflower 1) targets detecting the COS compensation point at two temperatures. Experiments 2 (Sunflower 2, 3, and 4) and 3 (Sunflower 2 and 4) explore the responses of V_{COS} and V_{CO2} to g_{s} and g_{m}, respectively. We controlled a designated variable in each experiment while other variables including light intensity, air flow rate, and mixing fan speed were kept constant.

Experiment (Control)	Experiment 1 ($[\mathrm{COS}]_{\mathrm{in}}$)		Experiment 2 (g_{sw})			Experiment 3 (T_{leaf})	
Sunflower number (-)	1	1	2	3	4	2	3
g_{sw} ($\mathrm{mol\,m^{-2}\,s^{-1}}$)	0.8 ± 0.0	0.9 ± 0.1	0.4–1.1	0.3–1.0	0.3–0.6	0.6 ± 0.1	0.6 ± 0.0
VPD (kPa)	0.5 ± 0.0	0.5 ± 0.0	0.6 ± 0.1	0.7 ± 0.2	0.9 ± 0.3	0.7 ± 0.2	0.9 ± 0.3
T_{leaf} (°C)	19.8 ± 0.0	25.0 ± 0.3	25.1 ± 0.0	26.4 ± 0.1	24.8 ± 0.3	19.1–30.9	19.0–29.8
$[\mathrm{COS}]_{\mathrm{in}}$ ($\mathrm{pmol\,mol^{-1}}$)	94.1–589.1	104.5–707.0	1096.4 ± 12.6	1181.9 ± 11.1	914.4 ± 29.6	1087.7 ± 41.1	926.8 ± 14.0
$[\mathrm{CO_2}]_{\mathrm{in}}$ ($\mu\mathrm{mol\,mol^{-1}}$)	446.5 ± 0.1	449.1 ± 0.3	441.0 ± 0.4	446.2 ± 1.5	447.5 ± 1.7	439.9 ± 3.1	447.3 ± 1.4

The measured V_{COS} and V_{CO2} were used to calculate the LRU (-), which was used to characterize differing response of COS and CO_2 from Experiments 2 and 3:

$$\mathrm{LRU} = \frac{V_{\mathrm{COS}}}{V_{\mathrm{CO_2}}} = \frac{A_{\mathrm{COS}}}{[\mathrm{COS}]_{\mathrm{out}}} \cdot \frac{[\mathrm{CO_2}]_{\mathrm{out}}}{A_{\mathrm{CO_2}}}, \tag{2.2}$$

where A_{COS} ($\mathrm{pmol\,m^{-2}\,s^{-1}}$) and A_{CO2} ($\mathrm{\mu mol\,m^{-2}\,s^{-1}}$) are assimilation rates of COS and CO_2, respectively. These rates were normalized by outflowing concentrations $[COS]_{\mathrm{out}}$ and $[CO_2]_{\mathrm{out}}$.

2.2.2 Conductance model

2.2.2.1 General concept

Since the observations were somewhat limited in exploring internal leaf processes, we developed a conductance model and applied an optimization method using 48 data points from Experiments 2 and 3. Experiment 1 (15 data points) was used to provide initial information of Γ_{COS} and its temperature dependence to the model (Sect. 2.2.2.4). This modeling framework was designed to mechanistically link experimental observations to internal gas-exchange processes.

Our leaf conductance model simulates the concurrent exchange of COS, CO_2, and H_2O in a plant leaf with the conditions of the laboratory experiments. Since these gases share the same stomatal pathway, their simultaneous modeling helps us understand the mechanisms of leaf conductance. The model calculates mole fractions on a wet-air basis, while the measurements are reported on a dry-air basis (see Sect. 2.2.1.1). Accordingly, conversions between dry- and wet-air mole fractions were applied when comparing modeled and observed concentrations. Additionally, the model assumes that gas exchange reaches an equilibrium that we tried to attain in the conducted experiments (see Sect. 2.2.1.1). All model variables that remain constant in the model are listed in Table 2.2. Variables excluded from Table 2.2 are targets for optimization as explained in Sect. 2.2.4.1.

Fig. 2.2a schematically illustrates the methodology for the gas exchange experiments. As described in Sect. 2.2.1.2, environmental conditions, including $[COS]_{\mathrm{in}}$, T_{air}, and VPD, were manipulated to test the hypotheses while keeping other variables, such as light levels, constant. The cuvette received controlled mole fractions of the three gases via the airflow. Fig. 2.2b depicts the exchange pathways of COS, CO_2, and H_2O within the sunflower leaf, which form the basis for the conductance model. We assumed that COS, CO_2, and H_2O production or consumption within the plant were governed by three conductances: boundary layer conductance (g_{b} ($\mathrm{mol\,m^{-2}\,s^{-1}}$)), stomatal conductance (g_{s} ($\mathrm{mol\,m^{-2}\,s^{-1}}$)), and mesophyll conductance (g_{m} ($\mathrm{mol\,m^{-2}\,s^{-1}}$)) limited by physical or biochemical processes.

With a designated set of conductance values, the model simulates the mole fractions of the three gases in each layer: ambient air ($[gas]_{\mathrm{a}}$), boundary layer ($[gas]_{\mathrm{b}}$), and inter-cellular airspace ($[gas]_{\mathrm{i}}$)), and mesophyll level ($[gas]_{\mathrm{c}}$). The mole fractions of COS, CO_2, and H_2O are represented in units of $\mathrm{pmol\,mol^{-1}}$, $\mathrm{\mu mol\,mol^{-1}}$, and $\mathrm{mmol\,mol^{-1}}$, respectively.

The following rate equations describe the gas exchanges tendencies, assuming they achieve a steady state:

$$\frac{d[\mathrm{gas}]_a}{dt}\left(\frac{V_{\mathrm{cv}}}{V_m S}\right) = -g_b\left([\mathrm{gas}]_a - [\mathrm{gas}]_b\right) + \frac{AF}{S}\left([\mathrm{gas}]_{\mathrm{in}} - [\mathrm{gas}]_a\right) = 0, \tag{2.3}$$

$$\frac{d[\mathrm{gas}]_b}{dt}\left(\frac{V_{\mathrm{cv}}}{V_m S}\right) = g_b\left([\mathrm{gas}]_a - [\mathrm{gas}]_b\right) - g_s\left([\mathrm{gas}]_b - [\mathrm{gas}]_i\right) = 0, \tag{2.4}$$

Table 2.2: Model constants used in the model. Variables in all gases were used for all models, while those specific to COS, CO_2, and H_2O were applied to their respective models. The molar volume (V_m) is at standard temperature (298 K) and pressure (100 kPa).

Gas	Symbol	Description	Unit	Value	Q_{10}
All	S	Leaf area	cm^2	9.0	
	R	Universal molar gas constant	$\mathrm{J\,K^{-1}\,mol^{-1}}$	8.314	
	V_m	Molar volume	$\mathrm{m^3\,mol^{-1}}$	0.0248	
	V_cv	Cuvette volume	cm^3	109[a]	
COS	$\Delta H_\mathrm{a,CA}$	Activation energy of CA	$\mathrm{kJ\,mol^{-1}}$	40[b]	
	$\Delta H_\mathrm{eq,CA}$	Enthalpy change of CA	$\mathrm{kJ\,mol^{-1}}$	100[b]	
CO_2	τ_298K	Specificity factor between CO_2 and O_2 at 298 K	–	2600[c]	0.57
	$K_{c,\mathrm{298K}}$	Michaelis–Menten constant for carboxylation at 298 K	Pa	30[c]	2.1
	$K_{o,\mathrm{298K}}$	Michaelis–Menten constant for oxygenation at 298 K	Pa	30000[c]	1.2
	R_d	Dark respiration at 298 K	$\mathrm{\mu mol\,m^{-2}\,s^{-1}}$	3.0[c]	2.0
	$p[O_2]_\mathrm{i}$	Partial pressure of internal O_2	Pa	20900[c]	
H_2O	g_mw	Mesophyll conductance for H_2O	$\mathrm{mol\,m^{-2}\,s^{-1}}$	10	

[a] LI-COR 6800 documentation.
[b] Cho et al. (2023)
[c] Collatz et al. (1991).

$$\frac{d[\mathrm{gas}]_i}{dt}\left(\frac{V_\mathrm{cv}}{V_m S}\right) = g_s\left([\mathrm{gas}]_b - [\mathrm{gas}]_i\right) - g_m\left([\mathrm{gas}]_i - [\mathrm{gas}]_c\right) = 0. \tag{2.5}$$

Here, V_m ($\mathrm{m^3\,mol^{-1}}$) is the molar volume, and V_cv (m^3) is the effective air volume representing the gas-exchange region near the leaf surface. Under steady-state conditions, the first term on the left-hand side of Eqs. 2.3, 2.4, and 2.5, which represents the rate of gas accumulation, becomes negligible. To account for the different properties of COS and CO_2 to H_2O, the stomatal conductances ($g_\mathrm{s,COS}$ and $g_\mathrm{s,CO2}$) and the boundary layer conductances ($g_\mathrm{b,COS}$ and $g_\mathrm{b,CO2}$) are scaled proportionally to the conductance of water vapor (g_sw and g_bw) ($g_\mathrm{s,CO2} = g_\mathrm{sw}/1.6$, $g_\mathrm{b,CO2} = g_\mathrm{bw}/1.4$, $g_\mathrm{s,COS} = g_\mathrm{sw}/1.94$, $g_\mathrm{b,COS} = g_\mathrm{bw}/1.56$) (Bonan, 2008; Seibt et al., 2010; Stimler et al., 2010).

For the COS and CO_2 exchange at the stomatal level, a ternary system with H_2O and air should be considered, because the transpiration (F_H2O ($\mathrm{mol\,m^{-2}\,s^{-1}}$)) is significantly larger than COS and CO_2 assimilation (Jarman, 1974; Caemmerer et al., 1981). Thus, we added the ternary term in Eqs. 2.4 and 2.5 for the COS and CO_2 models:

$$\frac{d[\mathrm{gas}]_b}{dt}\left(\frac{V_\mathrm{cv}}{V_m S}\right) = g_b\left([\mathrm{gas}]_a - [\mathrm{gas}]_b\right) - g_s\left([\mathrm{gas}]_b - [\mathrm{gas}]_i\right) + F_\mathrm{H_2O}\frac{[\mathrm{gas}]_b + [\mathrm{gas}]_i}{2} = 0, \tag{2.6}$$

$$\frac{d[\mathrm{gas}]_i}{dt}\left(\frac{V_\mathrm{cv}}{V_m S}\right) = g_s\left([\mathrm{gas}]_b - [\mathrm{gas}]_i\right) - F_\mathrm{H_2O}\frac{[\mathrm{gas}]_b + [\mathrm{gas}]_i}{2} - g_m\left([\mathrm{gas}]_i - [\mathrm{gas}]_c\right) = 0. \tag{2.7}$$

Although accounting for the H_2O ternary system is important, its influence on the calculated mole fractions was found to be negligible. The smaller ternary effects within the leaf

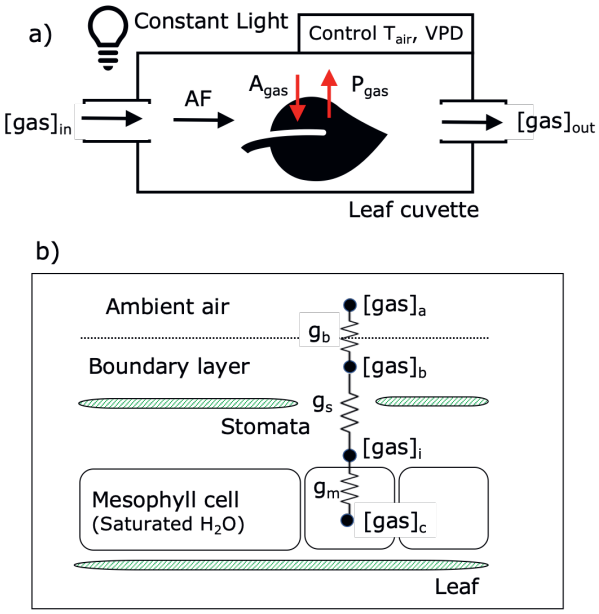


Figure 2.2: Schemes of leaf cuvette experiments (a) and diffusion pathways of COS, CO_2, and H_2O into and out of a leaf in the conductance model (b). A_{gas} and P_{gas} indicate the assimilation rate and production rate of each gas. g_{b}, g_{s}, and g_{m} represent boundary, stomatal, and mesophyll conductance, respectively.

boundary layer were therefore not included, as they scale with E/g_{bw} (Caemmerer et al., 1981) and are expected to be negligible under our experimental conditions (large g_{bw} and small E). Note that the mole fractions calculated by the model are expressed on a wet-air basis, whereas the observed mole fractions are reported on a dry-air basis. The moisture correction applied to model outputs is described at the end of this section.

To test Hypothesis 2, we analyzed how the intercellular mole fraction $[gas]_{\mathrm{i}}$ influences the net flux. The flux was computed using Eqs. 2.3, 2.6, 2.7 to determine $[gas]_{\mathrm{i}}$, and then applied to the flux-gradient relationship:

$$F_{\mathrm{gas}} = g_{\mathrm{b}\to\mathrm{s}} \left([\mathrm{gas}]_a - [\mathrm{gas}]_i \right). \tag{2.8}$$

Here, $g_{\mathrm{b}\to\mathrm{s}}$ denotes the conductance from the leaf boundary layer to the stomata. The deposition velocity (V_{gas} ($\mathrm{mol\,m^{-2}\,s^{-1}}$)) can be calculated as follows:

$$V_{\mathrm{gas}} = g_{b\to s} \left(1 - \frac{[\mathrm{gas}]_i}{[\mathrm{gas}]_a} \right). \tag{2.9}$$

The term $(1 - [gas]_{\mathrm{i}}\,[gas]_{\mathrm{a}}^{-1})$ represents the effect of changes between internal and ambient mole fractions on the gas conductance and deposition velocity, termed Ambient Fraction Remaining (AFR). This concept is utilized in Sect. 2.3.2.3 for interpreting Hypothesis 2. Strictly speaking, the mass flow difference between the inlet and outlet and the ternary effect should be considered in Eqs. 2.8 and 2.9. However, these effects are expected to be minor under our experimental conditions (see above), and Eqs. 2.8 and 2.9 were used only to examine the con-

ceptual relationship between $[gas]_{\mathrm{i}}$ and flux. Therefore, for simplicity, these correction terms were omitted. Note that this omission does not affect the interpretation of AFR in Sect. 2.3.2.3.

This set of coupled rate equations can be solved analytically, resulting in mole fractions of the three gases in each layer. Conductance at the mesophyll level (g_{m}) and $[gas]_{\mathrm{c}}$ were calculated using a different model for each gas. Descriptions of the individual biophysical processes at the mesophyll level for each gas are provided in subsequent sections.

From experiments, we measured $[gas]_{\mathrm{out}}$, while the leaf conductance model calculates $[gas]_{\mathrm{a}}$. Because the chamber air was well mixed, the modeled $[gas]_{\mathrm{out,est}}$ is considered equivalent to $[gas]_{\mathrm{a}}$ for model-observation comparison. Thus, $[gas]_{\mathrm{out,est}}$ is used for $[gas]_{\mathrm{a}}$ to interpret experimental data.

In the model, the estimated mole fractions for COS and CO_2 are based on wet air, whereas the QCLS measures dry-air mole fractions. Therefore, to compare model results with observations, the modeled wet-air mole fractions were converted to their dry-air equivalents using the observed outgoing H_2O mole fractions ($[H_2O]_{\mathrm{out,obs}}$ ($\mathrm{mmol\,mol^{-1}}$)):

$$[\mathrm{gas}]_{\mathrm{out,est}} = [\mathrm{gas}]_a \left(1 - \frac{[\mathrm{H_2O}]_{\mathrm{out,obs}}}{1000}\right)^{-1}. \tag{2.10}$$

For $[COS]_{\mathrm{in,obs}}$, which was measured after moisture removal, the same correction (Eq. 2.10) was applied using $[H_2O]_{\mathrm{in,obs}}$ instead of $[H_2O]_{\mathrm{out,obs}}$ to convert from the dry-air to the wet-air basis before use in the conductance model.

Finally, net fluxes of the three gases were calculated using the same methodology as employed for the observations (Eq. 2.1).

2.2.2.2 Water vapor model

In our experiments, we observed water evaporation from leaves. We aimed to model this evaporation at the mesophyll level and its subsequent transport out of the leaves, governed by g_{sw}. The unit of H_2O mole fractions in all layers is $\mathrm{mmol\,mol^{-1}}$, and the unit of the flux is $\mathrm{mmol\,m^{-2}\,s^{-1}}$.

To represent the internal water vapor conditions, $[H_2O]_{\mathrm{c}}$ was calculated assuming that water vapor within the mesophyll intercellular airspace is saturated. However, we allowed for relative humidity within the intercellular airspace (RH_{i} (%)) to be less than 100%, based on previous studies (Cernusak et al., 2018; Wong et al., 2022). To achieve this, we introduced a mesophyll conductance for water vapor (g_{mw}) and set it to an arbitrary value of $10\,\mathrm{mol\,m^{-2}\,s^{-1}}$, approximately ten times the largest observed value of g_{sw}. This parameter was included to test the sensitivity of the model to possible non-saturation within the intercellular airspace. The expression for $[H_2O]_{\mathrm{c}}$ relies on T_{leaf} (°C) and air pressure (P_{air} (Pa)):

$$[\mathrm{H_2O}]_c = 1000\,\frac{P_{\mathrm{H_2O}}}{P_{\mathrm{air}}}, \tag{2.11}$$

$$P_{\mathrm{H_2O}} = 613.5\,\exp\left(\frac{17.502\,T_{\mathrm{leaf}}}{T_{\mathrm{leaf}} + 240.97}\right). \tag{2.12}$$

Using these assumptions, we calculated the water vapor mole fractions in the atmosphere ($[H_2O]_{\mathrm{a}}$), boundary layer ($[H_2O]_{\mathrm{b}}$), and interior(($[H_2O]_{\mathrm{i}}$) by solving Eqs. 2.3, 2.4, and 2.5. Finally, we estimated the RH_{i} (%) from the calculated $[H_2O]_{\mathrm{c}}$ and $[H_2O]_{\mathrm{i}}$:

$$RH_{\mathrm{i}} = 100\,\frac{[\mathrm{H_2O}]_{\mathrm{i}}}{[\mathrm{H_2O}]_{\mathrm{c}}}. \tag{2.13}$$

2.2.2.3 CO_2 model

We aimed to simulate the gross CO_2 flux (F_{CO2}, $\mu mol\, m^{-2}\, s^{-1}$) and mole fractions of CO_2 in each layer ($\mu mol\, mol^{-1}$) using the model proposed by Farquhar et al. (1980). In this model, the gross CO_2 uptake rate is calculated as the minimum value among assimilation limited by enzymes (A_m), light (A_E), and sucrose synthesis (A_S), minus the dark respiration (R_d) :

$$F_{CO_2} \approx \min\left(A_m,\, A_E,\, A_S\right) - R_d. \tag{2.14}$$

Our experiments were conducted under a constant light intensity ($PAR = 600\, \mu mol\, m^{-2}\, s^{-1}$). We assumed that the A_E and A_S pathways were saturated, as light saturation points previously were obtained above 500 $\mu mol\, m^{-2}\, s^{-1}$ (Lobo et al., 2013). Consequently, we calculated $g_{m,CO2}$ ($[CO_2]_i - [CO_2]_c$) in Eq. 2.7 with $A_m - R_d$. R_d was estimated by Collatz et al. (1991).

Am is calculated by multiplying the maximum rate of RuBisCO carboxylation ($V_{max,Rub}$) with the partial pressure changes from RuBP partitioning between the CO_2 carboxylation and O_2 oxygenation reactions:

$$A_m = \frac{V_{max,Rub}\, f_{rub}(T_{leaf})\, \left(p[CO_2]_i - \Gamma^*_{CO_2}\right)}{p[CO_2]_i + K_C\left(1 + \frac{p[O_2]_i}{K_O}\right)}, \tag{2.15}$$

where $p[CO_2]_i$ (Pa) and $p[O_2]_i$ (Pa) are the partial pressures of CO_2 and O_2 in the intercellular air space. K_c (Pa) and K_o (Pa) are Michaelis-Menten constants for CO_2 and O_2, respectively. Γ^*_{CO2} (Pa) stands for the CO_2 compensation point independent of dark respiration.

Strictly speaking, RuBisCO carboxylation occurs within the chloroplast stroma and should depend on the chloroplast CO_2 partial pressure ($p[CO_2]_c$), rather than $p[CO_2]_i$. However, our model does not explicitly include mesophyll conductance ($g_{m,CO2}$), and thus $p[CO_2]_c$ cannot be directly resolved. Accordingly, $p[CO_2]_i$ was used as a proxy for $p[CO_2]_c$, following the classical formulation of Farquhar et al. (1980). The estimation of Γ^*_{CO2} is based on the partial pressure of oxygen linked to the side reaction of RuBisCO:

$$R_2 = R_1\, Q_{10}^{\left(\frac{T_2 - T_1}{10}\right)}. \tag{2.16}$$

Here, T_2 corresponds to T_{leaf}, and T_1 is 25 °C for the CO_2 parameters K_c, K_o, and Γ^*_{CO2}. The temperature function of $V_{max,Rub}$ ($\mu mol\, m^{-2}\, s^{-1}$) at T_{leaf} (°C) is calculated by (Badger et al., 1977):

$$f_{Rub}(T_{leaf}) = \exp\left(\frac{\left((T_{leaf} + 273.15) - T_{ref,Rub}\right)\, \Delta H_{a,Rub}}{T_{ref,Rub}\, R\, (T_{leaf} + 273.15)}\right), \tag{2.17}$$

where $\Delta H_{a,Rub}$ ($J\, mol^{-1}$) is the activation energy of RuBisCO, valued at 60.0 $kJ\, mol^{-1}$ (Caemmerer et al., 2015), and $T_{ref,Rub}$ (K) is the reference temperature (298 K). R is the universal molar gas constant ($8.3145\, J\, K^{-1}\, mol^{-1}$).

2.2.2.4 COS model

We constructed the COS model to estimate the gross COS flux rate (F_{COS} ($pmol\, m^{-2}\, s^{-1}$)) and mole fractions of COS in each layer ($pmol\, mol^{-1}$). Accurate modeling of COS leaf uptake requires mesophyll conductance, which integrates both the diffusional transport of COS and biochemical conversion by CA.

Earlier approaches treated mesophyll diffusion and CA activity as linearly proportional to Rubisco's $V_{\max}$ (Berry et al., 2013). However, this simplification was shown to bias COS flux estimates, leading to the introduction of a revised CA-based temperature formulation (Cho et al., 2023). More recently, Lai et al. (2024) emphasized the importance of explicitly accounting for mesophyll diffusion in COS uptake models but also noted the lack of reliable parameterization for COS-specific mesophyll diffusion.

Building on these previous findings, we modeled biochemical conductance of COS in the mesophyll ($g_{\mathrm{m,COS}}$ ($\mathrm{mol\,m^{-2}\,s^{-1}}$)) using the CA activity–based function proposed by Cho et al. (2023), which implicitly represents mesophyll diffusion while minimizing estimation bias through its revised temperature dependence. This function describes the temperature dependence of CA activity using a specified Arrhenius equation and Michaelis-Menten Kinetics (Cho et al., 2023; Daniel et al., 2010; Ogée et al., 2016; Sun et al., 2015):

$$g_{\mathrm{m,COS}} = V_{\mathrm{max,CA}}\, f_{\mathrm{CA}}(T_{\mathrm{leaf}}) = V_{\mathrm{max,CA}}\, A_T \frac{(T_{\mathrm{leaf}} + 273.15)\, \exp\left[-\frac{\Delta H_{\mathrm{a,CA}}}{R(T_{\mathrm{leaf}}+273.15)}\right]}{1 + \exp\left[-\frac{\Delta H_{\mathrm{eq,CA}}}{R}\left(\frac{1}{T_{\mathrm{leaf}}} - \frac{1}{T_{\mathrm{eq,CA}}+273.15}\right)\right]}. \quad (2.18)$$

Here, $V_{\mathrm{max,CA}}$ ($\mathrm{mol\,m^{-2}\,s^{-1}}$) is the maximum catalyzation velocity of CA, $\Delta H_{\mathrm{a,CA}}$ ($\mathrm{J\,mol^{-1}}$) represents the activation free energy of CA and $\Delta H_{\mathrm{eq,CA}}$ ($\mathrm{J\,mol^{-1}}$) is the enthalpy change when the enzyme transits from activation to inactivation. $T_{\mathrm{eq,CA}}$ (°C) stands for the optimum temperature at which the concentrations of activated and inactivated enzymes are equal (Daniel et al., 2010; Sun et al., 2015; Ogée et al., 2016). We adopted the normalization factor A_{T} as the value of $f_{\mathrm{CA}}(T_{\mathrm{eq,CA}})^{-1}$.

To incorporate temperature-dependent compensation point behavior, we applied the Γ_{COS} into $[COS]_{\mathrm{c}}$. We proposed four temperature functions of Γ_{COS} based on Experiment 1 data. For model S1, Γ_{COS} was set to zero across all temperatures, assuming no compensation point effects. For model S2, Γ_{COS} was represented as a linear function:

$$\Gamma_{\mathrm{COS}}(T_{\mathrm{leaf}}) = f_{\Gamma_{\mathrm{COS}}}(T_{\mathrm{leaf}}) = m_{\mathrm{COS}}\,(T_{\mathrm{leaf}} - T_{\mathrm{ref}}), \quad (2.19)$$

where T_{ref} (°C) is the intercept temperature (16.4 °C), determined from the linear regression of two Γ_{COS} values detected in Experiment 1 (Sect. 2.3.1.1). The slope m_{COS} ($\mathrm{pmol\,mol^{-1}\,K^{-1}}$) was set to 16.2 $\mathrm{pmol\,mol^{-1}\,K^{-1}}$, also derived from Experiment 1. At low temperatures, where Γ_{COS} becomes negative, we assumed $\Gamma_{\mathrm{COS}} = 0$. For model S3, Γ_{COS} was calculated using the Arrhenius function with an observation-based value of 55.0 $\mathrm{pmol\,mol^{-1}}$ at 293 K from Experiment 1:

$$\Gamma_{\mathrm{COS}}(T_{\mathrm{leaf}}) = 55.0\, \exp\left[\frac{((T_{\mathrm{leaf}} + 273.15) - 293)\, \Delta H_{\mathrm{a},\Gamma}}{293\, R\, (T_{\mathrm{leaf}} + 273.15)}\right], \quad (2.20)$$

and for model S4, Γ_{COS} was similarly computed using a reference value of 138.7 $\mathrm{pmol\,mol^{-1}}$ at 298 K:

$$\Gamma_{\mathrm{COS}}(T_{\mathrm{leaf}}) = 138.7\, \exp\left[\frac{((T_{\mathrm{leaf}} + 273.15) - 298)\, \Delta H_{\mathrm{a},\Gamma}}{298\, R\, (T_{\mathrm{leaf}} + 273.15)}\right], \quad (2.21)$$

where $\Delta H_{\mathrm{a},\Gamma}$ ($\mathrm{kJ\,mol^{-1}}$) represents the activation energy for Γ_{COS}. By solving for $\Delta H_{\mathrm{a},\Gamma}$ using the two derived Γ_{COS} values, we determined an initial activation energy of 134.3 $\mathrm{kJ\,mol^{-1}}$.

Figure 2.3 shows these four Γ_{COS} functions (S1–S4) representing the prior temperature-dependent parameterizations tested in the modeling framework with their imposed uncertainties. The figure also shows the experimental Γ_{COS} estimates from Experiment 1, included solely for reference to illustrate the initial parameter alignment.

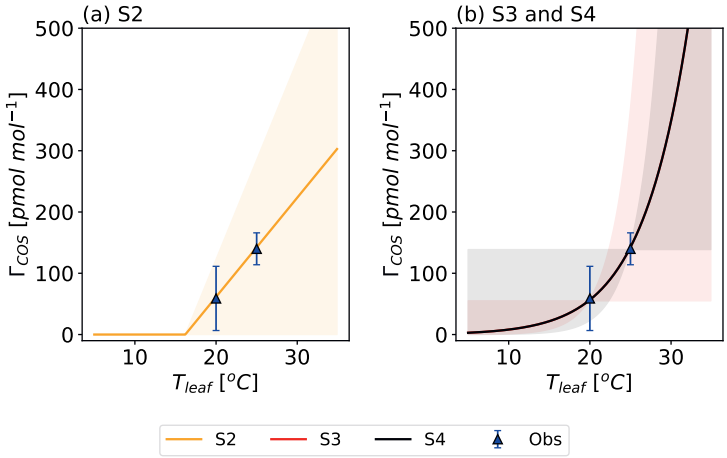


Figure 2.3: Prior temperature functions of the COS compensation point (Γ_{COS}) (lines) with their error ranges (shaded area). Blue triangles show the regression-derived Γ_{COS} from Experiment 1, included for reference to illustrate the initial parameter setup. The S1 model assumed $\Gamma_{\mathrm{COS}} = 0$ pmol mol^{-1}. Model S2 describes Γ_{COS} as a linear relationship with T_{leaf} (a), while models S3 and S4 use an Arrhenius equation (b).

2.2.3 Indirectly derived COS compensation point

Because the temperature-dependent behavior of Γ_{COS} in Experiment 1 was derived from a limited set of measurements under only a few temperatures, additional validation was required to test whether the modeled Γ_{COS} functions are consistent across broader environmental conditions. To support this validation, we incorporated the indirectly derived Γ_{COS} from 48 data points in Experiments 2 and 3. By calculating $[COS]_{\mathrm{c}}$ using our optimized model parameters in Eqs. 2.3, 2.6, and 2.7, we were able to indirectly estimate Γ_{COS} and compare it with the modeled Γ_{COS}. First, we calculated $[COS]_{\mathrm{b}}$ from the measured COS mole fractions with the rearranged Eq. 2.3:

$$[\mathrm{COS}]_b = [\mathrm{COS}]_a + \frac{AF}{S\, g_{\mathrm{b,COS}}} \left([\mathrm{COS}]_a - [\mathrm{COS}]_{\mathrm{in}}\right), \tag{2.22}$$

where $[COS]_{\mathrm{in}}$ and $[COS]_{\mathrm{a}}$, along with AF, S, and $g_{\mathrm{b,COS}}$, were applied from Experiments 2 and 3. Due to thorough mixing within the cuvette, we assumed $[COS]_{\mathrm{out}}$ to be equivalent to $[COS]_{\mathrm{a}}$ and used it accordingly (refer to Sect. 2.2.2.1). Although transpiration slightly increases the outlet air flow, this effect ($< 3\%$) was neglected to simplify the analytical expressions, consistent with the assumptions described in Equation 2.1. This formulation follows the same assumptions as in Equation 2.3 regarding ternary effects at the boundary layer, which were found to be negligible under our experimental conditions. Here, $[COS]_{\mathrm{in}}$ and $[COS]_{\mathrm{out}}$

were converted from a dry air basis to a wet air basis. We then used the derived $[COS]_{\mathrm{b}}$ to calculate $[COS]_{\mathrm{i}}$ using the rearranged Eq. 2.6:

$$[\mathrm{COS}]_{\mathrm{i}} = \frac{-g_{\mathrm{b,COS}}\,[\mathrm{COS}]_a + g_{\mathrm{b,COS}}\,[\mathrm{COS}]_b + g_{\mathrm{s,COS}}\,[\mathrm{COS}]_b - 0.5\,F_{\mathrm{H_2O}}\,[\mathrm{COS}]_b}{g_{\mathrm{s,COS}} + 0.5\,F_{\mathrm{H_2O}}}. \tag{2.23}$$

F_{H2O} was calculated using Eq. 2.1 with the observed $[H_2O]_{\mathrm{in}}$ and the modeled $[H_2O]_{\mathrm{a}}$ obtained by the H_2O model. We used optimized g_{sw} value in the H_2O model and $g_{\mathrm{s,COS}}$. The reason for using the model-calculated $[H_2O]_{\mathrm{a}}$ instead of the observed $[H_2O]_{\mathrm{out}}$ is to consider the optimized g_{sw} in F_{H2O}.

Finally, $[COS]_{\mathrm{i}}$ is used in Eq. 2.7 to derive $[COS]_{\mathrm{c}}$:

$$[\mathrm{COS}]_c = -\frac{g_{\mathrm{s,COS}}}{g_{\mathrm{m,COS}}}\left([\mathrm{COS}]_b - [\mathrm{COS}]_i\right) + \frac{F_{\mathrm{H_2O}}}{g_{\mathrm{m,COS}}}\left([\mathrm{COS}]_b + [\mathrm{COS}]_i\right) + [\mathrm{COS}]_i, \tag{2.24}$$

where $g_{\mathrm{m,COS}}$ was determined using Eq. 2.18 with optimized parameters $V_{\mathrm{max,CA}}$ and $T_{\mathrm{eq,CA}}$. These indirectly calculated Γ_{COS} values vary depending on the chosen temperature-dependent functions of Γ_{COS}, which influence other parameters. Consequently, the indirectly derived Γ_{COS} values differ from Γ_{COS} functions due to their impact on the optimized parameters used in the calculations.

2.2.4 Parameter optimization

2.2.4.1 Optimization setting

Beginning with the model state parameter (x), we calculated $[gas]_{\mathrm{out,est}}$ and compared these to the observed values $[gas]_{\mathrm{out,obs}}$ on a dry-air basis. We aimed to minimize the differences between our model and the observations during each optimization step. To accomplish this, we defined a cost function (J_{tot}) consisting of a background term (J_{bg}) and three observational terms that account for the differences between model estimations and observations of COS (J_{COS}), CO_2 (J_{CO2}), and H_2O (J_{H2O}):

$$\begin{aligned} J_{\mathrm{tot}} &= J_{\mathrm{bg}} + J_{\mathrm{COS}} + J_{\mathrm{CO_2}} + J_{\mathrm{H_2O}} \\ &= \frac{1}{W_{\mathrm{bg}}}\frac{(x - x_a)^2}{\sigma^2} + \frac{1}{W_{\mathrm{COS}}}\frac{\left([\mathrm{COS}]_{\mathrm{out,est}} - [\mathrm{COS}]_{\mathrm{out,obs}}\right)^2}{\sigma^2_{\mathrm{COS}}} \\ &\quad + \frac{1}{W_{\mathrm{CO_2}}}\frac{\left([\mathrm{CO_2}]_{\mathrm{out,est}} - [\mathrm{CO_2}]_{\mathrm{out,obs}}\right)^2}{\sigma^2_{\mathrm{CO_2}}} \\ &\quad + \frac{1}{W_{\mathrm{H_2O}}}\frac{\left([\mathrm{H_2O}]_{\mathrm{out,est}} - [\mathrm{H_2O}]_{\mathrm{out,obs}}\right)^2}{\sigma^2_{\mathrm{H_2O}}}. \end{aligned} \tag{2.25}$$

The first term of the cost function penalizes deviations of the state x from the prior state vector x_{a}. This penalty depends on σ, which represents the prior error in the state vector. This background term is introduced to keep state variables within reasonable boundaries (Brasseur et al., 2017). The last three terms of the cost function calculate the costs associated with deviations between modeled ($[gas]_{\mathrm{out,est}}$) and observed mole fractions ($[gas]_{\mathrm{out,obs}}$) for COS, CO_2, and H_2O, respectively. Each term is normalized by its observational uncertainty to ensure consistent treatment of measurement errors, and each is scaled by optimization weights (W_{bg}, W_{COS}, W_{CO2}, and W_{H2O}) to balance the relative influence of each gas. These weights do not modify the observational errors but instead prevent any single gas—particularly CO_2—from

dominating the total cost. The determination of these weights is described in the following section.

The costs related to observations (J_{COS}, J_{CO2}, and J_{H2O}) are influenced by observational errors (σ_{COS}, σ_{CO2}, and σ_{h2O}), derived from the measured COS, CO_2, and H_2O mole fractions. These observational errors were determined as the standard deviation of the measured mole fractions at outflow within the data point interval (150-second). Formally, σ_{COS}, σ_{CO2}, and σ_{H2O} should also reflect model errors caused by model parameters not included in the state or by processes that were not modeled (Brasseur et al., 2017). Note that we excluded data from Experiment 1 to validate the optimized temperature function of Γ_{COS} in Sect. 2.3.2.2.

Due to the larger relative error in $[H_2O]_{\mathrm{out,obs}}$ and $[COS]_{\mathrm{out,obs}}$ than in $[CO_2]_{\mathrm{out,obs}}$, the optimization procedure tended to focus on minimizing preliminary J_{CO2}. To better utilize the non-CO_2 observations, we introduced optimization weights for each cost component. The observed $[CO_2]_{\mathrm{out,obs}}$ values ranged from 379.4 to 390.0 $\mu\mathrm{mol\,mol}^{-1}$, with an average observational error of only 0.2 $\mu\mathrm{mol\,mol}^{-1}$ (0.05%). $[COS]_{\mathrm{out,obs}}$ values ranged from 748.2 to 1032.4 $\mathrm{pmol\,mol}^{-1}$, with an average error of 16.7 $\mathrm{pmol\,mol}^{-1}$ (1.91%). $[H_2O]_{\mathrm{out,obs}}$ values ranged from 15.2 to 32.5 $\mathrm{mmol\,mol}^{-1}$ with a mean error of 0.3 $\mathrm{mmol\,mol}^{-1}$ (1.14%).

The targeted state parameters, along with their initial values and errors, are listed in Table 2.3. We assumed that the parameters related to the temperature response of mesophyll cells are consistent across all experiments, as all sunflowers were cultivated in a similar climate. We constructed state vectors with variables that significantly impact the total cost and better quantify the combined leaf exchanges: $V_{\mathrm{max,CA}}$, $T_{\mathrm{eq,CA}}$, and m_{COS} for COS, $V_{\mathrm{max,Rub}}$ and $\Delta H_{\mathrm{a,Rub}}$ for CO_2, and g_{sw} for all gases.

Although we selected sunflower leaves at similar development stages, variations in biochemical functioning existed among individual leaves. Therefore, we optimized $V_{\mathrm{max,CA}}$ and $V_{\mathrm{max,Rub}}$ for each individual plant, as these largely determine mesophyll conductance (Williams et al., 1996; Le Roux et al., 2001; Cho et al., 2023). The initial $V_{\mathrm{max,CA}}$ was based on the averaged $V_{\mathrm{max,CA}}$ across different phenological stages from two observation sites, Hyytiälä (Finland) and Harvard Forest (United States), as introduced by Cho et al. (2023). The standard deviation of $V_{\mathrm{max,CA}}$ was used as the state error. For $V_{\mathrm{max,Rub}}$, we set the initial value as $V_{\mathrm{max,CA}}$ divided by the scaling factor 1400, derived from laboratory measurements of gas exchange in C_3 plants (Stimler et al., 2010; Stimler et al., 2011; Berry et al., 2013).

$T_{\mathrm{eq,CA}}$ is more crucial in determining CA's temperature function compared to other kinetic variables (Cho et al., 2023). We adopted the initial value and state error of $T_{\mathrm{eq,CA}}$ directly from Cho et al. (2023), ensuring consistency with previous characterizations of CA kinetics.

To further evaluate the temperature dependence of Γ_{COS}, four temperature functions (S1 to S4) were tested within the conductance model. Each function was optimized and compared against observation-based Γ_{COS}. The S1 model excludes Γ_{COS}, while S2 applies a linear function with m_{COS} of 16.2 $\mathrm{pmol\,mol}^{-1}$. Both S3 and S4 use a temperature dependence described by an Arrhenius relationship. All models were initialized with the same prior error for Γ_{COS}, including the zero-compensation point, as shown in Fig. 2.1.

For the CO_2 parameters, we optimized $\Delta H_{\mathrm{a,Rub}}$, as it is an unknown parameter for Sunflowers. We determine the initial value and error of $\Delta H_{\mathrm{a,Rub}}$ using the mean and standard deviation across nine species reported by Caemmerer et al. (2015). Other temperature-dependent parameters were adopted from Collatz et al. (1991).

The LI-6800 derives g_{sw} from water vapor exchange with its own uncertainties. Because g_{sw} similarly affects the exchange of H_2O, CO_2, and COS through the same shared stomatal pathway, we optimize g_{sw} in a coupled framework using flux information from all three gases to ensure internal consistency across species. The novelty of this framework lies in explicitly coupling these fluxes to derive a more physically consistent constraint on g_{sw}, while also ad-

dressing potential uncertainties in g_{sw} derived from LI-6800 measurements (e.g., stomatal ratio parameter K; Sect. 2.2.1.1).

Initial values for g_{sw} were taken from the LI-6800 measurements during Experiments 2 and 3. We applied a random error of 0.08 $\mathrm{mol\,m^{-2}\,s^{-1}}$, representing the standard deviation of g_{sw} from Experiment 3, despite efforts to maintain a constant g_{sw} ($\pm$ 0.06 $\mathrm{mol\,m^{-2}\,s^{-1}}$). In addition, we considered an extra measurement uncertainty of 0.02 $\mathrm{mol\,m^{-2}\,s^{-1}}$, based on known sources of instrumental bias—such as the leaf temperature underestimation (Garen et al., 2022) and background total leaf conductance to water observed in empty chambers (Hussain et al., 2024). We also added individual $[H_2O]_{\mathrm{out,obs}}$ errors by normalizing $[H_2O]_{\mathrm{out,obs}}$. The averaged initial g_{sw} value and its standard deviation (prior error) are 0.61 $\mathrm{mol\,m^{-2}\,s^{-1}}$ and 0.09 $\mathrm{mol\,m^{-2}\,s^{-1}}$, respectively.

Assuming a Gaussian probability density function for the state parameters could lead to nonphysical values in the optimization process. Thus, we minimized J_{tot} using the Sequential Least SQuares Programming optimizer (SLSQP) from the SciPy Python library. This optimizer enables the specification of lower and upper bounds on the state space and is well-suited for solving nonlinear problems. The parameter bounds are listed in Table 2.3.

Table 2.3: State parameters (x) and their prior and posterior values with their errors based on model S2. Posterior errors are calculated from 200 optimizations in a Monte Carlo method (Sect. 2.2.5). The last column denotes the error reduction. Prior and Posterior values for g_{sw} are averaged values across the dataset from Experiments 2 and 3. Values in "Bounds" column with brackets indicate lower and higher bounds provided to the optimization.

Parameter	Description	Unit	Bounds	Prior ± Error	Posterior ± Error	(b–a)/a[1] (%)
$V_{\mathrm{max,CA}}$	Maximum velocity for CA	$\mathrm{mol\,m^{-2}\,s^{-1}}$	[0.01, 0.50]	0.125 ± 0.060	0.217 ± 0.037[2] 0.189 ± 0.029[3] 0.230 ± 0.042[4]	38 52 30
$T_{\mathrm{eq,CA}}$	Optimum temperature for CA	°C	[1, 60]	30.0 ± 15.0	39.7 ± 5.0	66
m_{COS}	Slope of Γ_{COS}	$\mathrm{pmol\,mol^{-1}\,K^{-1}}$	[1, 300]	16.2 ± 16.2	22.4 ± 5.3	67
$V_{\mathrm{max,Rub}}$	Maximum velocity for RuBisCO	$\mu\mathrm{mol\,m^{-2}\,s^{-1}}$	[1, 200]	90.0 ± 20.0	94.4 ± 0.3[2] 87.4 ± 0.5[3] 82.9 ± 0.3[4]	98 98 98
$\Delta H_{\mathrm{a,Rub}}$	Activation energy for RuBisCO	$\mathrm{kJ\,mol^{-1}}$	[1, 100]	60.0 ± 12.0	54.5 ± 0.9	92
g_{sw}	Stomatal conductance of H_2O	$\mathrm{mol\,m^{-2}\,s^{-1}}$	[0, 3]	0.62 ± 0.09	0.64 ± 0.05	43

[1] 'a' is the prior error and 'b' is the posterior error; they are used to calculate the error reduction.
[2–4] Values correspond to Sunflower 2, 3, and 4, respectively.

2.2.4.2 Weight determination

We selected weights to achieve more balanced prior costs across four components in Eq. 2.25. The prior chi-squared value (χ^2_{prior}) was used to check the cost balance in the prior condition. We set seven possible weights, and the corresponding χ^2_{prior} value ranged from 3 to 200, as listed in Table 2.4. Then, we optimized parameters and calculated cost reduction rates for each part of the cost function. For H_2O, we found a χ^2_{prior} value of about 3, indicating that the H_2O model already performs well with the prior parameter settings.

Table 2.4: Candidates for weights in the observational terms (W_{COS}, W_{CO2}, and W_{H2O}) based on the chosen χ^2_{prior} values.

χ^2_{prior}	W_{COS}	W_{CO2}	W_{H2O}
3	0.337	238.8	3.24
10	0.101	71.6	0.97
30	0.034	23.9	0.32
50	0.020	14.3	0.19
100	0.010	7.2	0.10
150	0.007	4.8	0.06
200	0.005	3.6	0.05

We finally selected the weight combination that minimized the averaged reduction rates of J_{COS} and J_{CO2} and ensured that each χ^2_{poste} exceeded the value of 0.6 to avoid over-fitting, including J_{bg}. The selected weights ($W_{\text{COS}} = 0.034$, $W_{\text{CO2}} = 7.2$, $W_{\text{H2O}} = 3.24$, and $W_{\text{bg}} = 1.0$), correspond to χ^2_{prior} values of 30, 100, and 3 for COS, CO_2, and H_2O, respectively. These weights lead to a more balanced ratio of χ^2_{prior} across the observational parts (COS : CO_2 : H_2O = 10 : 33 : 1), compared to the ratio without weights (1 : 329 : 4). Note that the prior value of J_{bg} is zero by design.

2.2.5 Error statistics

We evaluated the model performance using χ^2 values, mean bias errors (MBEs), and root mean square errors (RMSEs). The χ^2 metric was calculated by dividing the partial cost function by the number of observations or state variables (Tarantola, 2005). A posterior chi-squared value (χ^2_{poste}) of 1 indicates a good fit, as the model predictions fall within the error distribution fall within the error distribution of the observations. A χ^2_{poste} significantly greater than 1 indicates a poor fit, while a value smaller than 1 suggests potential overfitting. MBE indicates bias, with a positive value for overestimation and a negative value for underestimation. RMSE is the quadratic mean of the differences between estimation and observation, with a value of 0 indicating a perfect fit.

Note that the optimization process targets for χ^2_{poste} to reach 1.0, but we also give the improvement in MBEs and RMSEs for completeness. To assess the posterior error associated with the optimized state, we employed a Monte Carlo method. In this process, we optimized the parameters using 200 distinct ensemble members, introducing random noise within the bounds of the respective state and observational errors (Chevallier et al., 2007; Bosman et al., 2023; Cho et al., 2023).

Furthermore, we conducted 500 perturbed forward simulations to assess the spread in both prior and posterior models. Parameters were randomly sampled from Gaussian distributions of both the prior and posterior. Prior uncertainties were assumed uncorrelated, while for the posterior parameters, we used the correlations that were determined using the

Monte Carlo optimization. We quantified the posterior covariance matrix and considered the cross-parameter correlations when sampling the parameters to evaluate the posterior model. Parameters more than three standard deviations from the mean were discarded. These simulations were conducted with designated environmental input variables: pressure = 103.100 Pa, air flow rate (AF) = 0.000 35 mol s^{-1}, $[CO_2]_{in}$ = 400 µmol mol^{-1}, $[COS]_{in} = 1000$ pmol mol^{-1}, $[H_2O]_{in} = 15$ mmol mol^{-1}, $g_b = 2.44$ mol m^{-2} s^{-1}, $g_s = 0.6$ mol m^{-2} s^{-1}, and $T_{leaf} = 25$ °C. We only varied one variable at the time, to evaluate its impact on the simulation.

2.3 Results

2.3.1 Experiments

2.3.1.1 COS compensation point (Experiment 1)

Fig. 2.4 presents the results from Experiment 1 with Sunflower 1, aimed at determining Γ_{COS} by measuring F_{COS} while controlling $[COS]_{out}$ and maintaining constant g_{sw} and T_{leaf}. Minor fluctuations in g_{sw} occurred during temperature adjustments, increasing from 0.76 to 0.90 mol m^{-2} s^{-1} at higher temperatures. F_{COS} shows a linear increase with increasing $[COS]_{out}$, in agreement with findings from earlier studies (Kesselmeier et al., 1993; Stimler et al., 2010; Gimeno et al., 2017). We quantified the regression-based Γ_{COS} using a linear function at two temperatures: Γ_{COS} was 55.0 ± 53.2 pmol mol^{-1} at 19.8 °C and 138.7 ± 26.1 pmol mol^{-1} at 25.0 °C (error estimates denote 95% confidence interval). These results indicate that Γ_{COS} increases with rising T_{leaf}, suggesting a potential temperature dependence.

Although the empty-chamber regression effectively removed the baseline COS emission, some residual variability likely remained (RMSE = 6.9 pmol mol^{-1} for $[COS]_a$ and 2.73 pmol m^{-2} s^{-1} for F_{COS}). To evaluate the potential influence of this unresolved background variability, we propagated these errors to the regression-derived Γ_{COS}. When the uncertainty is included, the 95% confidence interval of Γ_{COS} widened from ± 53.2 to ± 93.4 pmol mol^{-1} at 19.8 °C and from ± 26.1 to ± 48.9 pmol mol^{-1} at 25.0 °C.

The large uncertainty at 19.8 °C indicates that the corresponding Γ_{COS} value is statistically indistinguishable from zero. By contrast, the Γ_{COS} measured at 25 °C remains significant even when this propagated and instrumental uncertainty is considered. Even accounting for the reported QCLS uncertainty of approximately 7.5 pmol mol^{-1} for COS (Kooijmans et al., 2016), the Γ_{COS} value at 25 °C remains statistically robust.

2.3.1.2 Responses to stomatal conductance (Experiment 2)

Fig. 2.5 illustrates the observed relationships of V_{COS}, V_{CO2}, and LRU with optimized g_{sw} for three sunflower plants. The observed values show that both V_{COS} and V_{CO2} decrease with declining g_{sw}, albeit at a slower rate at higher g_{sw} values. Specifically, as g_{sw} decreases from 1.0 mol m^{-2} s^{-1} to 0.4 mol m^{-2} s^{-1}, V_{COS} declines by approximately 40%, compared to a decline of about 10% in V_{CO2}. This difference persists even after accounting for the g_{sw} ratio between COS and CO_2 (1.21).

The greater sensitivity of V_{COS} to changes in g_{sw} is also reflected in the LRU, which consistently increases with g_{sw} across all sunflowers. These findings support the hypothesis that COS uptake is more sensitive to variations in g_{sw} compared to CO_2 uptake. Meanwhile, slight differences in V_{COS} and V_{CO2} values among individual sunflowers result in variations in LRU as well.

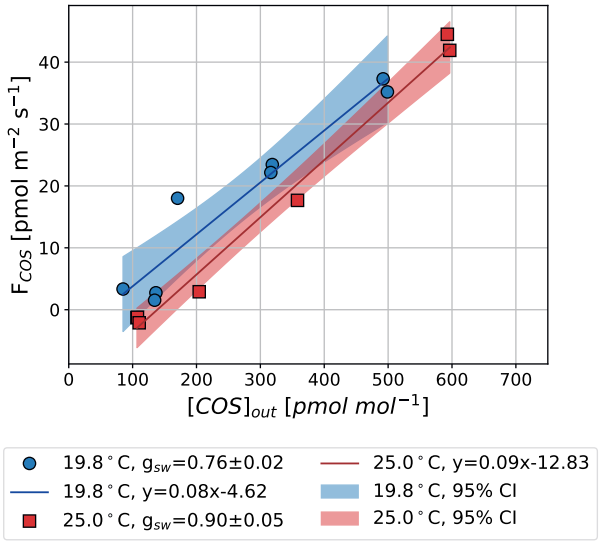


Figure 2.4: Observed mean COS net flux (F_{COS}) along an outflowing COS mole fraction ($[COS]_{\mathrm{out}}$) in the light at 25.0 °C (rectangle and red areas) and 19.8 °C (circle and blue areas) in Experiment 1. Lines and shaded areas represent linear fits with 95% confidence intervals. Positive values in F_{COS} (y axis) indicate COS uptake, and negative values indicate COS emissions.

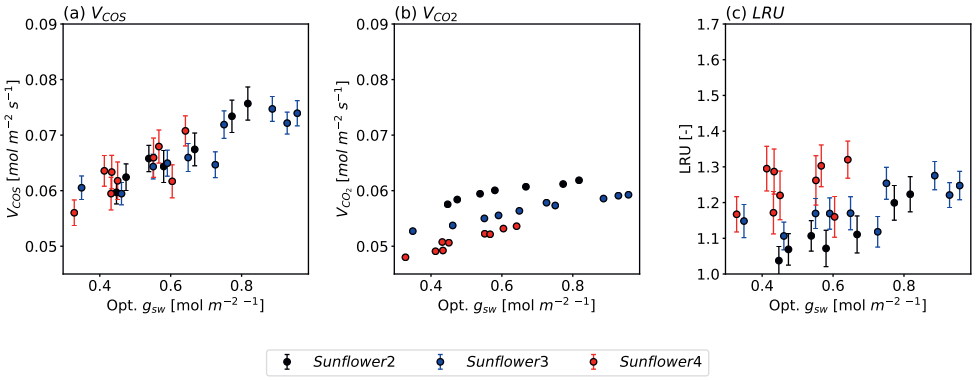


Figure 2.5: COS (a) and CO_2 (b) deposition velocities and LRU changes (c) along the optimized g_{sw} under leaf temperatures of approximately 25 °C for three different sunflower plants, each represented in a different color. The circles and error bars represent the median values and standard deviations of the data points for their respective 150-second intervals.

2.3.1.3 Responses to leaf temperature (Experiment 3)

Fig. 2.6 shows the observed V_{COS} and V_{CO2}, and LRU against T_{leaf} for two sunflowers, with g_{sw} held approximately constant. For all sunflowers, V_{COS} decreases when temperatures exceed 25 °C, whereas V_{CO2} increases with T_{leaf} up to approximately 30 °C. The absolute rate of de-

crease in V_{COS} is larger than the rate of increase in V_{CO2}. Consequently, LRU decreases as T_{leaf} increases. This trend can be attributed to the temperature responses of Γ_{COS} or/and the lower optimum temperature for CA than RuBisCO.

The temperature-dependent variations in V_{COS} and V_{CO2} also differ slightly between individual sunflower plants. While V_{COS} exhibited relatively large observational errors, V_{CO2} showed minimal errors. This suggests that while experimental uncertainties may influence V_{COS}, the variations in both V_{COS} and V_{CO2} are likely driven by micro-environmental differences, plant-to-plant variability, or other natural conditions, even within the same species grown in similar environments.

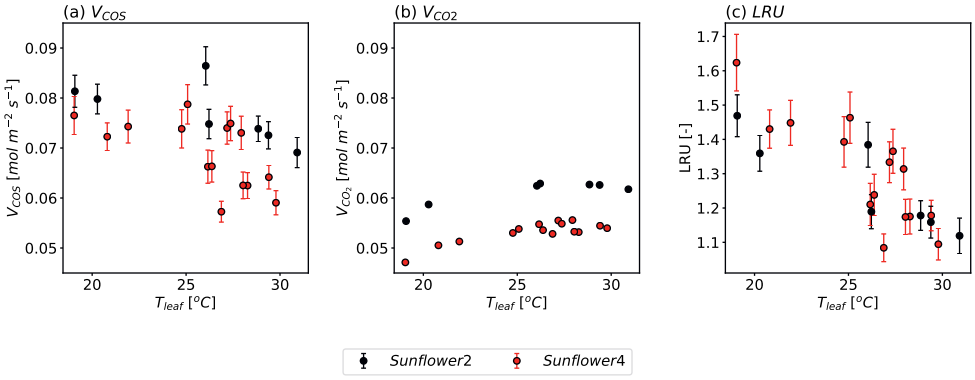


Figure 2.6: Same as Fig. 2.5, but as a function of T_{leaf} with maintained stomatal conductance at $0.6 \pm 0.1\ \mathrm{mol\,m^{-2}\,s^{-1}}$ (mean $\pm$ standard deviation).

2.3.2 Model-assisted analysis

2.3.2.1 Optimization performance

We present the optimized results of model S2, which provides the best fit to the observations (Sect. 2.3.2.2).

Table 2.5 quantifies how well the optimized model estimates $[COS]_{\mathrm{out}}$, $[CO_2]_{\mathrm{out}}$, and $[H_2O]_{\mathrm{out}}$ compared to observations. The optimized model simulated the mole fractions of all three gases more accurately, reflected by mostly reduced values of χ^2, MSE, and MBE. Notably, the model biases were mitigated, as shown by the low posterior MBE values for $[COS]_{\mathrm{out}}$ (0.15 $\mathrm{pmol\,mol^{-1}}$), $[CO_2]_{\mathrm{out}}$ (-0.01 $\mu\mathrm{mol\,mol^{-1}}$), and $[H_2O]_{\mathrm{out}}$ (0.07 $\mathrm{mmol\,mol^{-1}}$). The χ^2_{poste} values for $[COS]_{\mathrm{out}}$, $[CO_2]_{\mathrm{out}}$, $[H_2O]_{\mathrm{out}}$, and the state variables are 6.65, 1.68, 2.24, and 1.00, respectively. The large χ^2_{poste} and RMSE for $[COS]_{\mathrm{out}}$ likely result from its relatively larger observational error.

The statistical indices of the prior and posterior estimated $[COS]_{\mathrm{out}}$, $[CO_2]_{\mathrm{out}}$, and $[H_2O]_{\mathrm{out}}$ from model S2 compared to the observations with 2 changes of state term (x). The units of RMSE and MBE are in $\mathrm{pmol\,mol^{-1}}$ for $[COS]_{\mathrm{out}}$, in $\mu\mathrm{mol\,mol^{-1}}$ for $[CO_2]_{\mathrm{out}}$, and in $\mathrm{mmol\,mol^{-1}}$ for $[H_2O]_{\mathrm{out}}$.

To visualize these improvements, Fig. 2.7 presents scatter plots comparing the simulated atmospheric mole fractions from the prior and posterior models to the observed values. The optimized atmospheric mole fractions exhibit improved agreement with the observed values across all sunflowers, improving the performance of the prior simulations. The opti-

Table 2.5: The statistical indices of the prior and posterior estimated $[COS]_{\mathrm{out}}$, $[CO_2]_{\mathrm{out}}$, and $[H_2O]_{\mathrm{out}}$ from model S2 compared to the observations, with χ^2 changes of state term (x). The units of RMSE and MBE for $[\mathrm{COS}]_{\mathrm{out}}$ are $\mathrm{pmol\,mol^{-1}}$, for $[\mathrm{CO_2}]_{\mathrm{out}}$ are $\mathrm{\mu mol\,mol^{-1}}$, and for $[\mathrm{H_2O}]_{\mathrm{out}}$ are $\mathrm{mmol\,mol^{-1}}$.

Index	$[\mathrm{COS}]_{\mathrm{out}}$		$[\mathrm{CO_2}]_{\mathrm{out}}$		$[\mathrm{H_2O}]_{\mathrm{out}}$		Background (State x)	
	Prior	Posterior	Prior	Posterior	Prior	Posterior	Prior	Posterior
χ^2	30.00	6.65	100.00	1.68	3.00	2.24	0.00	1.00
RMSE	16.71	7.93	3.63	0.71	0.30	0.45	–	–
MBE	11.77	0.15	-1.52	-0.01	-0.14	0.07	–	–

mized model explains the variability in the observations with high R^2 values from 0.93 to 0.99. The simulation errors, represented by the standard deviation of 500 forward simulations, were substantially reduced after optimization. Specifically for $[COS]_{\mathrm{out}}$, errors decreased from 47.4 $\mathrm{pmol\,mol^{-1}}$ to 12.5 $\mathrm{pmol\,mol^{-1}}$, for $[CO_2]_{\mathrm{out}}$ from 10.8 $\mathrm{\mu mol\,mol^{-1}}$ to 0.8 $\mathrm{\mu mol\,mol^{-1}}$, and for $[H_2O]_{\mathrm{out}}$ from 0.6 $\mathrm{mmol\,mol^{-1}}$ to 0.3 $\mathrm{mmol\,mol^{-1}}$. However, discrepancies remain, such as in Sunflower 2. Several posterior $[COS]_{\mathrm{out}}$ and $[CO_2]_{\mathrm{out}}$ values of Sunflower 2 fall outside the weighted observational error range, likely due to measurement uncertainties.

In addition to reproducing the observations well, the optimization also reduced the parameter uncertainties. The optimized state values and their posterior errors, along with error reductions, are presented in Table 2.2. As expected, errors associated with all target parameters were significantly reduced, with an average error reduction of 48%. An error reduction of more than 92% was achieved for CO_2 parameters $\Delta H_{\mathrm{a,Rub}}$ and $V_{\mathrm{max,Rub}}$. Prior uncertainties of $T_{\mathrm{eq,CA}}$, m_{COS}, and $V_{\mathrm{max,CA}}$ were reduced by more than 30%, and the error reduction for g_{sw} was about 43%.

Parameter values also shifted meaningfully after optimization. The optimized slope of Γ_{COS} (m_{COS}, 22.4 $\mathrm{pmol\,mol^{-1}\,K^{-1}}$) is slightly increased to the initial setting (16.2 $\mathrm{pmol\,mol^{-1}\,K^{-1}}$). With the optimized value of m_{COS}, the variable $T_{\mathrm{eq,CA}}$ was adjusted to 39.7 °C, and the values of $V_{\mathrm{max,CA}}$ for each plant were optimized ranging from 0.189 to 0.230 $\mathrm{mol\,m^{-2}\,s^{-1}}$. These values increased significantly from their priors, 30.0 °C and 0.125 $\mathrm{mol\,m^{-2}\,s^{-1}}$, indicating higher optimum temperatures and higher catalyzation velocities compared to the prior settings. The optimized $V_{\mathrm{max,Rub}}$ ranged from 82.9 to 94.4 $\mathrm{\mu mol\,m^{-2}\,s^{-1}}$, while $\Delta H_{\mathrm{a,Rub}}$ did not change substantially. The ratio of $V_{\mathrm{max,CA}}$ to $V_{\mathrm{max,Rub}}$ which is crucial for calculating CA activity from $V_{\mathrm{max,Rub}}$ based on the assumption of a linear relationship, ranges from 2160 to 2770.

The optimized g_{sw} also showed consistent behavior. Comparisons of the optimized mean g_{sw} values of 0.64 $\mathrm{mol\,m^{-2}\,s^{-1}}$ with the prior values of 0.62 $\mathrm{mol\,m^{-2}\,s^{-1}}$ reveal slight differences. Errors in g_{sw} were reduced from 0.09 to 0.05 $\mathrm{mol\,m^{-2}\,s^{-1}}$. The optimized model yielded an average relative humidity within the leaf (RH_{i}) of 98.82 $\pm$ 0.04%. These results confirm that allowing for slight non-saturation in the intercellular airspace (through $g_{\mathrm{m,H2O}}$) had a negligible impact on the modeled fluxes, validating the assumption that the air within the intercellular airspace was effectively saturated under our experimental conditions. Simulations further confirmed that varying g_{mw} (< 10 $\mathrm{mol\,m^{-2}\,s^{-1}}$) did not alter the modeled fluxes or mole fractions, indicating that its effect was negligible under our experimental conditions.

Fig. 2.8 illustrates the posterior covariance matrix derived from Monte Carlo calculations. Although several state variables were highly correlated after optimization (values above 0.7), they were retained as state parameters because their simulation errors were substantially reduced. For instance, three variables of COS parameters ($T_{\mathrm{eq,CA}}$, m_{COS}, and $V_{\mathrm{max,CA}}$) were highly correlated, with values ranging from 0.69 to 0.87, as these parameters are all related to the mesophyll uptake of COS.

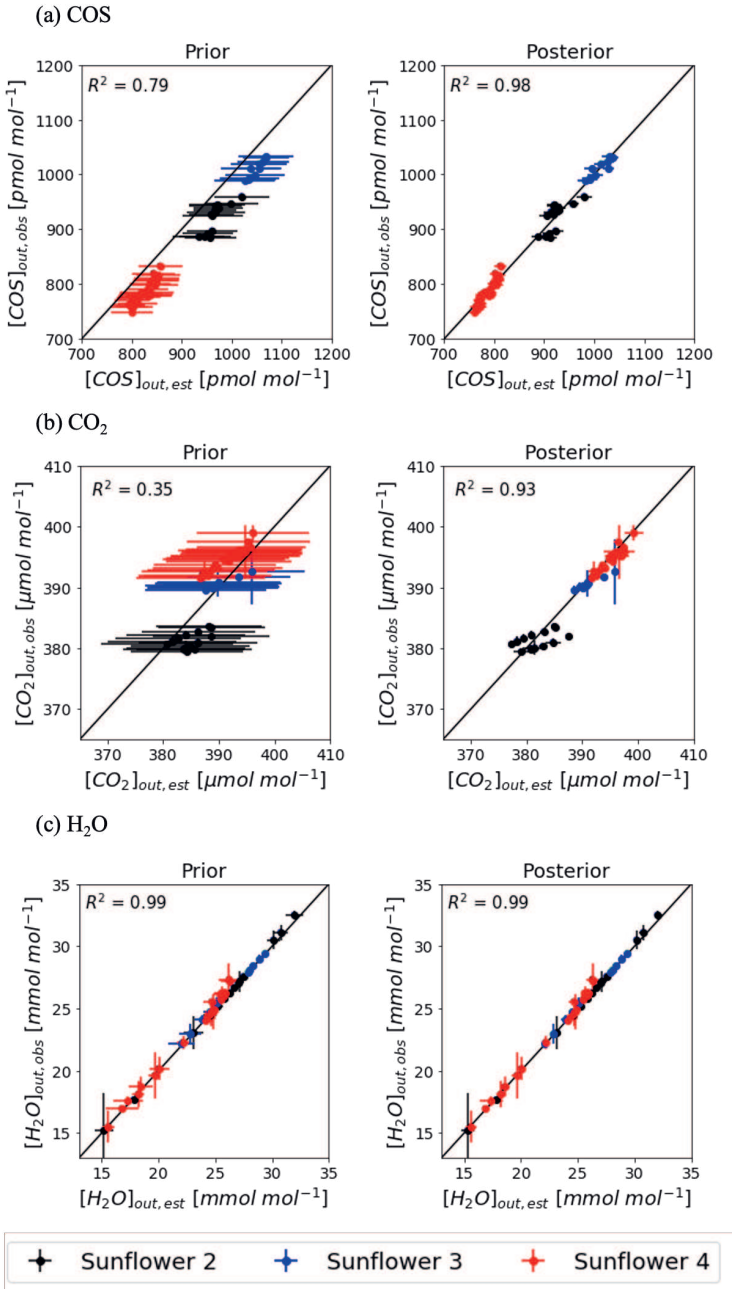


Figure 2.7: Scatter plots comparing the simulated (model S2) and observed atmospheric mole fractions of COS (a), CO_2 (b), and H_2O (c) with the prior parameters (left) and optimized parameters (right) with a 1:1 line indicating perfect agreement. The vertical error bars represent weighted observational errors, taken as the standard deviations of measurements, and the horizontal error bars represent prior errors (left) and posterior errors (right). Colors indicate different sunflower plants (black: Sunflower 2, blue: Sunflower 3, red: Sunflower 4).

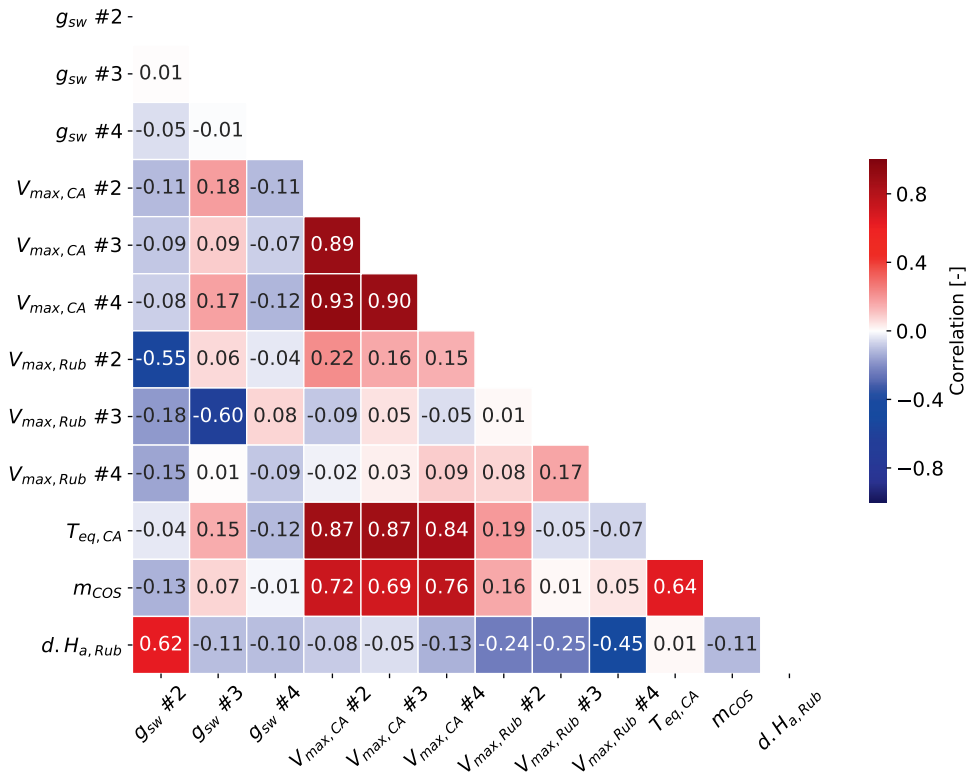


Figure 2.8: The covariance matrix for state variables. Regarding g_{sw}, only the first data point of each sunflower is marked.

2.3.2.2 COS compensation point (Hypothesis H1)

Table 2.6 summarizes the changes in total cost (J_{tot}) between prior and posterior estimations for each Γ_{COS} temperature function. Among the tested models, the lowest total cost was achieved with the linear model (S2), followed by the Arrhenius models S4 and S3, and the model without a compensation point (S1). These results confirm that incorporating Γ_{COS} with a linear temperature function into the leaf exchange model provides the best agreement with observations, as it minimizes the overall cost function and improves model performance. However, the total cost difference between the S2 model and the S4 model was only 1 unit.

To further evaluate the performance of these models, Fig. 2.9 compares estimated Γ_{COS} with two types of observation-based values across temperatures. The first type is regression-based measurements from 15 data points at two temperatures in Experiment 1 (blue triangles; see Fig. 2.4). The second type is indirectly derived Γ_{COS} in Experiments 2 and 3.

The optimized S2 model best captures the Γ_{COS} measurements derived from both regression and indirect methods, compared to other models. Specifically, the S2 model achieved the lowest RMSE with the indirectly derived Γ_{COS} (39 $\mathrm{pmol\,mol^{-1}}$). The RMSE values for the other models were: $S1 = 50\ \mathrm{pmol\,mol^{-1}}$, $S3 = 49\ \mathrm{pmol\,mol^{-1}}$, and $S4 = 41\ \mathrm{pmol\,mol^{-1}}$, respectively.

Table 2.6: Prior (Pri) and posterior (Poste) contributions to the cost function of the state term (J_{bg}), H_2O (J_{H2O}), CO_2 (J_{CO2}), and COS (J_{COS}), depending on the prescription of Γ_{COS} and its temperature dependence. J_{tot} is the total cost: $J_{\mathrm{tot}} = J_{\mathrm{bg}} + J_{\mathrm{H2O}} + J_{\mathrm{CO2}} + J_{\mathrm{COS}}$.

No.	Description of Γ_{COS}		J_{bg}	J_{H2O}		J_{CO2}		J_{COS}		J_{tot}
	Function	Based T [°C]	Post	Pri	Post	Pri	Post	Pri	Post	Post
S1	$\Gamma_{\mathrm{COS}} = 0$	–	54	144	97	4800	80	2437	349	580
S2	Linear	16.4	57		107		81	1440	320	564
S3	Linear	19.8	59		100		80	2634	335	574
S4	Arrhenius	25.0	61		106		80	2634	319	565

2.3.2.3 Response to stomatal conductance (Hypothesis H2)

In Experiment 2, we confirmed that V_{COS} responds more strongly than V_{CO2} at low g_{sw} values. To further interpret this behavior mechanistically, we explore how changes in deposition velocity due to g_{sw} are influenced by interactions with mesophyll conductance. We calculated AFR values ($1 - [gas]_{\mathrm{i}}\,[gas]_{\mathrm{a}}^{-1}$) for both gases using the optimized S2 model, as these values cannot be directly measured (Fig. 2.10). Simulations were performed at a constant T_{leaf} of 25 °C.

The model results indicate that for both gases, AFR decreases as g_{sw} increases, which provides support for Hypothesis 2. However, contrary to Hypothesis 2, which assumes that $[COS]_{\mathrm{i}}$ is nearly zero, thus resulting in AFR for COS close to 1, the actual modeled values range from 0.2 to 0.6 depending on g_{sw}. This deviation indicates that $[COS]_{\mathrm{i}}$ is not negligible and suggests a dynamic COS consumption within the leaf that does not bring $[COS]_{\mathrm{i}}$ close to zero.

The model also reveals a distinct LRU pattern, showing sharp increases at low g_{sw} values followed by stabilization at higher g_{sw}. This response is consistent with observations from Experiment 2, where LRU exhibited similar trends in response to g_{sw}. These results underscore the differing sensitivities of COS and CO_2 uptake to g_{sw}, as reflected in both experimental and modeled data.

2.3.2.4 Response to leaf temperature (Hypothesis H3)

To investigate the temperature function of enzyme activity separated from Γ_{COS} in V_{COS}, we calculated $g_{\mathrm{m,COS}}$ and $g_{\mathrm{m,CO2}}$ using the optimized model S2. Fig. 2.11 shows the temperature dependency of $g_{\mathrm{m,COS}}$ and $g_{\mathrm{m,CO2}}$ for three sunflowers. The magnitudes of these dependencies vary among plants due to differences in optimized V_{max} values. The optimum temperature for $g_{\mathrm{m,COS}}$ is around 35 to 40 °C, while for $g_{\mathrm{m,CO2}}$ it is approximately 35 °C, which contradicts Hypothesis 3, proposing a lower optimum temperature for $g_{\mathrm{m,COS}}$ than for $g_{\mathrm{m,CO2}}$.

The observed decline in V_{COS} above 25 °C in Experiment 3 (Fig. 2.6a) is explained by the model-predicted impact of Γ_{COS} on COS uptake. While the optimum temperature for $g_{\mathrm{m,COS}}$ is approximately 35 to 40 °C, the influence of temperature-dependent Γ_{COS} results in a much lower optimum temperature for V_{COS}, around 20 °C. This is significantly lower than the optimum temperature for V_{CO2}, which is approximately 30 °C.

Overall, the model results suggest that the temperature dependence of Γ_{COS} plays a critical role in shaping the distinct responses of V_{COS} and V_{CO2}.

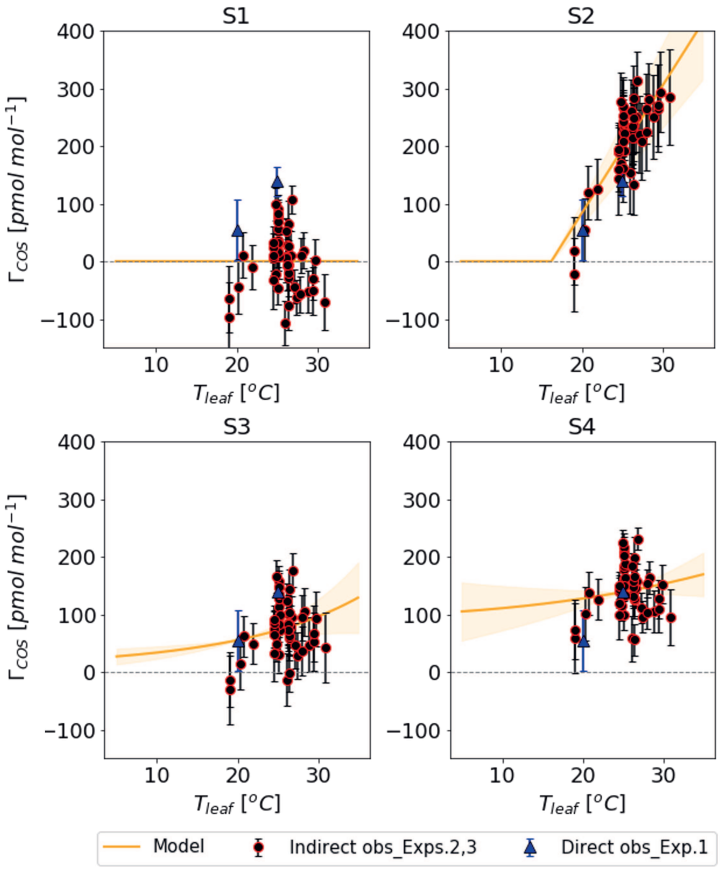


Figure 2.9: Posterior temperature functions for Γ_{COS} from S1 to S4 models, shown with orange lines and error ranges from 200 Monte Carlo simulations. These are compared with Γ_{COS} values from Experiment 1 (blue triangles, regression-derived from two temperature points) and Experiments 2 and 3 (black circles with red edges, derived indirectly). Regression-derived Γ_{COS} measurements are 55.0 ± 53.2 pmol mol^{-1} at 19.8 °C and 138.7 ± 26.1 pmol mol^{-1} at 25.0 °C, detailed in Sect. 2.3.1.1). Indirectly derived values are averages with standard deviation error bars, calculated from parameters optimized through 200 Monte Carlo simulations (See Sect. 2.2.5).

2.4 Discussion

This study aimed to investigate how leaf COS and CO_2 fluxes respond differently to environmental changes and to identify which internal processes within leaves govern these differences. Laboratory experiments were conducted under controlled conditions to isolate the effects of stomatal conductance and temperature. However, to provide more insights in the internal processes that control COS exchange, we developed and optimized a coupled CO_2–COS–H_2O conductance model to mechanistically interpret the measurement data. Although the model involves some simplified representations of internal processes, these simplifications are minor and do not affect the overall interpretation. In this section, we discuss the uncertainties in both

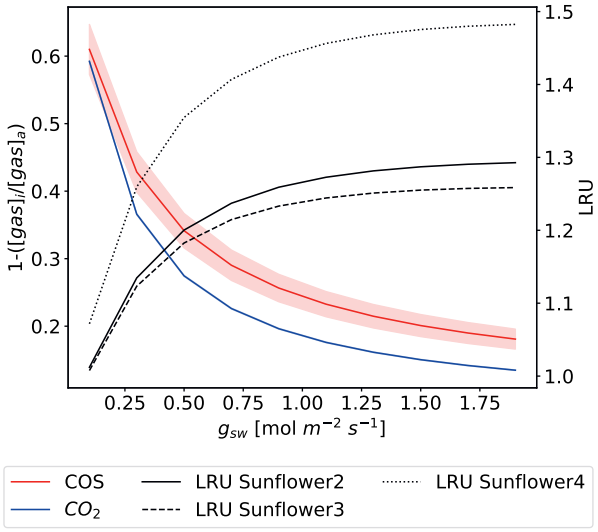


Figure 2.10: Simulated changes in $(1 - [gas]_i\ [gas]_a^{-1})$ for COS (red) and CO_2 (blue) averaged among sunflowers 2, 3, and 4, with LRU (black, secondary y-axis) as a function of g_{sw} each sunflower (Results from the S2 model). The lines represent averages, and the filled areas indicate the standard deviation of 500 simulations using posterior error propagation.

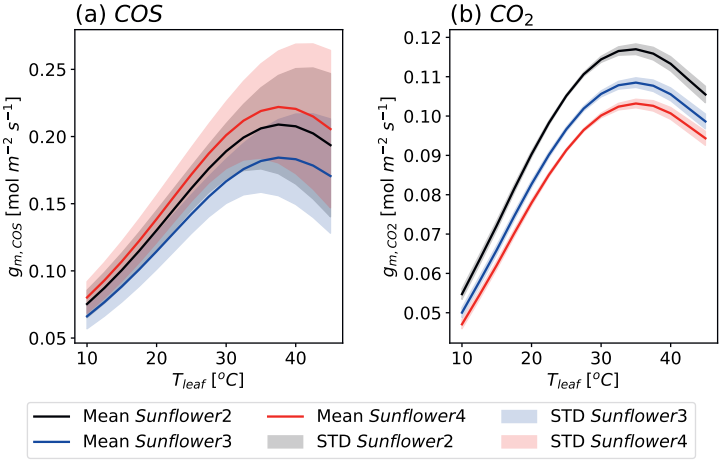


Figure 2.11: Modeled response of mesophyll conductances (g_m) to leaf temperatures (T_{leaf}) for COS (a) and CO_2 (b) with three sunflowers (black: sunflower 2, blue: sunflower 3, red: sunflower 4, results from the S2 model). The lines represent averaged values, and the filled areas indicate the standard deviation from 500 simulations using posterior error propagation.

observations and model representations, the physiological implications of the observed COS compensation points, and their broader significance for biochemical parameters and the global COS budget.

2.4.1 Uncertainties in measurements and models

Through improvements in our experimental setup, especially with the LI-6800 system incorporating new gasket materials (Advanced Polymer, Polyethylene, and Neoprene) and optimized flow paths, we minimized the gas leakage issues prevalent in previous systems like the LI-6400. No significant pressure differentials were observed during experiments, supporting the effectiveness of these enhancements. Additionally, maintaining the cuvette under slight positive pressure reduces the risk of inward leakage.

Although leakage issues were minimized, the high uncertainty in COS measurements and models still requires careful interpretation. Model S2 was selected as the best model due to its minimal posterior costs and lowest RMSE with observation-based Γ_{COS}, despite higher H_2O and background costs compared to S1, as shown in Table 2.6. Furthermore, the minor differences in posterior costs and RMSE with indirectly derived Γ_{COS} between S2 and S4 suggest that S4 is a viable alternative. The strong correlation between the temperature dependence of Γ_{COS} (m_{COS}) and $V_{\mathrm{max,CA}}$ complicates the precise and independent determination of these two parameters. Accordingly, the exact value and temperature dependence of Γ_{COS} remain uncertain, but including a compensation point in the models, as in models S2 and S4, significantly improves their alignment with observations.

Another limitation concerns the restricted temperature range of our experiments. Our optimization was based on data from Experiments 2 and 3, conducted at temperatures ranging from 19.0 °C to 29.8 °C. Therefore, additional experiments across a broader temperature range are necessary to confirm the existence and assess the temperature dependence of Γ_{COS}.

The choice of elevated COS concentration in the cuvette also introduces interpretative considerations. In our experiment, we increased the COS mole fraction in the cuvette to approximately 1000 $\mathrm{pmol\,mol^{-1}}$, significantly above natural ambient levels, to enhance signal detection and reduce noise. The primary purpose of our empty chamber experiments was to eliminate the effects of emissions from chamber materials. Conducting these tests at similarly high mole fractions also helped mitigate any emissions that could arise from this higher mole fraction setting.

This high COS mole fraction possibly contributed to slightly higher AFR (Fig. 2.10) because the high ambient mole fraction may influence the internal concentration. $[COS]_{\mathrm{i}}\,[COS]_{\mathrm{a}}^{-1}$ values of about 0.63 ± 0.13 were observed under elevated ambient $[COS]_{\mathrm{a}}$ conditions (Stimler et al., 2010), aligning with our results. Stimler et al. (2010) also reported a linear relationship between $[COS]_{\mathrm{i}}\,[COS]_{\mathrm{a}}^{-1}$ and $[COS]_{\mathrm{a}}$, likely due to retro-diffusion from the leaves. Therefore, when applying our results to natural conditions ($[COS]_{\mathrm{a}}$ about 500 $\mathrm{pmol\,mol^{-1}}$, the AFR may decrease. However, the high AFR is also possibly due to the influence of Γ_{COS}. The simulated $[CO_2]_{\mathrm{i}}\,[CO_2]_{\mathrm{a}}^{-1}$ ranges from 0.4 to 0.9, consistent with values previously reported for C_3 plants (0.5 – 0.8) (Black et al., 1985; Tanner et al., 2015; Seibt et al., 2010).

Nevertheless, in Experiments 2 and 3, despite the high COS mole fractions, their consistent level throughout the experiments likely negated any impact on analyzing how g_{sw} and temperatures relate to V_{COS} and V_{CO2}.

In addition to the experimental limitations discussed above, a practical limitation arises from the mole fraction range used for model optimization. Model parameters were optimized using data obtained under relatively high COS mole fraction conditions ($\approx$ 1000 $\mathrm{pmol\,mol^{-1}}$) to ensure stable and precise flux measurements, whereas Γ_{COS} was determined from experi-

ments conducted at lower inflowing concentrations (100–600 $\mathrm{pmol\,mol^{-1}}$). This discrepancy in concentration ranges may introduce some uncertainty when extrapolating parameters between optimization and compensation-point estimation. Nevertheless, the model formulation remains internally consistent, and the derived parameters are valid for interpreting the relative temperature-dependent behavior of COS exchange. Future experiments targeting near-ambient COS mole fraction levels will be valuable to further validate the applicability of these optimized parameters and to evaluate potential retro-diffusion effects under more natural conditions.

From a modeling perspective, only the enzyme CA is considered in determining the mesophyll conductance of COS. However, other enzymes, such as RuBisCO and phosphoenolpyruvate carboxylase (PEP-C), are known to also catalyze COS uptake (Lorimer et al., 1989; Protoschill-Krebs et al., 1992). The contribution of RuBisCO to COS uptake is relatively minor compared to CA (Protoschill-Krebs et al., 1996), and its activity has not yet been quantified.

An additional source of uncertainty arises from the simplified representation of COS mesophyll conductance in our model. While mesophyll diffusion was not explicitly parameterized, it was implicitly represented through the temperature-dependent CA activity function (Cho et al., 2023) that integrates both diffusional and biochemical processes. Nevertheless, this implicit treatment may not fully capture variations in diffusional resistance under different environmental or structural conditions, and thus its influence on the temperature dependence of COS uptake cannot be completely excluded. Future modeling studies incorporating explicit mesophyll diffusion parameterization—beyond the current CA-based formulation—would help to disentangle the relative contributions of diffusional and biochemical controls, as well as potential COS emissions from leaves, in regulating COS exchange.

Beyond these structural uncertainties in the model, it is important to note that the conductance model was designed as an exploratory diagnostic tool. Its purpose was to integrate the coupled behavior of CO_2, COS, and H_2O exchange and to mechanistically interpret the observed fluxes. Despite its simplifications in not considering minor features, such as outlet mass flow change and boundary ternary effect, this framework represents the first attempt to jointly optimize gas exchange for the three gases, thereby providing a process-based means to independently estimate the COS compensation point. Overall, this approach highlights the potential of combined gas-exchange measurement and modeling to advance our understanding of COS biogeochemistry.

2.4.2 Possible causes of a COS compensation point

COS emission can occur due to leaf stress induced by external factors during experiments. To minimize the risk of mechanical damage or stress, the chamber was gently attached, and leaves were inspected post-experiment for physical damage such as bruising, desiccation, or discoloration. No visible damage was observed, and the limited measurement duration further reduced the likelihood of stress-induced COS emissions.

Previous studies on COS leaf exchange experiments have reported positive Γ_{COS} values, but often concluded these are statistically indistinguishable from zero due to high variability. For example, Stimler et al. (2010) observed a Γ_{COS} of 60.7 $\mathrm{pmol\,mol^{-1}}$ at 25 °C and attributed it to potential retro-diffusion under high COS mole fractions. Similarly, our Γ_{COS} at 20.0 °C (55.0 ± 53.2 $\mathrm{pmol\,mol^{-1}}$) was statistically insignificant, whereas a significant Γ_{COS} (138.7 ± 26.1 $\mathrm{pmol\,mol^{-1}}$) was detected at 25 °C. Considering that our experiments, like those of Stimler et al. (2010), were conducted under relatively high COS mole fractions, this pattern suggests that higher temperature may enhance diffusion-driven feedback. It should also be noted that

our COS model does not explicitly account for mesophyll diffusion conductance, and thus part of the apparent emission function could be interpreted as an effect of internal diffusion-related mechanisms (e.g., retro-diffusion) within the leaf).

In addition to retro-diffusion, temperature-induced stress could also contribute to the observed COS compensation point. Previous studies, typically conducted below 25 °C, did not assess temperature dependence. Our modeling revealed a linear relationship between Γ_{COS} and temperature, consistent with Stimler et al. (2010), who reported higher Γ_{COS} in mosses at elevated temperatures. Although no visible stress was observed in our plants, temperature stress may have influenced Γ_{COS}. Gimeno et al. (2017) suggested that COS emissions could result from protein degradation under stress, releasing COS through the breakdown of sulfur-containing amino acids. This highlights the role of temperature-driven biochemical pathways in shaping Γ_{COS} values and supports the inclusion of Γ_{COS} in leaf gas exchange models.

Beyond temperature-driven stress, differences in species physiology also contribute to Γ_{COS}. Mosses studied by Stimler et al. (2010) exhibited higher Γ_{COS} values than in vascular plants, likely due to enzymatic activity of associated fungi and bacteria. While microbial activity is not directly applicable to vascular plants, it underscores the importance of species-specific factors in determining COS emissions. In vascular plants, rapeseed is known to produce COS due to its high sulfur content, with Γ_{COS} exceeding 100 $\mathrm{pmol\,mol^{-1}}$ during ripening and senescence (Belviso et al., 2022). However, no experiments have previously been conducted to detect Γ_{COS} in sunflowers.

Previous studies (e.g., Maseyk et al., 2014 and Belviso et al., 2022) reported that COS emissions occur during the ripening and senescence phases, indicating that senescence-related processes could explain COS emissions rather than active uptake from living tissues. In Maseyk et al. (2014), part of these emissions may have originated from the soil, whereas Belviso et al. (2022) provided strong evidence for plant-derived senescence emissions. Additionally, Kesselmeier et al. (1993) reported Γ_{COS} values ranging from 57 to 328 $\mathrm{pmol\,mol^{-1}}$ in rapeseed and corn during flowering. In our study, measurements were conducted during the flowering phase, which could explain the observed COS emissions, although the exact source remains unclear. Sulfur emissions during senescence have been linked to the translocation of sulfur-containing amino acids and sulfur regulation in plant cells (Rennenberg, 1991).

Apart from biological factors, methodological advances may explain the discrepancies between our results and previous studies. We employed the Li-6800 system, which offers improved measurement accuracy, and evaluated an optimized conductance model incorporating temperature-dependent Γ_{COS}. Our findings confirm that all observations support an increase in Γ_{COS} with temperature.

Taken together, the existence of Γ_{COS} and its increase at higher temperatures may result from a combination of the factors discussed above. However, our current formulation of Γ_{COS} is expressed solely as a temperature-dependent function and does not explicitly include retro-diffusion effects. As a result, while the observed increase in Γ_{COS} with temperature is consistent with thermally driven processes, the potential contribution of internal diffusion feedback—particularly under elevated COS mole fractions—cannot be fully excluded.

At present, reliable measurements can only be obtained under relatively high COS mole fractions, which limits our ability to fully constrain Γ_{COS} dynamics near ambient conditions. Improving detection precision at low COS concentrations and incorporating explicit representations of internal diffusion in future models would enable a more direct evaluation of whether Γ_{COS} variability originates from retro-diffusion or from physiological and biochemical processes. Moreover, extending such measurements to different phenological stages and species, and exploring interactions with microbial associations and environmental stressors, will be essential for developing a more mechanistic understanding of COS exchange in plants.

2.4.3 Impact of COS compensation point on $V_{\mathrm{max,CA}}$

When Γ_{COS} was explicitly considered in the optimization, the optimized ratio between $V_{\mathrm{max,CA}}$ and $V_{\mathrm{max,Rub}}$ ranges from 2160 to 2770, which is higher than previously obtained values of approximately 1200 from laboratory measurements with C_3 plants (Berry et al., 2013). Kooijmans et al. (2021) reported an average ratio of 1616 $\pm$ 562 based on field observations in summer months. In contrast, when Γ_{COS} was excluded (model S1) the optimized $V_{\mathrm{max,CA}}$ became smaller, resulting in ratios of 1197–1327, closely matching the values reported in previous studies. Thus, models that incorporate Γ_{COS} result in higher optimized values of $V_{\mathrm{max,CA}}$ and consequently to higher ratios between $V_{\mathrm{max,CA}}$ and $V_{\mathrm{max,Rub}}$, indicating a higher maximum catalyzation velocity of CA.

2.4.4 Consequences for the COS global budget

Our evidence of decreasing V_{COS} between 20 and 25 °C (Fig. 2.6a) supports lower biosphere uptake in high temperature regions. The current COS budget has a missing source of roughly 400 Gg S yr^{-1}, mainly due to the large biosphere sink calculated by the Simple Biosphere model (SiB4) in the tropics (Berry et al., 2013). In warm tropical forests, biosphere uptake would be significantly reduced.

The presence of Γ_{COS} could have implications for the global COS budget and the utilization of COS in estimating GPP, especially under conditions such as drought, where high temperatures and low humidity persist. Despite the uncertainty concerning Γ_{COS} in our experiments, including Γ_{COS} in our model better reproduced CO_2 and COS observations. This suggests that incorporating Γ_{COS} into global biosphere models could enhance the accuracy of COS flux estimates. Differences in temperatures and humidity responses between CO_2 and COS should also be considered. To further improve the large-scale modeling, it is recommended to measure Γ_{COS} and enzyme activity across diverse plant types, specifically tropical plants.

While our study focused on controlled conditions with a single species, larger variations would indeed be expected under natural conditions and across different species. Consequently, future research should therefore explore these factors in more diverse environmental settings to validate and generalize these findings.

Chapter 3

Optimizing the Carbonic Anhydrase temperature response and stomatal conductance of carbonyl sulfide leaf uptake in the simple biosphere model (SiB4)

Carbonyl Sulfide (COS) is a useful tracer to estimate Gross Primary Production (GPP) because it shares part of the uptake pathway with CO_2. COS is taken up in plants through hydrolysis, catalyzed by the enzyme carbonic anhydrase (CA), but is not released. The Simple Biosphere model version 4 (SiB4) simulates COS leaf uptake using a conductance approach. SiB4 applies the temperature response of the RuBisCo enzyme (used for photosynthesis) to simulate the COS leaf uptake, but the CA enzyme might respond differently to temperature. We introduce a new temperature response function for CA in SiB4, based on enzyme kinetics with an optimum temperature. Moreover, we determine Ball-Woodrow-Berry (BWB) model parameters for stomatal conductance (g_s) using observation-based estimates of COS flux, GPP, and g_s along with meteorological measurements in an evergreen needleleaf forest (ENF) and deciduous broadleaf forest (DBF). We find that CA has optimum temperatures of 20 °C (ENF) and 36 °C (DBF), which is lower than that of RuBisCo (45 °C), suggesting that canopy temperature changes can critically affect CA's catalyzation activity. Optimized values for the BWB offset parameter are similar to the original value (0.010 ± 0.003 mol m^{-2} s^{-1}), and optimized values for the BWB slope parameter (ENF: 16.4, DBF: 11.4) are higher than the original value (9.0) at both sites. The optimization reduces prior errors on all parameters by more than 50% at both stations. We apply the optimized g_i and g_s parameters in SiB4 site simulations, thereby improving the timing and peak of COS assimilation. In addition, we show that SiB4 underestimates the leaf humidity stress under conditions where high VPD should limit g_s in the afternoon, thereby overestimating g_s. Furthermore, global COS biosphere sinks with optimized parameters show smaller COS uptake in regions where the air temperature is over 25 °C, mostly in the tropics, and larger uptake in regions where the temperature is below 25 °C. This change corresponds with reported deficiencies in the global COS fluxes, such as missing sinks at high latitudes and required sources in the tropics. Using our optimization and additional observa-

Cho, A., Kooijmans, L. M. J., Kohonen, K.-M., Wehr, R., and Krol, M. C. (2023). Optimizing the carbonic anhydrase temperature response and stomatal conductance of carbonyl sulfide leaf uptake in the Simple Biosphere model (SiB4). *Biogeosciences*, 20, 2573–2594. https://doi.org/10.5194/bg-20-2573-2023

tions of COS uptake over various climate and plant types, we expect further improvements in global COS biosphere flux estimates.

3.1 Introduction

The leaf assimilation of the atmospheric trace gas carbonyl sulfide (COS) has been suggested as a proxy to overcome the limitations of estimating photosynthetic carbon dioxide (CO_2) assimilation (Whelan et al., 2018). Observations of the net ecosystem exchange (NEE) of CO_2 include both Gross Primary Production (GPP) and ecosystem respiration, and those two individual components cannot be directly observed during daytime. COS follows the same diffusional pathway into leaves through plant stomata as CO_2. COS is then destroyed through hydrolysis catalyzed by the enzyme carbonic anhydrase (CA) and is assumed not to be produced by any process within leaves (Protoschill-Krebs et al., 1996; Stimler et al., 2010). The CA chemistry is not light-dependent (Protoschill-Krebs et al., 1996), in contrast to photosynthetic CO_2 fixation, which requires light. Therefore, when the CA activity is accurately quantified, measurements of COS uptake can provide information on stomatal conductance (Kooijmans et al., 2017).

Atmospheric COS mole fractions vary around 500 parts per trillion (ppt) and are primarily influenced by biosphere uptake, ocean emissions, and anthropogenic emissions (Kettle et al., 2002). Depending on the environmental conditions, soils can act as a COS source or sink (Maseyk et al., 2014; Whelan et al., 2016). Recent studies have found that a source is missing in the tropical region (Berry et al., 2013; Glatthor et al., 2015; Kuai et al., 2015; Ma et al., 2021). Moreover, Berry et al. (2013) and Hu et al. (2021) showed that a sink is missing, or a source is overestimated at higher latitudes. These findings ask for careful evaluation of all sources and sinks, including the biosphere.

Biosphere models, such as the Simple Biosphere model, version 4 (SiB4) (Berry et al., 2013; Kooijmans et al., 2021) and the Organizing Carbon and Hydrology In Dynamic Ecosystems model (ORCHIDEE) (Launois et al., 2015a; Maignan et al., 2021; Remaud et al., 2022; Abadie et al., 2022) have been used to estimate ecosystem exchange of COS quantitatively. The SiB4 COS biosphere exchange was recently assessed against observations by Kooijmans et al. (2021). They stressed the need to account for spatial and temporal variations in atmospheric COS mole fractions, which largely reduce SiB4 COS biosphere uptake in the tropics (although observations to confirm this influence are lacking). The calculated reduction in the tropics was not large enough to explain the gap in the COS budget. Kooijmans et al. (2021) and Vesala et al. (2022) also found that SiB4 COS biosphere flux simulations were low compared to observations in the boreal region, consistent with the underestimations found by Ma et al. (2021). Our study follows one of the recommendations in Kooijmans et al. (2021) by focusing on the parameterization of the temperature dependence of the CA enzyme activity to improve simulations of the vegetation COS uptake in SiB4.

In SiB4, the COS assimilation is described as a series of resistances (i.e. inverse conductances) at the leaf boundary layer (g_{b}), the stomatal pores (g_{s}), and the leaves' interior (g_{i}). The g_{b} and g_{s} of COS are scaled relative to conductances for water vapor or CO_2 with diffusivity ratios and a calibration factor. For g_{i}, previous studies found that both the CA enzyme activity (Badger et al., 1994) and mesophyll conductance (Evans et al., 1994) scale with the maximum velocity of carboxylation by the enzyme RuBisCo ($V_{\mathrm{max,rub}}$). Therefore, the COS internal conductance in SiB4 is scaled to $V_{\mathrm{max,rub}}$ through a single calibration factor α based on laboratory leaf gas exchange measurements(Stimler et al., 2010; Stimler et al., 2011; Berry et al., 2013). However, the enzymatic control of COS and CO_2 assimilation differs. COS molecules are hydrolyzed by the enzyme CA in the mesophyll cells (Protoschill-Krebs et al., 1996). In contrast, photosynthesis is further controlled by the enzyme RuBisCo. Thus, CO_2 has a different point of uptake compared to COS. The enzyme activity depends on the enzyme abundance and is related to environmental parameters such as temperature and pH (Michaelis et al., 1913). In particular, the CA enzyme does not require light to catalyze COS hydrolysis, whereas the Ru-

BisCo enzyme does require light (Stimler et al., 2010). Different temperature responses of RuBisCo and CA were reported by Boyd et al. (2015) with the C4 plant *Setaria viridis*. They measured that $V_{\mathrm{max,rub}}$ increased with temperature in the range 10 to 40 °C, whereas the CA activity decreased above 30 °C. Currently, however, there is limited information about the temperature response function of CA.

Several studies found that the leaf relative uptake ratio (LRU, which is proportional to the ratio of COS and CO_2 deposition velocities) varies with temperature under conditions where light was not limiting photosynthesis (Cochavi et al., 2021; Stimler et al., 2010; Sun et al., 2018c; Kooijmans et al., 2019). More specifically, the LRU decreased with increasing temperatures above 15 °C, indicating that COS uptake has a lower optimum temperature than CO_2 uptake, possibly driven by different temperature responses of the CA and RuBisCo enzymes. Therefore, to accurately simulate the relation between COS and CO_2 exchange in leaves, it is necessary to use separate temperature response equations for the internal conductance to CO_2 and COS.

Besides uncertainties in g_{i}, uncertainties in g_{s} can also affect the accuracy of simulated COS assimilation. A common approach for simulating g_{s} is the semi-empirical Ball-Woodrow-Berry (BWB) model (e.g., Ball et al., 1987; Ball, 1988; Collatz et al., 1992). This model is also applied in SiB4 and utilizes a set of related variables (e.g., photosynthesis, relative humidity, and CO_2 concentration at the leaf surface) and two empirical constants. One of the constants (b_1) describes the slope of the relation between g_{s} and GPP. The other constant (b_0) represents the residual g_{s} in the dark. The current implementation of the BWB model in SiB4 has only one pair of b_1 and b_0 values for C_3 plants and only one pair for C_4 plants, whereas the BWB constants should ideally be prescribed for each plant functional type (PFT) separately to obtain accurate g_{s} (Miner et al., 2017). To constrain b_0 requires information on nighttime g_{s}. However, obtaining g_{s} estimates from nighttime water vapor flux measurements in the field is highly uncertain due to observational constraints (Papale et al., 2006; Wehr et al., 2017; Wehr et al., 2021). As an alternative, nighttime COS uptake was previously reported (White et al., 2010; Belviso et al., 2013; Commane et al., 2013; Commane et al., 2015; Berkelhammer et al., 2014; Billesbach et al., 2014; Wehr et al., 2017; Kooijmans et al., 2017), and when the soil uptake is properly accounted for, this flux could provide information on stomatal opening. Several multi-year measurement datasets of CO_2 and COS biosphere and soil fluxes are now available (Commane et al., 2015; Wehr et al., 2017; Vesala et al., 2022). Multi-year datasets make it possible to distinguish valid signals from noise and to use COS to provide information on g_{s} and constrain the BWB model parameters.

This research aims to optimize the temperature response of CA and BWB model parameters to better estimate COS assimilation in the SiB4 model. To do so, we will use eddy covariance (EC) measurements of the COS leaf flux, GPP derived from NEE, and g_{s} derived from the EC COS flux. The optimization will be based on observations from two PFTs: a boreal evergreen needleleaf forest (ENF) at Hyytiälä, Finland and a temperate deciduous broadleaf forest (DBF) at Harvard Forest, USA. The optimized parameters will be applied in a global simulation of the SiB4 biosphere model to evaluate the effects on the global COS biosphere sink.

3.2 Methodology

3.2.1 Modelling COS leaf uptake

3.2.1.1 SiB4 biosphere model

The SiB4 model is a prognostic land surface model that calculates the COS flux as described in Berry et al. (2013). The main application of the model is to estimate land-atmosphere exchange of carbon, energy, and water budgets (Sellers et al., 1986; Sato, 1989). SiB4 has a timestep of 10-minutes and operates on a spatial resolution of $0.5^\circ \times 0.5^\circ$. Unlike the previous SiB3 model, which relies on satellite information to specify the time-varying phenological leaf state, version 4 fully simulates the terrestrial carbon cycle using a process-based model (Haynes et al., 2019).

As each vegetation type has different physiological and phenological characteristics, SiB4 simulates photosynthesis in a heterogeneous land cover with different plant functional types (PFTs) per site or grid cell, each with separate fractions. These PFTs consist of nine natural vegetation classes and three specific crop types (maize, soybeans, and winter wheat), plus the separation of C_3 and C_4 plants in generic cropland and grassland. Besides responses of plant growth to temperature, humidity, radiation, and precipitation, the model accounts for environmental stress factors as a limitation to plant growth: the leaf humidity stress (F_{LH}), the root-zone water stress (F_{RZ}), and the canopy temperature stress (F_{T}). Several variables (e.g., $V_{\mathrm{max,rub}}$) are prescribed according to phenological stages: leaf-out, growth, maturity, senescence, and dormant stages. The leaf-out stage begins when the environmental conditions are suitable for photosynthesis to take place, and the growth stage is determined when the canopy is large enough to support photosynthesis. The maturity starts when the leaf amount is maintained. When plants experience stress and photosynthetic capacity is reduced, it is prescribed as senescence. In the dormant stage, plants do not have leaves in the canopy, or conditions are unsuitable for photosynthesis (Haynes et al., 2020).

3.2.1.2 Module for COS vegetation uptake in SiB4

SiB4 simulates COS vegetation assimilation as a combination of three conductances from the laminar boundary layer to the chloroplast (g_{b}, g_{s}, and g_{i}) multiplied by the atmospheric COS mole fraction (Berry et al., 2013):

$$F_{COS} = C_{COS}\left(\frac{1.94}{g_{\mathrm{s}}} + \frac{1.56}{g_{\mathrm{b}}} + \frac{1}{g_{\mathrm{i}}}\right)^{-1}, \tag{3.1}$$

where F_{COS} is the COS vegetation assimilation in the canopy ($\mathrm{pmol\,m^{-2}\,s^{-1}}$), and C_{COS} is the COS mole fraction in the canopy air space ($\mathrm{pmol\,mol^{-1}}$). The factors 1.94 and 1.56 account for the smaller diffusivity of COS with respect to H_2O through the boundary layer and stomatal pores, respectively (Seibt et al., 2010; Stimler et al., 2010). Note that g_{i} includes all conductances downstream of the stomata, such as the mesophyll conductance. Within SiB4, the aerodynamic conductance is used to connect the mole fraction in the canopy air space to the atmosphere.

The stomatal conductance g_{s} ($\mathrm{mol\,m^{-2}\,s^{-1}}$) in SiB4 is calculated by using the BWB model. This model relates g_{s} and GPP as a function of environmental factors with two empirical constants b_0 and b_1:

$$g_{\mathrm{s}} = b_1 \frac{\mathrm{GPP_{SiB4}}}{\mathrm{CO_{2s}}} F_{\mathrm{LH}} + b_0\,\mathrm{LAI}\,F_{\mathrm{RZ}}, \tag{3.2}$$

where GPP_{SiB4} ($\mathrm{mol\,m^{-2}\,s^{-1}}$) is the canopy CO_2 assimilation, CO_{2S} ($\mu\mathrm{mol\,mol^{-1}}$) is the CO_2 mole fraction at the leaf surface, F_{LH} (-) is the leaf humidity stress factor, LAI is the leaf

area index (-), and F_{RZ} is a non-dimensional term that accounts for root-zone water stress. F_{LH} is related to relative humidity at the leaf surface and is calculated as a ratio of the water vapor mixing ratio at the leaf surface to the water vapor mixing ratio in the leaf internal space (Sellers et al., 1992). The value of F_{LH} for ENF has a lower bound of 0.7, making ENF more resilient to humidity stress. However, Smith et al. (2020) found that with the 0.7 threshold in place, SiB4 did not accurately simulate the drought response for European ENF ecosystems. Therefore, we removed this lower bound in the optimization, but will show the impact in a sensitivity study in Sect. 3.3.5.1.

The empirical constant b_1 is the slope of the linear relationship between g_{s} and GPP_{SiB4} $F_{\mathrm{LH}}\, CO_{2s}^{-1}$, and b_0 ($\mathrm{mol\,m^{-2}\,s^{-1}}$) is the intercept indicating minimum g_{s} (Ball et al., 1987; Ball, 1988). The choice for b_1 significantly impacts simulated transpiration (Leuning et al., 1998; Lai et al., 2000; Bauerle et al., 2014) and is prescribed in SiB4 as 9.0 for C_3 plants and 4.0 for C_4 plants. The coefficient b_0 is 0.01 $\mathrm{mol\,m^{-2}\,s^{-1}}$ for most PFTs, but 0.04 $\mathrm{mol\,m^{-2}\,s^{-1}}$ for crops and C_4 plants. The prescribed b_0 term is converted from the leaf to the canopy scale by multiplying by LAI.

GPP_{SiB4} is explicitly calculated in SiB4 as the minimum of three assimilation rates limited by enzyme activity (w_c), light (w_e), and carbon compound export (w_s) (Haynes et al., 2020). The three rates are calculated by functions f_c, f_e, f_s described in detail in Sellers et al. (1996a) depending on a canopy temperature (T_{can} (K)):

$$w_c = f_c(V_{\max}(T_{\mathrm{can}}),\, pCO_{2i},\, pO_2(T_{\mathrm{can}}),\, \gamma^*)\,, \tag{3.3}$$

$$w_e = f_e(\mathrm{APAR},\, pCO_{2i},\, \gamma^*)\,, \tag{3.4}$$

$$w_s = f_s(V_{\max}(T_{\mathrm{can}}),\, F_{\mathrm{RZ}},\, pO_2(T_{\mathrm{can}}))\,, \tag{3.5}$$

Here, pCO_{2i} (Pa) is the internal partial pressure of CO_2, $pO_2(T)$ (Pa) is the temperature response of partial pressure of O_2, APAR ($\mathrm{mol\,m^{-2}\,s^{-1}}$) is the absorbed photosynthetically active radiation, and γ^* (Pa) is the CO_2 photo-compensation point. Note that GPP_{SiB4} is used in SiB4 to calculate the COS leaf flux via g_{s}, as described in Eq. 3.2 and evaluated independently from GPP calculated by the BWB model (GPP_{BWB}), which will be introduced in Sect. 3.2.3.1.

The COS molecules that have diffused into the leaf mesophyll cells are hydrolyzed in a reaction catalyzed by the CA enzyme (g_{i}). Since the enzyme activity and mesophyll conductance are analogous and the terminal COS concentration is assumed to be zero, SiB4 presumes that the two conductances can be combined and that the g_{i} ($\mathrm{mol\,m^{-2}\,s^{-1}}$) scales with $V_{\mathrm{max,rub}}$ ($\mathrm{mol\,m^{-2}\,s^{-1}}$) at 298 K as follows (Berry et al., 2013):

$$g_{\mathrm{i}}(\mathrm{PS}) = \alpha \cdot V_{\mathrm{max,rub}}(\mathrm{PS}) \cdot f(T_{\mathrm{can}})_{\mathrm{SiB4}} \cdot F_{\mathrm{LC}}(\mathrm{PS}) \cdot F_{\mathrm{RZ}} \cdot \left(\frac{P}{P_{\mathrm{sfc}}}\right) \cdot \left(\frac{T_{\mathrm{can}}}{T_0}\right). \tag{3.6}$$

$V_{\mathrm{max,rub}}$ varies with phenological stage (PS) (see Table 3.3) and is scaled with a T_{can} response function $f(T_{\mathrm{can}})_{\mathrm{SiB4}}$ that prescribes the relative increase per 10 K increase (Q_{10}) as 2.1:

$$f(T_{\mathrm{can}})_{\mathrm{SiB4}} = 2.1^{0.1\,(T_{\mathrm{can}} - 298)}. \tag{3.7}$$

In SiB4, the canopy temperature T_{can} is calculated from the temperature above the canopy using the leaf surface energy balance (Sellers et al., 1996b), and T_{can} is normally obtained from a meteorological analysis dataset. In this study, however, we use the air temperature measured

above the canopy to obtain T_{can} needed by SiB4. Likewise, we use the specific humidity measured above the canopy, which is used by SiB4 to calculate the leaf humidity stress factor F_{LH} at leaf surface level, needed in Eq. 3.2.

Other modifying factors in Eq. 3.6 are the ratio of atmospheric pressure (P, hPa) to the surface pressure ($P_{\mathrm{sfc}} = 1000\,\mathrm{hPa}$) and the ratio of the temperature to the reference temperature ($T_0 = 273.15\,\mathrm{K}$). F_{LC} (-) is the scaling factor from leaf to canopy, accounting for a fraction of absorbed PAR (FPAR) and other factors such as light scattering and leaf projection. The calibration parameter α (-) was obtained from simultaneous measurements of COS and CO_2 uptake (Stimler et al., 2010; Stimler et al., 2012; Berry et al., 2013) and was estimated as 1400 for C_3 and 8862 for C_4 plants. These numbers were derived from a limited number of observations, so the values of α do not capture variability between plant species and seasons. Kooijmans et al. (2021) derived α from ecosystem observations of six sites throughout the growing season and found an average α of 1616 ± 562 (C_3 plants). Here, the standard deviation indicates large variability over time and between sites. The impact of α on g_{i} will be described in Sect. 3.2.1.3.

3.2.1.3 A new approach to describe g_{i}

Each enzyme has its own kinetic characteristics, with activity generally increasing with temperature up to an optimum temperature and decreasing above this temperature. To derive a more realistic enzyme activity that also accounts for an optimum temperature, we propose a temperature response ($f(T_{\mathrm{can}})_{\mathrm{new}}$) based on an Arrhenius-type equation that applies Michaelis-Menten kinetics. The Arrhenius equation has been used for $V_{\mathrm{max,rub}}$ and maximum rate of photosynthetic electron transport to estimate GPP (e.g., Dreyer et al., 2001; Galmés et al., 2016). A similar model was previously used in COS soil models (Sun et al., 2015; Ogée et al., 2016). The equation is described as (Peterson et al., 2004; Daniel et al., 2010):

$$f(T_{\mathrm{can}})_{\mathrm{new}} = A_T \cdot \frac{T_{\mathrm{can}}\ \exp\left(-\frac{\Delta H_a}{R\,T_{\mathrm{can}}}\right)}{1 + \exp\left(-\frac{\Delta H_{\mathrm{eq}}}{R}\left(\frac{1}{T_{\mathrm{can}}} - \frac{1}{T_{\mathrm{eq}}}\right)\right)}. \tag{3.8}$$

Here, three variables for enzyme kinetics are included: ΔH_{a} ($\mathrm{J\,mol^{-1}}$) is the activation free energy of the CA enzyme; ΔH_{eq} ($\mathrm{J\,mol^{-1}}$) is the enthalpy change when the enzyme converts from an activated to inactivated state; T_{eq} (K) is the temperature at which activated and inactive enzymes' concentrations are equal (Daniel et al., 2010; Sun et al., 2015). The factor A_{T} normalizes Eq. 3.8 such that, equivalent to Eq. 3.7, $f(T_{\mathrm{can}})_{\mathrm{new}} = 1$ at $T_{\mathrm{can}} = 298\,\mathrm{K}$. We adopt A_{T} as the value of $f(T_{\mathrm{can}})^{-1}_{new}$ when T is equal to T_{eq}. R is the universal gas constant ($8.3145\,\mathrm{J\,K^{-1}\,mol^{-1}}$).

Figure 3.2 shows that α and the three kinetic parameters have different effects on the temperature response of g_{i} (Eq. 3.6). The calibration parameter α affects the strength of g_{i} (Fig. 3.2a) and its accuracy is therefore crucial for accurate COS flux simulations. With ΔH_{a} increasing (Fig. 3.2b), g_{i} decreases (increases) for temperatures above (below) the optimal temperature. ΔH_{eq} has the opposite effect, albeit with a different response to ΔH_{a} (Fig. 3.2c). Both ΔH_{a} and ΔH_{eq} affect g_{i} depending on the temperature range. Finally, Fig. 3.2d shows that T_{eq} determines the optimum of the temperature response curve without having an impact on the magnitude of g_{i}.

3.2.2 Observations

In optimizing the parameters g_{s} and g_{i}, we used the following variables obtained from observation to calculate COS leaf uptake (Eq. 3.1): the COS ecosystem flux, the COS soil flux, C_{COS},

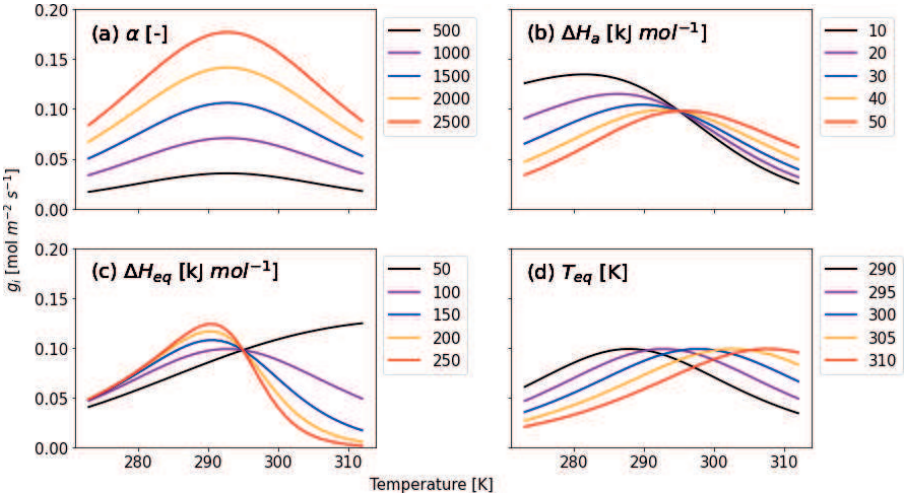


Figure 3.1: Calculated g_i as a function of canopy temperature for parameters (a) α, (b) ΔH_a, (c) ΔH_eq, and (d) T_eq from Eq. 3.6 and Eq. 3.8. Each parameter is set to five different values given in the caption to investigate the response of g_i to temperature. While the target parameter changes, the other variables are fixed as $\alpha = 1400$, $\Delta H_\mathrm{a} = 40\,\mathrm{kJ\,mol^{-1}}$, $\Delta H_\mathrm{eq} = 100\,\mathrm{kJ\,mol^{-1}}$, and $T_\mathrm{eq} = 295\,\mathrm{K}$ which are initial values for Hyytiälä (see Sect. 3.2.3.2).

temperature, and specific humidity, and GPP partitioned from NEE measurements. These data were collected and derived at Hyytiälä in Finland during 2013–2017 (Kooijmans et al., 2017; Sun et al., 2018c; Vesala et al., 2022) and at Harvard Forest in the United States during 2012 and 2013 (Commane et al., 2015; Wehr et al., 2017). To validate the optimization results, we used the observation-based g_s and g_i (Sect. 3.2.2.2).

3.2.2.1 COS flux, GPP, and mixing ratio

We used canopy COS uptake derived from COS EC measurements for Hyytiälä (Kohonen et al., 2020; Vesala et al., 2022) and Harvard Forest (Wehr et al., 2017). The effect of storage in the canopy airspace was included by collocated COS profiles (Kooijmans et al., 2017; Kohonen et al., 2020).

GPP at Hyytiälä has been obtained from NEE using multi-year parameter fits (Kolari et al., 2014; Kohonen et al., 2022). For Harvard Forest, we chose to use the GPP derived from the isotope spectrometer measurements, because it is more accurate and reliable with frequent and rigorous calibrations (Wehr et al., 2016).

COS soil flux measurements were available for the 2016 growing season at Hyytiälä, and for the 2012 and 2013 growing seasons at Harvard Forest. For the soil flux in other years at Hyytiälä, we applied the monthly average diurnal cycle of the soil flux from 2016 to the other years (2013–2015 and 2017). The seasonal and diurnal variation of the soil flux is small compared to the total ecosystem uptake of COS (Sun et al., 2018c). Hence, the averaged value of 2016 can be safely used for other years.

To convert the data frequency of observations to SiB4's three-hourly time resolution, we calculated the median value of each variable in each three-hourly interval and for each month. We only used data points when more than three data points were present and when all vari-

ables required for the optimization were available. Figure 3.2 shows the resulting average diurnal cycle per month for COS ecosystem, soil, and vegetation fluxes (ecosystem flux minus soil flux). Note that positive fluxes indicate uptake. Again, we note that we use the averaged soil flux at Hyytiälä, because its variability is much smaller than the leaf flux.

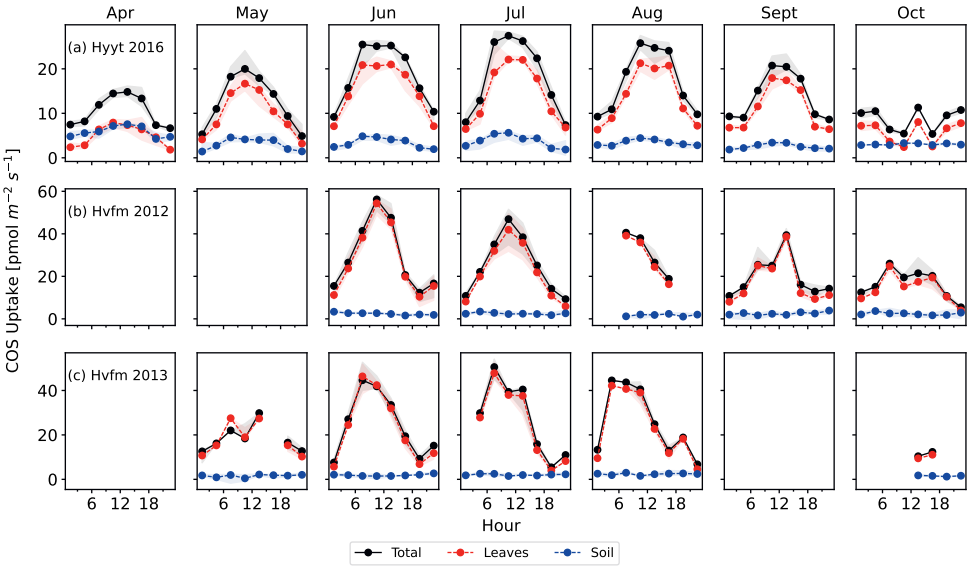


Figure 3.2: Monthly diurnal variation of COS fluxes in 2016 at Hyytiälä (a) and 2012–2013 at Harvard Forest (b, c). Lines are median values of each three hours period and filled areas indicate the interquartile range (25 to 75 percentiles). Black: COS ecosystem flux, blue: soil flux, red: vegetation flux estimated as ecosystem minus soil flux.

3.2.2.2 Conductances g_s and g_i

Observation-based g_s was derived from sensible heat flux and evapotranspiration measurements using the Flux Gradient (FG) equations (Baldocchi et al., 1991; Wehr et al., 2015; Wehr et al., 2021). A key step in the derivation of g_s is the estimation of transpiration from evapotranspiration. At Harvard Forest, transpiration was estimated by an empirical equation established during times of minimal non-stomatal evaporation (i.e. a few days after rain, removing mornings with dew evaporation), as described in Wehr et al. (2017). At Hyytiälä, we simply restricted our analysis to periods of minimal non-stomatal evaporation by eliminating data when the dew point was equal to or greater than the air temperature or when the accumulated precipitation for the past two days was more than 0.01 mm.

The FG approach leads to significant uncertainties for nighttime data because the leaf to air-water vapor gradient is too small under stable conditions (Wehr et al., 2017). We thus excluded nighttime g_s when the values were smaller than 0.05 $\mathrm{mol\,m^{-2}\,s^{-1}}$. To reduce the effect of random noise on g_s, we used an average diurnal cycle (based on three-hourly medians) for each month.

Observation-based g_i was extracted by rewriting Eq. 3.1:

$$g_{\mathrm{i}} = \left(\frac{C_{\mathrm{COS}}}{F_{\mathrm{COS}}} - \frac{1.94}{g_{\mathrm{s}}} - \frac{1.56}{g_{\mathrm{b}}} \right)^{-1}. \tag{3.9}$$

Here we used the observation-based g_{s} from the FG equation as discussed above and filtered observations of C_{COS} and F_{COS}. Additionally, we used simulated g_{b} from SiB4, as we don't have observed g_{b} available and as the value of g_{b} only has a minor effect on F_{COS}, which will be further discussed in Sect. 3.3.1. Although outliers of observed g_{s}, C_{COS}, and F_{COS} were removed already, a significant number of outliers in g_{i} appeared because of error propagation. To avoid excessive noise, we only retained g_{i} values in the interquartile range (25–75 percentile) of three hours for each month.

3.2.3 Optimization

3.2.3.1 Procedure

In the optimization steps, we minimized a quadratic cost function $J(x)$ based on Bayes' theorem (Tarantola et al., 1982; Enting et al., 1993):

$$J(x) = \frac{(x - x_{\mathrm{a}})^2}{2\sigma_{\mathrm{a}}^2} + \frac{(y - H(x))^2}{2\sigma_{\mathrm{y}}^2} \tag{3.10}$$

Here, x represents the state, x_{a} the prior settings of the state, and σ_{a} the error assigned to the parameters. In the second term, y represents the observations and $H(x)$ the model evaluation using the state x. The error σ_{y} represents the observational error. The details of σ_{a} and σ_{y} will be described in Sect. 3.2.3.2 and Sect. 3.2.3.3, respectively.

To optimize the g_{s} and g_{i} parameters, we intend to use the information from GPP and COS leaf uptake measurements sequentially. Thus, we propose a two-step approach in combination with an iterative minimization of the cost functions, as outlined in Fig. 3.3. In the first step, we optimally estimate g_{s} parameter b_1 by minimizing $J(x)$ which sums GPP differences between estimation ($H(b_1)$ in Eq. 3.10) and observation.

We select GPP for the first step optimization rather than g_{s}, because derived GPP from NEE has been evaluated more frequently than observation-based g_{s}. We use only positive GPP_{obs} values (uptake) because our target parameter b_1 in the first step cannot be optimized when GPP is zero. Here, we do not use GPP_{SiB4} because SiB4 does not apply the BWB model for GPP calculation as described in Eqs. 3.3–3.5. For this reason, we cannot optimize BWB parameters with GPP_{SiB4}. Instead, we estimated GPP by rewriting the BWB model using an observation-based g_{s} (Sect. 3.2.2.2), modelled RH at the leaf surface (F_{LH}), and simulated CO_{2S} from SiB4. Hereinafter the estimated GPP by the BWB model is called GPP_{BWB}:

$$\mathrm{GPP_{BB}} = \frac{(g_{\mathrm{s}} - b_0 \,\mathrm{LAI}\, F_{\mathrm{RZ}})\ \mathrm{CO_{2s}}}{b_1\, F_{\mathrm{LH}}}. \tag{3.11}$$

In the second optimization step, we optimize the b_0 and g_{i} parameters (α in Eq. 3.6 and T_{eq} in Eq. 3.8). These parameters are optimized by minimizing the differences between calculated and observed F_{COS}. F_{COS} is calculated with three conductances using Eq. 3.1. Specifically, g_{s} is estimated with Eq. 3.2 using the optimized b_1 from step 1. Here, we used GPP_{SiB4} to satisfy our aim of optimizing the SiB4 model parameters. Note that GPP_{BWB} from Eq. 3.11 cannot be used here, because it would make the estimated g_{s} equal to observation-based g_{s}. Based on sensitivity studies in Appendix A3.1, we decided to select α, b_0, and T_{eq} as target parameters and to fix ΔH_{eq} and ΔH_{a} at 100 kJ mol^{-1} and 40 kJ mol^{-1}, respectively.

In the optimization procedure, we specifically exploit the fact that the nighttime COS flux carries information about nighttime g_s through the parameter b_0. The alternative, i.e. optimizing b_0 already in step 1, would ignore the information of nighttime g_s brought by COS flux observations. Consequently, however, we have to iterate the procedure several times to reach convergence. Figure 3.3 specifies which observations and observation-based quantities are used in each step (g_s, GPP_{obs}, $F_{COS,obs}$, C_{COS} highlighted as gray) and which variables are simulated by SiB4 (e.g., T_{can}, F_{LH}, GPP_{SiB4}, CO_{2S}, and g_b).

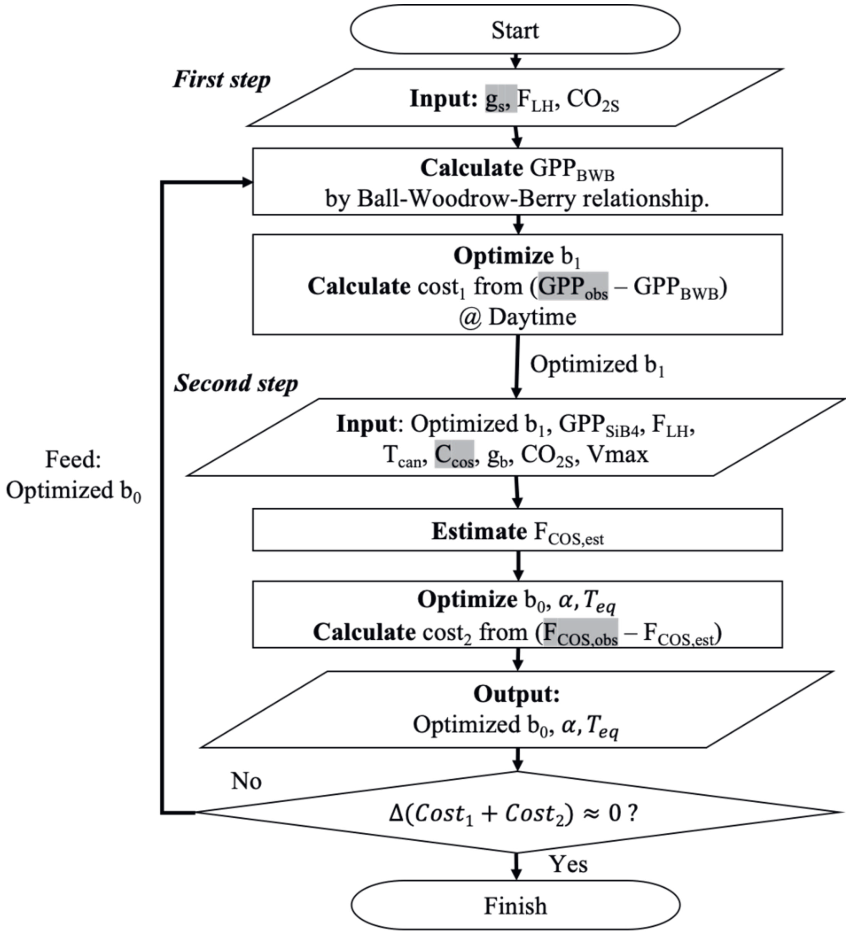


Figure 3.3: Flow chart of the procedure to optimize COS leaf uptake's parameters. The procedure has two steps: (1) Optimize b_1 by minimizing deviations between GPP_{BWB} and observations, (2) Optimize b_0, α, and T_{eq} by minimizing deviations between modelled and observed COS uptake. Variables highlighted in grey are from observations, and the other variables are estimated from SiB4.

We applied the Simplicial homology global optimization (SHGO) from the SciPy python library to minimize the cost functions. SHGO is appropriate for solving non-continuous, non-convex and non-smooth functions (Endres et al., 2018). SHGO also allows the definition of a valid parameter range, as will be discussed in Sect. 3.2.3.2 and in Appendix A3.1.

The $V_{\mathrm{max,rub}}$ was found to vary over the phenological stage and per PFT (Woodward et al., 1995; Wolf et al., 2006; Kattge et al., 2009; Walker et al., 2014), which also affects the calibration factor α. Therefore, we optimized α for each PFT and each phenological stage. In contrast, b_0, b_1, and T_{eq} were only separately determined for the different PFTs, assuming local characteristics for each PFT. We did not include $V_{\mathrm{max,rub}}$ in the state variables because this would require SiB4 CO_2 simulations. These simulations need several parameters, like carbon cycle pools, which are difficult to estimate. Therefore, we focus this research on estimating $V_{\mathrm{max,CA}}$ by optimizing g_{i}-related parameters.

3.2.3.2 Initial parameters and prior errors

The first term in the cost function (Eq. 3.10) ties the values of the parameters to realistic values. We additionally confined the parameter values within realistic physical ranges using the SHGO algorithm. Initial parameters and prior errors were chosen based on thresholds outlined in Appendix A3.1, and they will be compared with optimized results in Sect. 3.3.3. The variation in the resulting cost function shows distinct differences between Hyytiälä and Harvard Forest, which reinforces our strategy to optimize parameters for each station separately.

3.2.3.3 Observation Errors

To quantify the observational errors σ_{y}, we first calculated the three-hourly average coefficient of variation (CV) relative to the mean of the observed COS vegetation flux in each phenological stage and observed GPP for the entire growing season. Figure 3.4 shows the results of observational errors. The GPP error is applied in step 1 and the COS leaf uptake error is used in step 2 in the optimization. We multiplied the CV with the mean in each phenological stage. Here, we classify the error of the COS leaf uptake in each phenological stage because we optimized α in each stage. In Fig. 3.4, we found that the errors differ slightly per phenological stage. At Hyytiälä, the errors are larger in the growth stage compared to the maturity stage, possibly due to the unstable weather conditions in the growth stage. The COS leaf uptake error is larger at both stations during nighttime than during daytime. A potential reason can be the relatively higher uncertainty in the EC method during stable nighttime conditions.

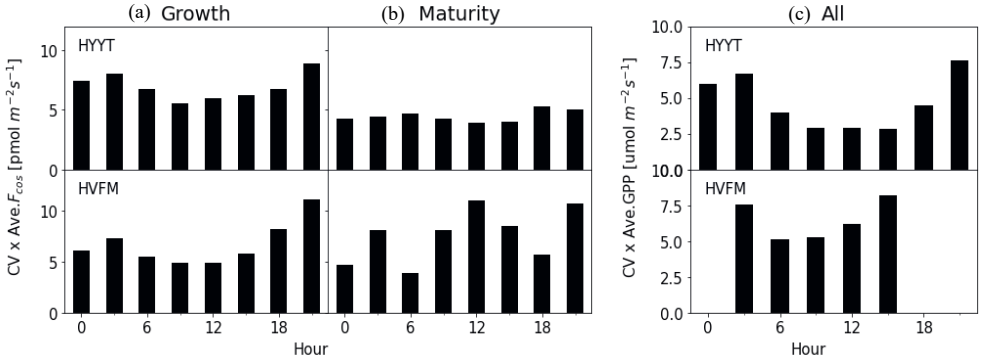


Figure 3.4: Distribution of the observation error in the growth (a) and maturity stages (b) for COS leaf uptake and all stages for GPP (c). The upper panel is the errors for Hyytiälä (HYYT) and the lower panel is for Harvard Forest (HVFM).

3.2.4 SiB4 simulations

We utilized several simulated variables from SiB4 in our optimization. Specifically, calculated GPP_{SiB4}, g_{b}, T_{can}, $V_{max,rub}$, functions F_{LH}, F_{RZ} and F_{LC} were used to calculate COS leaf uptake. In addition, LAI and CO_{2S} were used to estimate GPP_{BWB}. Furthermore, we introduced the new temperature function ($f(T_{\mathrm{can}})_{\mathrm{new}}$) in the g_{i} calculation (Sect. 3.2.1.3) to calculate COS leaf uptake, and excluded P P_{sfc}^{-1} and T_{can} T_0^{-1} from Eq. 3.6 due to minor impacts of these factors for these ecosystems.

To simulate the vegetation assimilation F_{COS} at the two stations, we used the Modern-Era Retrospective Analysis for Research and Application, version 2 (MERRA-2) (Gelaro et al., 2017) as meteorological driver data. Only air temperature and leaf specific humidity were taken from observations. To initialize the carbon pools, we spun up the model to equilibrate the pools. The spin-up was performed from 2000 to 2010 with ten iterations. We used observed C_{COS} and ambient CO_2 mole fractions were prescribed at 370 $\mu\mathrm{mol\,mol}^{-1}$.

To estimate the global impact of our findings, we performed a global SiB4 simulation from 2016 to 2018 to evaluate the influence of the new parameters on the monthly COS biosphere fluxes which are averaged for three years. The atmospheric COS mixing ratio C_{COS} was taken from optimizations using the TM5 chemical transport model (Ma et al., 2021; Kooijmans et al., 2021). We used three-hourly C_{COS} averaged over 2016 to 2018 by Kooijmans et al. (2021). As we found that all target parameters differ between ENF and DBF (Appendix A3.1), the application of the optimized parameters to other PFTs will likely be incorrect. Hence, we applied the optimized parameters only to ENF and DBF, and used the standard values of SiB4 for the other PFTs. However, to confirm the $f(T_{\mathrm{can}})_{\mathrm{new}}$ effect on COS leaf uptake, we applied $f(T_{\mathrm{can}})_{\mathrm{new}}$ to all PFTs with averaged optimum T_{eq} from the two stations (303 K) and fixed ΔH_{eq} (100 kJ mol^{-1}) and ΔH_{a} (40 kJ mol^{-1}) as described in Appendix A3.1. The soil flux is estimated following (Ogée et al., 2016) as implemented by Kooijmans et al. (2021).

To examine the humidity stress impact in SiB4, we performed a simulation with and without the lower threshold for F_{LH} of 0.7 for ENF (see Sect. 3.2.1.2). Additionally, we replaced the RH at leaf level calculated by SiB4 by RH measured above the canopy. Results will be shown in Sect. 3.3.5.1. To account for the optimized humidity impact on the global COS leaf uptake, we simulated the global COS leaf uptake without the 0.7 threshold of F_{LH} for ENF.

3.2.5 Error reduction and statistics

To determine the uncertainty in the optimized model parameters, we employed a Monte Carlo optimization procedure as described in detail in Appendix A3.2. In short, 100 optimizations were performed. In each optimization, we perturbed the state with random Gaussian noise on the state and the observations (Chevallier et al., 2007; Bosman et al., 2023), according to the errors in the state and observations (Fig. 3.4). Posterior error statistics will be reported in Table 3.3.

Additionally, we quantified the performance of the optimization by calculating the root mean square errors (RMSEs), mean bias errors (MBEs), and the chi-square metric (χ^2). The χ^2 metric quantifies the average deviation from the observations, expressed in σ_{y} units. Thus, $\chi^2 = 1$ signals that, on average, the model fits the observation within 1 σ indicating a realistic error setting.

3.3 Results and discussion

3.3.1 Impact of each conductance

Figure 3.5 investigates which conductance contributes most to the total conductance (g_t). In these plots, all conductances are prior values before optimization. g_s and g_i were derived from observations (Sect. 3.2.2.2). We find that g_t is determined mainly by g_i and g_s. During daytime, g_i is the lowest conductance in almost all months at Hyytiälä but is comparable to g_s in Harvard Forest. The value of g_b is the highest and hence has the smallest impact on g_t. Therefore, to improve the accuracy of COS leaf uptake simulation effectively, parameters of g_s and g_i are evaluated and optimized, and g_b is kept to its standard value.

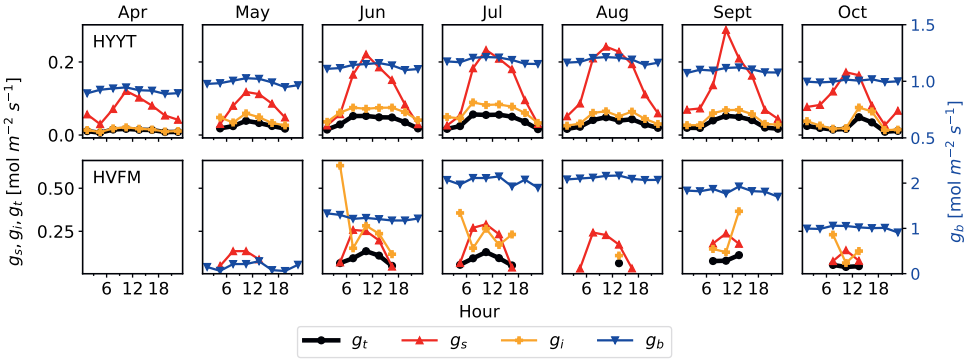


Figure 3.5: Monthly median value of diurnal conductances (black: g_t, red: g_s, orange: g_i, blue: g_b) at Hyytiälä (HYYT) and Harvard Forest (HVFM). g_b is estimated by SiB4, g_s and g_i are calculated based on observations as described in Sect. 3.2.2.2. Negative values are not displayed. The total conductance g_t is calculated from g_b, g_s, and g_i according to Eq. 3.1.

3.3.2 Optimization performance

We obtained optimized parameters after five iterations. By design, the optimized results reduced the deviations between model and observation of GPP and COS leaf uptake. This improvement is quantified by statistical indexes in Table 3.1 and Table 3.2, respectively. GPP_{BWB} is improved slightly compared to the prior (Table 3.1), with RMSEs reduction from 4.08 to 3.84 $\mu\mathrm{mol\,m^{-2}\,s^{-1}}$ at Hyytiälä and 8.35 to 7.89 $\mu\mathrm{mol\,m^{-2}\,s^{-1}}$ at Harvard Forest. MBEs are decreased from -1.48 to -0.61 $\mu\mathrm{mol\,m^{-2}\,s^{-1}}$ at Hyytiälä and from -4.97 to -3.46 $\mu\mathrm{mol\,m^{-2}\,s^{-1}}$ at Harvard Forest (Table 3.1). The χ^2 was reduced by about 0.09 at Hyytiälä and by 0.08 at Harvard Forest. The improvement in GPP_{BWB} reflects the effect of optimizing b_1 and b_0 in the BWB model.

The posterior result of COS leaf uptake ("Post" in Table 3.2) shows a slight improvement compared to the original state variables with $f(T_{\mathrm{can}})_{\mathrm{new}}$ in RMSE (from 7.67 to 5.73 $\mathrm{pmol\,m^{-2}\,s^{-1}}$ at Hyytiälä and from 10.45 to 9.54 $\mathrm{pmol\,m^{-2}\,s^{-1}}$ at Harvard Forest) but significantly improved MBE (from -5.10 to -0.01 $\mathrm{pmol\,m^{-2}\,s^{-1}}$ at Hyytiälä and from -2.53 to -1.99 $\mathrm{pmol\,m^{-2}\,s^{-1}}$ at Harvard Forest, see "Post" in Table 3.2). The large RMSE reflects the typically large random noise of COS flux observations (Kooijmans et al., 2016; Kohonen et al., 2020). However, χ^2 drops by 0.41 at Hyytiälä and by 0.38 at Harvard Forest, confirming that the optimization properly reduced the mismatch between observations and the model

Table 3.1: RMSE, MBE, and χ^2 for the estimation of GPP_{BWB} in daytime using prior stomata parameters (Pri) and posterior parameters (Post).

Station	Type	RMSE ($\mu\mathrm{mol\,m^{-2}\,s^{-1}}$)	MBE ($\mu\mathrm{mol\,m^{-2}\,s^{-1}}$)	χ^2
Hyytiälä	Pri	4.08	−1.48	0.78
	Post	3.84	−0.61	0.69
Harvard Forest	Pri	8.35	−4.97	0.99
	Post	7.89	−3.46	0.91

within the error statistics. Figure 3.6 compares the optimized COS leaf uptake to the original SiB4 simulation in scatter plots. Where the original simulation with $f(T_{\mathrm{can}})_{\mathrm{SiB4}}$ and previous state variables was often underestimating the observations, the optimized results resemble the observations over a larger range of the data.

Table 3.2: Same as Table 3.1 but for COS leaf uptake, as applied in the original $f(T_{\mathrm{can}})_{\mathrm{SiB4}}$ simulation with original conductance parameters (Org), with the new temperature response function $f(T_{\mathrm{can}})_{\mathrm{new}}$ using the initial g_{s} and g_{i} parameters (Pri), with optimized parameters (Post). Here, state parameters relevant for g_{i} are α and T_{eq}. The state parameters relevant for g_{s} are b_0 and b_1.

Station	Type	$g_{\mathrm{i}}\, f(T)$	RMSE ($\mathrm{pmol\,m^{-2}\,s^{-1}}$)	MBE ($\mathrm{pmol\,m^{-2}\,s^{-1}}$)	χ^2
Hyytälä	Previous SiB4 (org)	$f(T)_{\mathrm{SiB4}}$	7.67	−5.10	0.82
	Posterior (post)	$f(T)_{\mathrm{new}}$	5.73	0.01	0.41
Harvard Forest	Previous SiB4 (org)	$f(T)_{\mathrm{SiB4}}$	10.45	−2.53	1.19
	Posterior (post)	$f(T)_{\mathrm{new}}$	9.54	−1.99	0.81

3.3.3 Optimized parameters

The optimized parameter values with posterior errors are listed in Table 3.3. The optimized SiB4 parameters differ between the stations, likely because the dominant PFT and the climate conditions differ between Hyytiälä and Harvard Forest. For instance, the optimum temperature is smaller at Hyytiälä (19.85 °C) than in Harvard Forest (35.85 °C) which are slightly smaller than T_{eq}. Thus, the optimum temperature reflects the temperature dependence of the enzyme and its adaptation to temperature (Lee et al., 2007). This indicates that regional temperature information is important for correctly estimating g_{i} globally. The optimum temperature can be compared with other observations. For instance, Burnell and Hatch (1988) observed increasing CA activity with maize grown in a temperate temperature range from 20 to 30 °C, relative to a temperature of 17 °C. Thus, we can assume the optimal temperature lies above 17 °C. Another study by Boyd et al. (2015) observed the C_4 plant *Setaria viridis* with a temperature of 28 °C / 18 °C day/night, and a reduced CA activity is suggested at temperatures above 25 °C. This optimum temperature falls between our values derived for Hyytiälä and Harvard Forest.

The α, which is the enzyme activity of CA relative to the $V_{max,rub}$, is reduced from the default value of 1400 to 1316 (in growth) and 1331 (in maturity) at Hyytiälä. At Harvard Forest, α values are larger than the original values in SiB4 for leaf-out (1780), growth (1740), and maturity (2224) phenological stages. Here it should be noted that the change of α should be

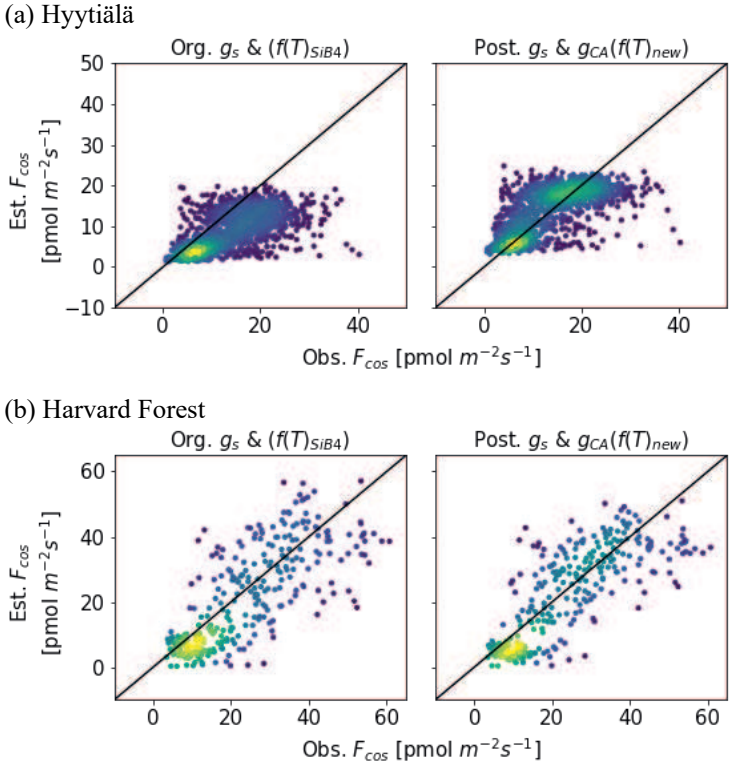


Figure 3.6: Scatter plots between observed and estimated COS leaf uptake from original parameters with $f(T_{\mathrm{can}})_{\mathrm{SiB4}}$ (left) and optimized parameters with $f(T_{\mathrm{can}})_{\mathrm{new}}$ (right) for two stations. The colors represent the density of data.

interpreted in combination with the new temperature function $f(T_{\mathrm{can}})_{\mathrm{new}}$ of g_{i}. Since we only optimize T_{eq} for two PFTs (with identical and fixed values for ΔH_{a} and ΔH_{eq}) and T_{eq} only shifts $f(T_{\mathrm{can}})_{\mathrm{new}}$ (Fig. 3.2), the magnitude of g_{i} is primarily determined by parameter α. The different values of α derived for different phenological stages will be discussed in Sect. 3.3.4.

The optimized results of the BWB model parameters b_0 are similar to the original values used in SiB4, but b_1 values are mostly higher. The parameter values b_0 for Hyytiälä ($0.013\ \mathrm{mol\,m^{-2}\,s^{-1}}$) and Harvard Forest ($0.007\ \mathrm{mol\,m^{-2}\,s^{-1}}$) are slightly changed compared to the initial value ($0.010\ \mathrm{mol\,m^{-2}\,s^{-1}}$). For the optimized BWB model parameter b_1, the empirical slope between g_{s} and GPP, we find a considerable increase at Hyytiälä (16.38) and a slight increase in Harvard Forest (11.43), compared to the prescribed SIB4 value of 9.0. Our optimized values are larger than the values presented in a review paper for the evergreen gymnosperm tree which showed $b_1 = 6.8$ and are similar to $b_1 = 8.7$ for the deciduous angiosperm tree (Miner et al., 2017). As will be discussed in Sect. 3.3.5.1, the higher slope at Hyytiälä is possibly related to an incomplete separation of observed transpiration rates from the latent heat flux.

Concerning the estimated errors in b_0, b_1, and T_{eq}, we find that errors have been reduced

significantly compared to the prior error range. This indicates that the available data constrain these parameters well. Only the α parameters of Harvard forest are less well constrained. Also, the skill of the optimization to independently optimize the parameters is high, as quantified by the posterior covariances that are presented in Appendix A3.2.

Table 3.3: Original (Org), initial (Pri), and optimized (Post) state vectors for Hyytiälä and Harvard Forest in different phenological stages as defined by SiB4. All values are reported as mean ± standard deviation. The definition of the prior values is outlined in Appendix A3.1, and the error reduction is described in Appendix A3.2

Approach	State vector	**Hyytiälä**		**Harvard Forest**		
		Growth	Maturity	Leaf out	Growth	Maturity
Previous SiB4 (org)	$V_{\mathrm{max,rub}}$ ($\mu\mathrm{mol\,m^{-2}\,s^{-1}}$)	52	54	96	94	92
	α (–)			1400		
	b_0 ($\mathrm{mol\,m^{-2}\,s^{-1}}$)			0.01		
	b_1 (–)			9.0		
Prior (pri)	α (–)	1400 ± 1000		2000 ± 1000		
	b_0 ($\mathrm{mol\,m^{-2}\,s^{-1}}$)	0.02 ± 0.02		0.01 ± 0.02		
	b_1 (–)	17 ± 5		12 ± 5		
	T_{eq} (K)	295 ± 20		310 ± 20		
Posterior (post)	α (–)	1316 ± 509	1331 ± 574	1798 ± 527	1740 ± 494	2224 ± 613
	b_0 ($\mathrm{mol\,m^{-2}\,s^{-1}}$)	0.013 ± 0.009		0.007 ± 0.006		
	b_1 (–)	16.36 ± 2.87		11.43 ± 1.98		
	T_{eq} (K)	295 ± 11		311 ± 10		

3.3.4 Optimized temperature response

The optimized parameters show significant improvement in temperature response of the COS leaf uptake. Figure 3.7 presents the temperature dependency of g_{i} and COS leaf uptake from the original and optimized simulations output and observations. As stated before, the original $f(T_{can})_{SiB4}$ describes the CA enzyme activity as an exponentially increasing response to temperature, which does not resemble the observations. The optimized g_{i} and COS leaf uptake follow the temperature dependence of the observation more closely than the original $f(T_{can})_{SiB4}$. In Harvard Forest, an underestimated bias is shown at a lower temperature under 10 °C, mostly corresponding to nighttime. This underestimate is related to the uncertainty in nighttime g_{s} and the small data volume at low temperatures (details in Sect. 3.2.2.2).

In the upper panel of Fig. 3.7, we see the different roles of α and $f(T_{can})_{new}$ in the improvement of g_{i} response to temperature as the red and orange lines. Without the α correction applied (Posterior with α = 1400; orange line), the optimized g_{i} resembles the fluctuations in the observations but there remains a bias in the amplitude. In contrast, when the optimized value of α is included (red line), the amplitude of g_{i} is improved. Compared to the optimization that excluded α, the MBE is reduced from 0.006 to 0.003 $\mu\mathrm{mol\,m^{-2}\,s^{-1}}$. Due to the different optimized α values in each phenological stage, the improvement of the red line shows the appropriate temperature responses. For instance, in Harvard Forest, α in leaf-out and growth (1798 and 1740) mostly corresponds to lower temperatures. At these stages, the impact on g_{i}

is smaller because g_i is smaller than that at high temperature. At high temperatures, there are more significant corrections of g_i, which correspond to the maturity stage value of α (2224).

The temperature responses of g_i and COS leaf uptake now show an optimum temperature. As can be observed in Fig. 3.7a, the optimum temperature of the observation-based g_i is seen as 293 K (19.85 °C) at Hyytiälä. At Harvard Forest, the optimum temperature is 309 K (35.85 °C), but falls outside the observation range. The optimum curve affects to the COS leaf uptake at both stations with changing peak temperatures (Fig. 3.7b). The accuracies of g_i and F_{COS} are improved significantly at temperatures both below and above around the optimum temperature at both sites.

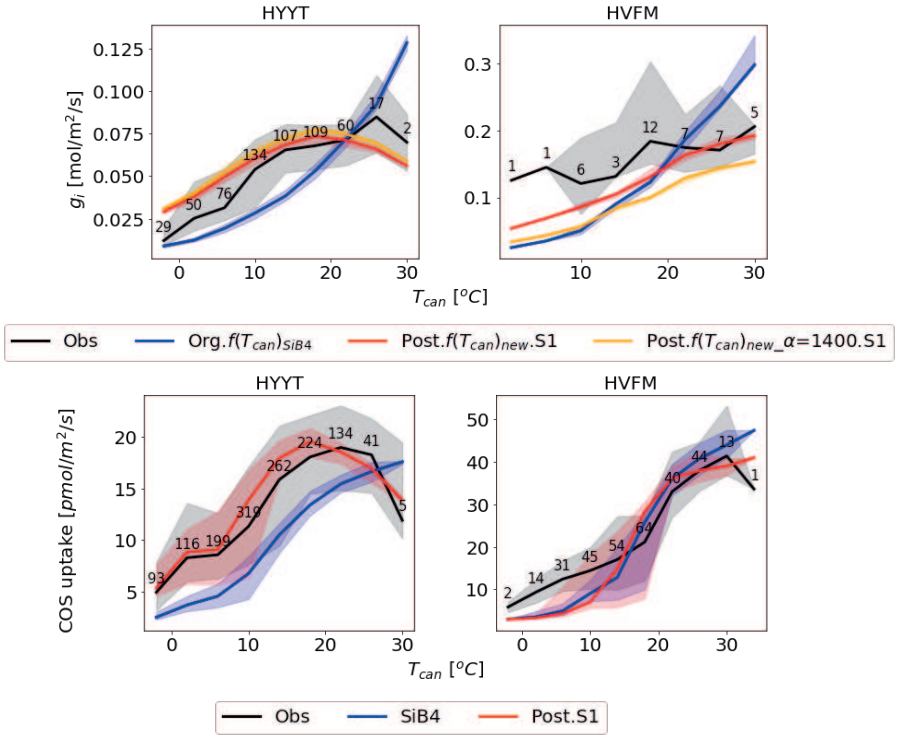


Figure 3.7: Temperature dependency on g_i (a) and COS leaf uptake (b) at Hyytiälä (HYYT, left) and Harvard Forest (HVFM, right). The lines are medians and the filled area represents the 25 to 75 percentiles of each temperature range with 3 ºC intervals. Black: data based on observations; blue: previous parameters with $f(T_{can})_{SiB4}$; red: optimized parameters with $f(T_{can})_{new}$ and g_s parameters of the BWB model; orange: same as the red line but now α is prescribed with original value (1400) and not optimized. The numbers indicate number of observations in each temperature bin.

3.3.5 Application in SiB4

3.3.5.1 Monthly diurnal variation

Figures 8 and 9 display the SiB4 simulation results obtained with the original and optimized parameterizations compared to observations for Hyytiälä and Harvard Forest, respectively. As

a result of the optimization, the monthly diurnal variation of the optimized COS vegetation flux, g_s, and g_i are closer to observations than the original SiB4 simulations. The observed COS leaf uptake and g_s show diurnal and seasonal fluctuations at both measurement sites, with the highest values around midday and in summer. For g_i, we observe a weak diurnal cycle throughout the year, and higher daytime maximum values in summer, driven by the temperature dependence of CA.

At Hyytiälä, COS leaf uptake in the original SiB4 model was underestimated during daytime in all months. The fluxes increased too slowly in the morning for all months (Fig. 3.8a). These issues are solved by optimizing the BWB model parameters and temperature response function. In the case of g_s (Fig. 3.8b), the original SiB4 simulation showed the correct timing of the increase and decrease of g_s in the morning and afternoon but underestimated the peak daytime values. The optimized model now better resembles the daytime g_s values.

However, the model still overestimates g_s in the late afternoon of summer months at Hyytiälä. We speculate that one of the reasons lies in an inaccurate humidity or humidity stress in SiB4. Figure 3.10 shows a diurnal cycle of g_s simulations averaged from April to August with different choices on how the humidity stress factor is treated (Sect. 3.2.5). When the default 0.7 threshold of humidity stress (F_{LH}) in ENF is applied in SiB4, g_s is overestimated in the afternoon at Hyytiälä (blue dotted line). When we removed the minimum threshold of F_{LH} for ENF, g_s simulations during mid-day are improved (note that the threshold was only implemented for ENF, not for DBF, and thus the blue dotted line is not visible for Harvard Forest in Figure 3.10).

However, SiB4 still tends to overestimate g_s in the morning and late afternoon. The overestimated F_{LH} in SiB4 can result from three factors: (1) an overestimated water vapor flux in the boundary layer to the leaf surface, (2) an underestimated boundary conductance, or (3) an underestimated leaf surface temperature. Since we do not have observations of the leaf surface temperature, we confirmed that the estimated canopy temperature has a tight 1 to 1 relation with the observed air temperature. We speculate that the main reason for the overestimated FLH is the uncertain water vapor flux. When we base the g_s calculation on the observed RH above the canopy, the diurnal cycle is better simulated (orange dashed line in Fig. 3.10). The overestimated water vapor pressure implies that SiB4 tends to underestimate the humidity stress in the late afternoon when converting observed specific humidity above the canopy to humidity at leaf surface level. We suggest evaluating the boundary conductance (point (2) above) with observations.

The optimized model still underestimates g_s at Hyytiälä in April, September, and October (Fig. 3.8b). This might indicate that we did not properly separate stomatal transpiration rates from the observed latent heat flux. The simulated mean ratios of evaporation to evapotranspiration in these three months are 66%, 60%, and 95%, respectively, and these values are higher compared to the other months (43 to 53%). Thus, we speculate that the observed evapotranspiration does not solely represent stomatal transpiration in these months due to larger evaporation rates, leading to overestimated g_s in the observations.

Figure 3.8c shows that the optimized g_i often resembles the observed daytime g_i better than the original SiB4 simulation. Only in April is the optimized g_i overestimated at Hyytiälä. Again, this can likely be explained by the underestimated g_s, which is used to derive observation-based of g_i (see Sect. 3.2.2.2).

At Harvard Forest, the optimized SiB4 model generally simulates the magnitude of the COS leaf uptake well (Fig. 3.9a). The model overestimates the COS leaf flux only in the afternoon during the summer months. However, g_s values are generally overestimated and SiB4 simulates two peaks during daytime. This indicates that humidity stress is only briefly occurring at mid-day in SiB4. However, in reality, the humidity stress likely remains a limiting factor

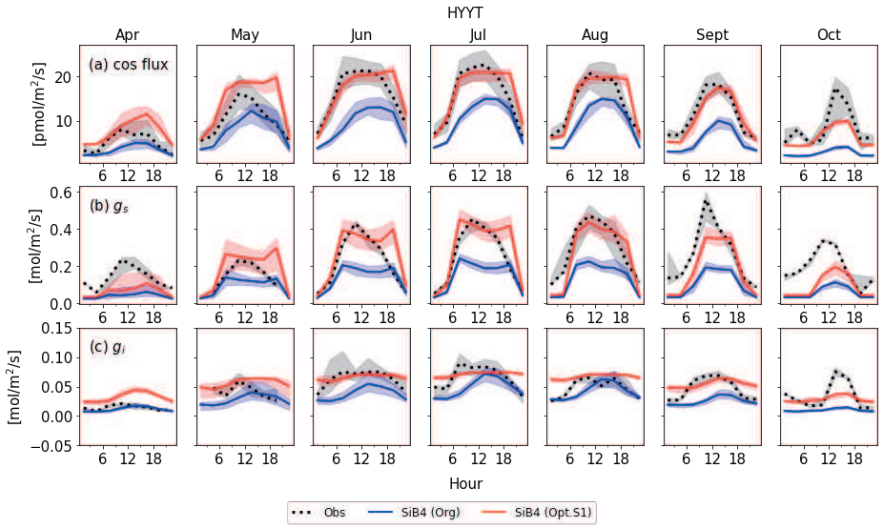


Figure 3.8: Monthly-diurnal cycle of COS leaf uptake (a), g_s (b), and g_i (c) at Hyytiälä (HYYT) from 2012 to 2016. Data include observations (black dots), the original SiB4 model with $f(T_{can})_{SiB4}$ (blue solid), and SiB4 with optimized g_s and g_i parameters with $f(T_{can})_{new}$ (red solid). The filled area corresponds to the 25-75 percentile of the data in each three-hourly interval of each month.

in the afternoon under conditions with high vapor pressure deficit (VPD) (Kooijmans et al., 2019). Observations show that g_s typically peaks in the early morning and decreases in the afternoon due to higher afternoon VPD. Figure 3.10 shows that, similar to the Hyytiälä simulation, the afternoon decrease in g_s at Harvard Forest is better simulated when we use the RH observed above the canopy. In Fig. 3.9c, the optimized g_i during the daytime agrees well with the observation-based g_i, except for several drops or peaks in July and October, likely caused by observational errors or uncertainty of the observed g_s.

3.3.5.2 Global application

Figure 3.11 shows the SIB4 calculated changes in the monthly COS biosphere flux after applying the optimized temperature function and stomatal parameters. The global COS sink remains almost preserved (Original: 701 Gg S yr^{-1}, Optimized: 704 Gg S yr^{-1}), but the regional budgets change significantly. For example, the optimized model estimates larger COS uptake for all seasons in boreal and temperate regions and smaller uptake in the tropics. These changes are explained by the new temperature function of g_i in Fig. 3.7. However, since the new temperature function is based on only two observation sites in the boreal and temperate regions, the calculated uptakes need more verifications with observations obtained in other areas and in different climate conditions, such as the tropics.

The higher uptake at high latitudes and lower uptake at the tropics are nevertheless consistent with inverse modelling results presented in previous studies (Ma et al., 2021; Hu et al., 2021) and would help towards closing the COS budget. Still, however, the temperature response function and BWB parameters are now based on measurements of only two sites in only two biomes. With more measurements over different vegetation types, these parameters could also be optimized for a wider range of ecosystems.

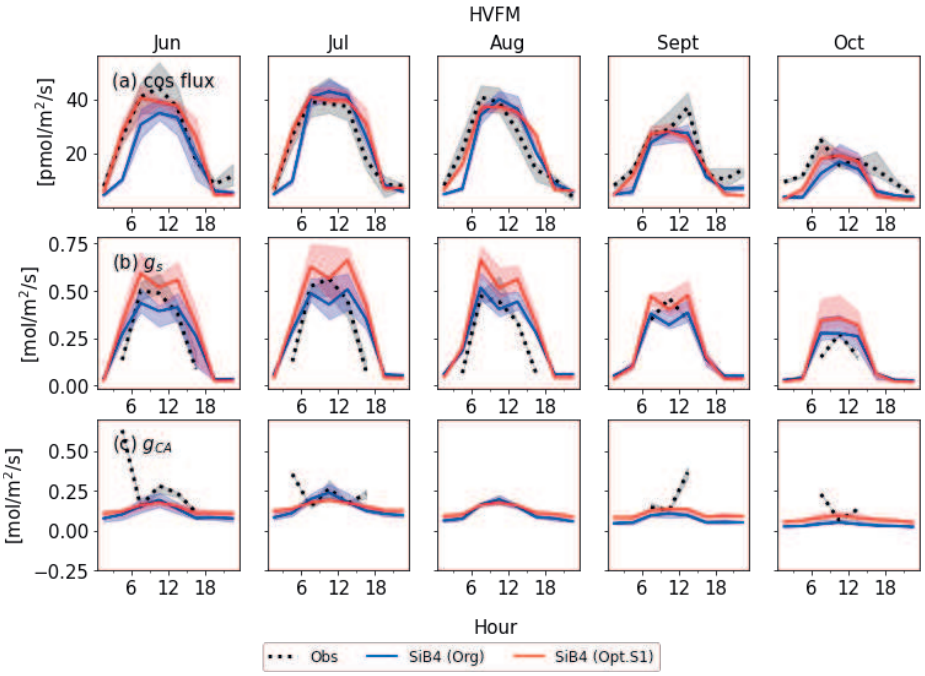


Figure 3.9: Same as Fig. 3.8 but for Harvard Forest (HVFM).

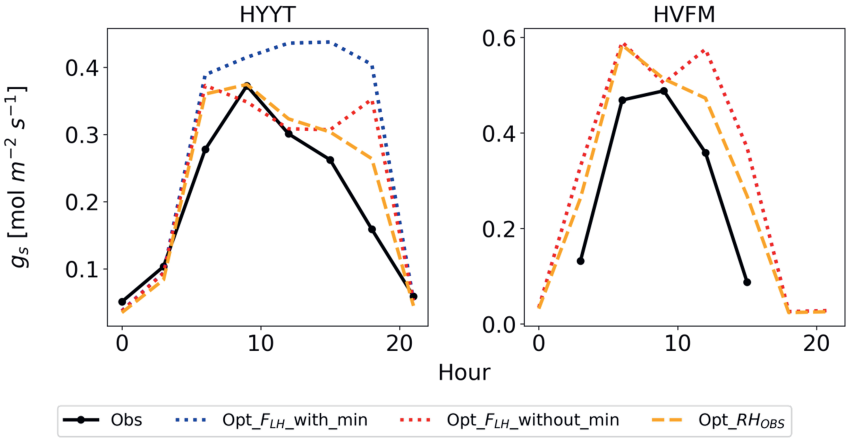


Figure 3.10: Average diurnal cycle of g_s at Hyytiälä (HYYT) and Harvard Forest (HVFM) from April to August. Data include observations (black solid), SiB4 simulation with optimized parameters with minimum bounds of F_{LH} (blue dotted), without bounds (red dotted), and with observed RH in air (orange dashed). Note that the blue and red lines overlap for HVFM.

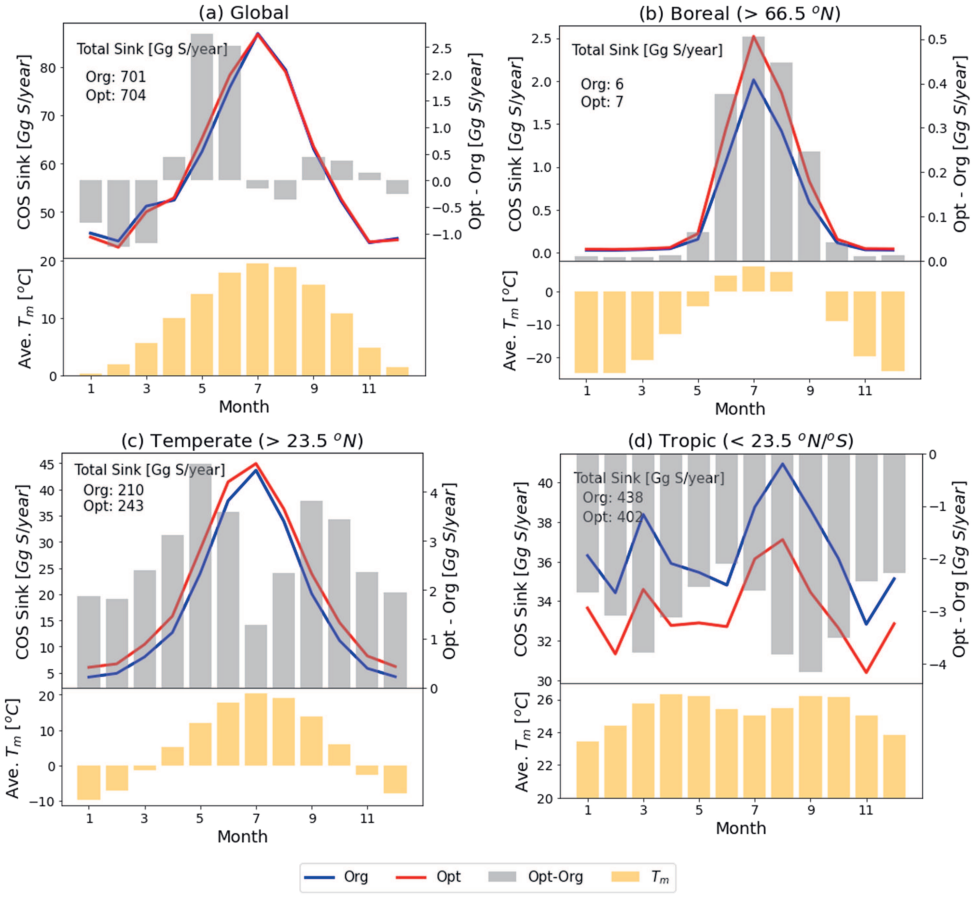


Figure 3.11: Monthly COS sink and averaged temperature in the mixed layer (T_m) over global (a) and specific regions (north boreal: (b), north temperate: (c), tropics: (d)) with the original (blue line) and the optimized (red line) SiB4 model. The grey bars represent the differences in COS sink between the original and the optimized model (right axis). The yellow bars are averaged temperatures in the mixed layer.

3.4 Conclusion

To simulate more accurate COS leaf uptake in the SiB4 model, we have proposed a new temperature function $f(T_{can})_{new}$ for the CA enzyme and have optimized g_s and g_i parameters using observations in ENF (Hyytiälä) and DBF (Harvard Forest) systems. The optimized model reduced the MBE from -5.10 to 0.01 $\mathrm{pmol\,m^{-2}\,s^{-1}}$ at Hyytiälä and from -2.53 to -1.99 $\mathrm{pmol\,m^{-2}\,s^{-1}}$ at Harvard Forest. Furthermore, χ^2 decreases by about 0.41 and 0.38, respectively.

The new function now considers an optimum temperature for enzyme activity, contrary to the initial temperature function used in SiB4 where an exponential increase of the temperature function was adopted from the RuBisCo enzyme activity. The new temperature function

is characterized by an optimum temperature of 293 K (19.85 °C) (Hyytiälä) and 309 K (35.85 °C) (Harvard Forest). The new temperature response increases g_{i}, and thereby the COS flux when the temperature is below the optimum temperature (mostly at high latitudes) and decreases the COS uptake at higher temperatures. (e.g., close to the equator). Globally, these modifications help to close gaps in COS budget that were identified in earlier studies. In this study, we have interpreted the decreasing g_{i} at higher temperatures as an optimum enzyme activity with the widely applied assumption that there are no COS emissions in leaves. However, COS emissions have recently been reported at high temperatures (Maseyk et al., 2014; Gimeno et al., 2017). To determine reasons for reducing COS leaf flux and internal conductance at high temperatures, it will be necessary to analyze the possibility that leaf emissions exist in observations in the future.

We have optimized the BWB model parameters for which we took advantage of the characteristics that the nighttime COS flux informs about nighttime g_{s}, and thus the parameter b_0. The improved correspondence between model and observations shows that COS observations can help to constrain the relation between g_{s} and GPP better. In addition, we showed that SiB4 underestimates the leaf humidity stress under conditions where high VPD should limit g_{s} in the afternoon. This can be improved by using more accurate relative humidity values and by removing the threshold of humidity stress that was implemented in SiB4 specifically for ENF.

The optimized parameters show different values depending on the PFT. Therefore, extending our approach with more observations in different climate zones and over different PFTs will help obtain accurate COS fluxes on a global scale. This approach would reduce the uncertainty in the global COS budget and provide additional constraints on GPP.

A3. Appendices

A3.1 State variable error settings

To evaluate the impact of the various parameters in $f(T_{can})_{new}$ in the optimization as state variables, we implemented a sensitivity test of a total cost function combined with cost1 and cost2, excluding the background term in the cost function equation (Eq. 3.10). Fig. A3.1 shows the shape of the cost function when one parameter is varied within an acceptable range, while the other parameters are fixed (Daniel et al., 2010; Sun et al., 2015) (details in Sect. 3.2.3.2). Based on the shape of the cost function, we used a pragmatic approach to select realistic parameter ranges. Variable values that push the cost function beyond 3.45 (Hyytiälä) and 5.14 (Harvard Forest) were considered outside the allowed physical range (red lines in Fig. A3.2). These thresholds are determined by the cost function value, assuming that the modeled H(x) is the 75-percentile value of observations in three-hourly observations in each month. Variables α, b_0, b_1, and T_{eq} (Fig. A3.1a, b, c, and f) have more significant impacts on the cost function than ΔH_{a} (Fig. A3.1d) and ΔH_{eq} (Fig. A3.1e). Overall, costs in Harvard Forest are higher than at Hyytiälä, likely because DBF has larger diurnal and seasonal variations in the observed fluxes than ENF. We set the optimization range as an initial value $\pm$ 1.5 state error to apply the SHGO algorithm.

Figure A3.2 shows contour diagrams of the cost function as a function of T_{eq} and other parameters of $f(T_{can})_{new}$. The gradient is the cost function indicates the relative importance of each parameter. ΔH_{eq} does not interact with T_{eq}, but ΔH_{a} is inverse proportional to T_{eq} to minimize the cost. The cost function is most sensitive to variations in T_{eq} and therefore we decided to fix ΔH_{eq} and ΔH_{a} at 100 kJ mol^{-1} and 40 kJ mol^{-1}, respectively and to base our optimization on the state variables α, b_0, b_1 and T_{eq}.

A3.2 Posterior uncertainties

To evaluate the ability of constrain the parameters, we performed an ensemble optimization with 100 different members. In each optimization, noise was added to the parameters (σ_{a}) and to the observation (σ_{y}). Random perturbations were drawn from a normal distribution with zero mean and standard deviations σ_a for the state parameters (x) and σ_y for the observations (y). The new cost function of an individual optimization thus becomes:

$$J(x) = \frac{(x - x_a + \varepsilon_a)^2}{2\sigma_a^2} + \frac{(y + \varepsilon_y - H(x))^2}{2\sigma_y^2}. \tag{3.12}$$

We optimized each ensemble with the same y (observationally derived GPP and COS leaf uptake) and x but added noise to each ensemble member (Chevallier et al., 2007). Subsequently, we calculated the posterior uncertainty as the one-standard deviation of the posterior distribution of the optimized parameters.

Figure A3.3 shows the prior and posterior distributions of the parameters at the two stations. All posterior parameters show considerable reductions of variations (error), with optimized values that are listed in the main text, Table 3.3.

Additionally, we calculated a correlation matrix between the posterior state parameters at the two stations, which is shown in Fig. A3.4. Overall, each parameter does not interact significantly (covariances < 0.7).

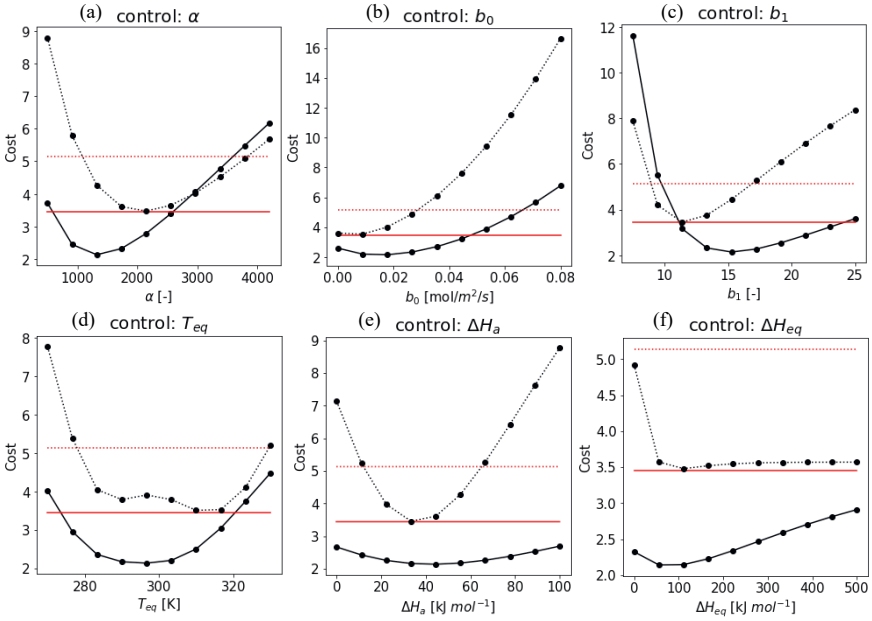


Figure A3.1: Cost function values plotted against the value of the state vector elements at Hyytiälä (solid line) and Harvard Forest (dotted line). The red lines indicate a criteria cost calculated by H(x) as the 75-percentile value of every three-hourly observation in each month. While the target parameter changes, the other variables are fixed as α = 1400 (Hyytiälä), 2000 (Harvard Forest), ΔH_{a} = 40 kJ mol^{-1} ΔH_{eq} = 100 kJ mol^{-1}, and T_{eq} = 295 K (Hyytiälä), 310 K (Harvard Forest), b_0 = 0.02 $\mathrm{mol\,m^{-2}\,s^{-1}}$(Hyytiälä), 0.01 $\mathrm{mol\,m^{-2}\,s^{-1}}$ (Harvard Forest), and b_1 = 17 (Hyytiälä), 12 (Harvard Forest). These values were based on the value where the cost reached a minimum.

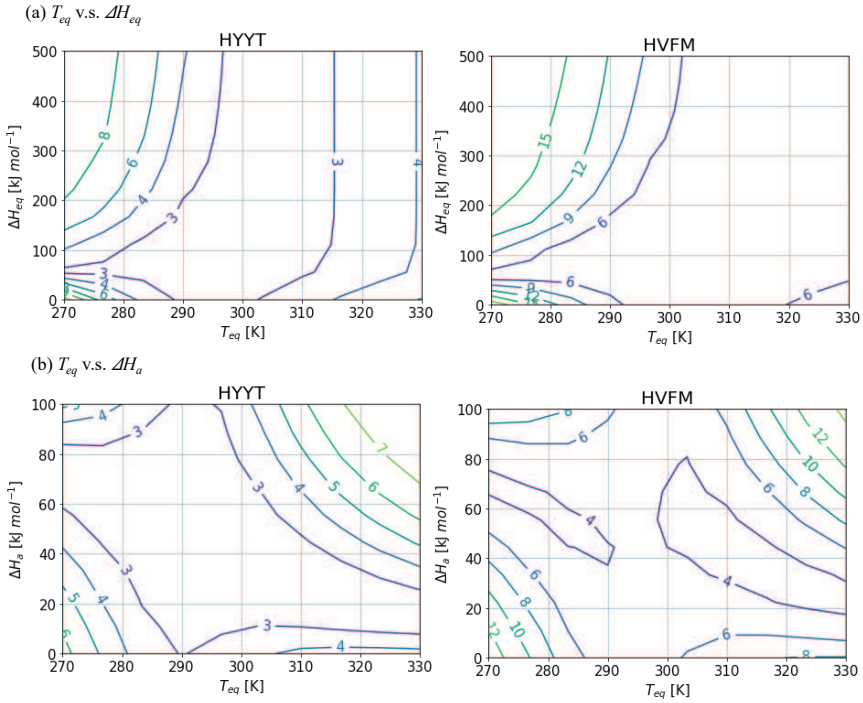


Figure A3.2: Contour diagram of the cost function value as a function of T_{eq} and (a) ΔH_{eq} and (b) ΔH_{a} at Hyytiälä (left) and Harvard Forest (right). While the target parameter changes, the other variables are fixed as Figure A3.1.

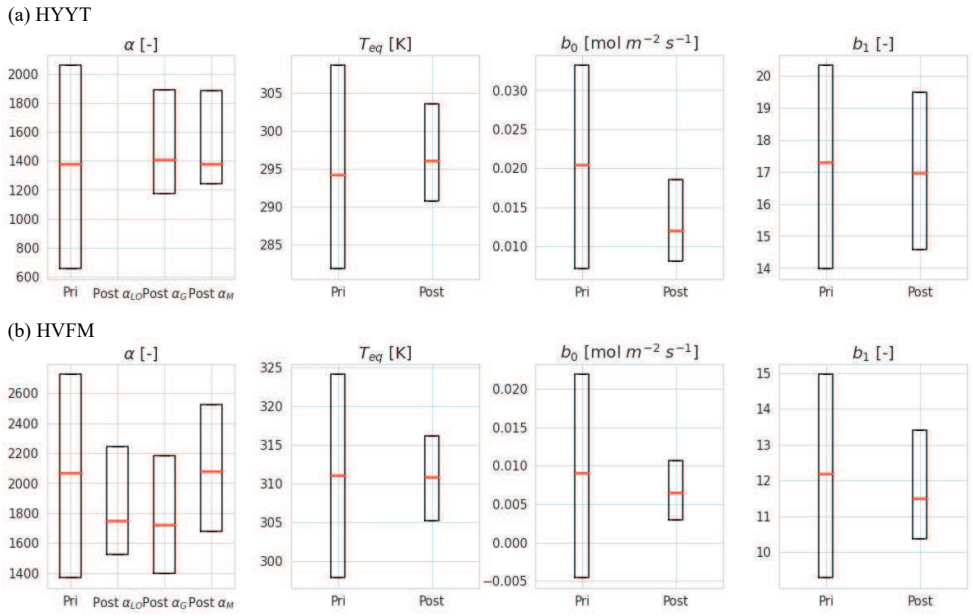


Figure A3.3: Error reduction of state variables in two stations (Hyytiälä (HYYT) and Harvard Forest (HVFM)). The red lines represent median values, and the boxes represent errors. Column 'Pri' shows the initial value and state error. Column 'Post' represents the mean of the optimized state variables and the corresponding standard deviation. α_{LO}, α_{G}, α_{M} indicate α in each phenological stage (leaf-out, growth, and maturity, respectively).

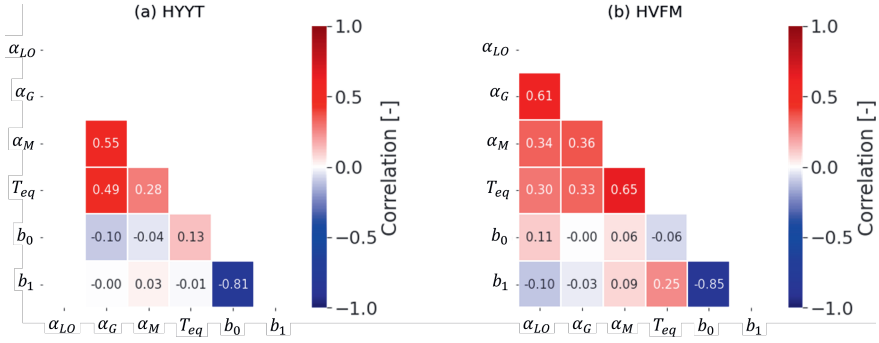


Figure A3.4: Covariance matrix for all state variables at Hyytiälä (HYYT) and Harvard Forest (HVFM)

Chapter 4

Simultaneous optimization of global Carbonyl Sulfide and CO_2 budgets using the coupled inverse modeling framework TM5-4DVAR

We present a coupled CO_2-carbonyl sulfide (COS) inversion system that jointly optimizes global surface fluxes of both gases using the TM5-4DVar framework for the year 2016. By linking Gross Primary Productivity (GPP) and COS vegetation uptake through grid-cell-specific monthly scaling factors, the system leverages observations of both gases to inform one another and provide new insights into their global budgets.

Our results indicate that current land surface models underestimate COS vegetation uptake in the high-latitude Northern Hemisphere (NH). When the prior COS vegetation sink above 40 °N was doubled, the inversion produced better agreement with atmospheric COS and CO_2 observations. This adjustment primarily affected the prior fluxes rather than posterior corrections, resulting in only a moderate increase in the posterior global vegetation uptake from -675 to -763 Gg S yr^{-1}. Most of this increase originated from high-latitude regions (above 40 °N), where posterior uptake changed from -117 to -276 Gg S yr^{-1}, a change that was mostly driven by the prior.

The previously reported missing tropical COS source is attributed to underestimated prior oceanic emissions of carbon disulfide (CS_2) in prior inventories and overestimated vegetation uptake. The inversion increased the posterior global CS_2 oceanic emissions to a range of 173–196 Gg S yr^{-1}, nearly doubling the prior value. This adjustment was accompanied by a reduction of approximately 55 Gg S yr^{-1} in tropical vegetation uptake (25 °S–25 °N), suggesting that overestimated prior biospheric sinks contributed to the previously inferred missing tropical COS source.

Our system also estimates a strong global oceanic CO_2 sink of -3.6 Pg C yr^{-1}, larger than values from the inversions included in the Global Carbon Budget 2024 (GCB2024) for the same period (-2.4 Pg C yr^{-1}). The land sink is weaker (-1.4 Pg C yr^{-1}), than GCB2024 (-2.2 Pg C yr^{-1}). This possibly reflects the omission of diurnal cycles in GPP and COS uptake. Additional possible causes include a strong regularization of Total Ecosystem Respiration (TER).

Cho, A., Luijkx, I., Basu, S., Ma, J., and Krol, M. C. (2026). Simultaneous optimization of global Carbonyl Sulfide and CO_2 budgets using the coupled inverse modeling framework TM5-4DVAR. manuscript in preparation

Although net ecosystem exchange of CO_2 was significantly adjusted, tight prior constraints on TER and the scaling between GPP and COS limited the flexibility of the system to appropriately update COS vegetation fluxes. As a result, the inversion compensated by adjusting the anthropogenic CS_2 emissions, producing negative posterior values of $-23\,\mathrm{Gg\,S\,yr^{-1}}$ north of 40 °N, even when the prior COS vegetation flux was doubled in the region. These findings highlight the need to reassess COS vegetation fluxes and better characterize unknown sources and sinks in the global COS budget. Despite these limitations, our inversion estimates a global COS budget balance of $-104\,\mathrm{Gg\,S\,yr^{-1}}$ from July 2016 to June 2017, consistent with the observed atmospheric decline during this period reported in previous studies. This flux corresponds to a global mean atmospheric decrease of about $-18\,\mathrm{pmol\,mol^{-1}\,yr^{-1}}$, which is slightly larger than, but on the same order of magnitude as, the observed decline of roughly $-5\,\mathrm{pmol\,mol^{-1}\,yr^{-1}}$reported in previous studies.

4.1 Introduction

The CO_2 biosphere flux plays an essential role in accurately predicting long-term climate change (Campbell et al., 2008; Montzka et al., 2007; Berry et al., 2013). Terrestrial ecosystems act as a net sink of atmospheric CO_2, quantified as net ecosystem exchange (NEE), which reflects the balance between gross primary productivity (GPP) and total ecosystem respiration (TER) (Friedlingstein et al., 2025). Global GPP estimates vary significantly, from 112 to 169 $\mathrm{Pg\,C\,yr^{-1}}$ depending on the model or observation-based estimates used, indicating substantial uncertainty (Anav et al., 2015). Since NEE is the small residual between GPP and TER, uncertainties in GPP can disproportionately affect NEE estimates, leading to substantial uncertainty in the global CO_2 budget.

While NEE can be measured using the eddy covariance method (EC) on a local scale, it is not feasible to directly measure GPP separately from TER, as they occur simultaneously. To estimate GPP, researchers have developed indirect methods that partition GPP and respiration from NEE. These approaches employ temperature response curves aligned with nighttime NEE, which represents respiration (Reichstein et al., 2005; Kohonen et al., 2022). However, the difficulty of performing nighttime EC measurements introduces significant uncertainties in this partitioning (Aubinet, 2008).

To address these uncertainties, machine learning has been applied to flux partitioning (Tramontana et al., 2020; Desai et al., 2008). More recently, machine learning upscaling approaches have extended EC-based partitioning from site level to global scale, showing clear improvements in reproducing seasonal variations (Jung et al., 2020). Nevertheless, substantial uncertainties remain regarding tropical GPP fluxes, interannual variability, and long-term trends.

Isotopic flux partitioning presents an alternative and utilizes the unique stable isotopic characteristics of photosynthesis and respiration. However, current knowledge about isotopic signatures and the precision of in-situ isotope measurements is limited when applied to partitioning (Wehr et al., 2015). Extensive research has been conducted on the regression approach using solar-induced fluorescence (SIF) retrieved by satellite (Frankenberg et al., 2011; Frankenberg et al., 2012; Parazoo et al., 2014; Bowman et al., 2017). However, the constraints of satellite remote sensing are highly uncertain in high latitude ecosystems due to weaker vegetation signals to satellite instruments, rapid seasonal transitions, high solar angles, and limited temporal coverage of satellite measurements (Parazoo et al., 2018; Sun et al., 2018c).

Carbonyl sulfide (COS), a trace gas abundant in the atmosphere at about $500 \pm 100\,\mathrm{pmol\,mol^{-1}}$ (Montzka et al., 2007), has been reported as a promising tracer to estimate GPP due to its similar absorption pathways into leaves as CO_2 (Wohlfahrt et al., 2012; Campbell et al., 2017; Lai et al., 2024). Both gases share the same environment within the leaf boundary layers and stomata. Furthermore, COS is believed to be only absorbed and not emitted, as it is rapidly and irreversibly hydrolyzed by the enzyme carbonic anhydrase (CA) in mesophyll cells (Protoschill-Krebs et al., 1996; Sandoval-Soto et al., 2005; Seibt et al., 2010).

Many studies have estimated GPP from leaf uptake of COS by calculating the relative leaf uptake index (LRU), defined as the ratio of the deposition velocity of COS to that of CO_2 during leaf uptake (Asaf et al., 2013; Commane et al., 2015; Kooijmans et al., 2019; Spielmann et al., 2023; Lai et al., 2024). The LRU approach is most effective to estimate GPP when the deposition velocities of COS and CO_2 can be approximated as a simple linear function of environmental and vegetation-specific factors. In practice, however, their uptake responses to environmental conditions—such as light intensity, temperature, and humidity—as well as physiological characteristics including vegetation characteristics and climate zone, differ systematically, making it difficult to represent their relationship with a single functional form. For example, while CO_2 biochemical conductance—defined here as the internal enzymatic capacity of leaves—depends

on photosynthetically active radiation (PAR), that of COS does not, resulting in significantly higher LRU values at low PAR levels (Stimler et al., 2010; Lai et al., 2024). Additionally, increases in temperatures and vapor pressure deficit (VPD) have been shown to increase LRU values (Kooijmans et al., 2019; Cho et al., 2023; Sun et al., 2018a; Cochavi et al., 2021; Wohlfahrt et al., 2018). These sensitivities have been shown to vary depending on plant characteristics (e.g., species) (Berkelhammer et al., 2014; Stimler et al., 2011; Sun et al., 2018b) and climate conditions (Kooijmans et al., 2019; Yang et al., 2018).

Recent studies also challenge the previous assumption of unidirectional COS exchange, suggesting potential COS emissions from both vascular and non-vascular plants (Blezinger et al., 2000; Geng et al., 2004; Goldan et al., 1988; Kuhn et al., 2000; Gimeno et al., 2017). Nevertheless, COS-based approaches have demonstrated strong potential. For example, Lai et al. (2024) estimated global GPP at $157 \pm 8.5\,\mathrm{Pg\,C\,yr^{-1}}$ using a tracer-based inversion constrained by atmospheric COS, achieving substantially lower uncertainty than traditional model- or flux-based methods. This demonstrates how COS-informed approaches can complement CO_2-based estimates and help reduce uncertainty in the global carbon budget.

In this context, the long-term behavior of the atmospheric COS provides an additional constraint on its global budget. Observations indicate that the tropospheric mole fraction of COS remained stable at approximately 500 $\mathrm{pmol\,mol^{-1}}$between 2000 and 2005, with a minimal increase of less than 5% (Montzka et al., 2007; Toon et al., 2018; Kremser et al., 2015). More recently, Serio et al. (2023) analyzed the time series of COS mole fractions observed at NOAA surface stations from 2000 to 2020. They found that COS mole fractions generally increased at all sites until around 2015, with a temporary decline in 2009. However, a decreasing trend was observed from 2016 to 2020, which is consistent with the results of Hannigan et al. (2022).

The observed variations in atmospheric COS are driven by changes in its sources and sinks. COS in the atmosphere is known to be produced primarily in the oceans and by anthropogenic activities such as coal use and viscose-rayon production (Zumkehr et al., 2018). It is predominantly absorbed by plant leaves, while smaller fractions are oxidized by OH or photolyzed in the stratosphere. COS can be absorbed and emitted from soils as well (Watts, 2000; Kettle et al., 2002; Berry et al., 2013). Finally, precursors such as carbon disulfide (CS_2) and dimethyl sulfide (DMS) contribute significantly to indirect COS emissions (Chin et al., 1993; Watts, 2000).

The global distribution of these COS sources and sinks has been quantified using inverse modeling approaches that minimize the discrepancies between the observed and estimated mole fractions (Kettle et al., 2002; Campbell et al., 2008; Berry et al., 2013; Launois et al., 2015b; Lennartz et al., 2017; Ma et al., 2021; Launois et al., 2015a; Remaud et al., 2022; Ma et al., 2024). These studies consistently reported an imbalance in the COS global budget, with missing sources in the tropics and missing sinks at high latitudes in the northern hemisphere (NH) (Berry et al., 2013; Kuai et al., 2015; Lennartz et al., 2017; Lennartz et al., 2019; Ma et al., 2021).

Satellite observations such as the Michelson Interferometer for Passive Atmospheric Sounding (MIPAS) (Glatthor et al., 2017) and the Tropospheric Emissions Spectrometer (TES) (Kuai et al., 2015) have contributed to COS inversion studies by extending spatial coverage, particularly over remote areas not covered by ground-based networks. For example, Stinecipher et al. (2022) used MIPAS data to suggest that the tropical plant sink may be smaller than previously estimated, potentially explaining 25–67% of the missing source. However, the limited temporal coverage of past missions (e.g., MIPAS ended in 2012; TES in 2018), along with the coarse vertical sensitivity and retrieval uncertainties of current instruments (e.g., IASI, ACE-FTS), limits their utility for surface flux estimation and must be carefully considered (Whelan et al., 2018; Cartwright et al., 2025).

Compared to COS, CO_2 has been observed over a longer period with better global coverage. However, many previous studies on CO_2 flux inversions have revealed substantial uncer-

tainties in estimating biospheric and oceanic CO_2 fluxes, leading to a wide range of inversion results (Peylin et al., 2013; Friedlingstein et al., 2025; Woude et al., 2025). These uncertainties are particularly significant in regions with sparse observational networks or limitations in satellite-derived XCO_2 columns, such as the tropics and northern Asia—areas crucial to annual variability in CO_2 growth rates (Peylin et al., 2013). Nevertheless, the joint use of CO_2 and COS in an inverse modeling framework, leveraging their shared leaf uptake pathways, can improve constraints on both biospheric carbon fluxes and the global COS budget by compensating for the limitations of each individual tracer.

Launois et al. (2015b) and Remaud et al. (2022) both implemented inverse approaches that estimated COS biosphere fluxes using the LRU concept, whereby COS vegetation uptake was calculated as a linear function of prescribed GPP and species- or PFT-specific LRU values. Launois et al. (2015b) optimized a global scaling factor on COS vegetation flux derived from GPP, using only COS observations. Recently, Remaud et al. (2022) assimilated both CO_2 and COS data into a coupled inversion system to jointly optimize GPP and other COS components such as oceanic and anthropogenic sources. These approaches rely heavily on assumptions about LRU, for which observational constraints remain limited (Remaud et al., 2022).

In this study, we present results from a new coupled COS-CO_2 inverse modeling framework in Tracer Model version 5 (TM5) (Krol et al., 2005). The primary objective is to develop a coupled inversion system to optimize the global budgets of both CO_2 and COS by jointly adjusting their surface fluxes. The coupling between the two gases is achieved through a monthly scaling factor defined for each model grid cell, which links the GPP to COS vegetation uptake calculated using the Simple Biosphere Model version 4 (SiB4) (Haynes et al., 2019). To assess the limitations of the underlying assumption of a linear GPP–COS relationship, we test alternative COS vegetation flux scenarios and evaluate their impacts on the global budgets of both gases. These coupling analyzes allow us to identify structural improvements needed for future coupled CO_2–COS systems.

To address these objectives, we first describe the surface observational datasets, modeling framework, and optimization strategy used in the coupled inversion (Section 4.2). We then present the inversion results, including evaluation against aircraft observations and optimized flux estimates for both gases (Section 4.3). This is followed by a discussion of the implications of our findings for the global carbon and COS cycles, as well as directions for improving the coupling framework (Section 4.4). Finally, we summarize the main conclusions in Section 4.5.

4.2 Data and methods

To use the coupled optimization approach that will be described in Sect. 4.2.6, in situ observations of CO_2 and COS are assimilated to jointly optimize their coupled surface fluxes. The optimized fluxes are then used in the TM5 chemical transport model to simulate atmospheric model fractions, which are validated against independent in situ and aircraft-based measurements.

This section describes the observational datasets, the TM5 model, the SiB4 land surface model, the 4D-Var optimization framework, the flux scenarios tested, and the statistical evaluation metrics. Although the current analysis focuses on a one-year period (July 2016 to June 2017), the primary objective is to demonstrate the feasibility and utility of the newly developed coupled CO_2–COS inversion system. Future work will extend this framework to multi-year applications.

4.2.1 In-situ observations

CO_2 and COS mole fractions were provided by the Global Monitoring Laboratory (GML) of the National Oceanic and Atmospheric Administration Earth System Research Laboratory-Global Monitoring Division flask program (NOAA/ESRL-GMD). This dataset comprises observations by multiple laboratories from 172 stations for CO_2 (ObsPack Globalviewplus version 6.1), including both surface flask and tower in-situ observations (Schuldt et al., 2021), and 14 COS stations across the globe (Montzka et al., 2007). Fig. 4.1 shows the spatial distribution of CO_2 and COS observation sites. Although the CO_2 stations are globally distributed, the COS observation sites are mainly located in North America. The figure also includes aircraft observation trajectories from the Atmospheric Tomography (ATom) campaign, which are described in the following section.

COS measurements were conducted at weekly or biweekly intervals with an average measurement error reported as approximately 8 $\mathrm{pmol\,mol^{-1}}$ (Montzka et al., 2007). We applied the observational error settings from Ma et al. (2021) for these stations. In contrast, CO_2 mole fractions were measured more frequently, either continuously or from flask samples, typically at a weekly resolution. We have utilized the observational error for CO_2 reported in the ObsPack dataset.

Since we want to avoid COS observations that may be affected by sub-grid-scale or local flux anomalies near the observation site, we apply a strict filter to remove outliers. This filtering step was not applied to the CO_2 data, which generally have lower observational uncertainty. Using Python's Scipy library, a median filter was applied to identify anomalous values by evaluating each data point along with the four preceding and four following observations. Data points that deviated by more than 1.2 standard deviations (σ) from the local median over the study period were considered outliers and excluded. The 1.2 σ threshold was chosen to balance strict filtering (e.g., 1σ, which may discard valid signals) and lenient filtering (e.g., 2σ, which may allow problematic outliers to remain). After applying the filter, 179 data points were removed from all stations, leaving a total of $7,835$ NOAA COS observations available for assimilation in the flux optimization.

4.2.2 Aircraft observations

To validate the results, mole fractions CO_2 and COS were simulated using optimized surface fluxes. We compared the simulated vertical mole fraction profiles of CO_2 and COS with the mole fractions observed from the Atom (2016–2018) aircraft campaign (Wofsy et al., 2018). This campaign measured trace gases including COS and CO_2 at various altitudes in remote marine locations over the Pacific and Atlantic Oceans. For this study, we specifically used data from the ATom-1 (July–August 2016) and ATom-2 campaigns (January–February 2017) that matched our analysis period.

Fig. 4.1 shows the observational trajectories of ATom-1 and ATom-2. Considering regional differences in emissions and the spatio-temporal distribution of mole fractions for COS and CO_2, we divided the study area into four regions to validate spatially distinct mole fractions of CO_2 and COS using ATom observations: North Pacific Ocean (R1), North Atlantic Ocean (R2), South Pacific Ocean (R3), South Atlantic Ocean (R4).

4.2.3 Forward simulation of CO_2 and COS atmospheric mole fraction

We simulated atmospheric CO_2 and COS mole fractions using the chemical transport model TM5 (Krol et al., 2005), operated at a horizontal resolution of $3^\circ \times 2^\circ$ with 34 vertical levels and

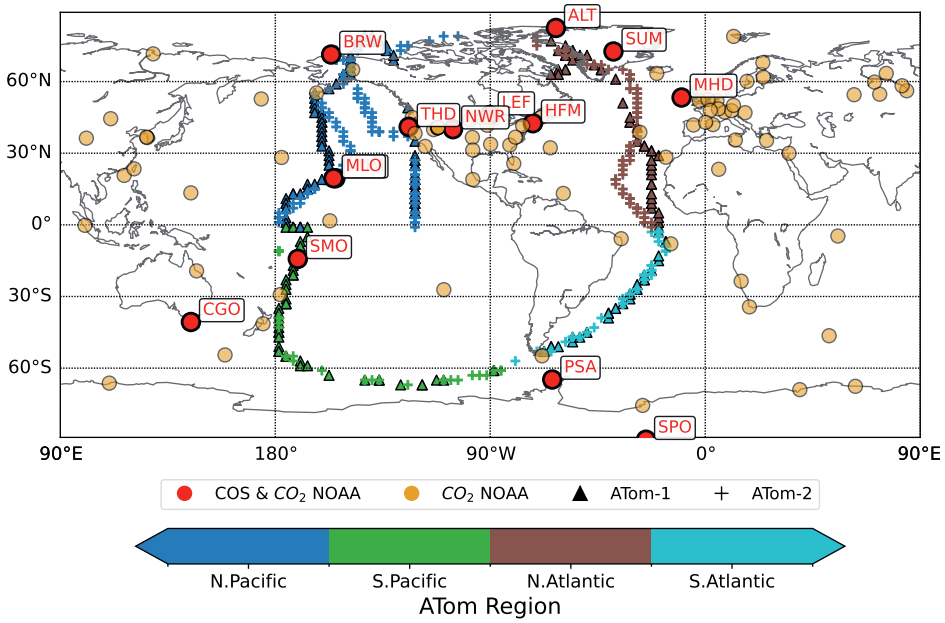


Figure 4.1: Surface-based measurement locations and flight trajectories used in this study. CO_2 surface observations are taken from the ObsPack GlobalviewPlus v6.1 product, while COS observations are provided by NOAA surface monitoring sites. COS cites overlap with ObsPack locations where both CO_2 and COS are observed. Red dots represent stations measuring both CO_2 and COS, while orange dots denote stations that do not measure COS, but measure CO_2 and other trace gases. Flight trajectories correspond to the ATom-1 and ATom-2 campaigns, which are divided into four regions as shown by different colors. Surface-based observations were used for flux optimization, whereas ATom-1 and ATom-2 measurements were used for independent evaluation. Stations with distinct geographic characteristics include ALT, SUM, and BRW in the Arctic; MLO at an altitude of 3397 m in Hawaii; SMO in the central South Pacific; and SPO and PSA in Antarctica. The remaining stations are located in inland, near-surface environments.

driven by ERA5 meteorology (Hersbach et al., 2020). The simulation was initialized in September 2014 using the background mole fractions of 400 $\mu\mathrm{mol\,mol}^{-1}$ for CO_2 and 500 $\mathrm{pmol\,mol}^{-1}$ for COS. Our main analysis focuses on July 2016 to June 2017. A six-month spin-down was applied after the analysis period.

We summarize the underlying prior surface fluxes dataset for both gases in Table 4.1. This table lists the surface fluxes inventories, model products, and references used for each source and sink category. For CO_2, the global budget represents the aggregated net surface fluxes, consistent with the CarbonTracker Europe setup (Van Der Laan-Luijkx et al., 2017), which is one of the ensemble members in the Global Carbon Budget 2024 (GCB2024) inversions (Friedlingstein et al., 2025). Prior flux components include contributions from fossil fuel emissions ($F_{\mathrm{CO_2,ff}}$), biosphere exchange ($F_{\mathrm{CO_2,NEE}}$), ocean exchange ($F_{\mathrm{CO_2,oc}}$), and fire emissions ($F_{\mathrm{CO_2,fr}}$).

For COS, prior fluxes followed the setup of Ma et al. (2021). These include (i) surface fluxes from anthropogenic ($F_{\mathrm{COS,ff}}$), biomass burning ($F_{\mathrm{COS,bb}}$), vegetation ($F_{\mathrm{COS,bio}}$), soil ($F_{\mathrm{COS,soil}}$), and ocean sources and sinks ($F_{\mathrm{COS,oc}}$), (ii) chemical production from oxidation of precursors

(CS_2 and DMS), and (iii) atmospheric removal processes such as OH oxidation and photolysis. Unlike CO_2, which is chemically inert, COS undergoes significant chemical production and removal throughout the three-dimensional atmosphere. These processes are explicitly represented in TM5 following Ma et al. (2021). CS_2 originates mainly from anthropogenic and oceanic emissions, whereas DMS is produced from both terrestrial and oceanic sources.

Table 4.1: Summary of prior surface flux datasets for CO_2 and COS used in this study. Precursors for COS (CS_2 and DMS) are also listed as they are used in the COS flux modeling. Symbols correspond to the flux terms used in the text.

Gas	Source/Sink (symbol)	Dataset (Reference)
CO_2	Fossil fuel ($F_{CO_2,ff}$)	GridFED v2023 (EDGAR-based) (Jones et al., 2021)
	Biosphere ($F_{CO_2,NEE}$)	SiB4 land surface model (Haynes et al., 2019)
	Ocean ($F_{CO_2,oc}$)	CarboScope v2022 (Rödenbeck et al., 2013)
	Fire ($F_{CO_2,fr}$)	GFAS (Copernicus CAMS) (Di Giuseppe et al., 2018)
COS	Anthropogenic ($F_{COS,ff}$)	Global gridded inventories (Campbell et al., 2015; Zumkehr et al., 2018)
	Biomass burning ($F_{COS,bb}$)	GFED v4.1 (Randerson et al., 2017), updated emission factor (Andreae, 2019), CEDS biofuel (Hoesly et al., 2018)
	Vegetation uptake ($F_{COS,veg}$)	SiB4 model (Berry et al., 2013; Haynes et al., 2019)
	Soil uptake ($F_{COS,soil}$)	SiB4 model (Ogée et al., 2016; Kooijmans et al., 2021)
	Ocean ($F_{COS,oc}$)	Ma et al. (2021) based on climatology (Kettle et al., 2002; Suntharalingam et al., 2008)
CS_2	Anthropogenic ($F_{CS2,ff}$)	Global gridded inventory (Zumkehr et al., 2018)
	Ocean ($F_{CS2,oc}$)	Ma et al. (2021) based on climatology (Kettle et al., 2002; Suntharalingam et al., 2008)
DMS	Land ($F_{DMS,ld}$)	Global gridded inventory (Zumkehr et al., 2018)
	Ocean ($F_{DMS,oc}$)	Ma et al. (2021) based on climatology (Kettle et al., 2002; Suntharalingam et al., 2008)

4.2.4 Land surface model

We utilized the land surface model SiB4 version 4.2 (Berry et al., 2013; Haynes et al., 2019) to estimate prior surface fluxes for GPP, TER, and COS vegetation and soil fluxes. The SiB4 model, as a successor of the original SiB model (Sellers et al., 1986), integrates complex interactions among vegetation, the atmosphere, and soil, enhancing the accuracy and realism of spatio-temporal calculations for COS and CO_2 biosphere fluxes across 15 plant functional types. The model was configured with a temporal resolution of 10 minutes and a spatial resolution of 0.5 degrees. For more detailed information on the SiB4 model, see Haynes et al. (2019).

We spun up the SiB4 model 10 times for 10 years, from 2000 to 2010 to initiate the carbon pools. With the data from the spin-up, we ran the SiB4 model from 2010 to 2020, including our analysis period. This simulation was implemented with the meteorological data by Modern-Era Retrospective Analysis for Research and Application, version 2 (MERRA-2) (Gelaro et al., 2017).

All simulations were conducted under a constant ambient CO_2 mole fraction of 370 $\mu\mathrm{mol\,mol}^{-1}$, representative of the conditions of the early 2000s. This fixed value was applied throughout spin-up and analysis periods to ensure model consistency. Consequently, year-to-year increases in atmospheric CO_2 were not taken into account, which can lead to an underestimate of photosynthesis due to the omitted CO_2 fertilization effects. These implications are further discussed in Sect. 4.4.3 in the context of our inversion results.

In contrast, for COS, we prescribed monthly varying mole fractions, calculated as monthly gridded averages over 2016–2018 using the TM5 chemical transport model (Kooijmans et al., 2021), to better capture its spatial and temporal variability.

In this study, we do not provide a detailed description of the estimation of CO_2 and COS vegetation uptake calculated in SiB4, as this is thoroughly documented in Haynes et al. (2019). For the COS vegetation flux, SiB4 uses a module originally developed by Berry et al. (2013). Here, we focus on evaluating the established temperature function for COS internal conductance ($g_{i,\mathrm{org}}$) and comparing it with a newly proposed temperature function ($g_{i,\mathrm{new}}$) introduced by Cho et al. (2023) as described below.

Calculating $g_{i,\mathrm{org}}$ involves estimating the maximum catalyzation velocity of the CA enzyme through a linear relationship with that of Ribulose-1,5-bisphosphate carboxylase/oxygenase (RuBisCo) (V_{max} ($\mathrm{mol\,m^{-2}\,s^{-1}}$)), employing a calibration factor α. The original calculation of $g_{i,\mathrm{org}}$ at the canopy temperature (T_{can} (K)) (Berry et al., 2013) is given as:

$$g_{i,\mathrm{org}}(T_{\mathrm{can}}) = \alpha\, V_{\mathrm{max}}\, Q_{10}^{0.1\,(T_{\mathrm{can}}-T_{\mathrm{ref}})} \tag{4.1}$$

This approach employs the Q_{10} (-) scaling to the reference temperature ($T_{ref} = 298$ K), which increases exponentially with a factor of Q_{10} calculated for the RuBisCo activity (Q_{10} = 2.1) as described in the SiB4 model (Berry et al., 2013; Haynes et al., 2019).

To estimate $g_{i,\mathrm{new}}$, the computation of the COS mesophyll conductance is based on an Arrhenius-type equation with Michaelis-Menten kinetics (Peterson et al., 2007; Daniel et al., 2010). The parameters associated with this method were optimized by Cho et al. (2023), using observations collected at two stations in Hyytiälä, Finland (Kooijmans et al., 2017; Kohonen et al., 2020; Vesala et al., 2022), and Harvard Forest, USA (Commane et al., 2015; Commane et al., 2021):

$$g_{i,\mathrm{new}}(T_{\mathrm{can}}) = \alpha V_{\mathrm{max}} A_T \cdot \frac{T_{\mathrm{can}} \exp\left(\frac{\Delta H_a}{R T_{\mathrm{can}}}\right)}{1 + \exp\left[-\frac{\Delta H_{\mathrm{eq}}}{R}\left(\frac{1}{T_{\mathrm{can}}} - \frac{1}{T_{\mathrm{eq}}}\right)\right]} \tag{4.2}$$

The variables ΔH_a ($\mathrm{J\,mol^{-1}}$), ΔH_{eq} ($\mathrm{J\,mol^{-1}}$), and T_{eq} (K) represent the enzyme kinetic parameters, and we adopted values of 40 $\mathrm{kJ\,mol^{-1}}$, 100 $\mathrm{kJ\,mol^{-1}}$, and 295 K, respectively (Cho et al., 2023). The normalization factor A_T ensures that the temperature function attains a value of 1 at T_{can} equal to T_{eq}. The universal gas constant is denoted as R ($8.3145\,\mathrm{J\,K^{-1}\,mol^{-1}}$). We evaluate both approaches by using the calculated COS vegetation fluxes as prior in two different optimizations (Sect. 4.2.7).

Lastly, we simulated the COS soil flux using a module developed by Ogée et al. (2016) and implemented in SiB4 by Kooijmans et al. (2021).

4.2.5 Coupling of CO_2 and COS

To establish a coupling between CO_2 and COS in our optimization, we introduced a dimensionless scaling factor ($s(i,j,m)$) that linearly links GPP with the COS vegetation flux, both calculated by the SiB4 model as prior estimates ($GPP_{SiB4}(i,j,m)$, $F_{COS,bio,SiB4}(i,j,m)$). Here, i and j denote the horizontal grid indices, and m denotes the month. In contrast to GPP, which is held fixed and only enters the system through this scaling, TER is treated as an independent optimization variable. This coupling yields $F_{CO_2,NEE}(i,j,m)$ ($\mu\mathrm{mol\,m^{-2}\,s^{-1}}$) and $F_{COS,veg}(i,j,m)$ ($\mathrm{pmol\,m^{-2}\,s^{-1}}$) at a grid cell and month as follows:

$$F_{\mathrm{CO_2,NEE}}(i,j,m) = s(i,j,m)\,GPP_{\mathrm{SiB4}}(i,j,m) + TER(i,j,m), \tag{4.3}$$

$$F_{\mathrm{COS,veg}}(i,j,m) = s(i,j,m)\,F_{\mathrm{COS,veg,SiB4}}(i,j,m). \tag{4.4}$$

The scaling factor $s(i,j,m)$ was initialized to 1 for all grid cells and months, which was subsequently adjusted by the 4D-Var system along with other states (surface fluxes in the CO_2 and COS budgets) (see Sect. 4.2.6). These two biosphere fluxes were then applied to the calculations of CO_2 and COS global budgets.

4.2.6 Inverse model

We optimized the sources and sinks of CO_2 and COS by employing the TM5 4D-Var system, an offline global inverse framework (Krol et al., 2005; Krol et al., 2008; Meirink et al., 2008; Bergamaschi et al., 2010). This system refines fluxes by minimizing a cost function, which consists of the deviation of prior optimization states from the prior and deviations from observed and simulated CO_2 and COS mole fractions. The total cost J_{Tot} with state $\mathbf{x}$ consists of the background cost (J_{bg}), the CO_2 cost (J_{CO_2}), and the COS cost (J_{COS}). These costs are based on Bayes' theorem (Tarantola et al., 1982; Brasseur et al., 2017):

$$\begin{aligned} J_{\mathrm{Tot}}(\mathbf{x}) &= J_{\mathrm{bg}} + w_{\mathrm{CO_2}}\,J_{\mathrm{CO_2}} + w_{\mathrm{COS}}\,J_{\mathrm{COS}} \\ &= (\mathbf{x}-\mathbf{x_a})^{\top}\,\mathbf{B}^{-1}\,(\mathbf{x}-\mathbf{x_a}) \\ &\quad + w_{\mathrm{CO_2}}\,(\mathbf{H}(\mathbf{x})-\mathbf{y}_{\mathrm{CO_2}})^{\top}\,\mathbf{R}_{\mathrm{CO_2}}^{-1}\,(\mathbf{H}(\mathbf{x})-\mathbf{y}_{\mathrm{CO_2}}) \\ &\quad + w_{\mathrm{COS}}\,(\mathbf{H}(\mathbf{x})-\mathbf{y}_{\mathrm{COS}})^{\top}\,\mathbf{R}_{\mathrm{COS}}^{-1}\,(\mathbf{H}(\mathbf{x})-\mathbf{y}_{\mathrm{COS}}). \end{aligned} \tag{4.5}$$

Here, $\mathbf{x_a}$ represents the prior state vector, and $\mathbf{B}$ denotes the covariance matrix associated with the state vector. $\mathbf{H}(\mathbf{x})$ represents the estimated atmospheric mole fractions, and $\mathbf{y}_{\mathrm{gas}}$ represents the observed mole fractions of CO_2 ($\mu\mathrm{mol\,mol^{-1}}$) and COS ($\mathrm{pmol\,mol^{-1}}$). The observational error covariance matrices, $\mathbf{R_{CO2}}$ and $\mathbf{R_{COS}}$, are each assumed to be diagonal. $\mathbf{R_{CO2}}$ includes measurement and representation errors, while $\mathbf{R_{COS}}$ includes measurement error,

flux-related error, and representation error. Their values vary by observation site. The flux-related error represents the additional uncertainty in observed mole fractions that arises from uncertainties in large surface fluxes, particularly under boundary layer conditions where such fluxes strongly influence near-surface concentrations (Bergamaschi et al., 2010). For COS, we followed the implementation of Ma et al. (2021), as the dominance of large fluxes makes it important to include this component in the observational error covariance.

The background covariance matrix $\mathbf{B}$ reflects the uncertainty in prior surface fluxes and their spatial and temporal correlations. Table 4.2 presents the background error and correlation length for each surface flux of CO_2 and COS. Given that fire and anthropogenic emissions in the CO_2 budget are relatively well constrained, we optimize only the more uncertain oceanic and vegetation fluxes.

Initially, we set a background error of 50% for the CO_2 ocean flux and specified the spatial-temporal correlation length as 3 months and 2000 km. The spatial and temporal correlations are modeled using an exponential decay function (e.g., Chevallier et al., 2012).

To constrain TER within realistic bounds, we prescribed a relatively small prior uncertainty of 5% at the grid scale. While this value is not derived directly from uncertainty propagation, it is broadly consistent with the global-scale estimate by (Tagesson et al., 2024), who reported a mean annual TER of 105.6 ± 2.3 Pg C yr^{-1} for the period 1982–2015, corresponding to approximately 2% global uncertainty. However, spatial and temporal variability at finer scales may be larger, justifying a conservative grid-level error setting in the inversion. For the field s, we used a larger grid-scale error of 10%. This accounts for uncertainties in the biosphere model modules used to compute GPP and COS vegetation uptake, as well as the incomplete understanding and potential biases in the assumed linear relationship between COS uptake and photosynthetic CO_2 assimilation in terrestrial ecosystems. Both s and TER were assigned temporal and spatial correlation lengths of 4 months and 2000 km.

For COS, indirect emissions from DMS, which have relatively minor contributions and significant uncertainty, were excluded from the optimization. The soil COS flux, which is calculated by the SiB4 model and operates on vegetated land grid cells, was also excluded from the optimization to reduce the degree of freedom and to avoid aliasing with the COS vegetation flux. All other COS fluxes were assigned a background error of 50% on the grid level, and the correlation lengths for all emissions were set to 12 months and 4000 km according to Ma et al. (2021).

Table 4.2: Background errors and temporal and spatial correlation lengths for the optimizing surface fluxes of CO_2 and COS.

Trace gas	Surface flux	Background error (%)	Correlation length	
			Temporal (month)	Spatial (km)
CO_2 and COS	Scaling factor	10	4	2000
CO_2	TER	5	4	2000
	Oceanic	50	3	2000
COS	Direct anthropogenic	50	12	4000
	Indirect anthropogenic CS_2	50	12	4000
	Direct oceanic	50	12	4000
	Indirect oceanic CS_2	50	12	4000
	Biomass burning	50	12	4000

Our 4D-Var system uses the M1QN3 algorithm (Gilbert et al., 1989) to optimize CO_2 and

COS surface fluxes through a maximum of 200 iterations and until the gradient norm reduction reaches a factor of 1000. Although the inverse problem is formally linear, M1QN3 is employed because it provides a robust and numerically stable minimization method for the coupled optimization. All prior fluxes were optimized with a monthly time scale, and no diurnal cycle in the emissions was considered.

Technically, TM5 forward simulations use $F_{\mathrm{CO2,NEE}}$ and $F_{\mathrm{COS,bio}}$ as input. To optimize the scale factor s and TER, the derivatives of the cost function with respect to s and TER are obtained as:

$$\begin{aligned}\frac{\delta J}{\delta s} &= \frac{\delta J}{\delta F_{\mathrm{CO_2,NEE}}}\frac{\delta F_{\mathrm{CO_2,NEE}}}{\delta s} + \frac{\delta J}{\delta F_{\mathrm{COS,bio}}}\frac{\delta F_{\mathrm{COS,bio}}}{\delta s} \\ &= \mathrm{GPP_{SiB4}}\frac{\delta J}{\delta F_{\mathrm{CO_2,NEE}}} + F_{\mathrm{COS,bio,SiB4}}\frac{\delta J}{\delta F_{\mathrm{COS,bio}}}.\end{aligned} \tag{4.6}$$

$$\frac{\delta J}{\delta TER} = \frac{\delta J}{\delta F_{\mathrm{CO_2,NEE}}} \cdot \frac{\delta F_{\mathrm{CO_2,NEE}}}{\delta TER} = \frac{\delta J}{\delta F_{\mathrm{CO_2,NEE}}}, \tag{4.7}$$

where $\frac{\delta J}{\delta F_{CO2,NEE}}$ and $\frac{\delta J}{\delta F_{COS,bio}}$ are obtained from an adjoint run of TM5-4DVar.

The number of CO_2 observations is significantly larger than that of COS observations. To balance their contributions in the cost function (Eq. 4.5), weights were applied to the cost functions of CO_2 and COS (w_{CO2} and w_{COS}). We fixed w_{COS} at 1 and tested three values of w_{CO2} (0.2, 0.5, and 1.0) to evaluate their impact on convergence. Based on these tests, we selected $w_{CO2} = 0.2$ as the baseline setting, since larger values (e.g., 0.5 or 1.0) failed to achieve the target gradient reduction of 1000 within the maximum of 200 iterations. Consequently, the results presented in this study are based on $w_{CO2} = 0.2$.

4.2.7 Optimization scenarios

To evaluate the impact of prior COS vegetation fluxes on the coupled inversion system and to examine the potential role of unknown vegetation sinks in the COS budget, we designed three optimization scenarios with varying prior COS vegetation fluxes. We then compared the resulting inversion outcomes across these scenarios.

The first scenario (S1) utilizes the COS vegetation flux calculated using the formulation of the existing internal conductance in mesophyll cells ($g_{i,\mathrm{org}}$) in SiB4. The second scenario (S2) employs the new internal conductance formulation, $g_{i,\mathrm{new}}$, previously described in Sect. 4.2.4. By comparing the inversion results of S1 and S2, we evaluate the potential improvement caused by the use of $g_{i,\mathrm{new}}$.

As will be shown in the result section (Sect. 4.3.4.2), the optimized COS surface fluxes from S1 and S2 exhibit nonphysical negative values for several source fluxes at high latitudes in the NH, likely indicating a significant underestimation of the prior sink in these regions. This suggests that the prior COS vegetation uptake at high latitudes in the NH is too low in both S1 and S2. To investigate this further, we introduced a third scenario (S3) in which the COS vegetation flux above 40 °N was arbitrarily doubled relative to S2. Inversions were performed for each scenario, and the optimized surface fluxes were evaluated by comparing the resulting mole fractions with assimilated and non-assimilated observations.

4.2.8 Statistical indices

We evaluated the inversion by comparing changes in the cost reduction between prior and posterior results using the statistical metric χ^2. The χ^2 is calculated by dividing the partial cost function by the number of observations or state variables (Tarantola, 2005).

$$\chi^2 = \frac{1}{N} \sum_{i=1}^{N} \frac{(k_i - k_{true,i})^2}{\sigma_i^2} \tag{4.8}$$

Here, N represents the total number of data points, which could include both the number of observations and the number of state variables. σ_i denotes the error associated with each data point, reflecting the expected error in the state or observations. k_i represents the evaluation variable values derived either from observations or state estimates, and $k_{true,i}$ refers to the true or reference values for these variables (i.e., the atmospheric observations or the prior state). A χ^2 value close to 1 indicates a good fit to observations, whereas values significantly higher or lower than 1 indicate a poor model fit or overfitting, respectively.

4.3 Results

4.3.1 Convergence results

Table 4.3 presents the prior and posterior values of the cost functions (Eq. 4.5) for the three optimization scenarios. The posterior χ^2 values are also shown in the table and will be discussed in Sect. 4.3.2. Note that the prior J_{COS} is larger than the prior J_{CO2} due to the low weight assigned to CO_2 ($w_{CO2} = 0.2$).

All three scenarios show successful optimization, with the total cost significantly reduced from 26,154 to 7,112 for S1, 22,559 to 6,937 for S2, and 21,792 to 6,412 for S3. Among the three, S3 yields the lowest posterior costs, indicating the best overall performance, followed by S2 and S1 in order of increasing total cost. Consistent with the posterior results, the prior J_{COS} is also lowest in S3, followed by S2 and S1. This implies that using $g_{i,\text{new}}$ instead of $g_{i,\text{org}}$ and applying the doubled COS vegetation flux in high northern latitudes improves the accuracy of the prior COS simulation. Moreover, since all three scenarios exhibit substantial reductions in cost compared to their priors, the optimization process itself can be considered effective across all cases.

Table 4.3: Prior and posterior costs from three scenarios for background term (J_{bg}), observational terms of CO_2 (J_{CO2}) and COS (J_{COS}), and total cost (J_{Tot}) with posterior χ^2 results for CO_2 and COS. Note that the prior J_{bg} is by default zero. S1 assumes a linear GPP–COS relationship (Berry et al., 2013), S2 includes a temperature-dependent formulation of COS internal conductance (Cho et al., 2023), and S3 is identical to S2 but with doubled vegetation COS uptake north of 40 °N.

Scenario	J_{bg}	J_{CO2}		J_{COS}		J_{Tot}		χ^2_{Poste}	
	Poste	Prior	Poste	Prior	Poste	Prior	Poste	CO_2	COS
S1	467	5,780	3,989	20,374	2,655	26,154	7,112	1.40	4.42
S2	431	5,780	3,976	16,779	2,528	22,559	6,937	1.40	4.34
S3	389	5,780	3,895	16,011	2,127	21,792	6,412	1.38	4.14

Fig. 4.2 shows the changes in total cost and gradient norm reduction as the iterations progress for the three optimization scenarios. In all scenarios, the cost decreases significantly, with a particularly steep drop during the first 20 iterations. The gradient norm reduction also consistently increases, with all scenarios eventually reaching the optimization threshold of 1000.

Scenario S3, which applies a doubled COS vegetation flux at high latitudes, converges in 116 iterations, while S1 and S2 require 141 and 149, respectively. The fact that S3 converges with the fewest iterations further supports the earlier cost function analysis (Table 4.3), where S3 shows

the lowest prior and posterior costs among the three scenarios. Together, these findings suggest that enhancing COS vegetation uptake in the Northern Hemisphere improves consistency with atmospheric constraints, thereby facilitating a more efficient optimization.

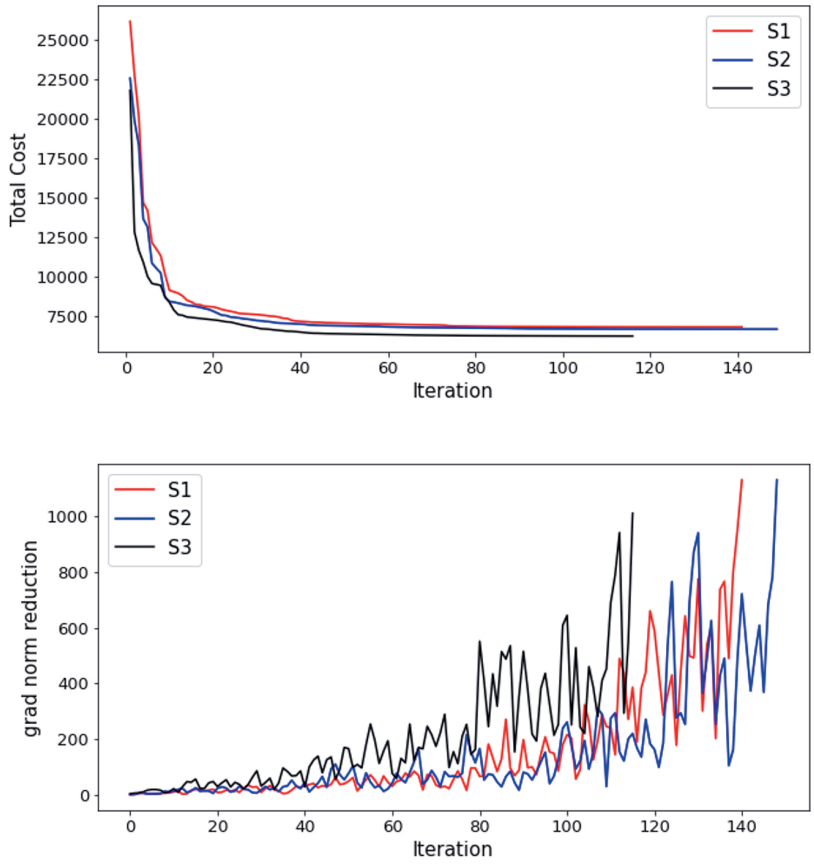


Figure 4.2: Changes in total cost reductions and gradient norm reduction (-) with increasing number of iterations for different scenarios. S1: linear GPP–COS vegetation flux relationship; S2: temperature-dependent internal conductance specific to COS; S3: same as S2 but with doubled vegetation uptake north of 40 °N.

4.3.2 Evaluation with surface-based observations

We assess the consistency between the posterior mole fractions simulated for each optimization scenario and the surface observations of COS and CO_2, which were assimilated during the optimization. This consistency is quantified using the χ^2 metric. The total prior chi-squared values (χ^2_{prior}) of CO_2 and COS are 3.1 and 40.1, respectively. The posterior chi-squared values (χ^2_{poste}) for CO_2 and COS are reduced significantly to 1.38–1.40 and 4.14–4.42, respectively, as

presented in Table 4.3.

All scenarios show that the χ^2_{poste} of the CO_2 values are reduced from χ^2_{prior} and close to 1, indicating that 4D-Var optimization improves CO_2 simulations. S3 shows the largest reduction to 1.38, while S1 and S2 both have slightly higher values. This similarity in χ^2_{poste} indicates that the COS vegetation flux does not significantly affect the CO_2 optimization. While S3 shows the lowest value (1.38), the differences among the scenarios are small, suggesting that the impact of COS vegetation flux variation on CO_2 optimization is limited.

For COS, the χ^2_{poste} values are significantly reduced from their prior values, demonstrating the effectiveness of the optimization. These values (4.14–4.42) fall within the range reported by Ma et al. (2021) for single-species inversions (1.9–4.9), despite our system jointly optimizing both CO_2 and COS. The slightly higher posterior values from this study may reflect the challenges of simultaneously constraining two species with shared but uncertain biospheric fluxes. Nonetheless, having achieved comparable performance to single-species inversions highlights the robustness of our coupled framework.

Fig. 4.3 shows the spatial distribution of χ^2_{prior} and χ^2_{poste} values for COS and CO_2 at surface stations. Results are shown for the scenario S3 only, as it achieved the lowest posterior cost and total χ^2_{poste} value among the three scenarios. For COS, χ^2_{prior} values in all sites range from 5.8 to 138, while χ^2_{poste} values significantly decrease to a range of 2.4 to 18.5. The reductions of the χ^2 values before and after optimization are larger below 30 °N, because the χ^2_{prior} values are relatively larger in this region. CO_2 shows considerable improvements as well, particularly in the high-latitude SH, where χ^2_{prior} values greater than 10 are reduced to less than 2.

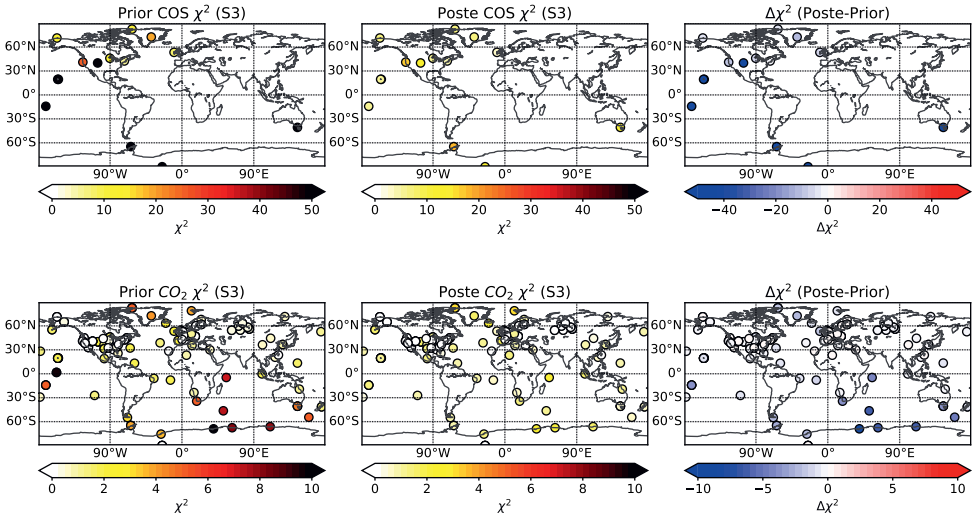


Figure 4.3: Spatial distribution of prior and posterior χ^2 values compared between surface observations and estimates from S3, including their differences (posterior minus prior) for COS (upper panels) and CO_2 (lower panels) mole fractions.

Fig. 4.4 shows the χ^2_{poste} values for COS and CO_2 at the surface stations where both species are measured, arranged from south (left) to north (right). For COS, relatively lower χ^2_{poste} values are observed at low to mid-latitude stations (from SMO to MHD) compared to those at higher latitudes, except for the NWR station. For scenario S2, which used $g_{i,\mathrm{new}}$, most stations

in the NH show slightly lower χ^2 than S1. Scenario S3, which doubled the COS vegetation flux above 40 °N, shows more distinct enhancements at HFM, BRW, and SUM, located in northeastern North America. In other regions, the differences between scenarios are not significant. At NWR (3,523 m above sea level), χ^2_{poste} is slightly higher in S3 compared to S1 and S2, suggesting that an increase in COS vegetation flux is not beneficial in that area. This implies a need for adjustments in COS vegetation flux, especially considering specific geographical characteristics such as altitude. In the SH, all scenarios show similar results because of a less significant impact of the COS vegetation flux on this region.

For CO_2, χ^2_{poste} values at most stations are below 2.5. However, CGO and THD show χ^2 values close to zero, indicating potential overfitting, while most locations demonstrate values χ^2_{poste} in the range of 1.0 to 2.0, suggesting a good fit to the observations. χ^2_{poste} values for CO_2 are similar in all scenarios.

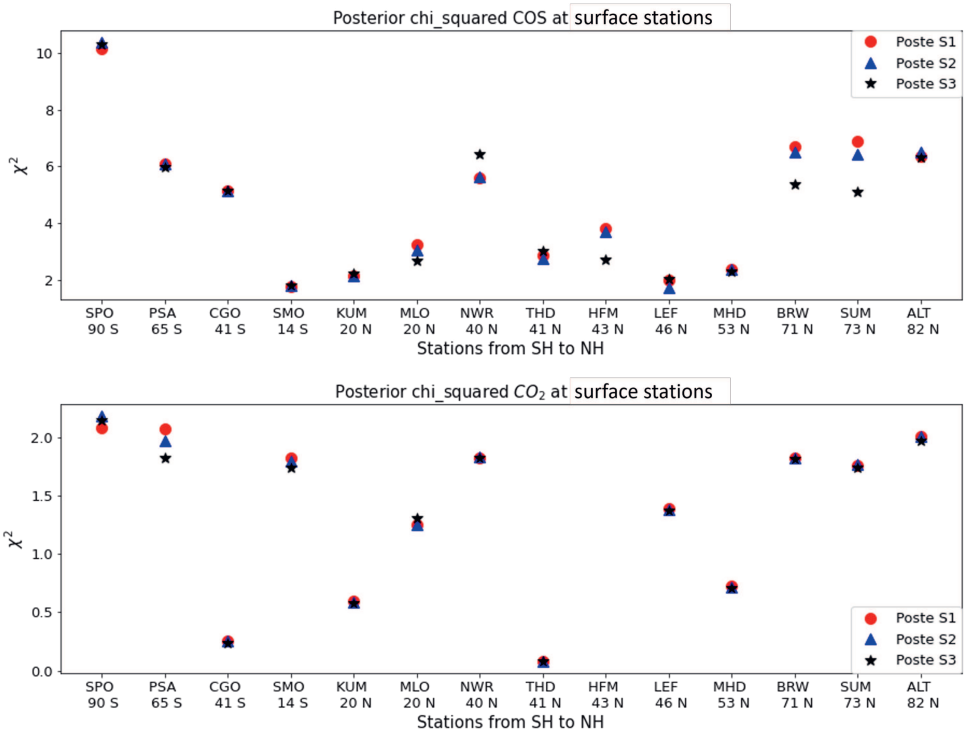


Figure 4.4: Posterior χ^2 values of COS (upper panel) and CO_2 (lower panel) at surface stations from south (left) to north (right) on the horizontal axis, for the three scenarios. S1: linear GPP–COS vegetation flux relationship; S2: temperature-dependent internal conductance specific to COS; S3: same as S2 but with doubled vegetation uptake north of 40 °N.

Fig. 4.5 compares the observed and modeled seasonal variations in COS mole fractions, using prior (S1) and posterior fluxes (from S1 to S3), to evaluate how well each model scenario reproduces the observed seasonal patterns at surface sites. The selected sites are those where both CO_2 and COS are measured simultaneously. To facilitate a clearer comparison with the dense observation time series, both model outputs and observations are averaged to 8-day

means. In general, the COS mole fractions show their lowest mole fractions between September and October, and highest values in May. This seasonal pattern is mainly driven by vegetation uptake, which steadily removes COS from the atmosphere during the growing season (Campbell et al., 2008). The late-summer minimum reflects cumulative biosphere absorption, while the spring maximum results from winter accumulation of emissions combined with limited uptake.

The prior model generally overestimates COS mole fractions except for the period from March to May. All posterior results capture the seasonal variations more accurately, and the observed values are within the error range at all stations. However, the optimized model results fail to fully explain the minimum COS mole fractions that occur around October at the ALT, SUM, THD, MLO, KUM, and PSA stations. These stations are mostly located in coastal regions, where the observations mainly reflect land biosphere uptake, whereas the model grid cells are influenced by nearby oceanic fluxes and transport processes. As a result, the simulated mole fractions tend to be higher during this period (Riley et al., 2005; Ma et al., 2021). Our 4D-Var system has limited capability to represent such local flux contrasts.

Fig. 4.6 presents the seasonal variations of CO_2 mole fractions from prior S1 and all posterior scenarios at the same stations shown in Fig. 4.5. Typically, CO_2 mole fractions reach their lowest values in July and August and remain at higher levels from January to May, showing seasonal patterns that differ in timing from those observed for COS. These differences arise because CO_2 is influenced by both biosphere uptake and respiratory release, leading to a more immediate seasonal response, while COS is removed solely through uptake and exhibits a delayed minimum due to cumulative absorption over the growing season.

The prior S1 optimization scenario overestimates the CO_2 mole fraction up to 5 $\mu\mathrm{mol\,mol^{-1}}$. After optimization, all posterior scenarios show closer alignment with the observational data, staying within the error assigned to the observations (R_{CO_2}). There are no significant differences between the scenarios, because compensating adjustments between GPP and TER, which kept NEE relatively constant even when COS vegetation fluxes vary.

4.3.3 Evaluation of the simulated vertical profiles

In this section, we evaluate the simulated vertical profile with aircraft measurements, which are independent of our assimilation and provide additional insights into the optimization results. Fig. 4.7 shows the vertical distribution of COS mole fractions from ATom airborne observations and those simulated using prior and optimized surface fluxes for the three optimization scenarios. The analysis is divided into two periods, July–August 2016 and January–February 2017, corresponding to the ATom 1 and ATom 2 campaigns.

For COS, prior results show a notable negative bias, except in the North Atlantic in January-February. The posterior results significantly reduce these biases, especially in the South Pacific and South Atlantic during both the ATom 1 and ATom 2 missions. Despite these optimizations, the North Pacific and North Atlantic still display considerable underestimations during winter, with mean bias values of $-18.6\ \mathrm{pmol\,mol^{-1}}$ and $-10.6\ \mathrm{pmol\,mol^{-1}}$, respectively, suggesting the need for additional sources.

The differences between the three optimization scenarios are minimal in all regions, indicating a small impact of the vegetation fluxes in these areas. Thus, improvements in factors other than the COS vegetation flux (e.g., advection, unknown emissions) are necessary during the January-February period in the North Pacific and North Atlantic. These possible factors will be discussed in more detail in Sect. 4.4.1.

Fig. 4.8 shows the vertical distribution of CO_2 mole fractions. Prior results generally exhibited positive biases with respect to ATom observations, and the optimization reduces these

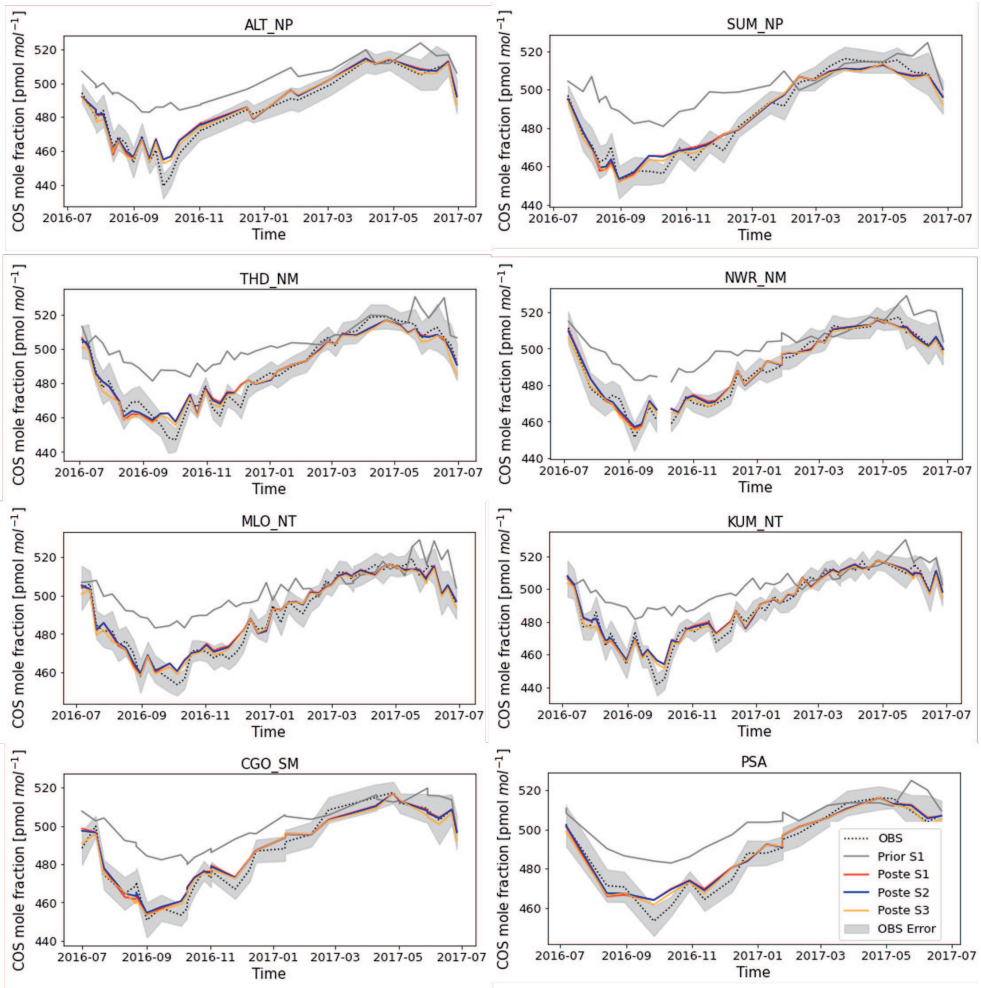


Figure 4.5: Time series of 8-day moving averaged COS mole fractions at eight surface stations, comparing measurements from July 2016 to June 2017 with modeled results from prior S1 (dotted) and posterior S1 to S3 scenarios (solid lines). The shaded area represents the R_{COS} used in the inversion, which combines measurement error, flux error, and representation error (see sect. 4.2.6). S1: linear GPP–COS vegetation flux relationship; S2: temperature-dependent internal conductance specific to COS; S3: same as S2 but with doubled vegetation uptake north of 40 °N.

biases except over the North Pacific and North Atlantic during January-February. Specifically, prior simulations over the north Pacific during this period show a slight positive bias of 0.13 $\mu\text{mol}\,\text{mol}^{-1}$, but the posterior results underestimate the observations with a mean bias of about $-0.95\,\mu\text{mol}\,\text{mol}^{-1}$. In the North Atlantic during January-February, posterior estimates up to 5 km altitude align more closely with ATom observations, whereas estimates above this altitude continue to be underestimated. Similarly to the findings for COS, the vertical distribution of CO_2 mole fractions exhibits minimal variation between scenarios.

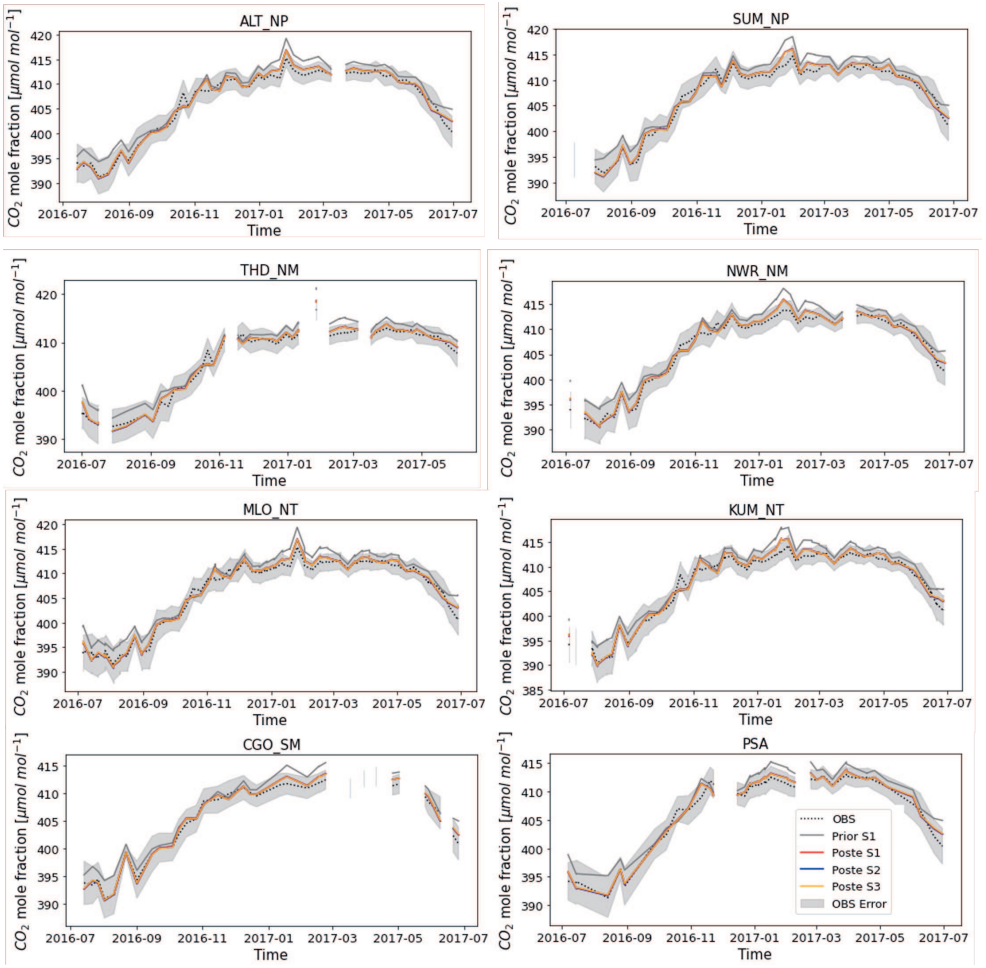


Figure 4.6: Same as Fig. 4.5 but for CO_2 mole fractions. The shaded area represents the R_{CO2} used in the inversion, which includes measurement and representation errors (see sect. 4.2.6).

4.3.4 Optimized COS surface fluxes

4.3.4.1 COS global budget

In this section, we quantify the COS sources and sinks using the three optimization scenarios and summarize their global budget in Table 4.4. As DMS emissions and COS soil fluxes are not included in the state vector of the optimization, their posterior values remain the same as the priors. A visual comparison of the prior and posterior COS budget in all scenarios is provided in Appendix Fig. A4.2.

Net anthropogenic emissions exhibit mixed behavior across scenarios, showing only minor differences from the prior in total but with contrasting patterns. Specifically, S1 and S2 show slight decreases, while S3 shows a substantial increase. This pattern results from a combina-

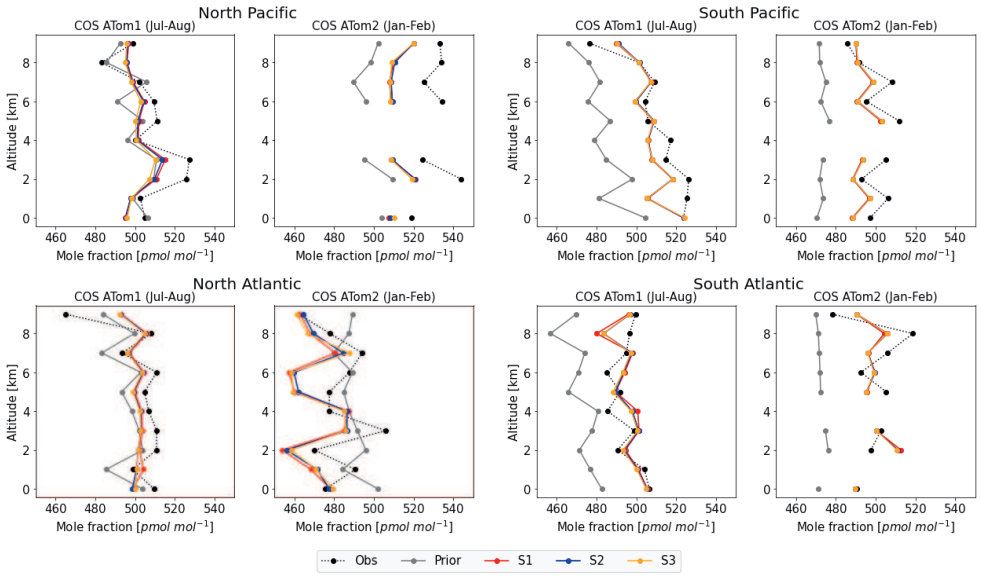


Figure 4.7: Vertical distribution of COS mole fractions from the ATom aircraft campaigns (ATom 1: July–August 2016, ATom 2: January–February 2017), compared with S1 prior results and posterior estimates from the three scenarios optimized through the 4D-Var system. Results are shown for four geographic regions (North/South Pacific and North/South Atlantic), which are indicated in Fig. 4.1.

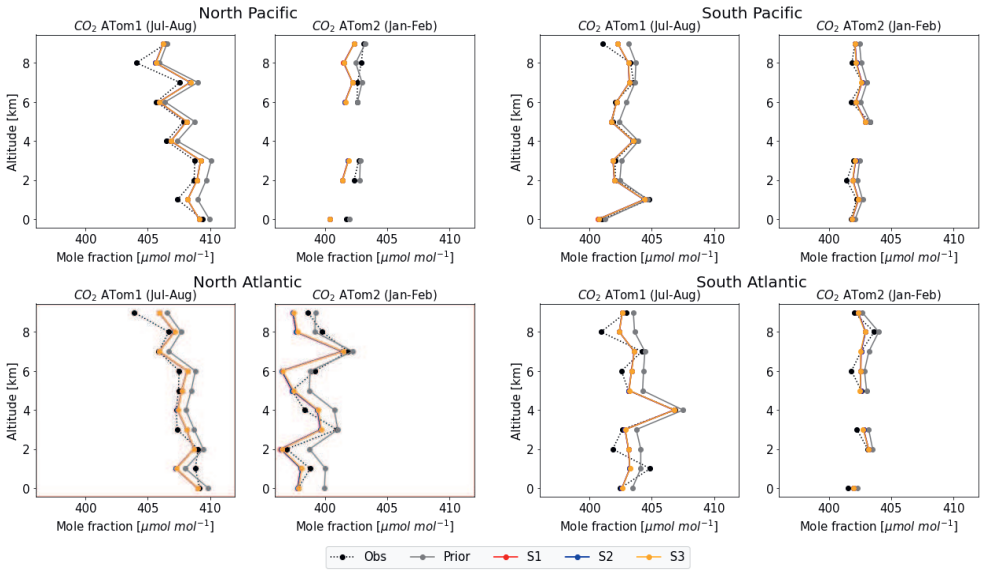


Figure 4.8: Same as Fig 4.7 but for the CO_2 vertical distribution.

tion of increased direct COS emissions and decreased indirect CS_2 emissions in all scenarios, with S3 showing a smaller reduction in CS_2 compared to S1 and S2. Direct COS emissions increase markedly in all scenarios, from a prior value of 161 to 219–225 Gg S yr^{-1}, which is larger than the 153 Gg S yr^{-1} reported by Ma et al. (2021). In contrast, CS_2 anthropogenic emissions decrease significantly from 236 to 115–175 Gg S yr^{-1}. These posterior values are smaller than the 188 Gg S yr^{-1} reported by Ma et al. (2021).

Oceanic emissions exhibit substantial adjustments in the optimization. Notably, COS direct oceanic emissions are converted from source to sink, ranging from -3 to -36 Gg S yr^{-1}. This behavior aligns with findings from Ma et al. (2021). Indirect emissions from oceanic CS_2 oxidation increased substantially, from 83 to 173–196 Gg S yr^{-1}, exceeding the 96 Gg S yr^{-1} estimate in Ma et al. (2021). As a result, despite the conversion of direct emissions to sink, the total oceanic emission increases from a prior value of 278 to 297–328 Gg S yr^{-1} in the three scenarios.

Biomass burning emissions show only minor changes, increasing slightly from 142 to 143–159 Gg S yr^{-1} in all scenarios.

The biospheric flux, the largest sink of COS, the vegetation uptake shows slight reductions in posterior values compared to the prior. Specifically, vegetation uptake decreases from -675 to -666 Gg S yr^{-1} in S1, from -640 to -625 Gg S yr^{-1} in S2, and from -783 to -775 Gg S yr^{-1} in S3. In comparison, Ma et al. (2021) reported a much larger adjustment in the combined soil and vegetation uptake, with a reduction from -1053 Gg S yr^{-1} to -557 Gg S yr^{-1} in their inversion. Although our results show the same direction of change (weaker sink after inversion), the magnitude of adjustment is considerably smaller. These limited adjustments are discussed further in Sect. 4.4.2.

Atmospheric chemical loss, not included in the optimization but changing due to modified 3D distributions of COS, remains relatively stable between -142 and -146 Gg S yr^{-1} in all scenarios.

The prior net fluxes exhibit a wide range of imbalances in the three scenarios, from -51 Gg S yr^{-1} in S2 to -191 Gg S yr^{-1} in S3. The large imbalance in S3 is attributable to the arbitrarily increased vegetation uptake imposed in the prior at high latitudes. After optimization, the posterior net fluxes become more consistent across the scenarios, ranging from -77 Gg S yr^{-1} (S2) to -104 Gg S yr^{-1} (S3). These posterior imbalances are more negative than those reported in previous studies (Ma et al., 2021; Remaud et al., 2022), and this discrepancy is further discussed in Sect. 4.4.3.

Table 4.4: Summary of COS budget estimates from previous studies and the three scenarios in this study. The scenarios differ only in biospheric COS fluxes: S1 uses the default SiB4 conductance; S2 applies an updated CA temperature response in the internal conductance calculation; and S3 doubles vegetation uptake north of 40 °N.

COS budget ($GgS\ yr^{-1}$)	Ma et al. (2021) (2000-2012) [a]	Remaud et al. (2022) (2008-2019)	This study (2016.07-2017.06)					
			Prior			Posterior		
			S1	S2	S3	S1	S2	S3
Anthropogenic	**381**	**327**	**397**	**397**	**397**	**345**	**341**	**488**
— Direct COS	153	-	161	161	161	219	225	223
— Indirect CS_2	188	-	236	236	236	115	116	175
Indirect DMS from land [b]	**6**	-	**6**	**6**	**6**	**6**	**6**	**6**
Oceanic	**234**	**526**	**278**	**278**	**278**	**318**	**297**	**328**
— Direct COS	−18	-	41	41	41	−36	−29	−3
— Indirect CS_2	96	-	83	83	83	196	173	177
— Indirect DMS [b]	156	-	155	155	155	155	155	155
Biomass burning	**124**	**65**	**142**	**142**	**142**	**159**	**143**	**155**
Biosphere	**−557**	**−829**	**−768**	**−732**	**−876**	**−759**	**−717**	**−868**
Soil flux	-	−209	−94	−94	−94	−94	−94	−94
Vegetation flux	-	−620	−675	−640	−783	−666	−625	−775
Atmospheric chemical loss [c]	**−143**	**−100**	**−142**	**−143**	**−139**	**−142**	**−146**	**−146**
Residual	**−6**	**−11**	**−87**	**−51**	**−191**	**−82**	**−77**	**−104**

[a] This budget represents the inversion result of S1 model in Ma et al. (2021)
[b] These fluxes are not optimized in the inversion.
[c] These fluxes are not optimized in the inversion. However, they are updated because atmospheric chemical losses are represented as first-order processes proportional to COS mole fractions, which themselves change as a result of flux optimization.

4.3.4.2 Latitudinal variation of COS surface fluxes

To examine the latitudinal characteristics of COS surface fluxes, we analyze the zonal mean distributions of prior and posterior fluxes in all scenarios. Fig. 4.9 presents these latitudinal variations, highlighting the changes introduced by optimization.

Fig. 4.9a depicts the COS vegetation flux, showing a bimodal distribution with peaks at low (25 °S–20 °N) and high latitudes (40 °N–75 °N). Due to the strong constraints from coupling with GPP and the limited freedom of the TER flux to compensate GPP changes (error 5%), the COS vegetation fluxes from all scenarios are only slightly updated. Compared to S1, S2 shows a reduced COS uptake at low latitudes and increased uptake at high latitudes in the NH. This shift reflects the behavior of the temperature-dependent CA function implemented in S2, which increases uptake under cooler conditions, but suppresses it at higher temperatures (Cho et al., 2023). Posterior S3, prescribed with double the prior vegetation flux S2, shows the largest sink at high Northern latitudes, with a latitudinal distribution pattern similar to its prior.

To quantify these regional shifts, we also computed the total vegetation uptake integrated over key latitude bands. Between 25 °S and 25 °N (tropical region), the posterior flux decreased from -420 Gg S yr^{-1} in S1 to -365 Gg S yr^{-1} in S2 and S3. Conversely, the high-latitude uptake above 40 °N increased from -117 to -138 Gg S yr^{-1} in S2, and reached -276 Gg S yr^{-1} in S3.

Fig. 4.9b shows COS oceanic fluxes, where prior estimates predominantly indicate a source, whereas posterior values from the optimization scenarios reflect sinks at higher latitudes in both hemispheres. In the SH, uptake levels are similar across all scenarios. In the NH, S1 and S2 predict strong COS absorption by the ocean, while S3 suggests a source at latitudes lower than 50 °N and a weak sink at higher latitudes. This smaller uptake in posterior S3 is likely due to the doubling of the COS vegetation sink prescribed in high northern latitudes. As the inversion system balances total fluxes to match atmospheric constraints, the larger vegetation uptake in this region may have diminished the need for additional oceanic compensation, resulting in weaker oceanic sinks.

Fig. 4.9c illustrates anthropogenic COS emissions, where prior fluxes primarily concentrate over the NH mid-latitudes. The posterior fluxes indicate increased emissions between 15 °N and 50 °N and a reduction around 50 °N. In particular, near 50 °N, scenario S3 results in higher emissions compared to the other optimization scenarios, with S1 showing the lowest emissions.

Fig. 4.9d displays COS biomass burning fluxes, with prior emissions occurring between 25 °S and 75 °N. In the posterior fluxes, emissions increase at low latitudes (25 °S to 15 °N) and decrease northward of 15 °N. S1 and S2 reveal significant unphysical negative fluxes at high latitudes in NH. This feature is absent in the optimization scenario S3 due to the larger vegetation uptake of COS at high latitude prescribed in the prior fluxes.

Fig. 4.9e illustrates the prior and posterior distributions of CS_2 oceanic fluxes. Overall, posterior emissions more than double across all latitudes, increasing the global oceanic CS_2 flux from a prior estimate of approximately 83 Gg S yr^{-1} to 196 (S1), 173 (S2), and 176 Gg S yr^{-1} (S3). At low latitudes, where the prior fluxes exhibit a peak, the posterior distributions also retain the highest values, reflecting both the global increase and the preservation of the latitudinal pattern. S1 shows a larger increase compared to S2 and S3, likely due to a larger biospheric sink at low latitudes in S1, which amplifies CS_2 oceanic emissions. The minimal differences between the results of S2 and S3 suggest that the adjustments of the high-latitude vegetation fluxes do not significantly affect the CS_2 oceanic sources.

Fig. 4.9f shows the anthropogenic CS_2 emissions. After optimization, all scenarios exhibit a substantial reduction of north of 40 °N, where prior fluxes indicate a source. This results in a transition from source to sink in that region. When integrated high latitude band (north of

40 °N), the posterior fluxes become negative in all scenarios, with total negative emissions of $-97\,\mathrm{Gg\,S\,yr^{-1}}$ in S1, $-81\,\mathrm{Gg\,S\,yr^{-1}}$ in S2, and $-23\,\mathrm{Gg\,S\,yr^{-1}}$ in S3.

These nonphysical results are most likely related to the limited ability of the inversion system to sufficiently adjust the biospheric sink, which is tightly constrained by the strong prior error setting. Notably, while the negative values in biomass burning are largely resolved under the S3 scenario with enhanced vegetation fluxes, negative emissions in CS_2 anthropogenic fluxes persist. The spatial and seasonal distributions of these negative CS_2 anthropogenic fluxes are examined in the following section.

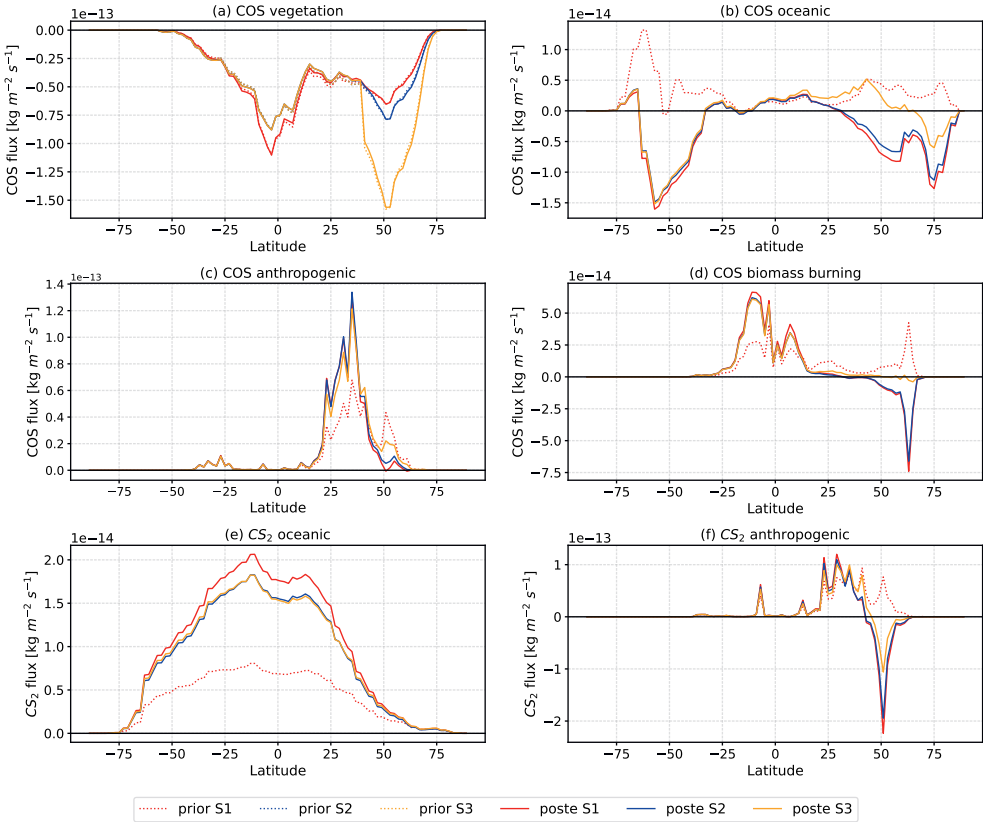


Figure 4.9: Latitudinal variation of COS fluxes, comparing prior (dotted lines) and posterior (solid lines) values for three scenarios. Each scenario is shown in a distinct color: red for S1, blue for S2, and orange for S3.

4.3.4.3 Analysis of nonphysical negative emissions

Despite doubling the high-latitude COS vegetation flux in S3, posterior CS_2 anthropogenic emissions and biomass burning COS emissions still exhibit nonphysical negative values, particularly around the 50 °N region. To investigate the regions where these negative values occur and to assess whether similar patterns appear in direct COS anthropogenic emissions, we ex-

amine the spatial distributions of the prior and posterior anthropogenic emissions for both CS_2 and COS under scenario S3, along with their differences, as shown in Appendix Fig. A4.1.

After optimization CS_2 anthropogenic emissions show notable decreases over Europe and eastern North America, while increases are observed over the Indian subcontinent and eastern China. In particular, the posterior values over Europe (latitude 30 °N–60 °N, longitude 10 °W–30 °E) decrease significantly, resulting in negative posterior fluxes. In contrast, the corresponding posterior fluxes of direct COS anthropogenic emissions in the same regions remain positive, despite some local reductions. This contrasting behavior suggests that the inversion interprets a larger portion of the anthropogenic COS-related to uncertainty to CS_2 emissions, rather than to direct COS emissions.

Although both fluxes were assigned identical prior uncertainties and spatial correlation settings, the inversion preferentially adjusts CS_2 emissions, likely because they are more spatially concentrated in Europe, leading to stronger localized sensitivity to observational constraints. This regional concentration may also reflect differences in emission sources: CS_2 emissions are associated with industrial and high-tech manufacturing sectors, whereas anthropogenic COS is more closely linked to coal combustion, particularly in East Asia. This behavior is discussed further in Sect. 4.4.3.

To explore the causes behind the nonphysical negative values of the CS_2 anthropogenic emissions over Europe, we examine the monthly variations of the posterior emissions. Fig. 4.10 presents the seasonal variation of prior and posterior CS_2 anthropogenic emissions, together with COS anthropogenic emissions and COS vegetation fluxes from S3 over Europe. The inclusion of these additional fluxes aims to explore whether the nonphysical seasonal patterns observed in CS_2 anthropogenic emissions are related to adjustments in other surface fluxes.

The prior CS_2 anthropogenic emissions show positive values throughout the year with no seasonal variation, while the posterior emissions display significant seasonal fluctuations with negative values, most negative in September and the highest in February. This pattern is also visible in the posterior COS anthropogenic emissions, which also show a reduction compared to the prior fluxes.

Over Europe, the COS vegetation uptake peaks in June and July and decreases in December and January, while posterior CS_2 anthropogenic emissions exhibit negative values peaking in September. Although their seasonal patterns do not align exactly, the strong vegetation uptake during summer can reduce atmospheric COS mole fractions in the following months. The fact that the inversion does not increase oceanic COS uptake at high latitudes (Fig. 4.9(b)), but instead reduces CS_2 anthropogenic emissions over inland regions, suggests that the model requires additional sinks specifically over land. This highlights a potential underestimation of biospheric COS uptake or soil uptake in these regions. Therefore, simply doubling the vegetation flux values (S3) is insufficient to resolve this issue, suggesting that further improvements in the COS biosphere fluxes calculations in SiB4 are necessary. Note here that the COS budget over Europe is poorly constrained, as updates in this region are influenced almost exclusively by the Mace Head station, the only observational site providing constraints.

4.3.5 Optimized CO_2 surface fluxes

4.3.5.1 CO_2 global budget

Table 4.5 shows the global CO_2 budget, comparing posterior estimates from each optimization scenario with the prior model. The CO_2 sources from anthropogenic and fire emissions remain unchanged, as these fluxes were not optimized.

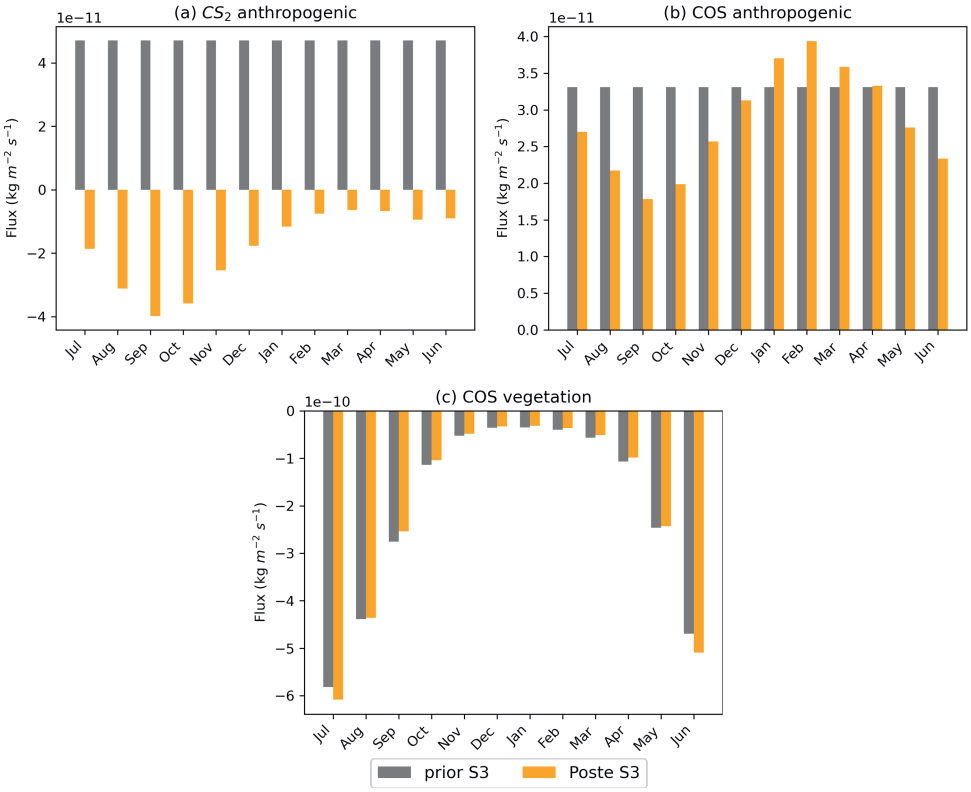


Figure 4.10: Monthly variations of CS_2 anthropogenic, COS anthropogenic, and COS vegetation fluxes in the region spanning latitudes 30 °N–60 °N and longitudes 10 °W–30 °E, where generally CS_2 anthropogenic emissions show negative values. Comparisons between Prior S3 (grey) and Posterior S3 (orange) are shown.

To place our posterior estimates in a broader context, we compare them with global CO_2 inversion results from the Global Carbon Budget 2024 (GCB2024, Friedlingstein et al. (2025)), which consists of results from 14 inverse systems covering the period 1976-2023 (Luijkx et al., 2024). For consistency, we extracted and analyzed the inversion outputs corresponding to our analysis period. Note that the GCB2024 inversions provide only the total land flux, which is the sum of NEE and fire fluxes ($F_{CO2,NEE} + F_{CO2,fr}$). Therefore, we compare the total land flux rather than the individual components. GCB2024 inversion land fluxes were adjusted to match fossil fuel and cement emissions from the GridFEDv2024 inventory, whereas we do not apply this adjustment for our results. The riverine carbon flux adjustment is not applied to either the GCB2024 or our results, and therefore, they cannot be directly compared to bottom-up estimates.

We also refer to results from another coupled CO_2-COS model (Remaud et al., 2022), which analyzed the coupled COS and CO_2 budgets in the period 2008-2019, to provide additional context. Appendix Fig. A4.3 provides a visual comparison of the estimated CO_2 budgets from both the prior and posterior models.

The oceanic flux from the three optimization scenarios is $-3.6\,\mathrm{Pg\,C\,yr^{-1}}$, which is substan-

tially larger than the estimate from the GCB2024 inversions of -2.4 Pg C yr^{-1}. A larger discrepancy is found with -1.9 Pg C yr^{-1} reported by Remaud et al. (2022), likely because their oceanic fluxes were prescribed and not optimized, and their values are reported for a different period. Note that a river adjustment was not applied, and therefore these numbers cannot be directly compared to the GCB2024 bottom-up estimates.

All optimization scenarios yield land CO_2 fluxes between -1.3 and -1.4 Pg C yr^{-1}, indicating a stronger sink than the prior estimate of -0.7 Pg C yr^{-1}, and are more consistent with the results of the inversions included in GCB2024 and Remaud et al. (2022). However, the land sink in our study is still slightly smaller than those reported in the two previous studies. This discrepancy may be due to an underestimation of GPP or an overestimation of TER or uncertainties in fire emissions, or settings in the coupled inversion system, as discussed in Sect. 4.4.3. The similar NEE values across all three optimization scenarios suggest that variations in the prior COS vegetation flux do not significantly affect the optimized CO_2 biosphere flux.

The surface flux residual with respect to the atmospheric CO_2 growth rate decreases from 5.4 Pg C yr^{-1} in the prior to 4.7 Pg C yr^{-1} in the posterior. This posterior value is in line with reported estimates from the inversions included in GCB2024 (4.8 Pg C yr^{-1}) and Remaud et al. (2022) (4.9 Pg C yr^{-1}).

Table 4.5: Summary of CO_2 budget estimates from different studies and three optimization scenarios in this study. Scenarios differ only in COS biospheric fluxes: S1 uses default SiB4 conductance, S2 updates CA temperature response in the internal conductance calculation, and S3 doubles vegetation uptake north of 40 °N.

CO_2 budget ($PgC\ yr^{-1}$)	Mean inversions in GCB2024 (Friedlingstein et al., 2025) (July 2016–June 2017)	Remaud et al. (2022) (2008–2019)	This study (July 2016–June 2017)			
			Prior	Posterior		
			S1–S3	S1	S2	S3
Anthropogenic	**9.5**	**9.6**	**9.6**	**9.6**	**9.6**	**9.6**
Oceanic	**−2.4**	**−1.9**	**−3.5**	**−3.6**	**−3.6**	**−3.6**
Land	**−2.2**	**−2.8**	**−0.7**	**−1.3**	**−1.3**	**−1.4**
Fire		1.9	1.9	1.9	1.9	1.9
GPP		−119.8	−122.0	−120.8	−121.3	−121.2
TER		115.1	119.4	117.6	118.1	117.9
Residual flux	**4.8**	**4.9**	**5.4**	**4.7**	**4.7**	**4.7**

Fig. 4.11 compares the distribution of global CO_2 ocean and land fluxes of the three optimizations in this study with results from 14 CO_2 inverse models included in GCB2024 (Friedlingstein et al., 2025) and from Remaud et al. (2022). To ensure consistency, the GCB2024 inversion data were subset for the period July 2016 to June 2017 for comparison with our results. In contrast, Remaud et al. (2022) data represented a 2008–2019 average, as no corresponding annual data were available. Note again that the ocean CO_2 flux in Remaud et al. (2022) was prescribed rather than optimized. The land fluxes from GCB2024 and Remaud et al. (2022) generally range between -1.5 and -3.0 Pg C yr^{-1}, while ocean fluxes fall within a similar range of -1.5 to -3.0 Pg C yr^{-1}. In contrast, our results show slightly weaker land fluxes and stronger oceanic sinks.

The diagonal line represents the global budget constraint, indicating all possible combinations of land and ocean fluxes that by design should sum up to the total net CO_2 emissions minus the atmospheric growth rate (-4.6 ± 0.25 Pg C yr^{-1}, including fire emission). Our model estimates are approximately -4.9 Pg C yr^{-1}, showing general agreement with this constraint. Note that such comparisons are typically made over periods longer than 1 year (e.g., in Friedlingstein et al. (2025)).

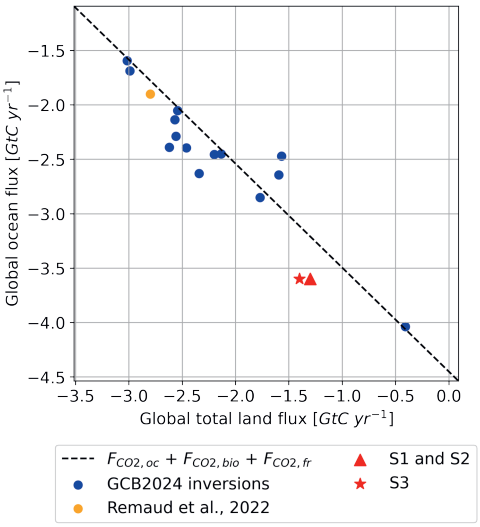


Figure 4.11: Global CO_2 ocean flux ($F_{CO2,oc}$) and land fluxes ($F_{CO2,bio} + F_{CO2,fr}$) obtained from the GCB2024 inversion ensemble (blue dots, from July 2016 to June 2017), the LRU-based CO_2-COS coupled system from Remaud et al. (2022) (orange dot, from 2008 to 2019), and our posterior estimates from the three optimization scenarios (red symbols, from July 2016 to June 2017). The diagonal line represents the global carbon budget constraint, where land and ocean fluxes balance total net CO_2 emissions minus the atmospheric growth rate. Note that $F_{CO2,oc}$ and $F_{CO2,bio}$ are negative values indicating sinks, while $F_{CO2,fr}$ is positive, representing a source.

4.3.5.2 Latitudinal variation of CO_2 fluxes

Fig. 4.12 shows the latitudinal distribution of the prior and posterior CO_2 fluxes for the three optimization scenarios. Anthropogenic emissions and fire fluxes are excluded, as they were not optimized. For comparison, the GCB2024 inversion results are also included for the land flux

(NEE plus $F_{CO2,fr}$) and CO_2 oceanic flux (Fig. 4.12(d) and (e)). The GCB2024 inversion results are shown as the ensemble mean and the minimum-maximum range across 14 ensemble members. This ensemble reflects a diversity of inversion frameworks and prior assumptions, providing a useful benchmark for evaluating the robustness of our results.

Fig. 4.12a shows the prior and optimized GPP distribution, with two prominent peaks, one at low-latitudes and another around 50 °N, similar to the S1 COS vegetation flux pattern (see sect. 4.3.4.2), as the latter was derived linearly from GPP. The differences between the prior and posterior fluxes are small, but the posterior fluxes show a slightly stronger uptake, except over the 0 to 30 °N latitude band.

Fig. 4.12b shows the latitudinal distribution of TER. The posterior TER remains similar to the prior flux overall, likely because the prior error assigned to TER (5%) was smaller than that for GPP (10%).

Fig. 4.12c shows the latitudinal distribution of the CO_2 net biosphere flux (NEE). While prior and posterior changes in GPP and TER are relatively small, NEE exhibits substantial adjustments across all latitude bands. This is partly because NEE, being the difference between GPP and TER, has a smaller magnitude and weaker latitudinal variation. The prior NEE is relatively constant across latitudes, whereas the posterior shows pronounced CO_2 uptake between 50 °S–0 ° and 40 °N–75 °N and net CO_2 emissions between 0 °–40 °N. These patterns arise because GPP decreases more than TER between 0 °–40 °N, leading to a net source, while GPP increases above 50 °N, strengthening the sink. Differences across scenarios are minor, suggesting that NEE is robustly constrained by CO_2 data, with limited sensitivity to variations in COS biosphere flux. Although differences are small, S3 shows the largest uptake, followed by S2 and S1.

Fig. 4.12d shows the latitudinal variation of the total land flux, combining NEE and fire flux, for comparison with the GCB2024 inversion results. Notably, our system produces a stronger net sink in the SH tropics (25 °S–0 °), whereas the Northern Hemisphere tropics (0 °–25 °N) show a stronger net source relative to GCB2024 inversions. In addition, north of ≈50 °N our model simulates a stronger sink. A detailed discussion of the possible drivers of these hemispheric asymmetries is provided in Sect. 4.4.2.

Fig. 4.12e shows the latitudinal distribution of the CO_2 oceanic flux. Prior sinks are evident at 75 °S–30 °S and most latitudes in the NH. Posterior sinks decrease compared to prior fluxes in the SH but increase from 25 °N–50 °N. Posterior fluxes exhibit only small adjustments across all latitudes. This corresponds to a slight global adjustment from -3.5 to -3.6 Pg C yr^{-1} (see Table 4.5). There are no differences in updates across the COS optimization scenarios.

While our posterior ocean fluxes broadly align with the latitudinal patterns reported by GCB2024, regional discrepancies remain. For instance, the sink is overestimated in parts of the Southern Ocean (≈50 °S) and the mid-latitude Northern Hemisphere (5 °N–50 °N), while it is underestimated in the subtropical Southern Hemisphere (50 °S–10 °S). A localized source anomaly near 50 °N–65 °N and a stronger than expected sink north of 75 °N are also apparent. These differences may reflect the limited constraint from oceanic CO_2 observations in our setup, which hampers regional adjustments. A detailed discussion is provided in Sect. 4.4.2.

Fig. 4.12f illustrates the latitudinal variation of anthropogenic CO_2 emissions. Since these emissions were not optimized in our inversion framework, only the prior values are shown. The prior distribution used in our system closely matches the results from the inversions included in GCB2024, with both datasets showing strong positive emissions between 25 °N and 50 °N in the NH.

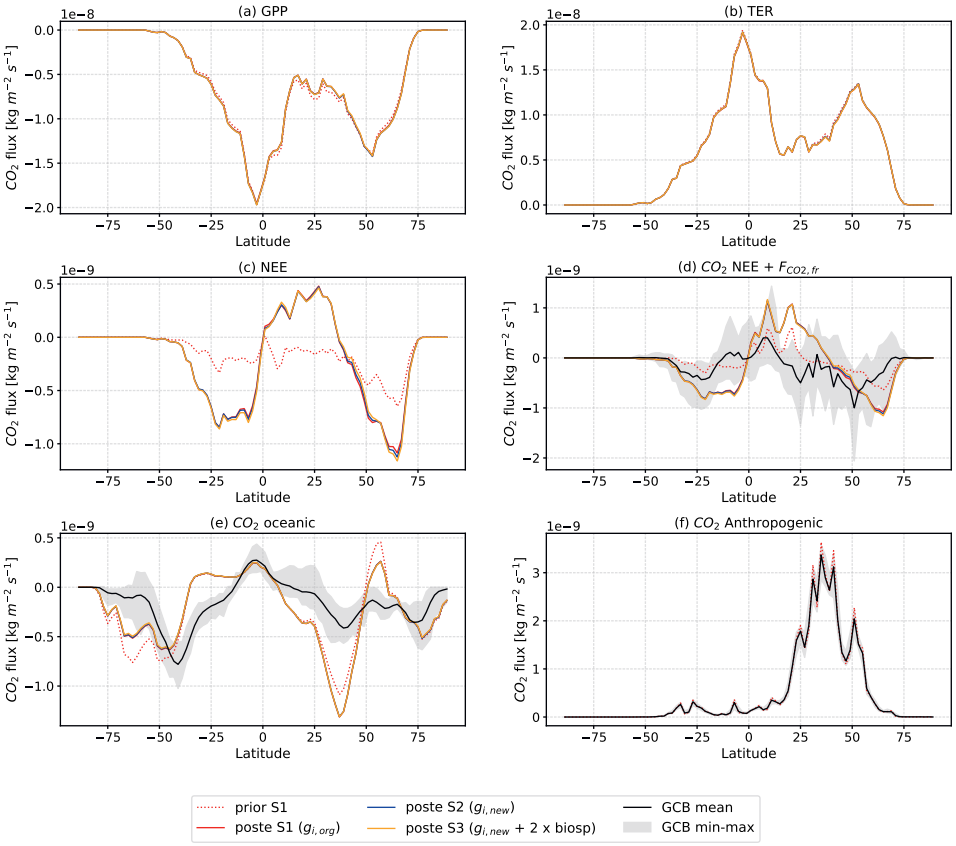


Figure 4.12: Latitudinal distribution of (a) GPP, (b) TER, and (c) net CO_2 biosphere flux (NEE), (d) net CO_2 land flux (fire and NEE), (e) CO_2 oceanic flux, (f) CO_2 anthropogenic flux for the three optimization scenarios. Shaded areas in (d), (e), and (f) indicate the range across 14 GCB2024 inverse models (Friedlingstein et al., 2025) for July 2016–June 2017.

4.4 Discussion

4.4.1 Direction to improve the coupling system

We successfully implemented a coupled CO_2 and COS optimization system in the TM5-4DVAR framework. Our inversions reached convergence, and the overall comparison with assimilated (surface flask) and independent (ATom aircraft) observations generally improved. Here, we discuss possible future improvements to the system.

First, while our 4D-Var system currently operates at monthly resolution for both COS and CO_2 biosphere fluxes, future developments should explicitly incorporate diurnal cycles. Unlike CO_2, which is respired at night, COS continues to be taken up when stomata remain open, resulting in distinct diurnal patterns between the two gases (Berkelhammer et al., 2014; Kooijmans et al., 2019). This challenges the assumption that COS uptake can be linearly scaled from GPP, especially since our prior COS fluxes followed this approach. Munassar et al. (2025)

showed that neglecting diurnal variations in CO_2 mole fractions can introduce substantial regional biases—up to 48% in annual NEE over Europe—while the global land sink impact was relatively small ($\approx 2\%$). Given that our prior COS vegetation uptake was derived by scaling GPP, similar underestimation may have occurred, especially in high-latitude regions where diurnal variation is more pronounced and nighttime COS uptake is non-negligible. Moreover, the lack of diurnal cycle representation may have limited the model's ability to fully utilize physiological improvements, such as the temperature response of mesophyll conductance introduced in S2.

Second, although various types of COS and CO_2 observations are available, including aircraft, satellite, and in situ measurements, this study used only in situ observations. Utilizing diverse observational data within the 4D-Var system in the future could provide new information in regions not covered by in situ observations. However, data quality control is critical in the use of satellite data to avoid inaccurate information, such as cloud contamination in signals, low sensitivity, and artifacts due to orography (Ma et al., 2024).

In our current setup, CO_2 observations exert a dominant constraint on the coupled system, owing to their higher precision, greater spatial coverage, and more reliable prior flux estimates compared to COS. As a result, posterior biospheric fluxes are primarily adjusted to satisfy the CO_2 budget, with COS providing only a secondary constraint. This imbalance was evident even when observational weights were applied, and in some regions, station-level posterior χ^2 values fell below 0.5—an indication of potential overfitting. Such behavior suggests that the system may have relied excessively on adjusting NEE to fit land-based CO_2 data, particularly where oceanic fluxes remained weakly constrained due to a lack of observational coverage.

To enhance the robustness of the coupled inversion, it is essential to establish a global observation network capable of jointly constraining both CO_2 and COS surface fluxes. Improved spatial and temporal coverage, along with reduced observational and prior uncertainties, would enable COS to play a more effective role in complementing CO_2 as a tracer of terrestrial photosynthesis.

Third, the observed low bias in the COS vertical profiles in the NH (Fig. 4.7) suggests that improving the COS vegetation flux alone is insufficient to fully reconcile the discrepancies. Notably, the posterior vertical profiles show only minor differences in the three scenarios, indicating that adjustments to the prior vegetation flux had limited influence on the vertical distribution of COS. A similar underestimation in the free troposphere (above 2 km) of both the NH and tropics was also reported by Ma et al. (2023).

One potential explanation is the incomplete representation of oceanic DMS-derived COS production. Previous studies have highlighted significant uncertainties in oceanic DMS emissions (Belviso et al., 2012; Lana et al., 2011). The conversion from DMS to COS involves a poorly understood multi-step reaction mechanism (Lennartz et al., 2017). Recent findings suggest that DMS oxidation in the marine boundary layer may proceed via hydroperoxymethyl thioformate (HPMTF), which can further oxidize to COS (Jernigan et al., 2022; Wu et al., 2015; Ye et al., 2022). Moreover, the uptake and reaction of HPMTF within cloud droplets may suppress this pathway regionally (Kilgour et al., 2025), adding further complexity. These emerging insights highlight the importance of improving our understanding and quantification of the highly uncertain DMS–HPMTF–COS pathway, which remains a poorly constrained yet potentially significant contributor to the atmospheric COS budget in inversion frameworks.

Ma et al. (2023) also suggested that missing COS or CS_2 emissions from Asia could explain part of the low biases in the free troposphere, especially in the NH. This indicates the need to improve regional emission inventories, particularly for anthropogenic and indirect sources in East Asia.

Finally, due to computational cost constraints, we performed inversions of a two-year time

period and analyzed a single year. As CO_2 and COS mole fractions exhibit interannual variability (Friedlingstein et al., 2025; Serio et al., 2023), this poses limitations in comparison to previous studies (e.g., GCB). Future work should apply the coupling system to multi-year inversion. Additionally, the prior biosphere fluxes derived from the SiB4 model were simulated using a fixed atmospheric CO_2 mole fraction ($370\ \mu\mathrm{mol\,mol^{-1}}$), which suppresses the CO_2 fertilization effect, potentially leading to underestimated photosynthetic uptake.

Despite these limitations, our coupled system, which utilizes COS and CO_2 biosphere fluxes from a land surface model (SiB4) offers advantages over previous studies that relied on fixed and uncertain LRU estimates (Launois et al., 2015a; Remaud et al., 2022). Although our approach still depends on the LRU concept through the SiB4-calculated relationship between COS and CO_2 uptake, it benefits from the use of process-based physiological modeling, which can be improved as new measurements become available to better evaluate and tune the coupled COS and CO_2 exchange. In this sense, we rely on prior fluxes derived from SiB4 rather than directly on prescribed LRU values.

The following section outlines how the adjustments to the COS vegetation flux improved our estimates and how we took the first steps to improve the COS biosphere fluxes and assess their impact on the inversion results.

4.4.2 Evaluation of COS vegetation flux scenarios

The three biosphere flux scenarios (S1, S2, and S3) revealed distinct impacts on the inversion performance and optimized fluxes, particularly for the COS global budget.

Although the reduction in the χ^2 for S2 after optimization is modest (from 4.42 to 4.34), the change observed, particularly in the tropics suggests that applying the independent temperature response for CA ($g_{i,\mathrm{new}}$) improves the representation of COS uptake in these regions. This result is consistent with Stinecipher et al. (2022), who reported the overestimation of tropical COS vegetation uptakes based on MIPAS satellite observations. These findings highlight the importance of incorporating temperature-dependent COS uptake independently from photosynthesis, especially under high-temperature conditions.

S3 achieved the lowest posterior cost and fastest convergence, suggesting that additional biospheric sinks in northern high latitudes may be required. One possible reason for an underestimated prior COS biospheric sink is the omission of diurnal cycles in our system, as previously discussed. Since S3's flux enhancement was implemented as an arbitrary adjustment, future studies should explore more ecologically realistic representations that account for regional vegetation types and their climatic responses.

Our finding that COS vegetation uptake is underestimated at high northern latitudes is consistent with Kuai et al. (2022), who optimized COS plant uptake using aircraft profiles over Alaska and found that the optimized uptake was about 25% greater than the ensemble mean of GPP-based estimates. This supports the interpretation that the prior COS vegetation flux, derived proportionally from SiB4 GPP, may be underestimated in northern high latitudes.

The COS vegetation flux may exhibit independent characteristics relative to photosynthesis—such as nighttime stomatal responses and distinct environmental sensitivities—that are not yet fully represented in the land surface model. A better representation of these physiological processes may be the key to improving prior COS flux estimates and overall inversion performance. In addition, the soil flux was not optimized in our inversion, but its high uncertainty and limited process representation may also contribute to the model-observation mismatch.

4.4.3 Implications for the global budgets of CO_2 and COS

The optimized global budgets of CO_2 and COS from our coupled inversion provide new insights into the redistribution of sources and sinks for each gas. Compared to previous single-species inversion studies, our system highlights how jointly assimilating CO_2 and COS observations can influence the partitioning of surface fluxes.

For CO_2, our results show a weaker land sink (-1.4 PgC yr^{-1} in S3) and a stronger ocean sink (-3.6 PgC yr^{-1}) for July 2016–June 2017, compared to the ensemble mean of the GCB2024 inversion systems (land: -2.2 PgC yr^{-1}; ocean: -2.4 PgC yr^{-1}).

A likely contributor to this discrepancy is the absence of diurnal cycle representation in our inversion system and the use of prior biosphere fluxes driven by a fixed atmospheric CO_2 mole fraction, as already identified as a limitation of our system (Sect 4.4.1). These limitations may have also influenced the latitudinal distribution of the inferred land and oceanic fluxes, contributing to the differences observed between our results and the GCB2024 inversions (Fig. 4.12(d), (e)). In addition, the persistent underestimation of COS vegetation fluxes at high latitudes may imply that GPP is likewise underestimated in these regions.

Although strong prior constraints on TER (5%) and the GPP–COS scaling factor (10%) are essential for inversion stability, they also limit the system's ability to adjust GPP and TER. Consequently, COS vegetation flux updates remained minimal, forcing the inversion to reconcile COS residuals through adjustments in other fluxes, such as anthropogenic CS_2 emissions. This tendency led to physically implausible negative posterior estimates, particularly over Europe, where CS_2 emissions are spatially concentrated and more responsive to inversion adjustments.

The regional differences in anthropogenic COS and CS_2 fluxes mainly reflect contrasting emission structures. In China, anthropogenic COS arises from both coal combustion and industrial production such as rayon and titanium dioxide, with coal contributing more strongly than in other regions (Zumkehr et al., 2018). This mixture produces clear spatial contrasts between regions dominated by direct COS and those by CS_2. The Zumkehr et al. (2018) inventory has been shown to underestimate Chinese anthropogenic COS emissions (Yan et al., 2019), consistent with the slightly higher posterior emissions than prior in our inversion.

In Europe, anthropogenic CS_2 emissions mainly originate from viscose-rayon and other chemical manufacturing sectors. These industries have declined and implemented stronger emission controls in recent years (Belviso et al., 2023; Berchet et al., 2025). Consequently, the posterior tendency toward reduced CS_2 anthropogenic emissions in Europe is consistent with these trends and suggests that the prior was biased high. However, the negative posterior values are non-physical and most likely arise from weak constraints and modeled structure, not true sinks.

Regarding COS global budget, our inversion suggests that additional biospheric sinks at high northern latitudes and enhanced oceanic CS_2 emissions in the tropics are needed to reconcile observed atmospheric mole fractions. The attribution of the tropical "missing source" to oceanic precursors aligns with previous studies (Ma et al., 2024; Remaud et al., 2022). However, uncertainties in the conversion pathways of oceanic DMS and CS_2 remain substantial (Lennartz et al., 2021), underscoring the need for further research to constrain these fluxes.

Our analysis estimates a larger negative COS budget imbalance (-77 to -104 GgS yr^{-1}) than earlier studies (Ma et al., 2021; Remaud et al., 2022), which reported near-zero imbalances. This discrepancy partly arises because previous studies covered periods with a slight increase in atmospheric COS (2000–2015), whereas our analysis focuses on 2016–2017, a period marked by declining mole fractions (Serio et al., 2023).

Appendix Fig. A4.4 illustrates decreasing trends in anthropogenic COS, CS_2, and oceanic CS_2 emissions. The decreasing trend in anthropogenic COS emissions aligns with the obser-

vational evidence presented by Hannigan et al. (2022), who reported a strong correlation between free tropospheric COS concentrations and the revised anthropogenic emission inventory by Zumkehr et al. (2018). The inventory includes both COS and its precursor CS_2, suggesting that reductions in both may contribute to the observed decline. Complementary satellite observations from ACE-FTS further support this interpretation, showing that COS mole fractions increased from 2004 to 2017 and then declined approximately -4.5 pmol mol^{-1} yr^{-1} (Schmidt et al., 2024). Serio et al. (2023) similarly reported a decline of about -5 pmol mol^{-1} yr^{-1} over the same period.

By contrast, our inversion (S3) implies a stronger decline of roughly -18 pmol mol^{-1} yr^{-1}. While the sign of the change is consistent with observations, the magnitude is larger, likely reflecting remaining uncertainties in this coupling system. Given the 5–10% retrieval uncertainty, the exact onset of this transition cannot be dated precisely; however, 2016—the focus year of our inversion—falls at the end of the increasing phase, and both ACE-FTS and NOAA surface records point to a transition in the 2015–2017 period.

Furthermore, this explanation is supported by recent findings that natural processes alone would lead to increasing atmospheric COS (Serio et al., 2023). Direct oceanic COS and indirect CS_2 oceanic emissions have shown a slight long-term increasing trend (Lennartz et al., 2021). Likewise, ecosystem uptake, especially in boreal forests, has been weakened due to climate-related stressors such as prolonged drought, which should have led to increased atmospheric COS levels (Vesala et al., 2022). Therefore, the observed multi-year decrease in atmospheric COS during 2016–2017 strongly suggests that reductions in anthropogenic emissions are the most plausible driver of the negative budget imbalance (Hannigan et al., 2022; Serio et al., 2023).

Our results show that the ability of the coupled system to constrain COS surface fluxes varies regionally. Fluxes in the mid-latitudes appear relatively well-constrained, as indicated by lower χ^2_{poste}, whereas high-latitude regions remain weakly constrained, exhibiting unrealistic negative emissions with relatively higher χ^2_{poste}. Such limitations are not unique to our study, but are also evident in previous studies such as Launois et al. (2015b) and Remaud et al. (2022), which rely on simplified LRU parameterizations. In all cases, these approaches impose substantial constraints on the flexibility of the CO_2–COS coupling. To overcome these limitations, future work should aim to refine land surface models by (i) incorporating COS-specific processes such as nighttime stomatal conductance and CA activity, or (ii) developing LRU parameterizations that account for geographic, environmental, and species-level variability and integrating them into land surface models. Such improvements would enable the coupled system to calculate more accurate prior COS biosphere fluxes and provide deeper insights into the global exchange of CO_2 and COS.

4.5 Conclusion

We developed and implemented a coupled inversion system for CO_2 and COS using the TM5-4DVar, enabling the joint optimization of their surface fluxes. By linking GPP and COS vegetation uptake through a grid-cell-specific monthly scaling factor, our approach allows simultaneous adjustments of biospheric fluxes constrained by atmospheric observations of both species. This approach represents a methodological advance over previous studies that relied on fixed LRU values or globally uniform scaling parameters. By using COS vegetation fluxes simulated by a land surface model, which internally jointly represents photosynthesis and COS uptake, our approach inherently accounts for physiological processes. Moreover, it provides a flexible framework to incorporate future improvements in modeling COS uptake, informed by emerg-

ing experimental and observational studies on biosphere–atmosphere interactions.

The results revealed notable differences in the redistribution of global carbon and sulfur budgets compared to previous studies. Our coupled system estimates a weaker CO_2 land sink and a stronger ocean sink relative to the estimates from the inversions included in GCB2024. This discrepancy is likely driven primarily by the absence of a diurnal cycle in our inversion framework. Additionally, the lack of oceanic CO_2 observations in our optimization may have limited flux adjustments over the oceans, leading to compensatory adjustments in terrestrial fluxes. For COS, reconciling observed atmospheric mole fractions required additional biospheric sinks at high northern latitudes and enhanced tropical CS_2 oceanic emissions. While our system successfully reproduces surface observations, the emergence of negative posterior anthropogenic CS_2 emissions–particularly over Europe, where prior CS_2 sources are spatially concentrated but observational constraints are limited. This pattern suggests that tight prior constraints on TER and the GPP–COS scaling factor limited the model's ability to adjust biospheric uptake processes appropriately. This underscores the need to improve the representation of COS biosphere fluxes in inversion frameworks, particularly through improving the COS uptake modules within land surface models, instead of relying on simplified first-order schemes.

Importantly, this study demonstrates the potential of a coupled CO_2-COS inversion system leveraging land surface model–derived biospheric fluxes from SiB4. Future work should focus on refining land surface models and expanding COS observational networks, particularly in underrepresented regions, to strengthen constraints on the global COS budget. Ultimately, such advances may enable COS to fulfill its potential as a tracer of global photosynthetic carbon uptake.

A4. Appendices

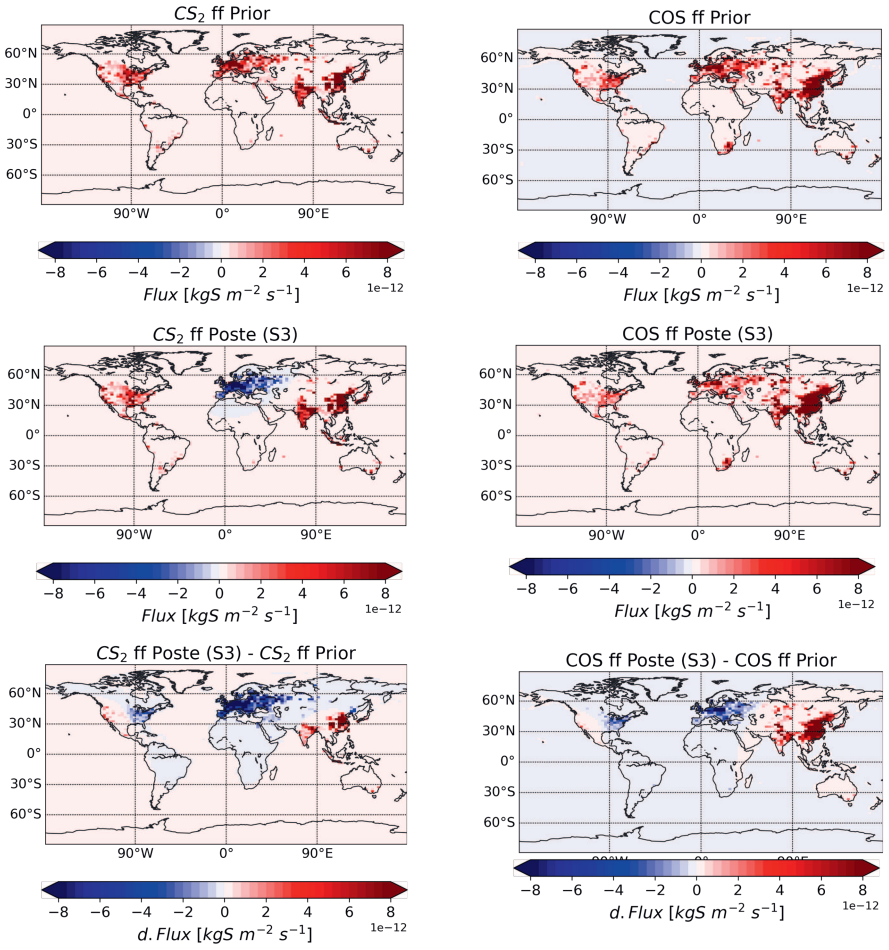


Figure A4.1: Spatial distribution of anthropogenic emissions of CS_2 (left column) and COS (right column) under the S3 scenario. Rows show prior (top) and posterior (middle) estimates, and their differences (bottom).

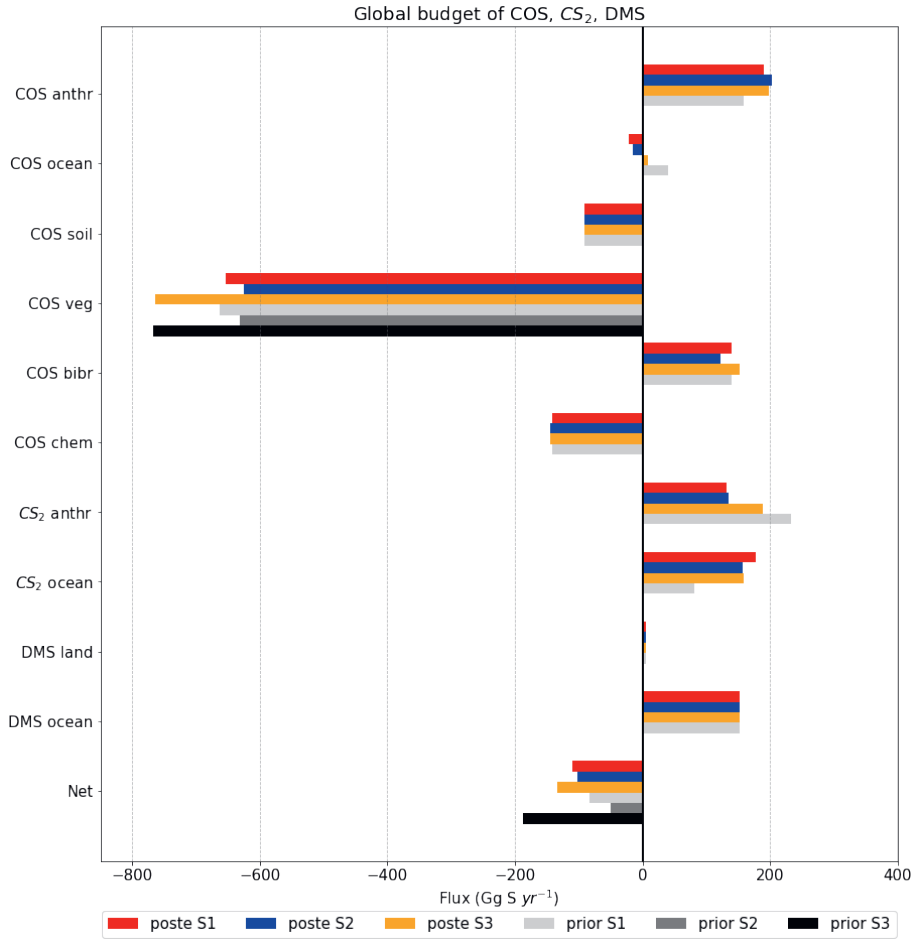


Figure A4.2: Global budget of COS with contributions from precursors CS_2 and DMS in prior and posterior emissions from three scenarios for the period July 2016 to June 2017.

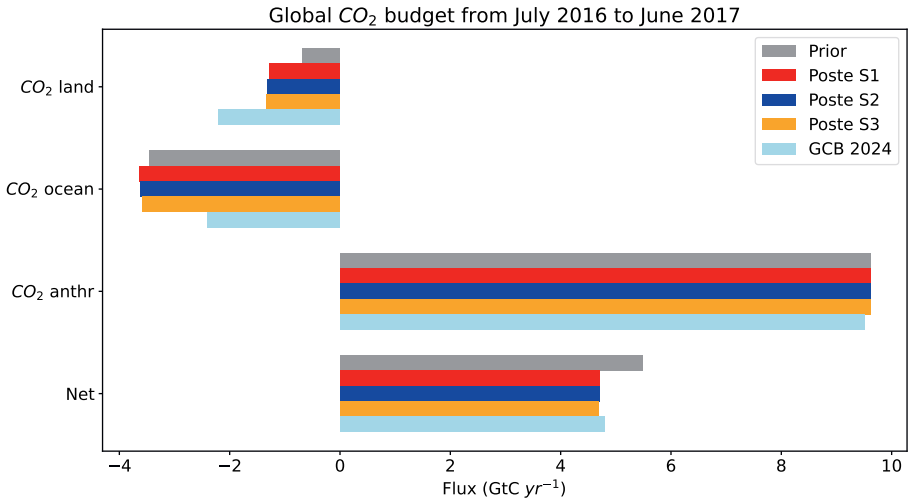


Figure A4.3: Global CO_2 budget from the prior and posterior inverse results in comparison to the mean of the GCB2024 inversions for the period July 2016 to June 2017.

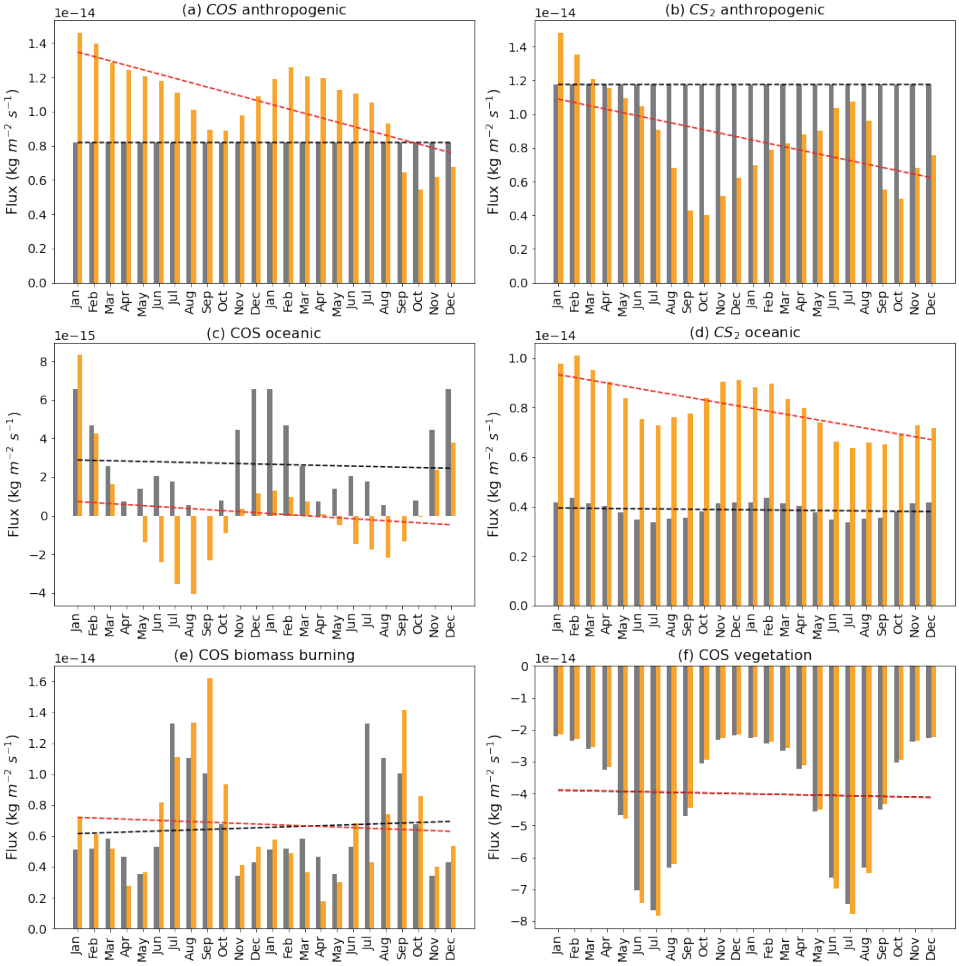


Figure A4.4: Histogram of the monthly mean flux values for COS and CS_2 surface fluxes designated as state variables in the COS optimization from 2016 to 2017. Gray bars represent prior fluxes, and orange bars represent posterior fluxes. The bars indicate surface fluxes, while the dotted lines show the linear regression trends over the corresponding period.

Chapter 5

General discussion & Synthesis

5.1 Integrated summary across scales

This thesis evaluates the potential of carbonyl sulfide (COS) as a tracer for Gross Primary Productivity (GPP) by integrating analyses across leaf, canopy, and global scale using inverse modeling frameworks. Although COS shares its primary uptake pathway with CO_2, our results show that COS leaf uptake responds differently from CO_2 uptake to temperature and stomatal conductance at the leaf scale. These differences, when carried forward to the canopy scale, support refinements in stomatal and mesophyll conductance parameterizations, which currently rely primarily on CO_2-based leaf uptake relationships.

The improved representation of COS biospheric fluxes, in turn, provided more realistic priors for global inversions, enhancing the accuracy of COS flux optimization and enabling evaluation of the validity of the previously assumed linear relationship between CO_2 and COS plant uptakes. Through this pathway, COS serves as a complementary tracer of photosynthesis, offering independent constraints on GPP that extend beyond those derived from CO_2 alone. In the following, I summarize the main findings at the leaf, canopy, and global scales to highlight both the insights gained and the remaining challenges.

At the leaf scale, important insights were obtained through chamber experiments and an optimized conductance model coupling H_2O, CO_2, and COS exchange (Chapter 2). First, we identified a likely temperature-dependent COS compensation point, showing that under high temperatures, leaf exchange can shift from net uptake to net emission. These findings challenge the widespread assumption of negligible direct COS emissions from vegetation and indicates that additional processes—potentially involving sulfur-related metabolism as well as mechanisms such as retro-diffusion or senescence processes—should be explicitly considered in leaf exchange estimations. Second, although the conductance model already accounts for the distinct sensitivities of COS and CO_2 to stomatal conductance (g_s), the greater sensitivity of COS to g_s means that uncertainties in g_s propagate more strongly into COS flux estimates than into CO_2 flux estimates. This amplified impact of stomatal dynamics is further discussed in Sect. 5.3.2.

At the canopy scale, we implemented a temperature-dependent mesophyll conductance (g_i) function for COS in the SiB4 land surface model and optimized both g_i and g_s parameters. These refinements improved the agreement between modeled and observed COS vegetation fluxes at both evergreen needleleaf forest (Hyytiälä, Finland) and deciduous broadleaf forest (Harvard Forest, USA). When propagated to the global scale, these improvements modified the magnitude of vegetation COS uptake, increasing uptake in high-latitude regions during the peak growing season, and reducing uptake throughout the year in tropical regions.

Although SiB4 already represents key canopy-scale processes—including sun–shade canopy structure, vertical microclimate gradients—translating leaf-level insights to canopy-scale behavior still requires caution. Leaf measurements are inherently local, whereas canopy fluxes integrate across heterogeneous environmental and physiological conditions. Thus, leaf-derived parameter behavior may not map linearly to canopy responses, underscoring the importance of cross-scale evaluation when constraining COS–based GPP estimates.

At the global scale, a coupled CO_2–COS inversion system was implemented within the TM5-4DVar framework. By jointly optimizing the fluxes of both gases, the system was used to evaluate the assumption of a linear coupling between COS uptake and photosynthesis. While posterior simulations better matched atmospheric CO_2 and COS mole fractions at surface observation sites, they remained insufficient to fully resolve the high-latitude COS sink discrepancy, underscoring the limitations of current model structures and the incomplete observational basis for COS. Furthermore, comparison across three different COS biosphere priors showed that estimates of other COS surface fluxes were highly sensitive to the choice of biosphere prior. This highlights the importance of using more realistic COS flux priors to improve the COS global budget, particularly in better constraining missing sources and sinks. At the same time, the small influence of COS vegetation flux priors on CO_2 fluxes suggests that, under current observational density and model structures (including the lack of a diurnal cycle representation in the inversion), coupled COS inversions provide limited additional constraint on CO_2 and hence GPP. This underlines the need for expanded COS observations and improved process representations before its full potential as a complementary tracer for GPP can be realized.

Overall, integrating analyses from leaf to global scales has shown how the distinct temperature and stomatal responses of COS, compared to CO_2 propagate through scales and influence canopy and global flux estimates. This stepwise approach was essential to disentangle where COS provides independent information on photosynthesis and where structural limitations remain. Across scales, the shared stomatal pathway among COS, CO_2, and H_2O enabled joint constraints that strengthened parameter estimation, particularly for stomatal conductance. While refinements in COS mesophyll conductance enhanced canopy-scale flux representation and contributed to more realistic priors at the global scale, they were not sufficient to resolve all remaining challenges. Coupled inversions at the global scale still revealed issues such as nonphysical negative values of anthropogenic emissions, emphasizing that incomplete process understanding in overall COS budget terms and sparse observations continue to limit the extent to which COS can be used as a robust tracer of GPP.

Thus, inverse modeling of COS across scales evaluated its potential as a tracer for GPP, while also revealing that its effective use remains constrained by methodological and structural uncertainties. In this chapter, I revisit the critical limitations of the approaches applied at each scale, synthesize their implications, and propose improvements to the prevailing assumptions that currently underpin COS-based GPP estimation. A summary of key findings, limitations, and future priorities is presented in Fig. 5.1.

5.2 Methodological limitations and uncertainties

Across the different scales considered in this dissertation, several methodological limitations and uncertainties emerged. These do not undermine the overall findings but define the boundaries within which the results can be interpreted. Highlighting them is essential both for cautious interpretation and for identifying where future methodological improvements are most urgently needed.

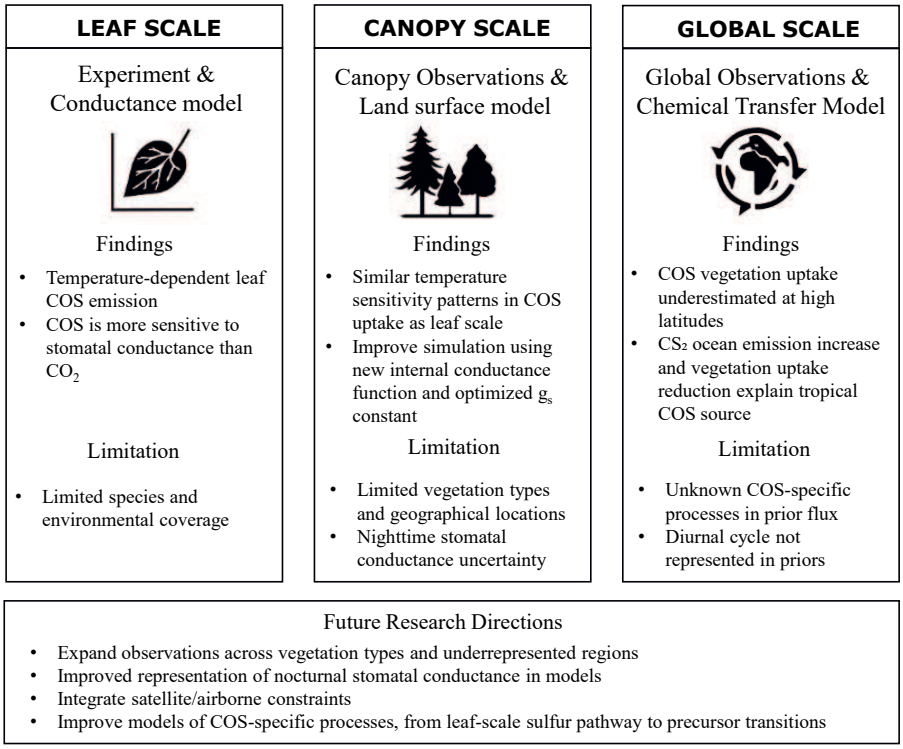


Figure 5.1: Summary of findings, limitations, and future research directions across leaf-ecosystem-global scales.

5.2.1 Limitations in COS observations

Limitations in current COS observational network influenced interpretation across leaf-, canopy-, and global-scale analyses in this dissertation. Below, I summarize the key observational factors that shaped the analyses and constrained the extent to which COS can currently serve as a tracer for photosynthesis.

A primary constraint lies in the precision of COS measurements. Observational uncertainty arises from both the inherently high random noise of COS flux measurements (Kooijmans et al., 2016; Kohonen et al., 2020) and persistent instrumental challenges, including calibration and sampling artifacts (Berkelhammer et al., 2014).

At the leaf scale, elevated COS mole fractions (approximately 1000 $\mathrm{pmol\,mol^{-1}}$) were required to obtain robust chamber signals, and temperature-dependent chamber emissions were observed. The reported precision of a quantum cascade laser spectrometer (QCLS) for COS is approximately 7.5 $\mathrm{pmol\,mol^{-1}}$(Kooijmans et al., 2016), and the uncertainty associated with empty-chamber corrections widened the uncertainty of COS compensation point from 53.2 to 93.4 $\mathrm{pmol\,mol^{-1}}$at 19.8 °C. Consequently, the interpretation of COS compensation points, derived under inflowing mole fractions of 100–600 $\mathrm{pmol\,mol^{-1}}$, must be made with caution.

At the canopy scale, eddy-covariance COS fluxes exhibited relatively high noise, and noc-

turnal g_s was subject to both observational uncertainty and incomplete model representation in the SiB4 land surface model, complicating inference of the temperature response of COS mesophyll conductance.

Second, limitations in the representativeness of COS observations persist across scales. Chamber-based COS uptake experiments remain sparse compared to CO_2-focused experiments, with limited representation of plant functional diversity. In this work, leaf-level analysis was conducted on a single species and a single phenological stage (flowering), over a relatively narrow temperature range, restricting generalization across plant types, phenological phases, and environmental gradients. At the canopy scale, parameter optimization was conducted at only two sites, yet applied globally. At the global scale, the inversion framework relied primarily on surface observations concentrated in North America and on a single simulation year, limiting constraints in regions with sparse observational coverage.

Likewise, at the canopy scale, parameter optimization was conducted at only two sites, yet applied globally, and did not include winter conditions, limiting representation of seasonal variation in COS uptake.

Together, these limitations indicate that current COS-based constraints on photosynthesis across scales remain partial, reflecting both the precision limits inherent to trace-gas COS measurements and the still-developing global observational network.

5.2.2 Limits to identify parameters

A recurring limitation across scales was the difficulty of constraining model parameters, driven by relatively large observational uncertainties of COS and by incomplete mechanistic knowledge of COS leaf exchange.

We diagnose this limitation through posterior covariances, which were often large and indicated that many parameter combinations could fit the data equally well. In such cases, the selected set is simply the one that minimizes the cost function (see Introduction), which provides the most straightforward explanation supported by the data. While this is a useful working hypothesis, it also means that applying the optimized parameters beyond the conditions of their calibration may cause problems. For this reason, current COS-based parameter estimates should be interpreted with caution, as alternative explanations cannot be excluded.

At the leaf scale, the reduction of COS uptake at higher temperatures was interpreted primarily as evidence for temperature-dependent COS emissions from leaves. Alternative formulations—such as a lower optimum temperature of carbonic anhydrase activity relative to RuBisCO—were tested and resulted in only minor differences in cost function values. While these alternatives cannot be entirely excluded, the possibility of direct COS emissions from plants has been repeatedly reported in previous studies (Maseyk et al., 2014; Gimeno et al., 2017; Belviso et al., 2022). In our analysis, the minimum cost was obtained under an emission-based formulation; therefore, we adopt a COS compensation point as the primary explanation for the observed reduction of leaf uptake at high temperatures. The underlying cause of these emissions, however, remains uncertain: they may arise from retro-diffusivity (back-diffusion from internal storage pools), temperature stress, species-specific physiological traits, or depends on the phenological stage.

At the canopy scale (Chapter 3), a similar non-uniqueness in parameter estimation became evident in the conductance-related optimization. In this analysis, the proportionality constant b_1, which links g_s to photosynthetic rate, and the calibration factor α, which scales g_i, were both adjusted. Different combinations of these two parameters produced similarly low cost function values, highlighting challenges in parameter estimation. As a result, the observed

flux improvements cannot be uniquely attributed to either stomatal or mesophyll processes, limiting the mechanistic interpretability of the optimized parameters.

Taken together, these challenges limit the interpretability and generalization of optimized parameters across scales and should be considered when comparing model structures or applying the parameters beyond the conditions that were used in the optimization. To address this, we reported posterior parameter covariances in the leaf- and canopy-scale analyses (Chapter 2 and Chapter 3), which allows error propagation via Monte Carlo simulations. At the global scale, however, this level of reporting was not feasible because the 4D-Var inversion framework involves a very high-dimensional state space, making full posterior covariance estimation computationally impractical. This remains a limitation of the present study.

5.2.3 Structural simplification in land surface model

Current land surface models, including SiB4, typically prescribe COS vegetation fluxes as a linear function of photosynthesis, using fixed calibration factors for mesophyll and stomatal conductance that differ only between C_3 and C_4 plants. This simplification collapses diverse environmental responses and plant functional strategies into a single proportionality, introducing structural uncertainty in both CO_2 and COS flux estimates.

The leaf- and canopy-scale results presented in this dissertation highlight why such simplifications are problematic. The strong temperature dependence of COS uptake, which can even lead to emissions under high temperatures, together with the increased sensitivity of COS uptake to stomatal closure, challenge the assumption of a linear coupling with GPP. When implemented into global priors, refined parameterizations helped reduce some systematic biases, such as the tendency for underestimated vegetation uptake in the tropics and overestimated uptake at high latitudes, but they did not eliminate persistent mismatches, including the non-physical negative values of anthropogenic emissions in high-latitude regions.

These findings suggest that the widely used linear coupling of COS uptake with photosynthesis—the leaf relative uptake (LRU)—can serve only as a first-order approximation. Without more mechanistic representations of both stomatal and mesophyll processes, model–observation discrepancies will remain, limiting the robustness of COS as a tracer for GPP in current inversion systems.

5.3 Cross-scale linkages and interpretation

5.3.1 Mesophyll conductance and COS compensation point

When stomata are sufficiently open, g_i becomes the dominant factor controlling total conductance and thereby COS fluxes, as illustrated in Chapter 3 (Fig. 3.5). The newly adopted temperature-dependent g_i function improved canopy-scale flux representation, reducing systematic biases across temperature regimes and providing better alignment with observations.

Because canopy-scale analysis was conducted as the first step of this PhD research, the g_i function was introduced before leaf-level experiments were available. At that stage, the observed decline in COS uptake at higher temperatures was interpreted as a consequence of the lower optimum temperature of CA activity relative to RuBisCO. Subsequent leaf-level experiments with sunflower plants (Chapter 2), however, interpreted this phenomenon as the presence of a temperature-dependent COS compensation point. Model optimization showed that this compensation point provided a more convincing explanation for the decline in COS uptake at high temperatures than the lower optimum temperature of biochemical activity. Additional

experiments, in which inflowing COS mole fractions were gradually reduced, confirmed the existence of COS compensation point.

Although species-specific generalization remains premature given that our experiment was limited to sunflower, the observed decline in COS uptake at higher temperatures is most plausibly driven by temperature-dependent leaf processes. As discussed in Chapter 4, such behavior may arise from stress-induced protein degradation, which can release COS through the breakdown of sulfur-containing amino acids (Gimeno et al., 2017). However, the possibility of retro-diffusivity from internal COS pools cannot be excluded.

While our experiments in Chapter 2 were conducted below 30 °C, leaf-level COS behavior at higher temperatures can be inferred from recent drought- and heat-stress studies. For example, field measurements during heatwave and developing drought conditions in a Californian oak woodland show that elevated leaf temperatures can restrict internal diffusion and substantially alter COS uptake dynamics, with notable occurrences of COS emissions under extreme heat (Sun et al., 2024). Similarly, drought-stress studies demonstrate that stress can induce bidirectional COS exchange and cause shifts in LRU (species-specific), highlighting additional non-stomatal controls that become relevant under drought conditions (Spielmann et al., 2025). Together, these findings suggest that elevated temperatures may reduce internal diffusion capacity or biochemical activity and thereby suppress uptake—or even generate net emissions. Such responses diverge fundamentally from those of CO_2 and are likely to vary across species.

The experiments were conducted under relatively high inflowing COS mole fractions, which may have enhanced internal storage and subsequent release (Stimler et al., 2010). Importantly, such retro-diffusive processes are not represented in either the conductance model or the SiB4 land surface model, making it difficult to evaluate this mechanism through model optimization alone. Thus, while our findings support the presence of a compensation point, distinguishing between biochemical and diffusive contributions requires further investigation. Additionally, confirmation of COS compensation points across a broader range of species and environmental conditions remains essential.

Several uncertainties remain regarding the generalization of the COS compensation point. Although both leaf- and canopy-scale analyses consistently showed a decline in COS uptake at higher temperatures, and applying the new temperature-dependent g_{i} function improved model predictions, linking this decline directly to a compensation point remains tentative. This reflects not only incomplete mechanistic understanding but also experimental limitations, as already discussed in Sect. 5.2.1: temperature-dependent chamber emissions could not be fully eliminated, leaving residual uncertainty, and the current precision of QCLS instruments still challenges robust quantification of COS exchange at low COS mole fractions. Thus, while the compensation point interpretation is supported by our optimization results, alternative explanations for these observations cannot yet be fully excluded.

Taken together, these results highlight that the reduction of COS uptake at high temperatures cannot be fully captured by a current mesophyll conductance function, which is derived as a linear function of CO_2 biochemical activity. Whether this decline is primarily driven by a compensation point or by other mesophyll-level mechanisms remains a central uncertainty. Addressing this question will require more extensive observations across species, climatic regions, including evergreens, where seasonal variability is less pronounced.

5.3.2 Stomatal conductance and diurnal dynamics

Values of g_{s} have been typically derived from water vapor and CO_2 leaf exchange information. In this dissertation, incorporating COS alongside CO_2 and H_2O fluxes strengthened con-

straints on stomatal conductance, reducing the prior uncertainty of g_s ($0.09\ \mathrm{mol\,m^{-2}\,s^{-1}}$) to $0.05\ \mathrm{mol\,m^{-2}\,s^{-1}}$(Chapter 2). This improvement occurred while simultaneously optimizing mesophyll conductance–related parameters, highlighting that COS provides additional constraints on g_s estimation.

Particularly, COS observations are uniquely valuable for providing additional information on stomatal behavior under low light conditions, where conventional CO_2 flux data provide limited information. Zhu et al. (2024) further showed that COS assimilation is informative for parameters controlling the minimum stomatal conductance, the residual nocturnal g_s that remains even when stomata are nearly closed.

Leaf-scale experiments described in this dissertation also confirmed that COS uptake is much more sensitive to stomatal closure than CO_2 uptake, as already suggested by Sun et al. (2018a) and Kooijmans et al. (2019). Under conditions of high VPD or at night, when g_s is low, even small errors in simulating g_s can propagate into larger discrepancies in COS flux estimates than CO_2 estimates.

At the canopy scale, although mesophyll conductance contributes importantly to total conductance, stomatal dynamics dominated COS variability during transitions between opening and closure. Optimization of g_s and g_i parameters improved the overall representation of COS exchange, yet diurnal patterns of g_s remained poorly captured in land surface model SiB4, particularly at night and during the autumn (Chapter 3). Specifically, in our canopy-scale analysis at Hyytiälä (Chapter 3), located at high latitudes (61 °N), where even with 3-hourly fluxes and optimized stomatal and mesophyll conductance parameters, late autumn (October) uptake was underestimated both during day and night. This persistent underestimation might indicate that the current conductance formulation in SiB4 does not adequately represent nocturnal stomatal behavior. This is consistent with the findings of Berchet et al. (2025), who showed that for SiB4, monthly fluxes failed to capture nighttime uptake in summer, whereas 3-hourly fluxes reproduced these patterns more accurately. However, both fluxes underestimated both daytime and nighttime uptake in autumn and winter.

Empirical studies have shown that circadian control and environmental constraints together regulate nocturnal stomata closure (Caird et al., 2007; Zeppel et al., 2014; De Dios et al., 2015), processes that also explain why nocturnal transpiration can account for a non-negligible share of daily water loss. In the Ball–Woodrow–Berry (BWB) formulation for g_s estimation as implemented in the SiB4 model, nocturnal g_s is represented only through a constant intercept term, which in SiB4 is further scaled by LAI and soil moisture stress. However, dynamic physiological controls are not explicitly represented. As a result, systemic biases may arise in simulated energy and water fluxes (Wang et al., 2021), and for COS these errors are amplified due to its strong sensitivity to stomatal regulation. This highlights the need for improved parameterizations in SiB4 that explicitly represent nocturnal stomatal dynamics across vegetation types.

At the global scale, our TM5-4DVar inversion optimized fluxes only at monthly resolution, without resolving diurnal variability in the inversion (Chapter 4). For CO_2, neglecting subdaily variation already introduced regional biases of up to 48% in Europe (Munassar et al., 2025). While CO_2 accumulates in the boundary layer due to respiration, for COS, where uptake persists at night and responds more steeply to stomatal closure (see Fig. 1.7, such aggregation errors are likely even larger. This opposite behavior highlights that neglecting diurnal cycles might introduce structural biases. These biases may help explain the persistent underestimation of COS biosphere fluxes and the relatively large ocean CO_2 sink compared to the Global Carbon Budget (GCB) 2024 analysis in the global scale inversions.

5.3.3 Remaining gaps in the global COS budget

Despite recent progress, significant gaps remain in the global COS budget. In the tropics, a persistent "missing source" has been identified in multiple inversion studies (Suntharalingam et al., 2008; Berry et al., 2013; Lennartz et al., 2017; Ma et al., 2021). Explanations point either to underestimated emissions of oceanic precursors such as CS_2 and DMS (Lennartz et al., 2021; Remaud et al., 2022; Ma et al., 2024) or to an overestimation of the biospheric sink (e.g., Ma et al., 2021; Stinecipher et al., 2022). Our results support this dual interpretation.

At high northern latitudes, our inversions consistently suggest stronger vegetation sinks than those simulated by current land surface models, as previously suggested by Ma et al. (2021) and Kooijmans et al. (2021). While soil uptake may contribute, the magnitude of the discrepancy points more plausibly to underestimated vegetation uptake. These biases likely arise from the use of monthly biosphere fluxes that neglect diurnal cycles, as well as the incomplete representation of COS-specific mechanisms in current models. As discussed in Sect. 5.3.2, the simplified treatment of nocturnal stomatal conductance further propagates into global-scale underestimations. Supporting this interpretation, Kuai et al. (2022) showed that optimized COS vegetation fluxes in Alaska were about 25% larger than those derived by scaling GPP. This finding is consistent with our canopy-scale results, where SiB4 underestimated COS uptake during autumn, suggesting that linear GPP-based scaling may limit the capture of seasonal and stomatal controls on COS exchange at high latitudes.

In parallel, anthropogenic emissions remain a significant source of uncertainty. Our inversion results for Europe (Chapter 4) indicated overestimation in inventories, consistent with Belviso et al. (2023). Large uncertainties persist in other regions, notably Asia (Du et al., 2016). For instance, Yan et al. (2019) found that prior anthropogenic emissions over China based on Zumkehr et al. (2018) were underestimated, highlighting evaluation and improvement of anthropogenic COS and CS_2 emission is critical for resolving COS budget discrepancies.

Finally, other underlying processes remain poorly constrained. As discussed in Chapter 4, these include precursor conversion pathways such as hydroperoxymethyl thioformate (HPMTF) mechanism (Veres et al., 2020; Jernigan et al., 2022; Von Hobe et al., 2023), uncertainties in precursor lifetimes driven by OH availability and temperature (Lennartz et al., 2021; Berchet et al., 2025), and insufficiently quantified natural emissions from wetlands (Whelan et al., 2013) and volcanic activity (Whelan et al., 2018). These issues underscore the need for improved emission inventories, expanded observational coverage with for instance satellite data, and better mechanistic understanding.

5.4 Future research directions

5.4.1 Refining the physiological basis of COS leaf uptake

A key priority is to expand leaf-scale experiments across a broader range of plant functional types and growing environments. This should include plants adapted to contrasting climatic zones—such as tropical, arid, and boreal species—since their differing physiological strategies for coping with heat, drought, or cold may strongly influence COS exchange (Whelan et al., 2018). Furthermore, conducting observations across different phenological stages would help identify drivers of leaf-level emissions, including stress-induced or microbial pathways (Kesselmeier et al., 1993; Maseyk et al., 2014; Belviso et al., 2022).

Future progress will require direct observations of CA activity, which are currently lacking. Future studies should aim to quantify the temperature-response functions of CA across different plant types, and explore the minor but potentially relevant roles in COS uptake of

other enzymes such as RuBisCO and phosphoenolpyruvate carboxylase (PEP-C) (Lorimer et al., 1989; Protoschill-Krebs et al., 1992; Protoschill-Krebs et al., 1996).

Leaf-scale experiments across diverse plant species and climate zones would help uncover still unknown mechanisms of COS uptake, such as the existence and temperature response of COS compensation points, diffusivity properties within mesophyll cells, the temperature response of CA activity, and the physiological relationship between g_s and atmospheric COS mole fractions. Improving laboratory precision for COS at ambient mole fractions would enable leaf-level optimization experiments without elevated COS mole fractions. Such advances would improve the accuracy of estimating compensation points.

In addition, such experiments would provide critical insight into climate-dependent physiological adaptation, which is essential for accurately characterizing and modeling COS exchange under varying environmental conditions.

5.4.2 Improving land surface models

At the canopy scale, ecosystem-level datasets remain heavily biased toward temperate forests. Incorporating long-term data from more diverse biomes, including tropical, boreal, and semi-arid ecosystems, would enable more representative optimization of land surface model (LSM) parameters. Improved simulation of the diurnal cycle of the COS flux is particularly important, since COS provides unique constraints on nighttime stomatal conductance, a process difficult to resolve with CO_2 flux data alone.

Most current LSMs still rely on a linear relationship between COS uptake and CO_2 assimilation. However, leaf relative uptake (LRU) varies substantially with environmental conditions and plant species. COS modules should therefore be reformulated as dynamic and functional relationships rather than fixed ratios. In line with this, our 4D-Var results showed that doubling COS uptake in high northern latitudes improved model performance, highlighting the need to revisit flux estimates in that region.

As discussed in the previous section (Sect. 5.4.1), improving the mechanistic understanding of leaf-level COS exchange—including compensation point behavior, mesophyll diffusivity, and climate-dependent physiological adaptations—is essential. These findings must eventually be incorporated into land surface models to ensure that COS flux parameterizations reflect biological reality rather than empirical tuning.

Models should also incorporate more realistic formulations of g_s and g_i, particularly under conditions where current simplifications introduce structural biases. Nocturnal and residual g_s dynamics remain poorly represented in SiB4 and similar models, despite their large influence on COS exchange. Therefore, key directions for g_s improvements include (i) developing parameterizations for nocturnal g_s that reflect circadian and environmental controls, (ii) testing alternative formulations such as Medlyn et al. (2011) or Leuning (1995), (iii) constraining g_s through joint assimilation of CO_2, H_2O, and COS fluxes—as demonstrated in the leaf-level approach of this dissertation—and (iv) incorporating observations from a broader range of plant functional types and ecosystems to improve the representation of the g_s model. Addressing these aspects will allow models to capture COS dynamics more reliably across scales and reduce key uncertainties in GPP estimation.

5.4.3 Enhancing the global CO_2–COS coupled 4D-Var system

At present, the coupled inversion system represents vegetation COS fluxes as a single linear scaling of GPP, oversimplifying the physiological and environmental variability across species and conditions. Because stomatal and mesophyll conductances exhibit strong diurnal and

seasonal modulation, and because these responses differ between CO_2 and COS owing to their distinct biochemical and diffusional controls, a more physiologically informed—yet still simple and robust—coupling is required. Semi-dynamic formulations, for example, distinguishing day versus night or applying bounded responses to temperature and vapor pressure deficit—could better capture divergences between COS and CO_2 under low-g_s conditions. Any increase in model flexibility, however, must be paired with strong priors and regularization to avoid overfitting (see Sect. 5.2.2).

New techniques like Machine learning could provide complementary value by empirically parameterizing COS uptake as a function of multiple environmental drivers (e.g., VPD, temperature, radiation). For instance, Liu et al. (2025) showed that memory-based deep learning can capture COS and CO_2 flux dynamics in boreal forests, highlighting nonlinear dependencies on drivers such as temperature and vapor pressure deficit. However, predictive performance varied substantially across timescales, while still demonstrating the potential of such approaches as a complement to mechanistic modeling.

In our global inversion system (Chapter 4), we optimized monthly mean fluxes, similar to most existing global studies (e.g., Remaud et al., 2022), without considering the diurnal cycle on the surface fluxes. Neglecting diurnal variability introduces structural inconsistencies—especially for COS, which maintains a nocturnal uptake—leading to larger biases in high-latitude regions with long nights and strong seasonality. Moving beyond optimizations based on monthly mean fluxes toward formulations that resolve diurnal variability, together with plant-type-specific mesophyll conductance, will be essential for robust global applications. Independent single-gas optimizations could also help quantify the added value of coupled inversions. Refining error structures, for example, through weighting factors or covariance formulations, would further ensure consistent treatment of the distinct uncertainties of CO_2 and COS observations.

Integration of multi-platform measurements—surface stations and satellites—will be key to improving coverage in the tropics and high latitudes, where uncertainties in carbon fluxes are largest. Parallel improvements in emission inventories, including precursor transformations (e.g., CS_2, DMS), anthropogenic sources, and volcanic contributions, will further enhance the accuracy of coupled CO_2–COS inversions.

5.5 Outlook for estimating GPP from COS vegetation flux

Incorporating COS into GPP estimation offers clear advantages over approaches that rely solely on CO_2, because both gases share the stomatal diffusion pathway. However, unlike CO_2, COS is a sulfur compound with distinct intracellular mechanisms, and without good mechanistic understanding, its benefits as a tracer remain limited.

Addressing this uncertainty requires coordinated observations across leaf, canopy, and global scales to establish a consistent empirical basis, including a diverse range of species, more spatially balanced monitoring networks, and long-term measurement efforts. Building on this foundation, multi-tracer approaches, such as those already explored in site-level studies combining COS and SIF (Wohlfahrt et al., 2018), together with expanded satellite observations and the application of machine-learning methods, will be essential to fill observational gaps and improve prior process understanding.

Progress in this direction has the potential to improve carbon budget assessments at both global and regional scales. Using COS information to derive more reliable regional GPP constraints would strengthen confidence in climate-change projections and mitigation strategies. Yet, realizing this potential hinges on a deeper understanding of species- and phenology-

specific variability in COS uptake, accurate representation of conductance pathways, and explicit treatment of diurnal cycles.

Beyond photosynthesis, improving the accuracy of COS flux estimation also advances the modeling of land–atmosphere exchange. Because COS uptake is more sensitive to stomatal conductance than CO_2, and provides information on nocturnal stomatal behavior, it offers unique leverage for constraining stomatal dynamics. Such improvements in g_s and GPP estimation could jointly constrain transpiration and energy fluxes, thereby enhancing both vegetation and meteorological components of Earth system models. Ultimately, such integrative approaches will determine whether COS can fulfill its promise as a robust tracer of photosynthesis in a changing climate.

References

Abadie, C., F. Maignan, M. Remaud, J. Ogee, J. E. Campbell, M. E. Whelan, F. Kitz, F. M. Spielmann, G. Wohlfahrt, R. Wehr, et al. (2022). "Global modelling of soil carbonyl sulfide exchanges". *Biogeosciences* 19.9. DOI: 10.5194/bg-19-2427-2022.

Adnew, G. A., M. E. Hofmann, T. L. Pons, G. Koren, M. Ziegler, L. J. Lourens, and T. Röckmann (2021). "Leaf scale quantification of the effect of photosynthetic gas exchange on $\Delta 47$ of CO2". *Scientific Reports* 11.1. DOI: 10.1038/s41598-021-93092-0.

Adnew, G. A., T. L. Pons, G. Koren, W. Peters, and T. Röckmann (2020). "Leaf-scale quantification of the effect of photosynthetic gas exchange on δ17O of atmospheric CO2". *Biogeosciences* 17.14. DOI: 10.5194/bg-17-3903-2020.

— (2023). "Exploring the potential of Δ17O in CO2 for determining mesophyll conductance". *Plant Physiology* 192.2. DOI: 10.1093/plphys/kiad173.

Amthor, J. S., G. W. Koch, and A. J. Bloom (1992). "CO2 inhibits respiration in leaves of Rumex crispus L.1". *Plant Physiology* 98.2. DOI: 10.1104/pp.98.2.757.

Anav, A., P. Friedlingstein, C. Beer, P. Ciais, A. Harper, C. Jones, G. Murray-Tortarolo, D. Papale, N. C. Parazoo, P. Peylin, et al. (2015). "Spatiotemporal patterns of terrestrial gross primary production: A review". *Reviews of Geophysics* 53.3. DOI: 10.1002/2015RG000483.

Andreae, M. O. (2019). "Emission of trace gases and aerosols from biomass burning - An updated assessment". *Atmospheric Chemistry and Physics* 19.13. DOI: 10.5194/acp-19-8523-2019.

Anthony Vincent, R. and A. Dudhia (2017). "Fast retrievals of tropospheric carbonyl sulfide with IASI". *Atmospheric Chemistry and Physics* 17.4. DOI: 10.5194/acp-17-2981-2017.

Asaf, D., E. Rotenberg, F. Tatarinov, U. Dicken, S. A. Montzka, and D. Yakir (2013). "Ecosystem photosynthesis inferred from measurements of carbonyl sulphide flux". *Nature Geoscience* 6.3. DOI: 10.1038/ngeo1730.

Aubinet, M. (2008). "Eddy covariance CO2 flux measurements in nocturnal conditions: An analysis of the problem". *Ecological Applications* 18.6. DOI: 10.1890/06-1336.1.

Aydin, M., J. E. Campbell, T. J. Fudge, K. M. Cuffey, M. R. Nicewonger, K. R. Verhulst, and E. S. Saltzman (2016). "Changes in atmospheric carbonyl sulfide over the last 54,000years inferred from measurements in Antarctic ice cores". *Journal of Geophysical Research* 121.4. DOI: 10.1002/2015JD024235.

Badger, M. and G. Collatz (1977). "Studies on the kinetic mecha- nism of ribulose-1,5-bisphosphate carboxylase and oxygenase reactions with particular reference to the effect of temperature on kinetic parameters". *Carnegie Institution of Washington Yearbook* 76.1961.

Badger, M. R. and G. D. Price (1994). "The role of carbonic anhydrase in photosynthesis". *Annual Review of Plant Physiology and Plant Molecular Biology* 45.1. DOI: 10.1146/annurev.pp.45.060194.002101.

Baldocchi, D. D., R. J. Luxmoore, and J. L. Hatfield (1991). "Discerning the forest from the trees: an essay on scaling canopy stomatal conductance". *Agricultural and Forest Meteorology* 54.2-4. DOI: 10.1016/0168-1923(91)90006-C.

Ball, J. T., I. E. Woodrow, and J. A. Berry (1987). "A Model Predicting Stomatal Conductance and its Contribution to the Control of Photosynthesis under Different Environmental Conditions". *Progress in Photosynthesis Research*. Ed. by J. Biggins. Dordrecht: Springer Netherlands, pp. 221–224. DOI: 10.1007/978-94-017-0519-6_48.

Ball, J. T. (1988). *An analysis of stomatal conductance*. Vol. 670. Stanford University Stanford.

Barnes, I., K. H. Becker, and I. Patroescu (1996). "FTIR product study of the OH intiated oxidation of dimethyl sulphide: Observation of carbonyl sulphide and imethyl sulphoxide". *Atmospheric Environment* 30.10-11. DOI: 10.1016/1352-2310(95)00389-4.

Basu, S., D. F. Baker, F. Chevallier, P. K. Patra, J. Liu, and J. B. Miller (2018). "The impact of transport model differences on CO2 surface flux estimates from OCO-2 retrievals of column average CO2". *Atmospheric Chemistry and Physics* 18.10. DOI: 10.5194/acp-18-7189-2018.

Bauerle, W. L., A. B. Daniels, and D. M. Barnard (2014). "Carbon and water flux responses to physiology by environment interactions: A sensitivity analysis of variation in climate on photosynthetic and stomatal parameters". *Climate Dynamics* 42.9-10. DOI: 10.1007/s00382-013-1894-6.

Belviso, S., C. Abadie, D. Montagne, D. Hadjar, D. Tropée, L. Vialettes, V. Kazan, M. Delmotte, F. Maignan, M. Remaud, et al. (2022). "Carbonyl sulfide (COS) emissions in two agroecosystems in central France". *PLoS ONE* 17.12 December. DOI: 10.1371/journal.pone.0278584.

Belviso, S., I. Masotti, A. Tagliabue, L. Bopp, P. Brockmann, C. Fichot, G. Caniaux, L. Prieur, J. Ras, J. Uitz, et al. (2012). "DMS dynamics in the most oligotrophic subtropical zones of the global ocean". *Biogeochemistry* 110.1-3. DOI: 10.1007/s10533-011-9648-1.

Belviso, S., I. Pison, J. E. Petit, A. Berchet, M. Remaud, L. Simon, M. Ramonet, M. Delmotte, V. Kazan, C. Yver-Kwok, et al. (2023). "The Z-2018 emissions inventory of COS in Europe: A semiquantitative multi-data-streams evaluation". *Atmospheric Environment* 300. DOI: 10.1016/j.atmosenv.2023.119689.

Belviso, S., M. Schmidt, C. Yver, M. Ramonet, V. Gros, and T. Launois (2013). "Strong similarities between night-time deposition velocities of carbonyl sulphide and molecular hydrogen inferred from semi-continuous atmospheric observations in Gif-sur-Yvette, Paris region". *Tellus B: Chemical and Physical Meteorology* 65.1. DOI: 10.3402/tellusb.v65i0.20719.

Berchet, A., I. Pison, C. Huselstein, C. Narbaud, M. Remaud, S. Belviso, C. Abadie, and F. Maignan (2025). "Improved understanding of anthropogenic and biogenic carbonyl sulfide (COS) fluxes in western Europe from long-term continuous mixing ratio measurements". *Atmospheric Chemistry and Physics* 25.13, pp. 7499–7525. DOI: 10.5194/acp-25-7499-2025.

Bergamaschi, P., M. Krol, J. F. Meirink, F. Dentener, A. Segers, J. Van Aardenne, S. Monni, A. T. Vermeulen, M. Schmidt, M. Ramonet, et al. (2010). "Inverse modeling of European CH4 emissions 2001-2006". *Journal of Geophysical Research Atmospheres* 115.22. DOI: 10.1029/2010JD014180.

Berkelhammer, M., D. Asaf, C. Still, S. Montzka, D. Noone, M. Gupta, R. Provencal, H. Chen, and D. Yakir (2014). "Constraining surface carbon fluxes using in situ measurements of carbonyl sulfide and carbon dioxide". *Global Biogeochemical Cycles* 28.2. DOI: 10 . 1002 / 2013GB004644.

Bernath, P. F., J. Crouse, R. C. Hughes, and C. D. Boone (2021). "The Atmospheric Chemistry Experiment Fourier transform spectrometer (ACE-FTS) version 4.1 retrievals: Trends and seasonal distributions". *Journal of Quantitative Spectroscopy and Radiative Transfer* 259, p. 107409. DOI: https://doi.org/10.1016/j.jqsrt.2020.107409.

Berry, J., A. Wolf, J. E. Campbell, I. Baker, N. Blake, D. Blake, A. S. Denning, S. R. Kawa, S. A. Montzka, U. Seibt, et al. (2013). "A coupled model of the global cycles of carbonyl sulfide and CO2: A possible new window on the carbon cycle". *Journal of Geophysical Research: Biogeosciences* 118.2. DOI: 10.1002/jgrg.20068.

Bielecki, Z., T. Stacewicz, J. Wojtas, and J. Mikołajczyk (2015). "Application of quantum cascade lasers to trace gas detection". *Bulletin of the Polish Academy of Sciences: Technical Sciences* 63.2. DOI: 10.1515/bpasts-2015-0059.

Billesbach, D. P., J. A. Berry, U. Seibt, K. Maseyk, M. S. Torn, M. L. Fischer, M. Abu-Naser, and J. E. Campbell (2014). "Growing season eddy covariance measurements of carbonyl sulfide and CO2 fluxes: COS and CO2 relationships in Southern Great Plains winter wheat". *Agricultural and Forest Meteorology* 184. DOI: 10.1016/j.agrformet.2013.06.007.

Black, V. J. and H. G. Jones (1985). "Plants and Microclimate." *The Journal of Applied Ecology* 22.2. DOI: 10.2307/2403198.

Blake, N. J., J. E. Campbell, S. A. Vay, H. E. Fuelberg, L. G. Huey, G. Sachse, S. Meinardi, A. Beyersdorf, A. Baker, B. Barletta, et al. (2008). "Carbonyl sulfide (OCS): Large-scale distributions over North America during INTEX-NA and relationship to CO2". *Journal of Geophysical Research Atmospheres* 113.9. DOI: 10.1029/2007JD009163.

Blezinger, S., C. Wilhelm, and J. Kesselmeier (2000). "Enzymatic consumption of carbonyl sulfide (COS) by marine algae". *Biogeochemistry* 48.2. DOI: 10.1023/A:1006134213995.

Bonan, G. B. (2008). *Forests and climate change: Forcings, feedbacks, and the climate benefits of forests*. DOI: 10.1126/science.1155121.

Bosman, P. J. and M. C. Krol (2023). "ICLASS 1.1, a variational Inverse modelling framework for the Chemistry Land-surface Atmosphere Soil Slab model: description, validation, and application". *Geoscientific Model Development* 16.1. DOI: 10.5194/gmd-16-47-2023.

Bowman, K. W., J. Liu, A. A. Bloom, N. C. Parazoo, M. Lee, Z. Jiang, D. Menemenlis, M. M. Gierach, G. J. Collatz, K. R. Gurney, et al. (2017). "Global and Brazilian Carbon Response to El Niño Modoki 2011–2010". *Earth and Space Science* 4.10. DOI: 10.1002/2016EA000204.

Boyd, R. A., A. Gandin, and A. B. Cousins (2015). "Temperature responses of C4 photosynthesis: Biochemical analysis of Rubisco, phosphoenolpyruvate carboxylase, and carbonic anhydrase in Setaria viridis". *Plant Physiology* 169.3. DOI: 10.1104/pp.15.00586.

Brasseur, G. P. and D. J. Jacob (2017). *Modeling of atmospheric chemistry*. DOI: 10.1017/9781316544754.

Brühl, C., J. Lelieveld, P. J. Crutzen, and H. Tost (2012). "The role of carbonyl sulphide as a source of stratospheric sulphate aerosol and its impact on climate". *Atmospheric Chemistry and Physics* 12.3. DOI: 10.5194/acp-12-1239-2012.

Caemmerer, S. von and G. D. Farquhar (1981). "Some relationships between the biochemistry of photosynthesis and the gas exchange of leaves". *Planta* 153.4. DOI: 10.1007/BF00384257.

Caemmerer, S. von and J. R. Evans (2015). "Temperature responses of mesophyll conductance differ greatly between species". *Plant Cell and Environment* 38.4. DOI: 10.1111/pce.12449.

Caird, M. A., J. H. Richards, and L. A. Donovan (2007). "Nighttime stomatal conductance and transpiration in C3 and C4 plants". *Plant Physiology* 143.1. DOI: 10.1104/pp.106.092940.

Campbell, J. E., J. A. Berry, U. Seibt, S. J. Smith, S. A. Montzka, T. Launois, S. Belviso, L. Bopp, and M. Laine (2017). "Large historical growth in global terrestrial gross primary production". *Nature* 544.7648. DOI: 10.1038/nature22030.

Campbell, J. E., G. R. Carmichael, T. Chai, M. Mena-Carrasco, Y. Tang, D. R. Blake, N. J. Blake, S. A. Vay, G. J. Collatz, I. Baker, et al. (2008). "Photosynthetic control of atmospheric carbonyl sulfide during the growing season". *Science* 322.5904. DOI: 10.1126/science.1164015.

Campbell, J. E., M. E. Whelan, U. Seibt, S. J. Smith, J. A. Berry, and T. W. Hilton (2015). "Atmospheric carbonyl sulfide sources from anthropogenic activity: Implications for carbon cycle constraints". *Geophysical Research Letters* 42.8. DOI: 10.1002/2015GL063445.

Camy-Peyret, C., G. Liuzzi, G. Masiello, C. Serio, S. Venafra, and S. A. Montzka (2017). "Assessment of IASI capability for retrieving carbonyl sulphide (OCS)". *Journal of Quantitative Spectroscopy and Radiative Transfer* 201. DOI: 10.1016/j.jqsrt.2017.07.006.

Canadell, J. G., P. M. S. Monteiro, M. H. Costa, L. Cotrim da Cunha, P. M. Cox, A. V. Eliseev, S. Henson, M. Ishii, S. Jaccard, and C. Koven (2023). "Intergovernmental Panel on Climate Change (IPCC). Global carbon and other biogeochemical cycles and feedbacks". *Climate change 2021: The physical science basis. Contribution of working group I to the sixth assessment report of the intergovernmental panel on climate change*.

Cartwright, M. P., J. J. Harrison, D. P. Moore, R. J. Pope, M. P. Chipperfield, C. Wilson, and W. Feng (2025). "Global optimal estimation retrievals of atmospheric carbonyl sulfide over water from IASI measurement spectra for 2018". *Atmospheric Chemistry and Physics* 25.22, pp. 15913–15934. DOI: 10.5194/acp-25-15913-2025.

Cernusak, L. A., N. Ubierna, M. W. Jenkins, S. R. Garrity, T. Rahn, H. H. Powers, D. T. Hanson, S. Sevanto, S. C. Wong, N. G. McDowell, et al. (2018). "Unsaturation of vapour pressure inside leaves of two conifer species". *Scientific Reports* 8.1. DOI: 10.1038/s41598-018-25838-2.

Chen, A., J. Mao, D. Ricciuto, J. Xiao, C. Frankenberg, X. Li, P. E. Thornton, L. Gu, and A. K. Knapp (2021). "Moisture availability mediates the relationship between terrestrial gross primary production and solar-induced chlorophyll fluorescence: Insights from global-scale variations". *Global Change Biology* 27.6. DOI: 10.1111/gcb.15373.

Chen, H., H. Li, Y. Wei, E. McBean, H. Liang, W. Wang, and J. J. Huang (2024). "Partitioning eddy covariance CO2 fluxes into ecosystem respiration and gross primary productivity through a new hybrid four sub-deep neural network". *Agriculture, Ecosystems and Environment* 361. DOI: 10.1016/j.agee.2023.108810.

Chevallier, F., M. Fisher, P. Peylin, S. Serrar, P. Bousquet, F. M. Bréon, A. Chédin, and P. Ciais (2005). "Inferring CO2 sources and sinks from satellite observations: Method and application to TOVS data". *Journal of Geophysical Research Atmospheres* 110.24. DOI: 10.1029/2005JD006390.

Chevallier, F., F. M. Bréon, and P. J. Rayner (2007). "Contribution of the Orbiting Carbon Observatory to the estimation of CO2 sources and sinks: Theoretical study in a variational data assimilation framework". *Journal of Geophysical Research Atmospheres* 112.9. DOI: 10.1029/2006JD007375.

Chevallier, F., T. Wang, P. Ciais, F. Maignan, M. Bocquet, M. Altaf Arain, A. Cescatti, J. Chen, A. J. Dolman, B. E. Law, et al. (2012). "What eddy-covariance measurements tell us about prior land flux errors in CO2-flux inversion schemes". *Global Biogeochemical Cycles* 26.1. DOI: 10.1029/2010GB003974.

Chin, M. and D. D. Davis (1995). "A reanalysis of carbonyl sulfide as a source of stratospheric background sulfur aerosol". *Journal of Geophysical Research* 100.D5. DOI: 10.1029/95JD00275.

Chin, M. and D. D. Davis (1993). "Global sources and sinks of OCS and CS2 and their distributions". *Global Biogeochemical Cycles* 7.2. DOI: 10.1029/93GB00568.

Cho, A., L. M. Kooijmans, K. M. Kohonen, R. Wehr, and M. C. Krol (2023). "Optimizing the carbonic anhydrase temperature response and stomatal conductance of carbonyl sulfide leaf uptake in the Simple Biosphere model (SiB4)". *Biogeosciences* 20.13. DOI: 10.5194/bg-20-2573-2023.

Ciais, P., P. Rayner, F. Chevallier, P. Bousquet, M. Logan, P. Peylin, and M. Ramonet (2010). "Atmospheric inversions for estimating CO2 fluxes: Methods and perspectives". *Climatic Change* 103.1-2. DOI: 10.1007/s10584-010-9909-3.

Cochavi, A., M. Amer, R. Stern, F. Tatarinov, M. Migliavacca, and D. Yakir (2021). "Differential responses to two heatwave intensities in a Mediterranean citrus orchard are identified by

combining measurements of fluorescence and carbonyl sulfide (COS) and CO2 uptake". *New Phytologist* 230.4. DOI: 10.1111/nph.17247.

Collatz, G. J., J. T. Ball, C. Grivet, and J. A. Berry (1991). "Physiological and environmental regulation of stomatal conductance, photosynthesis and transpiration: a model that includes a laminar boundary layer". *Agricultural and Forest Meteorology* 54.2-4. DOI: 10.1016/0168-1923(91)90002-8.

Collatz, G., M. Ribas-Carbo, and J. Berry (1992). "Coupled Photosynthesis-Stomatal Conductance Model for Leaves of C4 Plants". *Functional Plant Biology* 19.5. DOI: 10.1071/pp9920519.

Commane, R., S. C. Herndon, M. S. Zahniser, B. M. Lerner, J. B. McManus, J. W. Munger, D. D. Nelson, and S. C. Wofsy (2013). "Carbonyl sulfide in the planetary boundary layer: Coastal and continental influences". *Journal of Geophysical Research Atmospheres* 118.14. DOI: 10.1002/jgrd.50581.

Commane, R., S. Wofsy, and R. Wehr (2021). "Fluxes of Carbonyl Sulfide at Harvard Forest EMS Tower since 2010". English. DOI: 10.6073/pasta/b43072ec4b5dbf1f069983e3d5d36a1b.

Commane, R., L. K. Meredith, I. T. Baker, J. A. Berry, J. W. Munger, S. A. Montzka, P. H. Templer, S. M. Juice, M. S. Zahniser, and S. C. Wofsy (2015). "Seasonal fluxes of carbonyl sulfide in a midlatitude forest". *Proceedings of the National Academy of Sciences of the United States of America* 112.46. DOI: 10.1073/pnas.1504131112.

Daniel, R. M., M. E. Peterson, M. J. Danson, N. C. Price, S. M. Kelly, C. R. Monk, C. S. Weinberg, M. L. Oudshoorn, and C. K. Lee (2010). "The molecular basis of the effect of temperature on enzyme activity". *Biochemical Journal* 425.2. DOI: 10.1042/BJ20091254.

De Dios, V. R., J. Roy, J. P. Ferrio, J. G. Alday, D. Landais, A. Milcu, and A. Gessler (2015). "Processes driving nocturnal transpiration and implications for estimating land evapotranspiration". *Scientific Reports* 5. DOI: 10.1038/srep10975.

De Mello, W. Z. and M. E. Hines (1994). "Application of static and dynamic enclosures for determining dimethyl sulfide and carbonyl sulfide exchange in Sphagnum peatlands: implications for the magnitude and direction of flux". *Journal of Geophysical Research* 99.D7. DOI: 10.1029/94jd01025.

Desai, A. R., A. D. Richardson, A. M. Moffat, J. Kattge, D. Y. Hollinger, A. Barr, E. Falge, A. Noormets, D. Papale, M. Reichstein, et al. (2008). "Cross-site evaluation of eddy covariance GPP and RE decomposition techniques". *Agricultural and Forest Meteorology* 148.6-7. DOI: 10.1016/j.agrformet.2007.11.012.

Di Giuseppe, F., S. Rémy, F. Pappenberger, and F. Wetterhall (2018). "Using the Fire Weather Index (FWI) to improve the estimation of fire emissions from fire radiative power (FRP) observations". *Atmospheric Chemistry and Physics* 18.8. DOI: 10.5194/acp-18-5359-2018.

Drake, B. G., M. A. Gonzàlez-Meler, and S. P. Long (1997). "More efficient plants: A Consequence of Rising Atmospheric CO2?" *Annual Review of Plant Biology* 48. DOI: 10.1146/annurev.arplant.48.1.609.

Dreyer, E., X. Le Roux, P. Montpied, F. A. Daudet, and F. Masson (2001). "Temperature response of leaf photosynthetic capacity in seedlings from seven temperate tree species". *Tree Physiology* 21.4. DOI: 10.1093/treephys/21.4.223.

Du, Q., C. Zhang, Y. Mu, Y. Cheng, Y. Zhang, C. Liu, M. Song, D. Tian, P. Liu, J. Liu, et al. (2016). "An important missing source of atmospheric carbonyl sulfide: Domestic coal combustion". *Geophysical Research Letters* 43.16. DOI: 10.1002/2016GL070075.

Endres, S. C., C. Sandrock, and W. W. Focke (2018). "A simplicial homology algorithm for Lipschitz optimisation". *Journal of Global Optimization* 72.2. DOI: 10.1007/s10898-018-0645-y.

Enting, I. G., C. M. Trudinger, R. J. Francey, and H. Granek (1993). *Synthesis Inversion of Atmospheric CO2 Using the GISS Tracer Transport Model*. Tech. rep. Technical Paper 29. Australia: Division of Atmospheric Research, CSIRO. URL: http://www.cmar.csiro.au/e-print/open/enting_1993a.pdf.

Enting, I. G. (2002). *Inverse Problems in Atmospheric Constituent Transport*. DOI: 10.1017/cbo9780511535741.

Evans, J. R., S. von Caemmerer, B. A. Setchell, and G. S. Hudson (1994). "The relationship between CO2 transfer conductance and leaf anatomy in transgenic tobacco with a reduced content of Rubisco". *Australian Journal of Plant Physiology* 21.4. DOI: 10.1071/PP9940475.

Farquhar, G. D. and T. D. Sharkey (1982). "Stomatal Conductance and Photosynthesis". *Annual Review of Plant Physiology* 33.1. DOI: 10.1146/annurev.pp.33.060182.001533.

Farquhar, G. D., S. von Caemmerer, and J. A. Berry (1980). "A biochemical model of photosynthetic CO2 assimilation in leaves of C3 species". *Planta* 149.1. DOI: 10.1007/BF00386231.

Flöck, O. R. and M. O. Andreae (1996). "Photochemical and non-photochemical formation and destruction of carbonyl sulfide and methyl mercaptan in ocean waters". *Marine Chemistry* 54.1-2. DOI: 10.1016/0304-4203(96)00027-8.

Forkel, M., N. Carvalhais, C. Rödenbeck, R. Keeling, M. Heimann, K. Thonicke, S. Zaehle, and M. Reichstein (2016). "Enhanced seasonal CO2 exchange caused by amplified plant productivity in northern ecosystems". *Science* 351.6274. DOI: 10.1126/science.aac4971.

Fowler, D. (1995). "Measurements of CH4 and N2O fluxes at the landscape scale using micrometeorological methods". *Philosophical Transactions - Royal Society of London, A* 351.1696. DOI: 10.1098/rsta.1995.0038.

Frankenberg, C., C. O'Dell, L. Guanter, and J. McDuffie (2012). "Remote sensing of near-infrared chlorophyll fluorescence from space in scattering atmospheres: Implications for its retrieval and interferences with atmospheric CO 2 retrievals". *Atmospheric Measurement Techniques* 5.8. DOI: 10.5194/amt-5-2081-2012.

Frankenberg, C., J. B. Fisher, J. Worden, G. Badgley, S. S. Saatchi, J. E. Lee, G. C. Toon, A. Butz, M. Jung, A. Kuze, et al. (2011). "New global observations of the terrestrial carbon cycle from GOSAT: Patterns of plant fluorescence with gross primary productivity". *Geophysical Research Letters* 38.17. DOI: 10.1029/2011GL048738.

Friedlingstein, P., M. O'Sullivan, M. W. Jones, R. M. Andrew, J. Hauck, P. Landschützer, C. Le Quéré, H. Li, I. T. Luijkx, A. Olsen, et al. (2025). "Global Carbon Budget 2024". *Earth System Science Data* 17.3, pp. 965–1039. DOI: 10.5194/essd-17-965-2025.

Friedlingstein, P., M. O'Sullivan, M. W. Jones, R. M. Andrew, D. C. Bakker, J. Hauck, P. Landschützer, C. Le Quéré, I. T. Luijkx, G. P. Peters, et al. (2023). "Global Carbon Budget 2023". *Earth System Science Data* 15.12. DOI: 10.5194/essd-15-5301-2023.

Galmés, J., C. Hermida-Carrera, L. Laanisto, and Ü. Niinemets (2016). "A compendium of temperature responses of Rubisco kinetic traits: variability among and within photosynthetic groups and impacts on photosynthesis modeling". *Journal of Experimental Botany* 67.17. DOI: 10.1093/jxb/erw267.

Garen, J. C., H. A. Branch, I. Borrego, B. Blonder, J. R. Stinziano, and S. T. Michaletz (2022). "Gas exchange analysers exhibit large measurement error driven by internal thermal gradients". *New Phytologist* 236.2. DOI: 10.1111/nph.18347.

Gelaro, R., W. McCarty, M. J. Suárez, R. Todling, A. Molod, L. Takacs, C. A. Randles, A. Darmenov, M. G. Bosilovich, R. Reichle, et al. (2017). "The modern-era retrospective analysis for research and applications, version 2 (MERRA-2)". *Journal of Climate* 30.14. DOI: 10.1175/JCLI-D-16-0758.1.

Geng, C. and Y. Mu (2004). "Carbonyl sulfide and dimethyl sulfide exchange between lawn and the atmosphere". *Journal of Geophysical Research D: Atmospheres* 109.12. DOI: 10.1029/2003JD004492.

— (2006). "Carbonyl sulfide and dimethyl sulfide exchange between trees and the atmosphere". *Atmospheric Environment* 40.7. DOI: 10.1016/j.atmosenv.2005.10.023.

Gilbert, J. C. and C. Lemaréchal (1989). "Some numerical experiments with variable-storage quasi-Newton algorithms". *Mathematical Programming* 45.1-3. DOI: 10.1007/BF01589113.

Gillon, J. and D. Yakir (2001). "Influence of carbonic anhydrase activity in terrestrial vegetation on the 18O content of atmospheric CO2". *Science* 291.5513. DOI: 10.1126/science.1056374.

Gimeno, T. E., J. Ogée, J. Royles, Y. Gibon, J. B. West, R. Burlett, S. P. Jones, J. Sauze, S. Wohl, C. Benard, et al. (2017). "Bryophyte gas-exchange dynamics along varying hydration status reveal a significant carbonyl sulphide (COS) sink in the dark and COS source in the light". *New Phytologist* 215.3. DOI: 10.1111/nph.14584.

Glatthor, N., M. Höpfner, I. T. Baker, J. Berry, J. E. Campbell, S. R. Kawa, G. Krysztofiak, A. Leyser, B. M. Sinnhuber, G. P. Stiller, et al. (2015). "Tropical sources and sinks of carbonyl sulfide observed from space". *Geophysical Research Letters* 42.22. DOI: 10.1002/2015GL066293.

Glatthor, N., M. Höpfner, A. Leyser, G. P. Stiller, T. Von Clarmann, U. Grabowski, S. Kellmann, A. Linden, B. M. Sinnhuber, G. Krysztofiak, et al. (2017). "Global carbonyl sulfide (OCS) measured by MIPAS/Envisat during 2002-2012". *Atmospheric Chemistry and Physics* 17.4. DOI: 10.5194/acp-17-2631-2017.

Goldan, P. D., R. Fall, W. C. Kuster, and F. C. Fehsenfeld (1988). "Uptake of COS by growing vegetation: a major tropospheric sink". *Journal of Geophysical Research* 93.D11. DOI: 10.1029/jd093id11p14186.

Hannigan, J. W., I. Ortega, S. B. Shams, T. Blumenstock, J. E. Campbell, S. Conway, V. Flood, O. Garcia, D. Griffith, M. Grutter, et al. (2022). "Global Atmospheric OCS Trend Analysis From 22 NDACC Stations". *Journal of Geophysical Research: Atmospheres* 127.4. DOI: 10.1029/2021JD035764.

Haynes, K. D., I. T. Baker, A. S. Denning, R. Stöckli, K. Schaefer, E. Y. Lokupitiya, and J. M. Haynes (2019). "Representing Grasslands Using Dynamic Prognostic Phenology Based on Biological Growth Stages: 1. Implementation in the Simple Biosphere Model (SiB4)". *Journal of Advances in Modeling Earth Systems* 11.12. DOI: 10.1029/2018MS001540.

Haynes, K. D., I. Baker, and A. S. Denning (2020). *The Simple Biosphere Model, Version 4.2: SiB4 Technical description*. Tech. rep. February.

Herig Coimbra, P. H., B. Loubet, O. Laurent, L. Bignotti, M. Lozano, and M. Ramonet (2024). "Eddy covariance with slow-response greenhouse gas analysers on tall towers: bridging atmospheric and ecosystem greenhouse gas networks". *Atmospheric Measurement Techniques* 17.22, pp. 6625–6645. DOI: 10.5194/amt-17-6625-2024.

Hersbach, H., B. Bell, P. Berrisford, S. Hirahara, A. Horányi, J. Muñoz-Sabater, J. Nicolas, C. Peubey, R. Radu, D. Schepers, et al. (2020). "The ERA5 global reanalysis". *Quarterly Journal of the Royal Meteorological Society* 146.730. DOI: 10.1002/qj.3803.

Hoesly, R. M., S. J. Smith, L. Feng, Z. Klimont, G. Janssens-Maenhout, T. Pitkanen, J. J. Seibert, L. Vu, R. J. Andres, R. M. Bolt, et al. (2018). "Historical (1750-2014) anthropogenic emissions of reactive gases and aerosols from the Community Emissions Data System (CEDS)". *Geoscientific Model Development* 11.1. DOI: 10.5194/gmd-11-369-2018.

Hooghiemstra, P. B., M. C. Krol, J. F. Meirink, P. Bergamaschi, G. R. Van Der Werf, P. C. Novelli, I. Aben, and T. Röckmann (2011). "Optimizing global CO emission estimates using a four-dimensional variational data assimilation system and surface network observations". *Atmospheric Chemistry and Physics* 11.10. DOI: 10.5194/acp-11-4705-2011.

Houweling, S., M. Krol, P. Bergamaschi, C. Frankenberg, E. J. Dlugokencky, I. Morino, J. Notholt, V. Sherlock, D. Wunch, V. Beck, et al. (2014). "A multi-year methane inversion using SCIAMACHY, accounting for systematic errors using TCCON measurements". *Atmospheric Chemistry and Physics* 14.8. DOI: 10.5194/acp-14-3991-2014.

Hu, L., S. A. Montzka, A. Kaushik, A. E. Andrews, C. Sweeney, J. Miller, I. T. Baker, S. Denning, E. Campbell, Y. P. Shiga, et al. (2021). "COS-derived GPP relationships with temperature and light help explain high-latitude atmospheric CO2 seasonal cycle amplification". *Proceedings of the National Academy of Sciences of the United States of America* 118.33. DOI: 10.1073/pnas.2103423118.

Hussain, S. B., J. Stinziano, M. O. Pierre, and C. Vincent (2024). "Accurate photosynthetic parameter estimation at low stomatal conductance: effects of cuticular conductance and instrumental noise". *Photosynthesis Research* 160.2, pp. 111–124. DOI: 10.1007/s11120-024-01092-8.

Intergovernmental Panel on Climate Change (2023). *Climate Change 2023: Synthesis Report*. Tech. rep. Geneva, Switzerland: IPCC, pp. 35–115. DOI: 10.59327/IPCC/AR6-9789291691647.

Jarman, P. D. (1974). "The diffusion of carbon dioxide and water vapour through stomata". *Journal of Experimental Botany* 25.5. DOI: 10.1093/jxb/25.5.927.

Jernigan, C. M., C. D. Cappa, and T. H. Bertram (2022). "Reactive Uptake of Hydroperoxymethyl Thioformate to Sodium Chloride and Sodium Iodide Aerosol Particles". *Journal of Physical Chemistry A* 126.27. DOI: 10.1021/acs.jpca.2c03222.

Jones, M. W., R. M. Andrew, G. P. Peters, G. Janssens-Maenhout, A. J. De-Gol, P. Ciais, P. K. Patra, F. Chevallier, and C. Le Quéré (2021). "Gridded fossil CO2 emissions and related O2 combustion consistent with national inventories 1959–2018". *Scientific Data* 8.1. DOI: 10.1038/s41597-020-00779-6.

Jung, M., C. Schwalm, M. Migliavacca, S. Walther, G. Camps-Valls, S. Koirala, P. Anthoni, S. Besnard, P. Bodesheim, N. Carvalhais, et al. (2020). "Scaling carbon fluxes from eddy covariance sites to globe: Synthesis and evaluation of the FLUXCOM approach". *Biogeosciences* 17.5. DOI: 10.5194/bg-17-1343-2020.

Kattge, J., W. Knorr, T. Raddatz, and C. Wirth (2009). "Quantifying photosynthetic capacity and its relationship to leaf nitrogen content for global-scale terrestrial biosphere models". *Global Change Biology* 15.4. DOI: 10.1111/j.1365-2486.2008.01744.x.

Kesselmeier, J. and L. Merk (1993). "Exchange of carbonyl sulfide (COS) between agricultural plants and the atmosphere: Studies on the deposition of COS to peas, corn and rapeseed". *Biogeochemistry* 23.1. DOI: 10.1007/BF00002922.

Kettle, A. J., U. Kuhn, M. Von Hobe, J. Kesselmeier, and M. O. Andreae (2002). "Global budget of atmospheric carbonyl sulfide: Temporal and spatial variations of the dominant sources and sinks". *Journal of Geophysical Research Atmospheres* 107.22. DOI: 10.1029/2002JD002187.

Kilgour, D. B., C. M. Jernigan, O. Garmash, S. Aggarwal, S. Zhou, C. Mohr, M. E. Salter, J. A. Thornton, J. Wang, P. Zieger, et al. (2025). "Cloud processing of dimethyl sulfide (DMS) oxidation products limits sulfur dioxide (SO2) and carbonyl sulfide (OCS) production in the eastern North Atlantic marine boundary layer". *Atmospheric Chemistry and Physics* 25.3, pp. 1931–1947. DOI: 10.5194/acp-25-1931-2025.

Kohonen, K. M., R. Dewar, G. Tramontana, A. Mauranen, P. Kolari, L. M. Kooijmans, D. Papale, T. Vesala, and I. Mammarella (2022). "Intercomparison of methods to estimate gross primary production based on CO2 and COS flux measurements". *Biogeosciences* 19.17. DOI: 10.5194/bg-19-4067-2022.

Kohonen, K. M., P. Kolari, L. M. Kooijmans, H. Chen, U. Seibt, W. Sun, and I. Mammarella (2020). "Towards standardized processing of eddy covariance flux measurements of carbonyl sulfide". *Atmospheric Measurement Techniques* 13.7. DOI: 10.5194/amt-13-3957-2020.

Kolari, P., T. Chan, A. Porcar-Castell, J. Bäck, E. Nikinmaa, and E. Juurola (2014). "Field and controlled environment measurements show strong seasonal acclimation in photosynthesis and respiration potential in boreal Scots pine". *Frontiers in Plant Science* 5.DEC. DOI: 10.3389/fpls.2014.00717.

Kooijmans, L. M., A. Cho, J. Ma, A. Kaushik, K. D. Haynes, I. Baker, I. T. Luijkx, M. Groenink, W. Peters, J. B. Miller, et al. (2021). "Evaluation of carbonyl sulfide biosphere exchange in the Simple Biosphere Model (SiB4)". *Biogeosciences* 18.24. DOI: 10.5194/bg-18-6547-2021.

Kooijmans, L. M., K. Maseyk, U. Seibt, W. Sun, T. Vesala, I. Mammarella, P. Kolari, J. Aalto, A. Franchin, R. Vecchi, et al. (2017). "Canopy uptake dominates nighttime carbonyl sulfide fluxes in a boreal forest". *Atmospheric Chemistry and Physics* 17.18. DOI: 10.5194/acp-17-11453-2017.

Kooijmans, L. M., W. Sun, J. Aalto, K. M. Erkkilä, K. Maseyk, U. Seibt, T. Vesala, I. Mammarella, and H. Chen (2019). "Influences of light and humidity on carbonyl sulfide-based estimates of photosynthesis". *Proceedings of the National Academy of Sciences of the United States of America* 116.7. DOI: 10.1073/pnas.1807600116.

Kooijmans, L. M., N. A. Uitslag, M. S. Zahniser, D. D. Nelson, S. A. Montzka, and H. Chen (2016). "Continuous and high-precision atmospheric concentration measurements of COS, CO2, CO and H2O using a quantum cascade laser spectrometer (QCLS)". *Atmospheric Measurement Techniques* 9.11. DOI: 10.5194/amt-9-5293-2016.

Kraft, D. (1988). *A Software Package for Sequential Quadratic Programming*. Tech. rep. 28.

Kremser, S., N. B. Jones, M. Palm, B. Lejeune, Y. Wang, D. Smale, and N. M. Deutscher (2015). "Positive trends in Southern Hemisphere carbonyl sulfide". *Geophysical Research Letters* 42.21. DOI: 10.1002/2015GL065879.

Krol, M., S. Houweling, B. Bregman, M. van den Broek, A. Segers, P. van Velthoven, W. Peters, F. Dentener, and P. Bergamaschi (2005). "The two-way nested global chemistry-transport zoom model TM5: Algorithm and applications". *Atmospheric Chemistry and Physics* 5.2. DOI: 10.5194/acp-5-417-2005.

Krol, M. C., J. F. Meirink, P. Bergamaschi, J. E. Mak, D. Lowe, P. Jöckel, S. Houweling, and T. Röckmann (2008). "What can 14CO measurements tell us about OH?" *Atmospheric Chemistry and Physics* 8.16. DOI: 10.5194/acp-8-5033-2008.

Kuai, L., J. Worden, S. S. Kulawik, S. A. Montzka, and J. Liu (2014). "Characterization of aura TES carbonyl sulfide retrievals over ocean". *Atmospheric Measurement Techniques* 7.1. DOI: 10.5194/amt-7-163-2014.

Kuai, L., N. C. Parazoo, M. Shi, C. E. Miller, I. Baker, A. A. Bloom, K. Bowman, M. Lee, Z. C. Zeng, R. Commane, et al. (2022). "Quantifying Northern High Latitude Gross Primary Productivity (GPP) Using Carbonyl Sulfide (OCS)". *Global Biogeochemical Cycles* 36.9. DOI: 10.1029/2021GB007216.

Kuai, L., J. R. Worden, J. E. Campbell, S. S. Kulawik, K. F. Li, M. Lee, R. J. Weidner, S. A. Montzka, F. L. Moore, J. A. Berry, et al. (2015). "Estimate of carbonyl sulfide tropical oceanic surface fluxes using aura tropospheric emission spectrometer observations". *Journal of Geophysical Research* 120.20. DOI: 10.1002/2015JD023493.

Kuhn, U. and J. Kesselmeier (2000). "Environmental variables controlling the uptake of carbonyl sulfide by lichens". *Journal of Geophysical Research Atmospheres* 105.D22. DOI: 10.1029/2000JD900436.

Lai, C. T., G. Katul, R. Oren, D. Ellsworth, and K. Schäfer (2000). "Modeling CO2 and water vapor turbulent flux distributions within a forest canopy". *Journal of Geophysical Research Atmospheres* 105.D21. DOI: 10.1029/2000JD900468.

Lai, J., L. M. J. Kooijmans, W. Sun, D. Lombardozzi, J. E. Campbell, L. Gu, Y. Luo, L. Kuai, and Y. Sun (2024). "Terrestrial photosynthesis inferred from plant carbonyl sulfide uptake". *Nature* 634.8035, pp. 855–861. DOI: 10.1038/s41586-024-08050-3.

Lana, A., T. G. Bell, R. Simó, S. M. Vallina, J. Ballabrera-Poy, A. J. Kettle, J. Dachs, L. Bopp, E. S. Saltzman, J. Stefels, et al. (2011). "An updated climatology of surface dimethlysulfide concentrations and emission fluxes in the global ocean". *Global Biogeochemical Cycles* 25.1. DOI: 10.1029/2010GB003850.

Lanczos, C. (1950). "An iteration method for the solution of the eigenvalue problem of linear differential and integral operators". *Journal of Research of the National Bureau of Standards* 45.4. DOI: 10.6028/jres.045.026.

Launois, T., S. Belviso, L. Bopp, C. G. Fichot, and P. Peylin (2015a). "A new model for the global biogeochemical cycle of carbonyl sulfide - Part 1: Assessment of direct marine emissions with an oceanic general circulation and biogeochemistry model". *Atmospheric Chemistry and Physics* 15.5. DOI: 10.5194/acp-15-2295-2015.

Launois, T., P. Peylin, S. Belviso, and B. Poulter (2015b). "A new model of the global biogeochemical cycle of carbonyl sulfide - Part 2: Use of carbonyl sulfide to constrain gross primary productivity in current vegetation models". *Atmospheric Chemistry and Physics* 15.16. DOI: 10.5194/acp-15-9285-2015.

Le Roux, X., T. Bariac, H. Sinoquet, B. Genty, C. Piel, A. Mariotti, C. Girardin, and P. Richard (2001). "Spatial distribution of leaf water-use efficiency and carbon isotope discrimination within an isolated tree crown". *Plant, Cell and Environment* 24.10. DOI: 10.1046/j.0016-8025.2001.00756.x.

Lee, C. K., R. M. Daniel, C. Shepherd, D. Saul, S. C. Cary, M. J. Danson, R. Eisenthal, and M. E. Peterson (2007). "Eurythermalism and the temperature dependence of enzyme activity". *The FASEB Journal* 21.8. DOI: 10.1096/fj.06-7265com.

Lee, C. L. and P. Brimblecombe (2016). "Anthropogenic contributions to global carbonyl sulfide, carbon disulfide and organosulfides fluxes". *Earth-Science Reviews* 160. DOI: 10.1016/j.earscirev.2016.06.005.

Lennartz, S. T., M. Gauss, M. Von Hobe, and C. A. Marandino (2021). "Monthly resolved modelled oceanic emissions of carbonyl sulphide and carbon disulphide for the period 2000-2019". *Earth System Science Data* 13.5. DOI: 10.5194/essd-13-2095-2021.

Lennartz, S. T., C. A. Marandino, M. Von Hobe, P. Cortes, B. Quack, R. Simo, D. Booge, A. Pozzer, T. Steinhoff, D. L. Arevalo-Martinez, et al. (2017). "Direct oceanic emissions unlikely to account for the missing source of atmospheric carbonyl sulfide". *Atmospheric Chemistry and Physics* 17.1. DOI: 10.5194/acp-17-385-2017.

Lennartz, S. T., M. Von Hobe, D. Booge, H. C. Bittig, T. Fischer, R. Gonçalves-Araujo, K. B. Ksionzek, B. P. Koch, A. Bracher, R. Röttgers, et al. (2019). "The influence of dissolved organic matter on the marine production of carbonyl sulfide (OCS) and carbon disulfide (CS2) in the Peruvian upwelling". *Ocean Science* 15.4. DOI: 10.5194/os-15-1071-2019.

Leuning, R. (1995). "A critical appraisal of a combined stomatal-photosynthesis model for C3 plants". *Plant, Cell & Environment* 18.4. DOI: 10.1111/j.1365-3040.1995.tb00370.x.

Leuning, R., F. X. Dunin, and Y. P. Wang (1998). "A two-leaf model for canopy conductance, photosynthesis and partitioning of available energy. II. Comparison with measurements". *Agricultural and Forest Meteorology* 91.1-2. DOI: 10.1016/S0168-1923(98)00074-4.

Liu, S., W. He, P. Xu, M. Zhao, C. Huang, and N. T. Nguyen (Dec. 2025). "Modeling carbonyl sulfide and carbon dioxide fluxes in a northern boreal coniferous forest using memory-

based deep learning". *Ecological Modelling* 510, p. 111283. DOI: 10.1016/J.ECOLMODEL.2025.111283.

Lobo, F. d. A., M. P. de Barros, H. J. Dalmagro, Â. C. Dalmolin, W. E. Pereira, É. C. de Souza, G. L. Vourlitis, and C. E. Rodríguez Ortíz (2013). "Fitting net photosynthetic light-response curves with Microsoft Excel - a critical look at the models". *Photosynthetica* 51.3. DOI: 10.1007/s11099-013-0045-y.

Long, S. P. and C. J. Bernacchi (2003). *Gas exchange measurements, what can they tell us about the underlying limitations to photosynthesis? Procedures and sources of error*. DOI: 10.1093/jxb/erg262.

Lorimer, G. H. and J. Pierce (1989). "Carbonyl sulfide: an alternate substrate for but not an activator of ribulose-1,5-bisphosphate carboxylase." *The Journal of biological chemistry* 264.5. DOI: 10.1016/s0021-9258(19)81679-4.

Luijkx, I., W. Peters, Z. Lloret, M. Zhao, Y. Niwa, A. R. Jacobson, J. Liu, B. Byrne, K. Bowman, A. Bloom, et al. (2024). *Global CO2 gridded flux fields from 14 atmospheric inversions in GCB2024*. [data set]. DOI: 10.18160/4R5W-VNBV.

Ma, J., L. M. J. Kooijmans, N. Glatthor, S. A. Montzka, M. von Hobe, T. Röckmann, and M. C. Krol (2024). "Combined assimilation of NOAA surface and MIPAS satellite observations to constrain the global budget of carbonyl sulfide". *Atmospheric Chemistry and Physics* 24.10, pp. 6047–6070. DOI: 10.5194/acp-24-6047-2024.

Ma, J., L. M. Kooijmans, A. Cho, S. A. Montzka, N. Glatthor, J. R. Worden, L. Kuai, E. L. Atlas, and M. C. Krol (2021). "Inverse modelling of carbonyl sulfide: Implementation, evaluation and implications for the global budget". *Atmospheric Chemistry and Physics* 21.5. DOI: 10.5194/acp-21-3507-2021.

Ma, J., M. Remaud, P. Peylin, P. Patra, Y. Niwa, C. Rodenbeck, M. Cartwright, J. J. Harrison, M. P. Chipperfield, R. J. Pope, et al. (2023). "Intercomparison of Atmospheric Carbonyl Sulfide (TransCom-COS): 2. Evaluation of Optimized Fluxes Using Ground-Based and Aircraft Observations". *Journal of Geophysical Research: Atmospheres* 128.18. DOI: 10.1029/2023JD039198.

Maignan, F., C. Abadie, M. Remaud, L. M. Kooijmans, K. M. Kohonen, R. Commane, R. Wehr, J. Elliott Campbell, S. Belviso, S. A. Montzka, et al. (2021). "Carbonyl sulfide: Comparing a mechanistic representation of the vegetation uptake in a land surface model and the leaf relative uptake approach". *Biogeosciences* 18.9. DOI: 10.5194/bg-18-2917-2021.

Manabe, S. and R. T. Wetherald (1967). "Thermal Equilibrium of the Atmosphere with a Given Distribution of Relative Humidity". *Journal of the Atmospheric Sciences* 24.3. DOI: 10.1175/1520-0469(1967)024<0241:teotaw>2.0.co;2.

Maseyk, K., J. A. Berry, D. Billesbach, J. E. Campbell, M. S. Torn, M. Zahniser, and U. Seibt (2014). "Sources and sinks of carbonyl sulfide in an agricultural field in the Southern Great Plains". *Proceedings of the National Academy of Sciences of the United States of America* 111.25. DOI: 10.1073/pnas.1319132111.

Mauldin, R. L., T. Berndt, M. Sipilä, P. Paasonen, T. Petäjä, S. Kim, T. Kurtén, F. Stratmann, V. M. Kerminen, and M. Kulmala (2012). "A new atmospherically relevant oxidant of sulphur dioxide". *Nature* 488.7410. DOI: 10.1038/nature11278.

Medlyn, B. E., R. A. Duursma, D. Eamus, D. S. Ellsworth, I. C. Prentice, C. V. Barton, K. Y. Crous, P. De Angelis, M. Freeman, and L. Wingate (2011). "Reconciling the optimal and empirical approaches to modelling stomatal conductance". *Global Change Biology* 17.6. DOI: 10.1111/j.1365-2486.2010.02375.x.

Meirink, J. F., P. Bergamaschi, and M. C. Krol (2008). "Four-dimensional variational data assimilation for inverse modelling of atmospheric methane emissions: Method and comparison

with synthesis inversion". *Atmospheric Chemistry and Physics* 8.21. DOI: 10.5194/acp-8-6341-2008.

Meirink, J. F., H. J. Eskes, and A. P. Goede (2006). "Sensitivity analysis of methane emissions derived from SCIAMACHY observations through inverse modelling". *Atmospheric Chemistry and Physics* 6.5. DOI: 10.5194/acp-6-1275-2006.

Michaelis, L., M. L. Menten, R. S. Goody, and K. A. Johnson (1913). "Die Kinetik der Invertinwirkung/ The kinetics of invertase action". *Biochemistry* 49.2.

Miner, G. L., W. L. Bauerle, and D. D. Baldocchi (2017). "Estimating the sensitivity of stomatal conductance to photosynthesis: a review". *Plant Cell and Environment* 40.7. DOI: 10.1111/pce.12871.

Moncrieff, J. B., J. M. Massheder, H. De Bruin, J. Elbers, T. Friborg, B. Heusinkveld, P. Kabat, S. Scott, H. Soegaard, and A. Verhoef (1997). "A system to measure surface fluxes of momentum, sensible heat, water vapour and carbon dioxide". *Journal of Hydrology* 188-189.1-4. DOI: 10.1016/S0022-1694(96)03194-0.

Montzka, S. A., P. Calvert, B. D. Hall, J. W. Elkins, T. J. Conway, P. P. Tans, and C. S. Sweeney (2007). "On the global distribution, seasonality, and budget of atmospheric carbonyl sulfide (COS) and some similarities to CO2". *Journal of Geophysical Research Atmospheres* 112.9. DOI: 10.1029/2006JD007665.

Munassar, S., C. Rödenbeck, M. Gałkowski, F.-T. Koch, K. U. Totsche, S. Botía, and C. Gerbig (2025). "To what extent does the CO2 diurnal cycle impact flux estimates derived from global and regional inversions?" *Atmospheric Chemistry and Physics* 25.1, pp. 639–656. DOI: 10.5194/acp-25-639-2025.

Naus, S., L. G. Domingues, M. Krol, I. T. Luijkx, L. V. Gatti, J. B. Miller, E. Gloor, S. Basu, C. Correia, G. Koren, et al. (2022). "Sixteen years of MOPITT satellite data strongly constrain Amazon CO fire emissions". *Atmospheric Chemistry and Physics* 22.22. DOI: 10.5194/acp-22-14735-2022.

Norton, A. J., P. J. Rayner, E. N. Koffi, M. Scholze, J. D. Silver, and Y. P. Wang (2019). "Estimating global gross primary productivity using chlorophyll fluorescence and a data assimilation system with the BETHY-SCOPE model". *Biogeosciences* 16.15. DOI: 10.5194/bg-16-3069-2019.

Notni, J., S. Schenk, G. Protoschill-Krebs, J. Kesselmeier, and E. Anders (2007). "The missing link in COS metabolism: A model study on the reactivation of carbonic anhydrase from its hydrosulfide analogue". *ChemBioChem* 8.5. DOI: 10.1002/cbic.200600436.

Ogée, J., J. Sauze, J. Kesselmeier, B. Genty, H. Van Diest, T. Launois, and L. Wingate (2016). "A new mechanistic framework to predict OCS fluxes from soils". *Biogeosciences* 13.8. DOI: 10.5194/bg-13-2221-2016.

Pandey, S., S. Houweling, M. Krol, I. Aben, F. Chevallier, E. J. Dlugokencky, L. V. Gatti, E. Gloor, J. B. Miller, R. Detmers, et al. (2016). "Inverse modeling of GOSAT-retrieved ratios of total column CH4 and CO2 for 2009 and 2010". *Atmospheric Chemistry and Physics* 16.8. DOI: 10.5194/acp-16-5043-2016.

Papale, D., M. Reichstein, M. Aubinet, E. Canfora, C. Bernhofer, W. Kutsch, B. Longdoz, S. Rambal, R. Valentini, T. Vesala, et al. (2006). "Towards a standardized processing of Net Ecosystem Exchange measured with eddy covariance technique: Algorithms and uncertainty estimation". *Biogeosciences* 3.4. DOI: 10.5194/bg-3-571-2006.

Parazoo, N. C., A. Arneth, T. A. Pugh, B. Smith, N. Steiner, K. Luus, R. Commane, J. Benmergui, E. Stofferahn, J. Liu, et al. (2018). "Spring photosynthetic onset and net CO2 uptake in Alaska triggered by landscape thawing". *Global Change Biology* 24.8. DOI: 10.1111/gcb.14283.

Parazoo, N. C., K. Bowman, J. B. Fisher, C. Frankenberg, D. B. Jones, A. Cescatti, Ó. Pérez-Priego, G. Wohlfahrt, and L. Montagnani (2014). "Terrestrial gross primary production inferred from satellite fluorescence and vegetation models". *Global Change Biology* 20.10. DOI: 10.1111/gcb.12652.

Pastorello, G., C. Trotta, E. Canfora, H. Chu, D. Christianson, Y. W. Cheah, C. Poindexter, J. Chen, A. Elbashandy, M. Humphrey, et al. (2020). "The FLUXNET2015 dataset and the ONEFlux processing pipeline for eddy covariance data". *Scientific Data* 7.1. DOI: 10.1038/s41597-020-0534-3.

Paul-Limoges, E., A. Damm, A. Hueni, F. Liebisch, W. Eugster, M. E. Schaepman, and N. Buchmann (2018). "Effect of environmental conditions on sun-induced fluorescence in a mixed forest and a cropland". *Remote Sensing of Environment* 219. DOI: 10.1016/j.rse.2018.10.018.

Peterson, M. E., R. M. Daniel, M. J. Danson, and R. Eisenthal (2007). "The dependence of enzyme activity on temperature: Determination and validation of parameters". *Biochemical Journal* 402.2. DOI: 10.1042/BJ20061143.

Peterson, M. E., R. Eisenthal, M. J. Danson, A. Spence, and R. M. Daniel (2004). "A new intrinsic thermal parameter for enzymes reveals true temperature optima". *Journal of Biological Chemistry* 279.20. DOI: 10.1074/jbc.M309143200.

Peylin, P., R. M. Law, K. R. Gurney, F. Chevallier, A. R. Jacobson, T. Maki, Y. Niwa, P. K. Patra, W. Peters, P. J. Rayner, et al. (2013). "Global atmospheric carbon budget: Results from an ensemble of atmospheric CO2 inversions". *Biogeosciences* 10.10. DOI: 10.5194/bg-10-6699-2013.

Pos, W. H., D. D. Riemer, and R. G. Zika (1998). "Carbonyl sulfide (OCS) and carbon monoxide (CO) in natural waters: Evidence of a coupled production pathway". *Marine Chemistry* 62.1-2. DOI: 10.1016/S0304-4203(98)00025-5.

Protoschill-Krebs, G., C. Wilhelm, and J. Kesselmeier (1996). "Consumption of carbonyl sulphide (COS) by higher plant carbonic anhydrase (CA)". *Atmospheric Environment* 30.18. DOI: 10.1016/1352-2310(96)00026-X.

Protoschill-Krebs, G. and J. Kesselmeier (1992). "Enzymatic Pathways for the Consumption of Carbonyl Sulphide (COS) by Higher Plants". *Botanica Acta* 105.3. DOI: 10.1111/j.1438-8677.1992.tb00288.x.

Ramonet, M., P. Ciais, F. Apadula, J. Bartyzel, A. Bastos, P. Bergamaschi, P. E. Blanc, D. Brunner, L. di Torchiarolo, F. Calzolari, et al. (2020). "The fingerprint of the summer 2018 drought in Europe on ground-based atmospheric CO2 measurements". *Philosophical Transactions of the Royal Society B: Biological Sciences* 375.1810, p. 20190513. DOI: 10.1098/rstb.2019.0513.

Randerson, J. T., G. R. van der Werf, L. Giglio, G. J. Collatz, and P. S. Kasibhatla (2017). *Global Fire Emissions Database, Version 4.1 (GFEDv4)*. [data set]. DOI: 10.3334/ORNLDAAC/1293.

Rastogi, B., M. Berkelhammer, S. Wharton, M. E. Whelan, M. S. Itter, J. B. Leen, M. X. Gupta, D. Noone, and C. J. Still (2018). "Large Uptake of Atmospheric OCS Observed at a Moist Old Growth Forest: Controls and Implications for Carbon Cycle Applications". *Journal of Geophysical Research: Biogeosciences* 123.11. DOI: 10.1029/2018JG004430.

Ravishankara, A. R. (1997). "Heterogeneous and multiphase chemistry in the troposphere". *Science* 276.5315. DOI: 10.1126/science.276.5315.1058.

Reichstein, M., E. Falge, D. Baldocchi, D. Papale, M. Aubinet, P. Berbigier, C. Bernhofer, N. Buchmann, T. Gilmanov, A. Granier, et al. (2005). "On the separation of net ecosystem exchange into assimilation and ecosystem respiration: Review and improved algorithm". *Global Change Biology* 11.9. DOI: 10.1111/j.1365-2486.2005.001002.x.

Remaud, M., F. Chevallier, F. Maignan, S. Belviso, A. Berchet, A. Parouffe, C. Abadie, C. Bacour, S. Lennartz, and P. Peylin (2022). "Plant gross primary production, plant respiration

and carbonyl sulfide emissions over the globe inferred by atmospheric inverse modelling". *Atmospheric Chemistry and Physics* 22.4. DOI: 10.5194/acp-22-2525-2022.

Rennenberg, H. (1991). "The Significance of Higher Plants in the Emission of Sulfur Compounds from Terrestrial Ecosystems". *Trace Gas Emissions by Plants*. DOI: 10.1016/b978-0-12-639010-0.50015-7.

Restrepo-Coupe, N., H. R. da Rocha, L. R. Hutyra, A. C. da Araujo, L. S. Borma, B. Christoffersen, O. M. Cabral, P. B. de Camargo, F. L. Cardoso, A. C. da Costa, et al. (2013). "What drives the seasonality of photosynthesis across the Amazon basin? A cross-site analysis of eddy flux tower measurements from the Brasil flux network". *Agricultural and Forest Meteorology* 182-183. DOI: 10.1016/j.agrformet.2013.04.031.

Riley, W. J., J. T. Randerson, P. N. Foster, and T. J. Lueker (2005). "Influence of terrestrial ecosystems and topography on coastal CO2 measurements: A case study at Trinidad Head, California". *Journal of Geophysical Research: Biogeosciences* 110.G1. DOI: https://doi.org/10.1029/2004JG000007.

Rödenbeck, C., R. F. Keeling, D. C. Bakker, N. Metzl, A. Olsen, C. Sabine, and M. Heimann (2013). "Global surface-ocean pCO2 and sea-Air CO2 flux variability from an observation-driven ocean mixed-layer scheme". *Ocean Science* 9.2. DOI: 10.5194/os-9-193-2013.

Salvucci, M. E., K. W. Osteryoung, S. J. Crafts-Brandner, and E. Vierling (2001). "Exceptional sensitivity of Rubisco activase to thermal denaturation in vitro and in vivo". *Plant Physiology* 127.3. DOI: 10.1104/pp.010357.

Sandoval-Soto, L., M. Stanimirov, M. von Hobe, V. Schmitt, J. Valdes, A. Wild, and J. Kesselmeier (2005). "Global uptake of carbonyl sulfide (COS) by terrestrial vegetation: Estimates corrected by deposition velocities normalized to the uptake of carbon dioxide (CO2)". *Biogeosciences* 2.2, pp. 125–132. DOI: 10.5194/bg-2-125-2005.

Sato, N. (1989). "Effects of implementing the Simple Biosphere Model in a general circulation model". *Journal of the Atmospheric Sciences* 46.18. DOI: 10.1175/1520-0469(1989)046<2757:EOITSB>2.0.CO;2.

Schenk, S., J. Kesselmeier, and E. Anders (2004). "How does the exchange of one oxygen atom with sulfur affect the catalytic cycle of carbonic anhydrase?" *Chemistry - A European Journal* 10.12. DOI: 10.1002/chem.200305754.

Schmidt, M., P. Bernath, C. Boone, M. Lecours, and J. Steffen (Oct. 2024). "Trends in atmospheric composition between 2004–2023 using version 5 ACE-FTS data". *Journal of Quantitative Spectroscopy and Radiative Transfer* 325, p. 109088. DOI: 10.1016/J.JQSRT.2024.109088.

Schuldt, K. N., J. Mund, I. T. Luijkx, T. Aalto, J. B. Abshire, K. Aikin, Arlyn Andrews, S. Aoki, F. Apadula, B. Baier, et al. (2021). *Multi-laboratory compilation of atmospheric carbon dioxide data for the period 1957-2019; obspack_co2_1_GLOBALVIEWplus_v6.1_2021-03-01* [*data set*]. DOI: 10.25925/20201204.

Seibt, U., J. Kesselmeier, L. Sandoval-Soto, U. Kuhn, and J. A. Berry (2010). "A kinetic analysis of leaf uptake of COS and its relation to transpiration, photosynthesis and carbon isotope fractionation". *Biogeosciences* 7.1. DOI: 10.5194/bg-7-333-2010.

Sellers, P. J., J. A. Berry, G. J. Collatz, C. B. Field, and F. G. Hall (1992). "Canopy reflectance, photosynthesis, and transpiration. III. A reanalysis using improved leaf models and a new canopy integration scheme." *Remote Sensing of Environment* 42.3. DOI: 10.1016/0034-4257(92)90102-P.

Sellers, P. J., Y. Mintz, Y. C. Sud, and A. Dalcher (1986). "A simple biosphere model (SiB) for use within general circulation models." *Journal of the Atmospheric Sciences* 43.6. DOI: 10.1175/1520-0469(1986)043<0505:ASBMFU>2.0.CO;2.

Sellers, P. J., D. A. Randall, G. J. Collatz, J. A. Berry, C. B. Field, D. A. Dazlich, C. Zhang, G. D. Collelo, and L. Bounoua (1996a). "A revised land surface parameterization (SiB2) for at-

mospheric GCMs. Part I: Model formulation". *Journal of Climate* 9.4. DOI: 10.1175/1520-0442(1996)009<0676:ARLSPF>2.0.CO;2.

Sellers, P. J., S. O. Los, C. J. Tucker, C. O. Justice, D. A. Dazlich, G. J. Collatz, and D. A. Randall (1996b). "A revised land surface parameterization (SiB2) for atmospheric GCMs. Part II: The generation of global fields of terrestrial biophysical parameters from satellite data". *Journal of Climate* 9.4. DOI: 10.1175/1520-0442(1996)009<0706:ARLSPF>2.0.CO;2.

Serio, C., S. A. Montzka, G. Masiello, and V. Carbone (2023). "Trend and Multi-Frequency Analysis Through Empirical Mode Decomposition: An Application to a 20-Year Record of Atmospheric Carbonyl Sulfide Measurements". *Journal of Geophysical Research: Atmospheres* 128.3. DOI: 10.1029/2022JD038207.

Sitch, S., P. Friedlingstein, N. Gruber, S. D. Jones, G. Murray-Tortarolo, A. Ahlström, S. C. Doney, H. Graven, C. Heinze, C. Huntingford, et al. (2015). "Recent trends and drivers of regional sources and sinks of carbon dioxide". *Biogeosciences* 12.3. DOI: 10.5194/bg-12-653-2015.

Smith, N. E., L. M. Kooijmans, G. Koren, E. Van Schaik, A. M. Van Der Woude, N. Wanders, M. Ramonet, I. Xueref-Remy, L. Siebicke, G. Manca, et al. (2020). "Spring enhancement and summer reduction in carbon uptake during the 2018 drought in northwestern Europe: Carbon uptake during 2018 Eur. drought". *Philosophical Transactions of the Royal Society B: Biological Sciences* 375.1810. DOI: 10.1098/rstb.2019.0509.

Spielmann, F. M., A. Hammerle, F. Kitz, K. Gerdel, G. Alberti, A. Peressotti, G. Delle Vedove, and G. Wohlfahrt (2023). "On the variability of the leaf relative uptake rate of carbonyl sulfide compared to carbon dioxide: Insights from a paired field study with two soybean varieties". *Agricultural and Forest Meteorology* 338. DOI: 10.1016/j.agrformet.2023.109504.

Spielmann, F. M., F. Kitz, T. Roach, I. Kranner, A. Hammerle, and G. Wohlfahrt (2025). "Effects of drought on carbonyl sulfide exchange in four plant species". *Plant Stress* 15, p. 100735. DOI: https://doi.org/10.1016/j.stress.2024.100735.

Stickel, R. E., M. Chin, E. P. Daykin, A. J. Hynes, P. H. Wine, and T. J. Wallington (Dec. 1993). "Mechanistic studies of the hydroxyl-initiated oxidation of carbon disulfide in the presence of oxygen". *The Journal of Physical Chemistry* 97.51, pp. 13653–13661. DOI: 10.1021/j100153a038.

Stimler, K., J. A. Berry, S. A. Montzka, and D. Yakir (2011). "Association between carbonyl sulfide uptake and 18Δ during gas exchange in C3 and C4 leaves". *Plant Physiology* 157.1. DOI: 10.1104/pp.111.176578.

Stimler, K., J. A. Berry, and D. Yakir (2012). "Effects of carbonyl sulfide and carbonic anhydrase on stomatal conductance". *Plant Physiology* 158.1. DOI: 10.1104/pp.111.185926.

Stimler, K., S. A. Montzka, J. A. Berry, Y. Rudich, and D. Yakir (2010). "Relationships between carbonyl sulfide (COS) and CO2 during leaf gas exchange". *New Phytologist* 186.4. DOI: 10.1111/j.1469-8137.2010.03218.x.

Stinecipher, J. R., P. Cameron-Smith, L. Kuai, N. Glatthor, M. Höpfner, I. Baker, C. Beer, K. Bowman, M. Lee, S. M. Miller, et al. (2022). "Remotely Sensed Carbonyl Sulfide Constrains Model Estimates of Amazon Primary Productivity". *Geophysical Research Letters* 49.9. DOI: 10.1029/2021GL096802.

Sun, W., K. Maseyk, C. Lett, and U. Seibt (2015). "A soil diffusion-reaction model for surface COS flux: COSSM v1". *Geoscientific Model Development* 8.10. DOI: 10.5194/gmd-8-3055-2015.

Sun, W., L. M. Kooijmans, K. Maseyk, H. Chen, I. Mammarella, T. Vesala, J. Levula, H. Keskinen, and U. Seibt (2018a). "Soil fluxes of carbonyl sulfide (COS), carbon monoxide, and carbon dioxide in a boreal forest in southern Finland". *Atmospheric Chemistry and Physics* 18.2. DOI: 10.5194/acp-18-1363-2018.

Sun, W., K. Maseyk, C. Lett, and U. Seibt (2018b). "Stomatal control of leaf fluxes of carbonyl sulfide and CO2 in a Typha freshwater marsh". *Biogeosciences* 15.11. DOI: 10.5194/bg-15-3277-2018.

— (2024). "Restricted internal diffusion weakens transpiration–photosynthesis coupling during heatwaves: Evidence from leaf carbonyl sulphide exchange". *Plant, Cell & Environment* 47.5, pp. 1813–1833. DOI: https://doi.org/10.1111/pce.14840.

Sun, Y., C. Frankenberg, M. Jung, J. Joiner, L. Guanter, P. Köhler, and T. Magney (2018c). "Overview of Solar-Induced chlorophyll Fluorescence (SIF) from the Orbiting Carbon Observatory-2: Retrieval, cross-mission comparison, and global monitoring for GPP". *Remote Sensing of Environment* 209. DOI: 10.1016/j.rse.2018.02.016.

Suntharalingam, P., A. J. Kettle, S. M. Montzka, and D. J. Jacob (2008). "Global 3-D model analysis of the seasonal cycle of atmospheric carbonyl sulfide: Implications for terrestrial vegetation uptake". *Geophysical Research Letters* 35.19. DOI: 10.1029/2008GL034332.

Tagesson, T., J. Kelly, G. Schurgers, F. Tian, J. Ardö, S. Horion, A. Ahlström, S. Olin, and R. Fensholt (2024). "Increasing global ecosystem respiration between 1982 and 2015 from Earth observation-based modelling". *Global Ecology and Biogeography* 33.1. DOI: 10.1111/geb.13775.

Talagrand, O. and P. Courtier (1987). "Variational Assimilation of Meteorological Observations With the Adjoint Vorticity Equation. I: Theory". *Quarterly Journal of the Royal Meteorological Society* 113.478, pp. 1311–1328. DOI: https://doi.org/10.1002/qj.49711347812.

Tanner, C. B. and T. R. Sinclair (2015). "Efficient water use in crop production: Research or re-search?" *Limitations to Efficient Water Use in Crop Production*. DOI: 10.2134/1983.limitationstoefficientwateruse.c1.

Tarantola, A. and B. Valette (1982). "Inverse problems = quest for information." *Journal of Geophysics* 50. URL: https://journal.geophysicsjournal.com/JofG/article/view/28.

Tarantola, A. (2005). *Inverse Problem Theory and Methods for Model Parameter Estimation*. DOI: 10.1137/1.9780898717921.

Tcherkez, G. G., G. D. Farquhar, and T. J. Andrews (2006). "Despite slow catalysis and confused substrate specificity, all ribulose bisphosphate carboxylases may be nearly perfectly optimized". *Proceedings of the National Academy of Sciences of the United States of America* 103.19. DOI: 10.1073/pnas.0600605103.

Toon, G. C., J. F. L. Blavier, and K. Sung (2018). "Atmospheric carbonyl sulfide (OCS) measured remotely by FTIR solar absorption spectrometry". *Atmospheric Chemistry and Physics* 18.3. DOI: 10.5194/acp-18-1923-2018.

Tramontana, G., M. Migliavacca, M. Jung, M. Reichstein, T. F. Keenan, G. Camps-Valls, J. Ogee, J. Verrelst, and D. Papale (2020). "Partitioning net carbon dioxide fluxes into photosynthesis and respiration using neural networks". *Global Change Biology* 26.9. DOI: 10.1111/gcb.15203.

Uher, G. and M. O. Andreae (1997). "Photochemical production of carbonyl sulfide in north sea water: A process study". *Limnology and Oceanography* 42.3. DOI: 10.4319/lo.1997.42.3.0432.

Valentini, R., P. De Angelis, G. Matteucci, R. Monaco, S. Dore, and G. E. Scarascia Mugnozza (1996). "Seasonal net carbon dioxide exchange of a beech forest with the atmosphere". *Global Change Biology* 2.3. DOI: 10.1111/j.1365-2486.1996.tb00072.x.

Van Der Laan-Luijkx, I. T., I. R. Van Der Velde, E. Van Der Veen, A. Tsuruta, K. Stanislawska, A. Babenhauserheide, H. Fang Zhang, Y. Liu, W. He, H. Chen, et al. (2017). "The CarbonTracker Data Assimilation Shell (CTDAS) v1.0: Implementation and global carbon balance 2001-2015". *Geoscientific Model Development* 10.7. DOI: 10.5194/gmd-10-2785-2017.

Van Der Tol, C., W. Verhoef, J. Verrelst, F. Magnani, G. Mohammed, J. Moreno, and J. Berry (2014). "Sensitivity of scope modelled GPP and fluorescence for different plant functional types". *Workshop on Hyperspectral Image and Signal Processing, Evolution in Remote Sensing*. Vol. 2014-June. DOI: 10.1109/WHISPERS.2014.8077544.

Van Diest, H. and J. Kesselmeier (2008). "Soil atmosphere exchange of carbonyl sulfide (COS) regulated by diffusivity depending on water-filled pore space". *Biogeosciences* 5.2. DOI: 10.5194/bg-5-475-2008.

Veres, P. R., J. Andrew Neuman, T. H. Bertram, E. Assaf, G. M. Wolfe, C. J. Williamson, B. Weinzierl, S. Tilmes, C. R. Thompson, A. B. Thames, et al. (2020). "Global airborne sampling reveals a previously unobserved dimethyl sulfide oxidation mechanism in the marine atmosphere". *Proceedings of the National Academy of Sciences of the United States of America* 117.9. DOI: 10.1073/pnas.1919344117.

Vesala, T., K. M. Kohonen, L. M. Kooijmans, A. P. Praplan, L. Foltýnová, P. Kolari, M. Kulmala, J. Bäck, D. Nelson, D. Yakir, et al. (2022). "Long-Term fluxes of carbonyl sulfide and their seasonality and interannual variability in a boreal forest". *Atmospheric Chemistry and Physics* 22.4. DOI: 10.5194/acp-22-2569-2022.

Von Hobe, M., G. A. Cutter, A. J. Kettle, and M. O. Andreae (2001). "Dark production: A significant source of oceanic COS". *Journal of Geophysical Research: Oceans* 106.C12. DOI: 10.1029/2000jc000567.

Von Hobe, M., D. Taraborrelli, S. Alber, B. Bohn, H. P. Dorn, H. Fuchs, Y. Li, C. Qiu, F. Rohrer, R. Sommariva, et al. (2023). "Measurement report: Carbonyl sulfide production during dimethyl sulfide oxidation in the atmospheric simulation chamber SAPHIR". *Atmospheric Chemistry and Physics* 23.18. DOI: 10.5194/acp-23-10609-2023.

Vries, A. de, G. Wohlfahrt, K.-M. Kohonen, C. Abadie, M. Remaud, J. Kesselmeier, A. Laasonen, M. Whelan, I. Mammarella, and T. Vesala (2025). "The Contribution of Boreal Wetlands to the Northern Hemisphere Carbonyl Sulfide Sink". *Geophysical Research Letters* 52.12, e2024GL112858. DOI: https://doi.org/10.1029/2024GL112858.

Walker, A. P., A. P. Beckerman, L. Gu, J. Kattge, L. A. Cernusak, T. F. Domingues, J. C. Scales, G. Wohlfahrt, S. D. Wullschleger, and F. I. Woodward (2014). "The relationship of leaf photosynthetic traits - Vcmax and Jmax - to leaf nitrogen, leaf phosphorus, and specific leaf area: A meta-analysis and modeling study". *Ecology and Evolution* 4.16. DOI: 10.1002/ece3.1173.

Wang, Y., L. Zhou, J. Zhuang, L. Sun, and Y. Chi (2021). "The spatial heterogeneity of the relationship between gross primary production and sun-induced chlorophyll fluorescence regulated by climate conditions during 2007–2018". *Global Ecology and Conservation* 29. DOI: 10.1016/j.gecco.2021.e01721.

Watts, S. F. (2000). "The mass budgets of carbonyl sulfide, dimethyl sulfide, carbon disulfide and hydrogen sulfide". *Atmospheric Environment* 34.5. DOI: 10.1016/S1352-2310(99)00342-8.

Wehr, R., J. W. Munger, J. B. McManus, D. D. Nelson, M. S. Zahniser, E. A. Davidson, S. C. Wofsy, and S. R. Saleska (2016). "Seasonality of temperate forest photosynthesis and daytime respiration". *Nature* 534.7609. DOI: 10.1038/nature17966.

Wehr, R. and S. R. Saleska (2015). "An improved isotopic method for partitioning net ecosystem-atmosphere CO2 exchange". *Agricultural and Forest Meteorology* 214-215. DOI: 10.1016/j.agrformet.2015.09.009.

Wehr, R., R. Commane, J. W. Munger, J. Barry Mcmanus, D. D. Nelson, M. S. Zahniser, S. R. Saleska, and S. C. Wofsy (2017). "Dynamics of canopy stomatal conductance, transpiration, and evaporation in a temperate deciduous forest, validated by carbonyl sulfide uptake". *Biogeosciences* 14.2. DOI: 10.5194/bg-14-389-2017.

Wehr, R. and S. R. Saleska (2021). "Calculating canopy stomatal conductance from eddy covariance measurements, in light of the energy budget closure problem". *Biogeosciences* 18.1. DOI: 10.5194/bg-18-13-2021.

Whelan, M. E., T. W. Hilton, J. A. Berry, M. Berkelhammer, A. R. Desai, and J. Elliott Campbell (2016). "Carbonyl sulfide exchange in soils for better estimates of ecosystem carbon uptake". *Atmospheric Chemistry and Physics* 16.6. DOI: 10.5194/acp-16-3711-2016.

Whelan, M. E., S. T. Lennartz, T. E. Gimeno, R. Wehr, G. Wohlfahrt, Y. Wang, L. M. Kooijmans, T. W. Hilton, S. Belviso, P. Peylin, et al. (2018). "Reviews and syntheses: Carbonyl sulfide as a multi-scale tracer for carbon and water cycles". *Biogeosciences* 15.12. DOI: 10.5194/bg-15-3625-2018.

Whelan, M. E., D. H. Min, and R. C. Rhew (2013). "Salt marsh vegetation as a carbonyl sulfide (COS) source to the atmosphere". *Atmospheric Environment* 73. DOI: 10.1016/j.atmosenv.2013.02.048.

White, M. L., Y. Zhou, R. S. Russo, H. Mao, R. Talbot, R. K. Varner, and B. C. Sive (2010). "Carbonyl sulfide exchange in a temperate loblolly pine forest grown under ambient and elevated CO2". *Atmospheric Chemistry and Physics* 10.2. DOI: 10.5194/acp-10-547-2010.

Williams, T. G. and L. B. Flanagan (1996). "Effect of changes in water content on photosynthesis, transpiration and discrimination against 13CO2 and C18O16O in Pleurozium and Sphagnum". *Oecologia* 108.1. DOI: 10.1007/BF00333212.

Wofsy, S. C., S. Afshar, H. M. Allen, E. C. Apel, E. C. Asher, B. Barletta, J. Bent, H. Bian, B. C. Biggs, D. R. Blake, et al. (2018). *ATom: Merged Atmospheric Chemistry, Trace Gases, and Aerosols*. [Data set]. DOI: 10.3334/ORNLDAAC/1581.

Wofsy, S. C. (2011). "HIAPER Pole-to-Pole Observations (HIPPO): Fine-grained, global-scale measurements of climatically important atmospheric gases and aerosols". *Philosophical Transactions of the Royal Society A: Mathematical, Physical and Engineering Sciences* 369.1943. DOI: 10.1098/rsta.2010.0313.

Wohlfahrt, G., K. Gerdel, M. Migliavacca, E. Rotenberg, F. Tatarinov, J. Müller, A. Hammerle, T. Julitta, F. M. Spielmann, and D. Yakir (2018). "Sun-induced fluorescence and gross primary productivity during a heat wave". *Scientific Reports* 8.1. DOI: 10.1038/s41598-018-32602-z.

Wohlfahrt, G., F. Brilli, L. Hörtnagl, X. Xu, H. Bingemer, A. Hansel, and F. Loreto (2012). "Carbonyl sulfide (COS) as a tracer for canopy photosynthesis, transpiration and stomatal conductance: Potential and limitations". *Plant, Cell and Environment* 35.4. DOI: 10.1111/j.1365-3040.2011.02451.x.

Wohlfahrt, G. and L. Gu (2015). "The many meanings of gross photosynthesis and their implication for photosynthesis research from leaf to globe". *Plant Cell and Environment* 38.12. DOI: 10.1111/pce.12569.

Wolf, A., K. Akshalov, N. Saliendra, D. A. Johnson, and E. A. Laca (2006). "Inverse estimation of Vcmax, leaf area index, and the Ball-Berry parameter from carbon and energy fluxes". *Journal of Geophysical Research Atmospheres* 111.8. DOI: 10.1029/2005JD005927.

Wong, S. C., M. J. Canny, M. Holloway-Phillips, H. Stuart-Williams, L. A. Cernusak, D. A. Márquez, and G. D. Farquhar (2022). "Humidity gradients in the air spaces of leaves". *Nature Plants* 8.8. DOI: 10.1038/s41477-022-01202-1.

Woodward, F. I., T. M. Smith, and W. R. Emanuel (1995). "A global land primary productivity and phytogeography model". *Global Biogeochemical Cycles* 9.4. DOI: 10.1029/95GB02432.

Woude, A. v. d., I. T. Luijkx, R. d. Kok, W. Peters, F. Chevallier, C. Rödenbeck, P. Ciais, N. Chandra, K. Wang, R. J. Achari, et al. (2025). "A top-down view of global and regional carbon budgets from an ensemble of atmospheric inversions". DOI: 10.22541/essoar.175376114.45413910/v1.

Wu, R., S. Wang, and L. Wang (2015). "New mechanism for the atmospheric oxidation of dimethyl sulfide. The importance of intramolecular hydrogen shift in a CH3SCH2OO radical". *Journal of Physical Chemistry A* 119.1. DOI: 10.1021/jp511616j.

Yan, Y., R. Li, L. Peng, C. Yang, C. Liu, J. Cao, F. Yang, Y. Li, and J. Wu (2019). "Emission inventory of carbonyl sulfide (COS) from primary anthropogenic sources in China". *Environmental Pollution* 247. DOI: 10.1016/j.envpol.2019.01.096.

Yang, F., R. Qubaja, F. Tatarinov, E. Rotenberg, and D. Yakir (2018). "Assessing canopy performance using carbonyl sulfide measurements". *Global Change Biology* 24.8. DOI: 10.1111/gcb.14145.

Ye, Q., M. B. Goss, J. E. Krechmer, F. Majluf, A. Zaytsev, Y. Li, J. R. Roscioli, M. Canagaratna, F. N. Keutsch, C. L. Heald, et al. (2022). "Product distribution, kinetics, and aerosol formation from the OH oxidation of dimethyl sulfide under different RO2 regimes". *Atmospheric Chemistry and Physics* 22.24. DOI: 10.5194/acp-22-16003-2022.

Yousefi, M., P. F. Bernath, C. D. Boone, and G. C. Toon (2019). "Global measurements of atmospheric carbonyl sulfide (OCS), OC34S and O13CS". *Journal of Quantitative Spectroscopy and Radiative Transfer* 238. DOI: 10.1016/j.jqsrt.2019.06.033.

Zanchetta, A., L. M. Kooijmans, S. Van Heuven, A. Scifo, H. A. Scheeren, I. Mammarella, U. Karstens, J. Ma, M. Krol, and H. Chen (2023). "Sources and sinks of carbonyl sulfide inferred from tower and mobile atmospheric observations in the Netherlands". *Biogeosciences* 20.16. DOI: 10.5194/bg-20-3539-2023.

Zeppel, M. J., J. D. Lewis, N. G. Phillips, and D. T. Tissue (2014). "Consequences of nocturnal water loss: A synthesis of regulating factors and implications for capacitance, embolism and use in models". *Tree Physiology* 34.10. DOI: 10.1093/treephys/tpu089.

Zhu, H., X. Xing, M. Wu, W. Ju, and F. Jiang (2024). "Optimizing the terrestrial ecosystem gross primary productivity using carbonyl sulfide (COS) within a two-leaf modeling framework". *Biogeosciences* 21.16. DOI: 10.5194/bg-21-3735-2024.

Zumkehr, A., T. W. Hilton, M. Whelan, S. Smith, L. Kuai, J. Worden, and J. E. Campbell (2018). "Global gridded anthropogenic emissions inventory of carbonyl sulfide". *Atmospheric Environment* 183. DOI: 10.1016/j.atmosenv.2018.03.063.

Summary

This dissertation evaluated the potential of carbonyl sulfide (COS) as a tracer for gross primary productivity (GPP) by combining experiments, modeling, and inverse analyses from leaf to global scales. The central finding is that COS provides valuable complementary information on plant carbon uptake, but its quantitative use as a global proxy for GPP remains constrained by both physiological and methodological uncertainties.

A key contribution of this work is to show that COS does not simply scale linearly with CO_2 uptake. Leaf-level experiments revealed conditions under which COS uptake responded differently from photosynthesis, including high-temperature emission potentials and amplified sensitivities to stomatal closure. At larger scales, these physiological characteristics necessitated refinements in model parameterizations of stomatal and mesophyll conductance. Although such improvements enhanced agreement with site-level flux observations after parameter optimization, the global inversions continued to reveal structural limitations—most notably a strong dependence on prior COS vegetation fluxes, incomplete representation of COS-specific processes, and the absence of diurnal variability in the inversion framework.

This dissertation further demonstrates that COS can provide information on photosynthesis that is not accessible from CO_2 alone. At the leaf scale, COS uptake offered additional constraints on stomatal conductance, complementing the traditional reliance on H_2O and CO_2 observations. At the canopy scale, COS fluxes revealed additional insights into stomatal dynamics during autumn and at night, and suggested improvements in the treatment of humidity stress as well as an original stomatal conductance model in SiB4. At the global scale, COS provided limited additional constraints on CO_2, primarily due to the sparse observational coverage of COS and the resulting weak constraints, compounded by structural limitations in current model. Nevertheless, the inversion results showing a persistent underestimation of the COS vegetation sink at high latitudes may point to biases in current GPP representations.

Taken together, these results show that COS contributes independent and complementary information across scales, underscoring its potential as a tracer of photosynthesis. At the same time, they emphasize that further progress depends on (i) refining the mechanistic understanding of COS exchange across species and environments, (ii) improving the representation of nocturnal and stress-related processes in land surface models, (iii) strengthening coupled CO_2–COS inversion frameworks, and (iv) expanding observational networks globally through coordinated campaigns and satellite missions. These advances will determine the extent to which COS vegetation fluxes can be integrated into robust global monitoring of GPP.

Acknowledgements

Completing this doctoral journey would not have been possible without the help and support of many people. The process has been both challenging and rewarding, shaping not only this thesis but also my growth as a researcher.

I am profoundly grateful to my promoter Maarten, who recognized my potential despite my lack of prior experience living abroad, and opened the door for me to step into a wider world. His patient guidance was always offered with pen and paper in hand, and those thoughtful, dedicated meetings have left a lasting impression on me. From him, I learned not only scientific knowledge but also wisdom for life. Coming from a culture where hierarchical relationships are deeply embedded, the opportunity to discuss and debate openly with him has helped shape a new vision of who I aspire to become as a researcher.

I would also like to express my sincere gratitude to my second promoter Linda, who continuously encouraged and supported me during the first two challenging years of my PhD. Her attentive guidance was invaluable as I navigated plant physiology, a field in which I initially had little background. I deeply appreciated being able to discuss research directions comfortably and openly with her. The conversations we shared as mothers during a similar period of life, and her stories about childbirth and parenting in the Netherlands, were a great source of comfort and strength.

I am thankful to all colleagues who shared discussions and knowledge related to Carbonyl Sulfide research. I truly enjoyed exchanging ideas and research experiences with Peter and Sophie from the MAQ group at Wageningen University, and with Jin from Utrecht University. I am also grateful to Wouter, Ingrid, Gerbrand, Auke, Anna-wil, Peiyi, Marnix, and all other colleagues in the Carbon group for the many insightful discussions we had. I appreciate Sandra for the joy of sharing an office at MAQ, as well as Michael, Mahrooz, and Julie for the camaraderie we built through the Air Quality course. I am especially grateful to Jordi for his warm and constant encouragement, to Folkert for the engaging conversations on Korean satellite research, and to Anja, Imme, MaryRose, Jianan, Raquel, Weibke, Kim, Esther, Farhan for the moments of rest and warmth we shared over coffee and walks. Although I cannot list every name here, every moment with my colleagues at MAQ has become an unforgettable memory.

I also extend my heartfelt appreciation to my co-authors. I am grateful to Kukka-Maaria and Richard for providing deep insights into Hyytiala and Harvard Forest sites for my first paper. My sincere thanks go to Steven M.D., Maarten W., Leon, Steven van H., Gerbrand, and Sophie for their collaboration during the sunflower experiment. I was pregnant at the time, and I am truly thankful for the kindness and understanding they showed, as well as for their continued support after the birth of my child, when my research pace inevitably slowed. I would also like to thank Ingrid for insightful input on the CO_2 aspects of the global-scale 4D-Var research, Sourish for helping develop the coupling concept, and Jin for assisting with the 4D-Var runs. Above all, I remain deeply grateful to my supervisors Maarten and Linda for their steady, dedicated supervision throughout this journey.

My heartfelt thanks also go to the friends who helped me build a life in the Netherlands. I

am especially grateful to Stella and Guus, who always rushed to my side during difficult and lonely moments, and to Hyemin, Hongeun, and Sieun, who became like family to me in Ede and offered warmth and comfort. I deeply appreciate Yiling and Oscar, with whom I shared our life story and taught me Dutch, and I am thankful to Penny, Frances, Garam, Bokyoung, Yeongjun, Hyeyeon, Jongbeom, Hestia, Mo, and Sony for their constant encouragement. I also thank the pastor and congregation of Amsterdam Jangro Church, whose faith and conversations provided great emotional and spiritual support. I would like to thank Professor Myung Suk Suh and Dr. Jongmin Yoon for laying the foundation that made my studies in the Netherlands possible, and for their enduring support. I would also like to thank my English teacher, Monica, as the daily conversations we shared meant so much to me.

After the birth of my child, my mother traveled all the way to the Netherlands every six months to care for my son, and without her help, completing this PhD would not have been possible. I also thank my father, who remained in Korea each time my mother came to help me, continuing to support me from afar and always staying on my side. I am deeply grateful to my parents-in-law for their constant concern and the Korean food they lovingly sent from home, and to my aunt, uncle, and my sister for their ongoing encouragement and thoughtful advice on parenting. I want to thank my husband, Jaeseong, who made the difficult decision to move to the Netherlands with me. His dedication to our family, even in an unfamiliar environment, allowed me to continue my research without financial worry. To my beloved son Harang, I express my deepest love. Life in a foreign country was not always easy, and without his bright spirit and boundless affection, I might have lost much of my own light along the way.

Authorship statement

Chapter 1 General introduction.

The general topic of this thesis and the broad scientific context were developed in discussion with my promotor and co-promotor. I defined the specific research questions addressed in this thesis, wrote the first draft of the chapter, and revised the text following comments from my promotors. In this chapter, I used generative Artificial Intelligence tools (ChatGPT, OpenAI) to assist with English language correction and to improve clarity of expression. I am fully responsible for the final content and interpretation.

Chapter 2 Leaf chamber experiments on the COS compensation point.

The research question and methodological approach were developed in discussion with my promotor and co-promotor. Together with co-authors, I performed the laboratory experiments and interpreted the results. I developed the conductance model with input from my promotors and co-authors. I prepared all figures and tables. I wrote the first draft of the chapter and revised the text following comments from my promotors and co-authors. I am the first author of the manuscript underlying this chapter. In this chapter, I used generative Artificial Intelligence tools (ChatGPT, OpenAI) to assist with English language correction and to improve clarity of expression.

Chapter 3 Optimizing parameters in the simple biosphere model.

The research question and experimental design were developed in discussion with my promotor and co-promotor. I implemented the land surface model, developed the inverse modelling framework, and conducted all sensitivity analyses. I interpreted the results with inputs from my promotors and co-authors, and prepared all figures and tables. I wrote the first draft of the chapter and revised the text following feedback from my promotors and co-authors. I am the first author of the manuscript underlying this chapter.

Chapter 4 Simultaneous optimization of global COS and CO_2.

I defined the research question and designed the modelling experiments in discussion with my promotor and co-authors. I performed the analyses presented in this chapter and discussed the results my promotor and co-authors. I evaluated the sensitivity of the results to different assumptions and discussed the implications with my promotors and co-authors. I prepared all figures and tables and wrote the initial draft of the chapter. I revised the text following comments from my promotor and co-authors. In this chapter, I used generative Artificial Intelligence tools (ChatGPT, OpenAI) to provide language support and improve clarity of expression.

Chapter 5 General discussion & Synthesis.

I developed the main themes and arguments of this chapter in discussion with my promotor and co-promotor.I wrote the first draft, integrated results from all previous chapters, and developed the overall synthesis. I revised the text following comments from my promotors. In this chapter, I used generative Artificial Intelligence tools (ChatGPT, OpenAI) solely for language editing and clarity.

List of Publications

Peer-reviewed Journal Articles

1. Ma, J., Kooijmans, L. M. J., **Cho, A.**, Montzka, S. A., Glatthor, N., Worden, J. R., Kuai, L., Atlas, E. L., and Krol, M. C. (2021). Inverse modelling of carbonyl sulfide: implementation, evaluation and implications for the global budget. *Atmospheric Chemistry and Physics*, 21, 3507–3529. https://doi.org/10.5194/acp-21-3507-2021

2. Kooijmans, L. M. J., **Cho, A.**, Ma, J., Kaushik, A., Haynes, K. D., Baker, I., Luijkx, I. T., Groenink, M., Peters, W., Miller, J. B., Berry, J. A., Ogée, J., Meredith, L. K., Sun, W., Kohonen, K.-M., Vesala, T., Mammarella, I., Chen, H., Spielmann, F. M., Wohlfahrt, G., Berkelhammer, M., Whelan, M. E., Maseyk, K., Seibt, U., Commane, R., Wehr, R., and Krol, M. (2021). Evaluation of carbonyl sulfide biosphere exchange in the Simple Biosphere Model (SiB4). *Biogeosciences*, 18, 6547–6565. https://doi.org/10.5194/bg-18-6547-2021

3. **Cho, A.**, Kooijmans, L. M. J., Kohonen, K.-M., Wehr, R., and Krol, M. C. (2023). Optimizing the carbonic anhydrase temperature response and stomatal conductance of carbonyl sulfide leaf uptake in the Simple Biosphere model (SiB4). *Biogeosciences*, 20, 2573–2594. https://doi.org/10.5194/bg-20-2573-2023

4. **Cho, A.**, Kooijmans, L. M. J., Driever, S. M., Wassenaar, M., Koren, G., Baartman, S. L., Mossink, L., and Krol, M. C. (2025). Leaf chamber experiments on sunflowers indicate a temperature-dependent compensation point of carbonyl sulfide. *Open Research Europe*, 5:223. https://doi.org/10.12688/openreseurope.20235.1

5. Baartman, S. L., Driever, S. M., Wassenaar, M. L. J., Kooijmans, L. M. J., Ubierna, N., Mossink, L., Popa, M. E., **Cho, A.**, Wingate, L., Röckmann, T., van Heuven, S. M. A. C., and Krol, M. C. (2025). Isotope discrimination of carbonyl sulfide (34S) and carbon dioxide (13C, 18O) during plant uptake in flow-through chamber experiments. *Biogeosciences*, 22, 5683–5703. https://doi.org/10.5194/bg-22-5683-2025

Netherlands Research School for the
Socio-Economic and Natural Sciences of the Environment

D I P L O M A

for specialised PhD training

The Netherlands research school for the
Socio-Economic and Natural Sciences of the Environment
(SENSE) declares that

Ara Cho

born on 06-07-1987 in Republic of Korea

has successfully fulfilled all requirements of the
educational PhD programme of SENSE.

Wageningen, 10 June 2026

SENSE coordinator PhD education

Dr Ir Peter Vermeulen

The SENSE Director

Dr Jampel Dell'Angelo

The SENSE Research School declares that **Ara Cho** has successfully fulfilled all requirements of the educational PhD programme of SENSE with a workload of 38.5 EC, including the following activities:

SENSE PhD Courses

- A1: Environmental Research in Context (2020)
- A2 Research in context activity: 'Organizing TransCom webinar' (2024)

Other PhD and Advanced MSc Courses

- Bayesian Statistics, PE&RC (2024)
- ICOS summer school Hyytiälä, Integrated Carbon Observing System (ICOS) (2021)
- Mindful writing?, I focus and write (2020)
- Basic Dutch I and II, Wageningen University (2021)

Management and Didactic Skills Training

- Teaching assistance in the BSc “Air Quality” (2020-2021))

Selection of Oral Presentations

- *Improved Estimation ofVegetation Uptake of Carbonyl Sulfide (COS) in a Biosphere Model (SiB4)*. European Geosciences Union, 9/12 2021, Online, Online
- *COS leaf uptake responses to temperature and vapor pressure deficit*. 3rd International COS workshop, 19/9 2022, Utrecht, Netherlands
- *Optimizing the global budget of CO2 and carbonyl sulfide using the 4D-Var coupling system*. TRANSCOM, 1/10 2024, Online, Online
- *Setting up a coupled COS-CO2 4DVAR inversion system*. 35th International TM5 meeting, 21/10 2024, Wageningen, Netherlands

The research described in this thesis was financially supported by the European Research Council (ERC) under the European Union's Horizon 2020 research and innovation programme (Grant agreement No. 742798).

Financial support from Wageningen University for printing this thesis is gratefully acknowledged.

The cover design was created by the author. Generative Artificial Intelligence tools (ChatGPT, OpenAI) were used to support the design refinement process.

